Design of confocal systems for spectral information coding

Dissertation

zur Erlangung des akademischen Grades

Doktoringenieur
(Dr.-Ing.)

vorgelegt der
Fakultät für Maschinenbau der
Technischen Universität Ilmenau

von Herrn

Dipl.-Ing. Matthias Hillenbrand

geboren am 27.01.1983 in Immenstadt/Deutschland

1. Gutachter: Prof. Dr. rer. nat. habil. Stefan Sinzinger
(Technische Universität Ilmenau)

2. Gutachter: Prof. Dr. Alois Herkommer
(Universität Stuttgart)

3. Gutachter: Prof. Dr. rer. nat. Robert Brunner
(Ernst-Abbe-Hochschule Jena)

Tag der Einreichung: 16. September 2015

Tag der Verteidigung: 29. Januar 2016

urn:nbn:de:gbv:ilm1-2016000026

Abstract

Chromatic confocal systems focus the spectral components of a polychromatic signal at different spatial positions where they are filtered with apertures. This approach is used for the encoding and decoding of information in the spectral distribution of an optical signal. The most common applications are distance sensors and hyperspectral imaging systems. In this thesis the design of chromatic confocal systems is discussed. Advanced signal models are developed systematically which take into account the physical properties of the optical system, its aberrations, and the properties of the detection system. They include incoherent light sources as well as illumination geometries of finite size and are implemented using fast numerical techniques. The signal models enable an accurate prediction of the spectral filtering characteristic which is used as the main performance criterion at all stages of the design process. Based on this performance criterion, strategies for the efficient development of starting systems are derived. They are accompanied by an aberration discussion which is focused on the compensation of aberrations in post processing and through specific optical layouts. In combination with the newly developed signal models, this approach enables the design of optimized, compact, and cost effective sensor systems which are tailored to the application-specific requirements and use cheap incoherent light sources like light-emitting diodes. The design strategies are used for the development of several demonstrators and commercial sensor systems.

Kurzzusammenfassung

Chromatisch-konfokale Systeme fokussieren die spektralen Kompenenten eines polychromatischen Signals auf unterschiedliche räumliche Positionen, an denen sie mit Hilfe von Blenden gefiltert werden. Auf diese Weise können Informationen einerseits in der Spektralverteilung eines optischen Signals gespeichert werden. Anderseits kann auch die Spektralverteilung eines polychromatischen Signals ermittelt werden. Chromatisch-konfokale Systeme werden häufig zur berührungslosen Abstandsmessung und für die ortsaufgelöste Spektroskopie eingesetzt. In dieser Arbeit werden Designstrategien für chromatisch-konfokale Systeme entwickelt. Ein Schwerpunkt liegt auf der systematischen Modellierung der Signalentstehung unter Berücksichtigung der physikalischen Eigenschaften des optischen Systems, der Abbildungsfehler und der Eigenschaften des Detektionssystems. Hierbei werden insbesondere auch inkohärente Lichtquellen und räumlich ausgedehnte Beleuchtungsgeometrien berücksichtigt. Schnelle numerische Implementationen dieser Modelle erlauben in allen Stadien des Designprozesses eine Vorhersage des spektralen Filterverhaltens. Das spektrale Filterverhalten wird als primäres Bewertungskriterium für die Leistungsfähigkeit des optischen Systems verwendet und wird zur Ableitung effektiver Designstrategien herangezogen. Die Designstrategien umfassen sowohl die Entwicklung von Startsystemen als auch den nachfolgenden Optimierungsprozess, bei dem monochromatische Abbildungsfehler berücksichtigt werden. Der Fokus liegt hierbei insbesondere auf der nachträglichen Korrektur der Abbildungsfehler während der Signalverabeitung und auf ihrer automatischen Kompensation durch bestimmte Systemanordnungen. In Kombination mit den neu entwickelten Signalerzeugungsmodellen ermöglicht dieser Ansatz die Entwicklung optimierter, kompakter und günstiger Sensorsysteme, die auf die Anforderungen des jeweiligen Anwendungsgebietes zugeschnitten sind und auf kostengünstigen Lichtquellen wie Leuchtdioden basieren. Die vorgestellten Designstrategien werden für die Entwicklung verschiedener Demonstrator- und kommerzieller Sensorsysteme eingesetzt.

Contents

Nomenclature

1 Abbreviations

1D, 2D, 3D	One-, two-, and three-dimensional
APSF	Amplitude point spread function
ASM	Angular spectrum method
CCSI	Chromatic confocal spectral interferometry
CZT	Chirp-z transform
DMD	Digital mirror device
DNI	Direct numerical integration
DOE	Diffractive optical element
EP	Entrance pupil
ENZ	Extended Nijboer-Zernike tehory
FFT	Fast Fourier transform
FP	Focal power
FR	Fourier Replicas
FWHM	Full width at half maximum
HSI	Hyperspectral imaging
IPSF	Intensity point spread function
LCA	Longitudinal chromatic aberration
LED	Light emitting diode
NA	Numerical aperture
OPL	Optical path length
OTF	Optical transfer function
PSF	Point spread function
RGB	Red green blue
RMS	Root mean square
ROE	Refractive optical element
RS_I	First Rayleigh-Sommerfeld diffraction integral
RSC	Rayleigh-Sommerfeld convolution
SA	Spatial artifacts
SNR	Signal to noise ratio
SR	Spatial replicas
SST	Sub-pixel sampling technique
TCA	Transversal chromatic aberration
XP	Exit pupil

2 Symbols and operators

a_x, a_y	Scaling factors of the chirp-z transform
$A, \tilde{A}, A_0$	Real-valued amplitude functions
AF	ENZ algebraic factor
B_1, B_2, B_3	Coefficients of the Sellmeier equation
c	Speed of light within an optical medium
c_0	Vacuum speed of light
C_1, C_2, C_3	Coefficients of the Sellmeier equation
D_1, D_2, D_3	Continuous chirp-functions of the chirp-z transform
$\tilde{D}_1, \tilde{D}_2, \tilde{D}_3$	Sampled chirp-functions of the chirp-z transform
$\mathrm{CZT}, \mathrm{CZT}^{-1}$	Forward and inverse chirp-z transforms
DF	ENZ defocus factor
$\boldsymbol{e_x}, \boldsymbol{e_y}, \boldsymbol{e_z}$	Unit vectors of the Cartesian coordinate system
E_e	Irradiance
$E_{e,\lambda}$	Spectral irradiance
f, f'	Object and image space focal lengths
$f/\#$	f-number
$fs_{\min}$	Minimum feature size
$\mathrm{FFT}, \mathrm{FFT}^{-1}$	Forward and inverse fast Fourier transforms
F'	Focal power
FP, FP'	Object and image space focal points
G	Scaling factor of the optical system
h	Space domain propagation kernel
H	Spatial frequency domain propagation kernel
$h_{m,i}$	Marginal ray height at lens element i
$\mathrm{PP}, \mathrm{PP}'$	Object and image space principal planes
I_e	Radiant intensity
$I_{e,\lambda}$	Spectral intensity
j	Imaginary unit
$\boldsymbol{k}$	Wave vector
k_x, k_y, k_z	Components of the wave vector
L_e	Radiance
$L_{e,\lambda}$	Spectral radiance
LE	Effective extent of an optical signal
LN	Numerical extent of an optical signal
m	Diffraction order
M_e	Radiant emittance
$M_{e,\lambda}$	Spectral radiant emittance
n	Refractive index of an optical medium
$\boldsymbol{n}$	Normal vector of a surface

n_x, n_y	Counting variables for the samples of a discretely sampled space domain field
n_{ν_x}, n_{ν_y}	Counting variables for the samples of a discretely sampled spatial frequency domain field
NA, NA′	Object and image space numerical apertures
N_f	Fresnel number
NP, NP'	Object and image space principal points
N_x, N_y	Number of samples in x- and y- directions
p_g	grating period
p_l	number of phase levels of a DOE
p_f	ENZ defocus parameter
P	Pupil function
Q	Radiant energy
r	Radius of curvature
$\tilde{r}$	ENZ scaled radial coordinate of the output plane
r_{z1}	Radius of a DOE's first zone
r_{AP}	Aperture radius
r_{det}	Radius of the detection pinhole
$\boldsymbol{R}, \tilde{\boldsymbol{R}}, \boldsymbol{R}_f$	Space domain position vectors
R_n^m	Zernike radial polynomials of orders n and m
s, s'	Axial object and image space distances
S	Optical path and sufraces of constant optical path
t	Time
t_x, t_y	Counting variables for the tiles of the summed field method
T	Number of tiles of the summed field method
$\tilde{u}$	scalar field in the space domain
u^z	complex amplitude in the space domain at the position z
U^z	complex amplitude in the spatial frequency domain at the position z
v_x, v_y	Counting variables for the samples within a tile of the summed field method
V	Number of samples within a single tile of the summed field method
w_x, w_y	scaled coordinates of the chirp-z transform
W	Wave aberration function
x, y, z	Cartesian object space coordinates
x', y', z'	Cartesian image space coordinates
$\mathrm{d}x, \mathrm{d}y, \mathrm{d}z, \mathrm{d}s$	Differential quantities in the space domain
$\Delta x, \Delta y$	Sampling intervals in x- and y-directions
Δz	Defocus distance
Z_n^m	Zernike polynomial of radial order n and of azimuthal order m

α, β, γ	Direction cosines
α_n^m	Real-valued Zernike coefficients
α'	Axial magnification
β_n^m	Complex-valued Zernike coefficients
β'	Lateral magnification
γ'	Angular magnification
δ_{comp}	Spectral losses within the optical system
δ_d	Spectral sensitivity of the detector
δ_t	Spectral reflection characteristics of the target
ϵ, ϵ'	Angles of incidence and exitance
ϵ_0	vacuum permittivity
ϵ_r	relative static permittivity
η	Diffraction efficiency
δ	target tilt angle
$\mathscr{F}, \mathscr{F}^{-1}$	Forward and inverse Fourier transforms
λ	Wavelength within an optical medium
λ_0	Vacuum wavelength
ν_{ref}	Abbe number of a refractive element
ν_{dif}	Abbe number of a diffractive element
ν_x, ν_y	Spatial frequencies
$\mathrm{d}\nu_x, \mathrm{d}\nu_y$	Differential quantities in the spatial frequency domain
$\Delta\nu_x, \Delta\nu_y$	Sampling intervals in the spatial frequency domain
ρ	normalized radial coordinate in the reference plane
σ, σ'	Object and image space marginal ray angles
$\mathrm{d}\sigma, \mathrm{d}\sigma'$	Paraxial object and image space marginal ray angles
σ_p, σ_p'	Object and image space chief ray angles
$\mathrm{d}\sigma_p, \mathrm{d}\sigma_p'$	Paraxial object and image space chief ray angles
ϕ	Real-valued phase function
Φ_e	Radiant power
$\Phi_{e,\lambda}$	Spectral power
Ψ	Real-valued aberration phase function
ω_i	haraxial height ratios
ω_x, ω_y	Scaled coordinates of the chirp-z transform
$\Delta\omega_x, \Delta\omega_y$	Sampling intervals of the chirp-z transform
Ω	Angular region of geometrical ray cone

3 Trademarks

ASAP® is a registered trademark of Breault Research Organization, Inc.
FRED® is a registered trademark of Photon Engineering, LLC.
MatLab® is a registered trademark of the MathWorks, Inc.
ZEMAX® is a registered trademark of Zemax, LLC.
Below, the ®-signs are omitted.

Preface

At this prominent position I want to thank the people who contributed to this thesis and influenced its content and style.

First, I want to thank my parents Monika and Gottfried Hillenbrand who taught me to choose my own path in life and supported me in all my decisions. They raised me with unquestioned love and provided a save haven at all times I struggled in life. Mom and Dad, I cannot thank you enough.

Second, I am greatly indebted to my advisor Prof. Stefan Sinzinger for all his contributions. During my diploma studies he awakened my fascination with optics, supervised all my student projects and provided me with funding through student research positions. Later, he gave me the opportunity to join his group and supervised my research. I am grateful for the freedom to choose my own research topic and to follow my own path. Additionally, I am indebted to him for his continuous support which ranged from advice on how to write my first paper to his feedback on the draft of this thesis. At same time I want to thank Prof. Robert Brunner and Prof. Alois Herkommer for examining my thesis and for serving on the thesis committee.

Further thanks go to all the current and former members of the Fachgebiet Technische Optik who accompanied me on my journey. Your company made the journey worthwhile and you are responsible for the creative environment and the nice working atmosphere. I will not forget our lively discussions, the celebrations and the many trips to the supermarket. Similarly, I want to thank all my coauthors and students who asked the right questions, supported me in the lab, helped me with mathematical and optical questions, revised the manuscripts, and inspired me to look at various topics from a different perspective.

I am extremely grateful to my partner Kerstin John who was my pillar of strength during the last twelve years. Thank you for staying calm in spite of all my questions and for giving me the time and freedom to work on my thesis. I also want to thank her, Prof. Stefan Sinzinger, Prof. Damien Kelly, Adrian Grewe, Lucia Grewe, and Dr. Sven van Haver for taking the time to read this thesis and for their help with the revisions. I am also grateful to Dr. Sven van Haver for his help with implementing the Extended Nijboer Zernike theory.

The research presented in this thesis was enabled by multiple public institutions. These are:

- Bundesministerium für Bildung und Forschung (grants 16SV3700, 16SV5384, 16SV5575K),
- Deutsche Forschungsgemeinschaft (grants 2667/1-1, SI 573/9-1)
- European Social Fund (grant 2012 FGR 0014),
- Thüringer Ministerium für Bildung, Wissenschaft und Kultur (grants PE 104-1-1, B514-10062);
- Thüringer Ministerium für Wirtschaft, Arbeit und Technologie (grant 2012 FGR 0014).

1 Introduction

Electromagnetic radiation is an important carrier of information. Several of its properties can be used to transmit information in nature and in technical systems. These properties are the intensity distribution, the spectral distribution, the propagation direction, the polarization state, the coherence state, and optical path length differences.

In this thesis technical systems are discussed which evaluate or modify the spectral intensity distribution of optical signals. For this purpose the spectral components of a polychromatic input signal are directed to different spatial positions by a chromatic confocal system. This system contains a hyperchromatic lens which focuses the spectral components at different distances along the propagation direction. The localized spectral components can then be accessed to encode or decode information in the spectral channel.

A widespread application is chromatic confocal distance sensing. It differs from confocal distance sensing in the use of a polychromatic light source in combination with a hyperchromatic lens. The hyperchromatic lens creates a range of foci and defines an axial measurement range which is evaluated in parallel, enabling high speed distance sensing. A surface brought within the measurement range reflects the incident radiation which passes the system a second time and is focused onto a detection pinhole. Only the spectral component in focus at the surface under test is also focused at the detection pinhole. All other spectral components are defocused and attenuated by the detection pinhole. In consequence, the spectral intensity distribution behind the detection pinhole contains a spectral peak and the distance between the surface under test and the sensor is encoded in the spectral position of the peak. To retrieve the distance information, the sensor signal is decoded with a spectrometer.

A chromatic confocal setup can also be used to evaluate the spectral power distribution of an optical signal. For this purpose a pinhole is shifted axially through the focal range which attenuates all spectral components but the one in focus at this specific pinhole position. An intensity measurement behind the pinhole gives the power within the focused wavelength range. The axial shift of the pinhole can be replaced by the combination of a static pinhole and a tunable chromatic confocal lens.

The extension of these applications from a single to multiple lateral channels is attractive for several reasons. First, the parallel use of several lateral channels enhances the system performance. Second, a multi-point sensor can be cheaper and smaller than a number of single-point sensors used in parallel. Third, chromatic confocal multi-point setups are suitable for new applications like one-shot three-dimensional object detection and hyperspectral imaging.

While single point sensors are usually designed for on-axis use, multi-point sensors have to image an extended field. To achieve a sufficient performance at all lateral channels, field dependent aberrations have to be well controlled. At the same time new criteria like telecentricity have to be fulfilled. In consequence, multi-point chromatic confocal sensors tend to have a significantly more complex layout than single-point sensors. To achieve optimum performance, low weight, and minimum costs, it is desirable to tailor the sensor system to the application-specific requirements. Typically, the resulting systems contain only a limited

number of off-the-shelf components like microscope objectives. The number and shape of the remaining optical components is determined in a sophisticated lens design process.

It is the main goal of this thesis to provide efficient tools and strategies for the design of chromatic confocal imaging systems. The presented methods cover all stages of the lens design process from the development of the first design concept to the prediction of the system performance in the presence of fabrication and alignment errors. Throughout the lens design process, the width and the shape of the spectral peak are used as the main performance criteria. To predict these parameters different types of signal models are developed. These signal models assume incoherently radiating illumination pinholes of finite size (e.g. 50 µm) which cannot be treated as point sources. At the same time, they include field dependent aberrations and vignetting effects. Several of these methods require extensive numerical calculations. To make these calculations feasible, new numerical methods and sampling schemes are developed.

The design strategies which build upon these methods are used for the development of several demonstrator systems and industrial sensors. These systems are either purely refractive or hybrid diffractive-refractive and range from single point sensing to one-shot three-dimensional profilometry. They show that the proposed design strategies and signal models are suitable for the development of complex sensor systems.

The thesis builds upon various publications on chromatic confocal systems. These publications cover aspects like the interpretation of the spectral peak, possible frame rates, stability, and accuracy. They also compare chromatic confocal distance sensing to other measurement principles ranging from mechanical probes to interferometry and structured-light 3D scanners. Aspects like the evaluation of the sensor signal are thus excluded from the discussion. Consequently, an uncertainty analysis of the full sensor system and the signal evaluation routines is of minor importance and is omitted. At the same time, this thesis does not provide a comparison to other measurement principles for surface topography. References to the relevant literature in these fields are given in Chap. 2.

The thesis has the following structure: Chap. 2 describes the used models of optical imaging and explains the mechanisms for spatially separating the spectral components of a polychromatic signal. It also discusses the state of the art of confocal and chromatic confocal distance sensing and lists related optical principles. While Chap. 2 presents no new material all subsequent chapters contain new contributions which exceed the state of the art. Chap. 3 provides a set of efficient methods for the wave optical calculation of the intensity distribution at defocused observation planes. Chap. 4 builds upon the results of Chap. 3 and provides signal models for spectral intensity response of chromatic confocal systems. These models are compared to experimental results. Chap. 5 describes the main factors which influence the performance of chromatic confocal systems. The results of this analysis lead to a set of concise design strategies. These strategies are used for the design of several demonstrator systems and industrial sensors which are presented in Chap. 6. Finally, Chap. 7 summarizes the main results of this thesis and provides an outlook to further research topics.

2 Fundamentals and state of the art

This chapter fulfills several purposes. First, fundamental principles and concepts which will be used throughout this thesis are introduced. The corresponding sections cover the sign convention, different models of optical imaging, basic concepts for separating spectral information, and a definition of spectral and non-spectral quantities. Second, the state of the art of confocal and chromatic confocal systems is discussed. This discussion is focused on confocal microscopy and chromatic confocal systems with an axial separation of spectral information. It includes point, line, and matrix sensors. Third, an overview of additional optical principles which make use of chromatic aberrations is provided.

2.1 Sign convention

Fig. 2.1 illustrates the sign convention used within this thesis. The coordinate system is right-handed with the positive z direction pointing to the right. The z-axis is the axis of rotational symmetry of the optical system and corresponds to the optical axis. Distances measured from the reference in the positive coordinate directions are positive while those measured in the opposing direction are negative. All angles measured in the mathematically positive direction are positive while those measured in the opposing direction are negative. This definition corresponds to the right hand rule [1]: If one looks from the base point to the tip of the coordinate vector, positive angles are measured clockwise. To indicate which line or surface is the reference, arrows pointing away from the reference are used. Distances and angles are represented by scalar quantities which possess a sign. The minus sign is not shown in figures but has to be considered in the equations. While based on a different definition, this sign convention is compatible to the one set up by Haferkorn in [2, 3]. In comparison, [4] uses the opposite sign for the definition of angles.

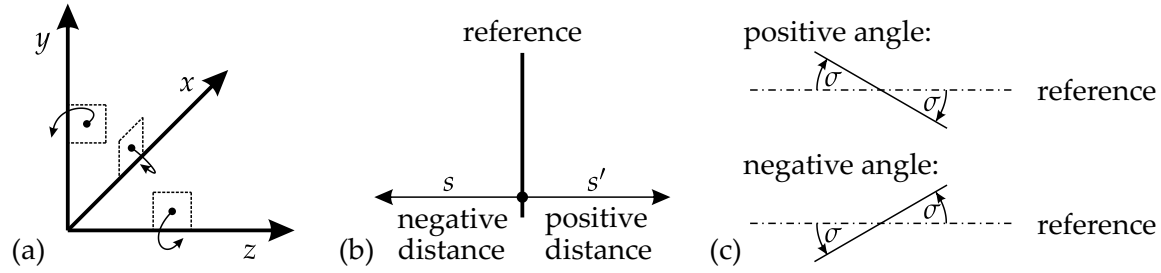

Fig. 2.1: (a) Orientation of the coordinate system and sign convention for (b) distances and (c) angles.

2.2 Models of optical imaging

In this section different models for the description of imaging optical systems are introduced. The discussion covers the wave optical model, the geometrical model, the paraxial model, and the collinear model. Typically, a combination of these models is used during the lens design process. The paraxial and the collinear models are idealized models which do not account for monochromatic aberrations. They lead to simple imaging equations which are well suited for the conceptual phase of the lens design process and for the definition of simple imaging parameters. The geometrical model is based on the tracing of rays and accounts for aberrations. Owing to its high efficiency in comparison to the wave optical model it is commonly used for the optimization phase of the development process. The wave optical model includes both aberrations and diffraction effects. It typically requires a large numerical effort and is thus mainly used to evaluate the performance of already optimized systems.

Another commonly used model is the analytical model. In this thesis it only plays a minor part and is excluded from a detailed discussion. It can be regarded as an approximation of the geometrical model and provides insight into the aberration mechanisms within the optical system. For this purpose different types of aberrations are introduced and calculated on a surface by surface basis. In the third order approximation five types of aberrations can be present in a rotationally symmetrical system: Spherical aberration, coma, astigmatism, field curvature, and distortion. The analytical model is commonly used for the development of starting systems and to identify ways of improving the performance of existing designs. The interested reader is referred to [2, 5, 6] for an in depth discussion of the analytical aberration theory.

2.2.1 Wave optical model

The wave optical model accounts for the wave nature of electromagnetic radiation. An exact analysis of wave optical effects would require a vectorial treatment of the electric and magnetic fields. In this thesis the wave optical model is used for the calculation of the irradiance distribution in the focal region of imaging systems. The analyzed systems possess apertures with diameters of thousands of wavelengths and are at the same time limited to numerical apertures (NAs) smaller than 0.5. For such systems the polarization effects and the interaction between the different components of these vectorial fields play a minor role [7, 8]. The full electromagnetic treatment can thus be reduced to a scalar analysis with only a small loss of precision [8, 9].

The dependence of the scalar field $u(\boldsymbol{R}, t)$ on the time t and the spatial position $\boldsymbol{R} = R_x \boldsymbol{e_x} + R_y \boldsymbol{e_y} + R_z \boldsymbol{e_z}$ is given by

$$\tilde{u}(\boldsymbol{R}, t) = u_0(\boldsymbol{R}) \cos\left(\phi(\boldsymbol{R}) + \omega t\right) = \mathrm{Re}\left[u_0(\boldsymbol{R}) \exp\left(j\left(\phi(\boldsymbol{R}) + \omega t\right)\right)\right] = \mathrm{Re}\left[u(\boldsymbol{R}) \exp\left(j\omega t\right)\right]. \tag{2.1}$$

Throughout this thesis, bold letters represent vectors while normal letters represent scalar values. u_0 corresponds to the magnitude of the electrical field vector. j is the imaginary unit and is defined by $j^2 = -1$. $\boldsymbol{e_x}$, $\boldsymbol{e_y}$ und $\boldsymbol{e_z}$ are the unit vectors of a Cartesian coordinate system. Together, the amplitude u_0 and the space dependent phase function $\exp(j\phi(\boldsymbol{R}))$ constitute the complex amplitude $u(\boldsymbol{R}) = u_0 \exp(j\phi(\boldsymbol{R}))$. The tilde-symbol is used to discern between the scalar field $\tilde{u}(\boldsymbol{R}, t)$ and the complex amplitude $u(\boldsymbol{R})$, see Eq. 2.1. The angular frequency ω is directly linked to the frequency ν of the electromagnetic radiation through

the equation $\omega = 2\pi\nu$. The frequency ν, the propagation speed c and the wavelength λ of the electromagnetic radiation are connected through the equation $c = \lambda\nu$. If the wave propagates in a homogeneous and isotropic medium, the wavelength λ within the medium and the vacuum wavelength λ_0 are connected through the equation

$$\lambda = \frac{\lambda_0}{n} = \frac{c_0}{n\nu} = \frac{c}{\nu}. \tag{2.2}$$

Here, n is the refractive index of the medium and c_0 is the vacuum speed of light.

In a homogeneous, isotropic, and dielectric medium $\tilde{u}(\boldsymbol{R}, t)$ follows the scalar wave equation [9]

$$\left(\frac{\partial^2\tilde{u}(\boldsymbol{R},t)}{\partial x^2} + \frac{\partial^2\tilde{u}(\boldsymbol{R},t)}{\partial y^2} + \frac{\partial^2\tilde{u}(\boldsymbol{R},t)}{\partial z^2}\right) - \frac{n^2}{c^2}\frac{\partial^2\tilde{u}(\boldsymbol{R},t)}{\partial t^2} = 0. \tag{2.3}$$

For $\tilde{u}(\boldsymbol{R}, t)$ to fulfill of the scalar wave equation for all times t, the complex amplitude $u(\boldsymbol{R})$ has to satisfy the Helmholtz equation [9]

$$\left(\frac{\partial^2 u(\boldsymbol{R})}{\partial x^2} + \frac{\partial^2 u(\boldsymbol{R})}{\partial y^2} + \frac{\partial^2 u(\boldsymbol{R})}{\partial z^2}\right) + k^2 u(\boldsymbol{R}) = 0. \tag{2.4}$$

The wave number k equals the magnitude of the wave vector:

$$k = |\boldsymbol{k}| = \sqrt{k_x^2 + k_y^2 + k_z^2} = \frac{2\pi}{\lambda}. \tag{2.5}$$

The wave vector $\boldsymbol{k} = k_x\boldsymbol{e_x} + k_y\boldsymbol{e_y} + k_z\boldsymbol{e_z}$ is perpendicular to the surfaces of constant phase. Throughout this thesis all optical media are assumed to be homogeneous and isotropic. Under this assumption the direction of the wave vector corresponds to the propagation direction of the electromagnetic wave. The following relations between the wave vector $\boldsymbol{k}$ and the direction cosines α, β and γ of the wave exist:

$$\boldsymbol{k} = k_x\boldsymbol{e_x} + k_y\boldsymbol{e_y} + k_z\boldsymbol{e_z} = \frac{2\pi}{\lambda}(\alpha\boldsymbol{e_x} + \beta\boldsymbol{e_y} + \gamma\boldsymbol{e_z}), \quad \text{with} \quad \alpha^2 + \beta^2 + \gamma^2 = 1. \tag{2.6}$$

In Fourier transform-based analyses the spatial frequencies ν_x, ν_y, and ν_z are commonly used. They are related to the components of the wave vector and to the direction cosines through the following equations:

$$\alpha = \frac{\lambda}{2\pi}k_x = \lambda\nu_x, \quad \beta = \frac{\lambda}{2\pi}k_y = \lambda\nu_y, \quad \gamma = \frac{\lambda}{2\pi}k_z = \lambda\nu_z = \sqrt{1 - (\lambda\nu_x)^2 - (\lambda\nu_y)^2}. \tag{2.7}$$

Two common solutions to the Helmholtz equation are the plane wave with the complex amplitude

$$u(\boldsymbol{R}) = \exp(j\boldsymbol{k}\boldsymbol{R}) = \exp(j(k_x x + k_y y + k_z z)) \tag{2.8}$$

and the spherical wave which is given by

$$u(R) = \frac{\exp(jkR)}{R}. \tag{2.9}$$

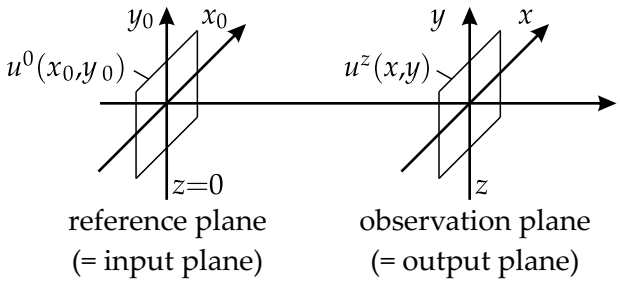

Fig. 2.2: Geometry of the considered wave optical propagation problem.

Non-paraxial propagation methods for scalar waves

Here, different wave optical propagation algorithms are discussed. It is assumed that all sources are located in the half space ($z < 0$) and that the complex amplitude is known in the plane ($z = 0$). Under these conditions the complex amplitude in the half space ($z > 0$) can be calculated without further approximations using the first Rayleigh-Sommerfeld diffraction integral ($\mathrm{RS_I}$) or equivalent analytical expressions [10, Chap. 4]. Using Green's functions the $\mathrm{RS_I}$ can be derived directly from the Helmholtz equation [11, 12]. For the solution of the $\mathrm{RS_I}$ only the complex amplitude $u^0(x,y) = u(x,y,0)$ in the plane ($z = 0$) is required. It is thus preferred to alternative integrals like the second Rayleigh-Sommerfeld diffraction integral and the Kirchhoff diffraction integral which require the derivative field $\partial u(x,y,z)/\partial z$.

The considered wave optical propagation problem is depicted in Fig. 2.2. According to the $\mathrm{RS_I}$ the complex amplitude $u^z(x,y)$ in the observation plane is linked to the complex amplitude $u^0(x_0, y_0, z = 0)$ in the reference plane through

$$u^z(x,y) = -\frac{1}{2\pi} \iint_{-\infty}^{\infty} u^0(x_0,y_0) \frac{\partial}{\partial z} \left[\frac{\exp(jkR)}{R} \right] \mathrm{d}x_0 \, \mathrm{d}y_0, \tag{2.10}$$

with

$$R = \sqrt{(x-x_0)^2 + (y-y_0)^2 + z^2} \tag{2.11}$$

and

$$\frac{\partial}{\partial z} \left[\frac{\exp(jkR)}{R} \right] = \frac{\exp(jkR)}{R} \frac{z}{R} \left(jk - \frac{1}{R} \right). \tag{2.12}$$

Eq. 2.10 is a convolution integral. It can be solved using the spatial forward and inverse Fourier transforms

$$U(\nu_x,\nu_y) = \mathscr{F}\{u(x,y)\} = \iint_{-\infty}^{\infty} u(x,y) \exp\left[-j2\pi(\nu_x x + \nu_y y)\right] \mathrm{d}x \, \mathrm{d}y, \tag{2.13}$$

$$u(x,y) = \mathscr{F}^{-1}\{U(\nu_x,\nu_y)\} = \iint_{-\infty}^{\infty} U(\nu_x,\nu_y) \exp\left[j2\pi(\nu_x x + \nu_y y)\right] \mathrm{d}\nu_x \, \mathrm{d}\nu_y. \tag{2.14}$$

Here, ν_x and ν_y are spatial frequencies and $U(\nu_x,\nu_y)$ is the angular spectrum of the space domain field $u(x,y)$. Fields defined in the space domain are indicated by lower case letters. For fields defined in the spatial frequency domain upper case letters are used. The Fourier transform representation of Eq. 2.10 is given by [13–16]:

$$u^z(x,y) = u^0(x_0,y_0) \otimes h(x_0,y_0) = \mathscr{F}^{-1}\left\{ \mathscr{F}\{u^0(x_0,y_0)\} \cdot \mathscr{F}\{h(x_0,y_0)\} \right\}, \tag{2.15}$$

with the space domain propagation kernel

$$h(x_0, y_0) = -\frac{1}{2\pi}\frac{\exp(jk\tilde{R})}{\tilde{R}}\frac{z}{\tilde{R}}\left(jk - \frac{1}{\tilde{R}}\right) \tag{2.16}$$

and

$$\tilde{R} = \sqrt{x_0^2 + y_0^2 + z^2}. \tag{2.17}$$

In focal field calculations the propagation distance is typically much larger than the wavelength. Thus, the approximation

$$jk - \frac{1}{R} \approx jk \tag{2.18}$$

can be applied. In combination with the relation $z/R = \cos\theta$ this approximation leads to Goodman's approximative version of the $\mathrm{RS_I}$ [9]:

$$u^z(x, y) \approx \frac{1}{j\lambda}\iint_{-\infty}^{\infty} u^0(x_0, y_0)\frac{\exp(jkR)}{R}\cos\theta\,\mathrm{d}x_0\,\mathrm{d}y_0. \tag{2.19}$$

Eq. 2.15 represents one of the two main propagation methods used in this thesis. It is called Rayleigh-Sommerfeld convolution (RSC). The second propagation method is known as "angular spectrum method," "spectral method," or "spectrum of plane waves propagation." Here, the expression angular spectrum method (ASM) is used. The ASM is given by [9, 10]

$$u^z(x, y) = \mathscr{F}^{-1}\left\{\mathscr{F}\left\{u^0(x_0, y_0)\right\} \cdot H(\nu_x, \nu_y)\right\}. \tag{2.20}$$

The propagation kernel $H(\nu_x, \nu_y)$ of the ASM is directly linked to the one of the RSC through a Fourier transform [14, 17, 18]:

$$H(\nu_x, \nu_y) = \mathscr{F}\{h\} = \begin{cases} \exp\left[j2\pi z\sqrt{\frac{1}{\lambda^2} - \nu_x^2 - \nu_y^2}\right] & \text{for } \nu_x^2 + \nu_y^2 \leq \frac{1}{\lambda^2} \text{ (propagating waves),} \\ \exp\left[-2\pi z\sqrt{\nu_x^2 + \nu_y^2 - \frac{1}{\lambda^2}}\right] & \text{for } \nu_x^2 + \nu_y^2 > \frac{1}{\lambda^2} \text{ (evanescent waves).} \end{cases} \tag{2.21}$$

The ASM is mathematically identical to the RSM. At the same time both methods may lead to different results when implemented numerically, see [16, 19, 20] and the discussion in Chap. 3.

Focal field calculations

The propagation of a wave field through an optical system is a demanding task. The wave field passes a number of optical interfaces and is truncated several times by different lens mounts and by the physical stop of the system. To limit the numerical effort, the full wave optical analysis is commonly replaced by a hybrid calculation method which combines a raytracing analysis of the optical system with a wave optical calculation step [10, 21]. This method is discussed in more detail in Chap. 3.1. From the raytracing data the complex amplitude $u^0(x_0, y_0)$ at the reference plane is determined. It is composed of the real amplitude function $A(x_0, y_0)$ and the phase function $\phi(x_0, y_0)$:

$$u^0(x_0, y_0) = A(x_0, y_0)\exp(j\phi(x_0, y_0)). \tag{2.22}$$

The geometry of the wave optical focal field calculation is depicted in Fig. 2.3. It is assumed that the reference plane is located at the position $z = 0$. The amplitude function $A(x_0, y_0)$ describes

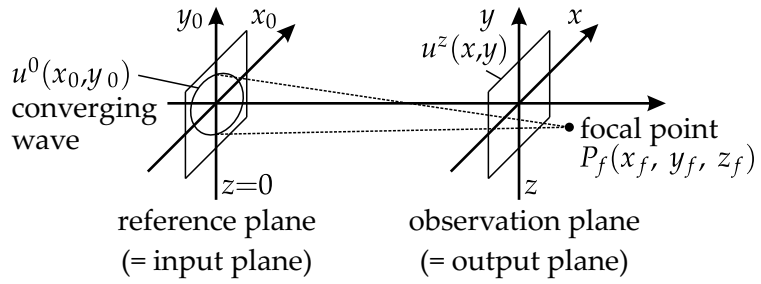

Fig. 2.3: Geometry of the considered wave optical propagation problem.

both the lateral extent of the wave field and amplitude variations. Amplitude variations are e.g. caused by absorption and reflection losses or by aperture filters. They also depend on the type of illumination. Aberrations of the optical system are modeled with the aberration phase function $\Psi(x_0, y_0)$, which is linked to the wave aberrations $W(x_0, y_0)$ through the equation

$$\Psi(x_0, y_0) = kW(x_0, y_0). \tag{2.23}$$

For a converging wave with the focus point $P_f(x_f, y_f, z_f)$ the complex amplitude $u^0(x_0, y_0)$ is given by

$$u^0(x_0, y_0) = A(x_0, y_0) \exp(j\phi(x_0, y_0)) = \tilde{A}(x_0, y_0) \exp(j\Psi(x_0, y_0)) \frac{\exp(-jkR_f)}{R_f}, \tag{2.24}$$

with

$$R_f = \sqrt{(x_f - x_0)^2 + (y_f - y_0)^2 + z_f^2}. \tag{2.25}$$

Two different models are commonly used to describe the truncation of the field $u^0(x_0, y_0)$ by the optical system: The Kirchhoff approximation and the Debye approximation. The Kirchhoff approximation operates in the space domain. Outside of the exit pupil the field is set to zero. See Chap. 2.2.4 for a definition of the exit pupil. Within the exit pupil the field is not modified:

$$\tilde{A}(x_0, y_0) = \begin{cases} A_0(x_0, y_0) & \text{within the rim of the exit pupil,} \\ 0 & \text{outside of the rim of the exit pupil.} \end{cases} \tag{2.26}$$

Possible disturbances of the field at the rim of the exit pupil are not considered. The application of the Kirchhoff approximation to the $\mathrm{RS_I}$ (Eq. 2.10) leads to the following expression for the field $u^z(x, y)$ at the observation point (x, y, z):

$$u^z(x, y) = -\frac{1}{2\pi} \iint_{AP} A_0(x_0, y_0) \frac{z}{R_f R^2} \exp\left[j\Psi(x_0, y_0)\right] \exp\left[jk\left(R - R_f\right)\right] \left(jk - \frac{1}{R}\right) \mathrm{d}x_0\, \mathrm{d}y_0. \tag{2.27}$$

In this equation the area of integration is reduced to the area of the exit pupil. The approximation $jk - \frac{1}{R} \approx jk$ which is valid for $z \gg \lambda$ leads to the simplified integral

$$u^z(x, y) = -\frac{j}{\lambda} \iint_{AP} A_0(x_0, y_0) \frac{z}{R_f R^2} \exp\left[j\Psi(x_0, y_0)\right] \exp\left[jk\left(R - R_f\right)\right] \mathrm{d}x_0\, \mathrm{d}y_0. \tag{2.28}$$

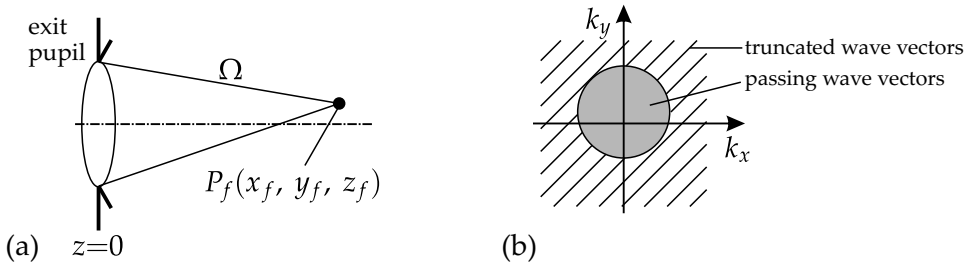

Fig. 2.4: Illustration of the Deybe approximation. (a) Geometric cone spanned by the exit pupil and the focal point. (b) Wave vectors passing the optical system.

In the Debye approximation the field is not truncated in the space domain but in the spatial frequency domain [22]. The basic concept of the Debye approximation is illustrated in Fig. 2.4: A geometrical cone spanned by the focus point P_f and the edge of the exit pupil is considered. Its angular region is labeled Ω. The cone limits the directions of wave vectors passing the optical system. If the slope of the wave vector exceeds the cone angle, the contribution of the corresponding field component is set to zero. Only the field components whose wave vectors fall within the region of the cone contribute to the image point. A detailed discussion of the Debye approximation is presented in [8, 10].

The authors of [8] write the $\mathrm{RS_I}$ in the Debye approximation in a form which is comparable to the $\mathrm{RS_I}$ in the Kirchhoff approximation:

$$u^z(x,y) = -\frac{j}{\lambda}\iint_{AP} A_0(x_0,y_0)\frac{z_f}{R_f^3}\exp\left[j\Psi(x_0,y_0)\right]\exp\left[j\boldsymbol{k}(\boldsymbol{R}-\boldsymbol{R_f})\right]\mathrm{d}x\,\mathrm{d}y. \tag{2.29}$$

They observe two differences between Eqs. 2.28 and 2.29. First, in the Debye approximation no distinction is made between the two radii R_f and R in the denominator of the amplitude function. Second, the phase difference $k(R-R_f)$ is replaced by the dot product $\boldsymbol{k}(\boldsymbol{R}-\boldsymbol{R_f})$.

If the exit pupil is located at infinity the Debye approximation will be equivalent to the Kirchhoff approximation. For finite exit pupil distances significant differences between both methods may be observed. The range of validity of the Debye approximation is analyzed in [8, 10, 23, 24]. [23] lists two criteria for its validity. The first criterion is based on the axial distance z_f between the diffracting aperture (the exit pupil) and the focal point and on the image space aperture angle θ:

$$z_f \gg \frac{\pi}{k\sin(\theta/2)}. \tag{2.30}$$

The second criterion is based on the Fresnel number N_f:

$$N_f = \frac{r_{\mathrm{AP}}^2}{\lambda z_f} \gg 1, \tag{2.31}$$

with r_{AP} being the radius of the diffracting aperture. Based on a numerical comparison between the Kirchhoff and the Debye approximations, Stamnes comes to the conclusion that for $40 < N_f$ "the difference between the Debye and Kirchhoff theories is too small to matter for most practical purposes" [10, S. 399]. Similarly, Braat et al. consider the Debye approximation valid for classical imaging systems [8].

Paraxial approximation of the first Rayleigh-Sommerfeld diffraction integral

In many wave optical analyses the paraxial approximation is used, see e.g. [9, 19]. It is based on the assumption that both the diffracting aperture and the lateral extent of the region of interest in the observation plane are small with respect to the propagation distance:

$$x_0, x, y_0, y \ll z \qquad \text{and} \qquad x_0, x_f, y_0, y_f, \ll z_f. \tag{2.32}$$

Under these conditions the truncation of the Taylor series expansion of the radii R and R_f behind the quadratic terms leads to negligible errors:

$$R = z\sqrt{1 + \frac{(x-x_0)^2}{z^2} + \frac{(y-y_0)^2}{z^2}} \approx z\left[1 + \frac{(x-x_0)^2}{2z^2} + \frac{(y-y_0)^2}{2z^2}\right] \tag{2.33}$$

$$R_f = z_f\sqrt{1 + \frac{(x_f-x_0)^2}{z_f^2} + \frac{(y_f-y_0)^2}{z_f^2}} \approx z_f\left[1 + \frac{(x_f-x_0)^2}{2z_f^2} + \frac{(y_f-y_0)^2}{2z_f^2}\right]. \tag{2.34}$$

With the additional approximations $\cos\theta \approx 1$ and $R \approx z$, the simplified version of the $\mathrm{RS_I}$ in Eq. 2.19 reduces to [9]

$$u^z_{\mathrm{par}}(x,y) = \frac{\exp(jkz)}{j\lambda z}\iint_{-\infty}^{\infty} u^0(x_0,y_0)\exp\left[\frac{jk}{2z}\left((x-x_0)^2 + (y-y_0)^2\right)\right]\mathrm{d}x_0\,\mathrm{d}y_0. \tag{2.35}$$

The same approach can also be applied to focal field calculations. Using the approximation $z/(R_f R^2) \approx 1/(zz_f)$, Eq. 2.28 can be simplified to the following expression:

$$u^z_{\mathrm{par}}(x,y) = \frac{\exp\left[jk(z-z_f)\right]}{j\lambda z z_f}\iint_{AP} A_0(x_0,y_0)\exp\left[j\Psi(x_0,y_0)\right]\cdot \exp\left[jk\left(\frac{(x-x_0)^2+(y-y_0)^2}{2z} - \frac{(x_f-x_0)^2+(y_f-y_0)^2}{2z_f}\right)\right]\mathrm{d}x_0\,\mathrm{d}y_0. \tag{2.36}$$

For very large propagation distances which fulfill the condition $(x_0^2+y_0^2)/z \ll \lambda$, Eq. 2.35 can be further simplified by neglecting the phase term $\exp\left[jk\left(x_0^2+y_0^2\right)/(2z)\right]$. In this case Eq. 2.35 reduces to the Fraunhofer diffraction integral which corresponds to a Fourier transform integral.

$$u^z_{\mathrm{Fh}}(x,y) = \frac{\exp\left[jkz + \frac{jk}{2z}\left(x^2+y^2\right)\right]}{j\lambda z}\iint_{-\infty}^{\infty} u^0(x_0,y_0)\exp\left[-\frac{jk}{z}\left(xx_0+yy_0\right)\right]\mathrm{d}x_0\,\mathrm{d}y_0. \tag{2.37}$$

Similarly, the Fresnel diffraction integral for a converging spherical wave (Eq. 2.36) can be written as a Fourier transform integral:

$$u^z_{\mathrm{par}}(x,y) = \frac{\exp\left[jk\left(z - z_f + \frac{x^2+y^2}{2z} - \frac{x_f^2+y_f^2}{2z_f}\right)\right]}{j\lambda z z_f}\iint_{AP} A_0(x_0,y_0)\exp\left[j\Psi(x_0,y_0)\right]\times \exp\left[jk\left(x_0^2+y_0^2\right)\frac{z_f-z}{2zz_f}\right]\exp\left[\frac{jk}{z_f}\left(x_f x_0 + y_f y_0\right)\right]\exp\left[-\frac{jk}{z}\left(xx_0+yy_0\right)\right]\mathrm{d}x_0\,\mathrm{d}y_0. \tag{2.38}$$

The term

$$\exp\left[jk\left(x_0^2+y_0^2\right)\frac{z_f-z}{2zz_f}\right]\approx\exp\left[jk\left(x_0^2+y_0^2\right)\frac{-\Delta z}{2z_f^2}\right],\ \text{with}\ \Delta z=z-z_f \tag{2.39}$$

corresponds to a defocus term. It can be treated separately or as a part of the aberration function $\Psi(x_0,y_0)$. For $(z=z_f)$ the observation plane coincides with the focus plane and the defocus term disappears. In this case the result agrees with the common assumption that the Fourier transform of a complex amplitude $A_0(x_0,y_0)\exp[j\Psi(x_0,y_0)]$ can be observed at the focus plane of a lens. The term $\exp\left[jk/z_f\left(x_fx_0+y_fy_0\right)\right]$ corresponds to a linear phase which leads to a lateral shift of the output field to the focal point (x_f,y_f).

2.2.2 Geometrical model

The geometrical optics model is used throughout this thesis for the analysis and optimization of imaging systems. The main concepts of geometrical optics can be derived from the wave equation by assuming that the wavelength λ approaches zero. One of the main quantities of geometrical optics is the optical path $S(r)$. It is often called the eikonal and follows the eikonal equation [5, Eq. 3.15b]

$$\left(\frac{\partial S}{\partial x}\right)^2+\left(\frac{\partial S}{\partial y}\right)^2+\left(\frac{\partial S}{\partial z}\right)^2=n^2(x,y,z), \tag{2.40}$$

n being the refractive index. The wave fields of geometrical optics are commonly described by surfaces of constant optical path ($S(x,y,z)=\text{const}$). These surfaces are called geometrical wavefronts or geometrical wave surfaces.

Most geometrical optics analyses are based on tracing rays which are defined as orthogonal trajectories to the geometric wavefronts $S(x,y,z)=\text{const}$. In isotropic media the ray direction coincides with the direction of the average Poynting vector. An important property of a ray is its optical path length (OPL). For a ray which links the points P_1 and P_2 it is given by

$$\mathrm{OPL}(P_1,P_2)=\int_{P_1}^{P_2}n\,\mathrm{d}s=S(P_2)-S(P_1). \tag{2.41}$$

In this thesis only homogeneous media are considered. All rays are thus represented by sections of straight lines. If the points P_1 and P_2 lie within a single optical medium with refractive index n, the optical path length $\mathrm{OPL}(P_1,P_2)$ is given by the product of the geometrical distance $\overline{P_1P_2}$ and n. The propagation time from P_1 to P_2 is given by

$$t(P_1,P_2)=\frac{\overline{P_1P_2}}{c}=\frac{\mathrm{OPL}(P_1,P_2)}{c_0}, \tag{2.42}$$

c_0 being the vacuum speed of light and $c=c_0/n$ being the speed of light within the medium.

At boundary surfaces between neighboring homogeneous and isotropic media the incident radiation is split into a reflected and a transmitted part according to the Fresnel formulas [5, Eqs. 20, 21]. The magnitudes of the reflected and transmitted parts depend on the polarization state of the incident radiation. This model can also be transferred to rays by assigning polarization

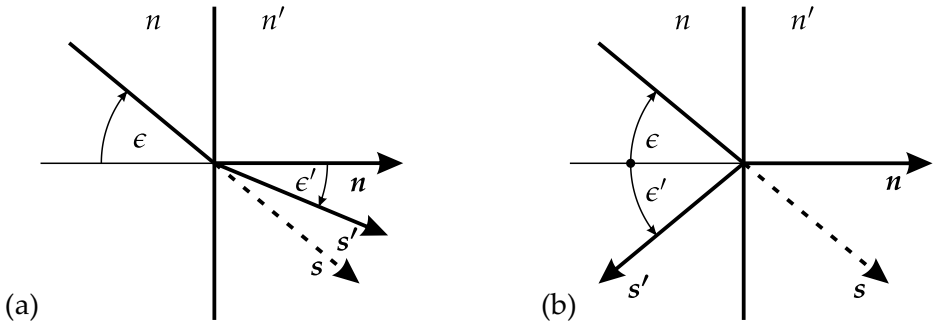

Fig. 2.5: Deflection of a ray at an optical interface according to (a) Snell's law of refraction and (b) the law of the reflection.

states to the rays and by performing a polarization raytrace. A polarization raytrace includes the calculation of the Fresnel formulas at the boundaries between adjacent media.

At these boundaries the rays are deflected according to Snell's law of refraction or the law of reflection. The scalar version of Snell's law is given by

$$n(\lambda)\sin(\epsilon) = n'(\lambda)\sin\left(\epsilon'\right). \tag{2.43}$$

It is valid within the incidence plane which is defined by the surface normal at the intersection point and the direction vector of the incident ray. The geometries within the incidence plane are shown in Fig. 2.5. Throughout this thesis non-primed values are object space values while image space values are primed. ϵ and ϵ' are the angles of incidence and exitance, while $n(\lambda)$ and $n'(\lambda)$ are the object and image space refractive indices. An evaluation of three-dimensional (3D) geometries is possible with the vectorial version of Snell's law [3, 25, Eq. 2.34]:

$$n(\boldsymbol{s}\times\boldsymbol{n}) = n'(\boldsymbol{s'}\times\boldsymbol{n}), \tag{2.44}$$

$\boldsymbol{s}$ being the unit vector of the incident ray, $\boldsymbol{s}'$ being the unit vector of the refracted ray, and $\boldsymbol{n}$ being the unit normal vector of the surface at the intersection point. Eq. 2.44 can be solved for the direction of the refracted ray:

$$\boldsymbol{s}' = \frac{n}{n'}\boldsymbol{s} - \boldsymbol{n}\left\{\frac{n}{n'}(\boldsymbol{ns}) - \sqrt{1-\left(\frac{n}{n'}\right)^2\left[1-(\boldsymbol{ns})^2\right]}\right\}. \tag{2.45}$$

In the same manner, the scalar and vectorial versions of the law of reflection are given by

$$\epsilon' = -\epsilon \qquad \text{and} \qquad \boldsymbol{s}\times\boldsymbol{n} = \boldsymbol{s}'\times\boldsymbol{n}. \tag{2.46}$$

The corresponding geometry is shown in Fig. 2.5(b). The direction of the reflected ray is given by

$$\boldsymbol{s}' = \boldsymbol{s} - 2(\boldsymbol{ns})\boldsymbol{n}. \tag{2.47}$$

The vectorial laws of refraction (Eq. 2.45) and reflection (Eq. 2.47) are the basis for an efficient raytracing-based analysis and optimization of imaging systems.

The geometrical model is valid if the changes in the magnitude of the electric and magnetic field components over regions of the wavelength are small with respect to their total magnitude, see [5, Chap. 3.1.4]. For finite wavelengths this condition is violated at the edge of an aperture and in the focal region. Geometrical optics thus provides wrong predictions of

the electromagnetic field close to an aperture and close to the focus. Apart from these two limitations the geometrical optics model often agrees well with the wave optical model.

2.2.3 Evaluation of aberrations in the wave optical and the geometrical model

Both the wave optical model and the geometrical model account for the aberrations of the optical system. These aberrations are typically analyzed either at the exit pupil (see Chap. 2.2.4) or in the focal region. At the exit pupil aberrations are evaluated by comparing the real wavefront with the ideal wavefront. The resulting phase and amplitude deviations have already been included in the wave optical model through the amplitude function A_0 and the aberration phase function Ψ. These functions can be approximated with Zernike polynomials. Zernike polynomials provide an orthogonal set of basis functions over the unit circle [26]. They are commonly used for the description of wavefronts and optical surfaces. The classical real-valued Zernike polynomials of radial order n and azimuthal order m are given by

$$Z_n^m = R_n^m(\rho)\cos m\theta \qquad \text{and} \qquad Z_n^{-m} = R_n^m(\rho)\sin m\theta, \tag{2.48}$$

with the positive integers n and m, where $m \leq n$. ρ is the normalized radial coordinate and θ is the azimuthal angle. The radial polynomials $R_n^m(\rho)$ are given by the equation

$$R_n^m(\rho) = \sum_{k=0}^{\frac{n-m}{2}} (-1)^k \frac{(n-k)!}{k!\left(\frac{n+m}{2}-k\right)!\left(\frac{n-m}{2}-k\right)!}\rho^{n-2k}, \tag{2.49}$$

for $n-m$ even. They are identical to 0 for odd values of $n-m$.

Typically, only the aberration phase function Ψ is expanded in a series of Zernike polynomials:

$$\Psi(\rho,\theta) = \sum_{n,m}\left[\alpha_n^m Z_n^m + \alpha_n^{-m} Z_n^{-m}\right]. \tag{2.50}$$

However, the amplitude function A_0 may be represented by a second series. This way the complex amplitude of an arbitrary field may be described analytically with two series of Zernike polynomials. Alternatively, the same field can be modeled with a single complex-valued series of Zernike polynomials. This approach is used in the Extended Nijboer Zernike theory which will be discussed in Chap. 3.3. There, the deviation between the real wavefront and the ideal spherical wave is represented by the complex pupil function

$$P(\rho,\theta) = A_0(\rho,\theta)\exp j\Psi(\rho,\theta). \tag{2.51}$$

With the complex Zernike polynomials

$$Z_n^m = R_n^m(\rho)\exp jm\theta \tag{2.52}$$

this pupil function is written as

$$P(\rho,\theta) = \sum_{n,m}\beta_n^m Z_n^m(\rho,\theta). \tag{2.53}$$

While the real-valued polynomial coefficients α_n^m for $\Psi(\rho,\theta)$ can be directly related to specific aberration types, this step is not easily possible with the complex coefficients β_n^m.

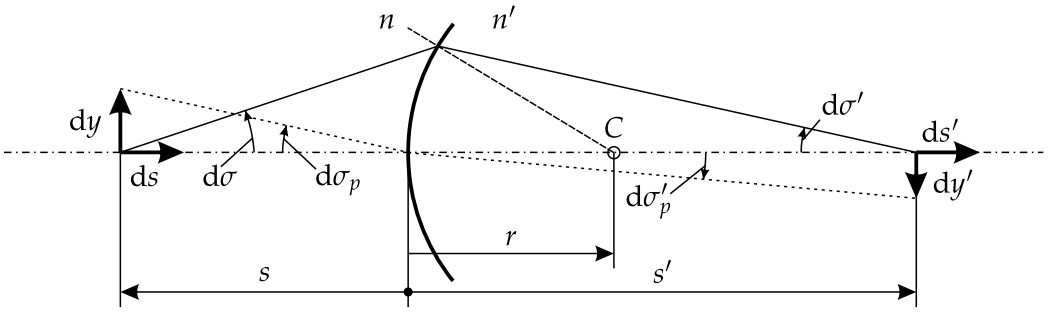

Fig. 2.6: Paraxial imaging at a single refractive surface with the radius r and the center of curvature C.

The effects of aberrations can be analyzed in the focal region by evaluating the field distribution caused by a point source in object space. This approach is called a point spread function (PSF) analysis. It is based either on the amplitude (amplitude PSF, APSF) or the intensity (intensity PSF, IPSF) of the resulting field. If the field at the exit pupil of the optical system is known, wave optical propagation methods may be used to calculate the resulting PSF without further approximations. The PSF corresponds to the impulse response of the optical system. Its Fourier transform is the optical transfer function (OTF). It provides insight into the contrast and phase shifts with which the spatial frequencies of the object are imaged by the optical system.

An approximation of the PSF may be obtained with the rays of the geometrical model. In this case the intensity in the observation plane is derived from the local ray density. Other ray-based analysis methods provide further insight into the aberrations of the optical system. A simple method is the spot diagram which shows how a bundle of rays from a single object point intersects the observation plane. Often, the root mean square (RMS) spot radius is used as a single-valued performance criterion. It is calculated from the data shown in the spot diagram. If all contributing rays have the same weight and intersect the observation plane at the coordinates x_i and y_i, the RMS spot radius is given by

$$R_{\mathrm{RMS}} = \sqrt{\frac{1}{N}\sum_{i=1}^{N}\left[(x_i - x_c)^2 + (y_i - y_c)^2\right]}. \tag{2.54}$$

x_c and y_c are the coordinates of the reference point which is typically given by the spot's center of mass ($x_c = 1/N \sum x_i$, $y_c = 1/N \sum y_i$) or by the intersection coordinates of the chief ray. Similar RMS spot calculations are commonly included in the merit function during the optimization of an optical system. Another frequently used analysis method is the lateral aberration ray fan which shows the change of the ray coordinate at observation plane in dependence on the pupil coordinate.

2.2.4 Paraxial and collinear model

Paraxial model

The paraxial model can be considered a simplified version of the geometrical model [2, 6, 27]. Its range of validity is limited to a narrow region surrounding the optical axis of a rotationally symmetrical imaging system. Within this region the non-linear effects are neglected and

simple imaging equations can be derived. Fig. 2.6 illustrates paraxial imaging at a single refractive surface. Infinitesimal object ($\mathrm{d}y$) an image heights ($\mathrm{d}y'$) as well as infinitesimal ray angles $\mathrm{d}\sigma$, $\mathrm{d}\sigma'$, $\mathrm{d}\sigma_p$, and $\mathrm{d}\sigma_p'$ are assumed.

The object distance s and the image distance s' are related to the radius of curvature r and the object space and image space refractive indices (n and n') through the Abbe invariant

$$Q = n\left(\frac{1}{r} - \frac{1}{s}\right) = n'\left(\frac{1}{r} - \frac{1}{s'}\right). \tag{2.55}$$

This equation defines a single image distance which is independent of the ray angle $\mathrm{d}\sigma$. All rays from a specific paraxial object point intersect in a single image point and blurring of the image point is absent. A second important equation valid within the paraxial region is the Helmholtz invariant

$$n\,\mathrm{d}y\,\mathrm{d}\sigma = n'\,\mathrm{d}y'\,\mathrm{d}\sigma'. \tag{2.56}$$

It links the object and image heights with the ray angles $\mathrm{d}\sigma$ and $\mathrm{d}\sigma'$. With the approximation $\mathrm{d}\sigma'\,/\,\mathrm{d}\sigma = s/s'$ it leads to an equation for the paraxial lateral magnification β':

$$\beta' = \frac{\mathrm{d}y'}{\mathrm{d}y} = \frac{n}{n'}\frac{s'}{s}. \tag{2.57}$$

Two additional paraxial relations are the paraxial angular ratio

$$\gamma' = \frac{\mathrm{d}\sigma'}{\mathrm{d}\sigma} = \frac{s}{s'} \tag{2.58}$$

and the paraxial axial magnification

$$\alpha' = \frac{\mathrm{d}s'}{\mathrm{d}s} = \frac{s'^2 n}{s^2 n'}. \tag{2.59}$$

$\mathrm{d}s'$ is the differential axial shift of the image point which is caused by a differential axial shift $\mathrm{d}s$ of the object point. The three quantities α', β', and γ' are related through the equation

$$\alpha'\gamma' = \beta'. \tag{2.60}$$

Eq. 2.57 establishes a linear relation between the extents of the image and the object. The paraxial model is thus free of distortion and monochromatic aberrations in general. As the refractive indices may change with wavelength, the paraxial model can be used to describe both longitudinal and transversal chromatic aberrations.

Complex optical systems may be analyzed by using Eqs. 2.55 to 2.59 iteratively on a surface-by-surface basis. Reflective surfaces may be included in the model by setting $n' = -n$. With its set of linear equations the paraxial model is well suited for an approximative analysis of the principal properties of an optical system. It also enables the efficient pre-design of optical systems based on first order properties.

Collinear model

In the paraxial model the optical system is described surface by surface. In contrast, the collinear model is a linear systems model [2, 5]. Typically, several optical elements are combined in an optical system which is described by cardinal elements. The layout of a collinear system

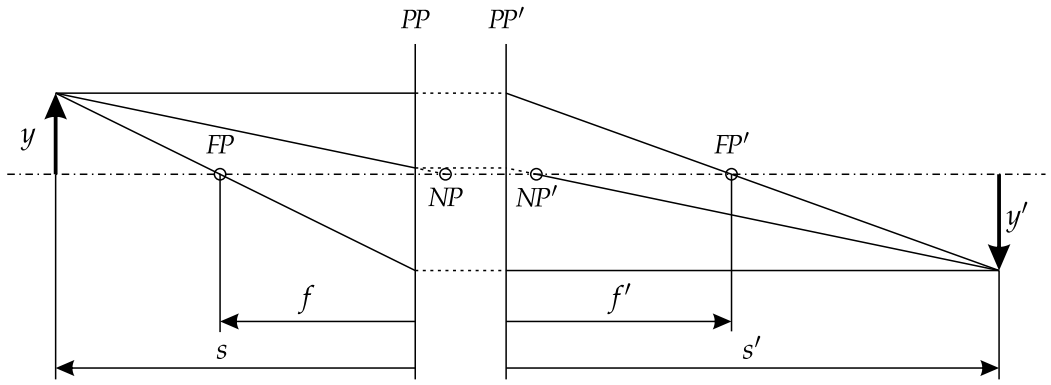

Fig. 2.7: Collinear model of an imaging optical system.

is shown in Fig. 2.7. Analogously to the paraxial quantities of Eqs. 2.57 to 2.59 the following quantities exist in the collinear model:

- Collinear lateral magnification:

$$\beta' = \frac{y'}{y} = -\frac{s'}{s}\frac{f}{f'}. \tag{2.61}$$

- Collinear angular ratio:

$$\gamma' = \frac{\tan\sigma'}{\tan\sigma} = \frac{s}{s'}. \tag{2.62}$$

- Collinear axial magnification:

$$\alpha' = \frac{\mathrm{d}s'}{\mathrm{d}s} = -\left(\frac{s'}{s}\right)^2 \frac{f}{f'}. \tag{2.63}$$

Based on these quantities two types of cardinal elements can be defined: The principal planes PP and PP' are defined by the relation $\beta' = 1$, i.e. an object positioned in PP is imaged with $\beta' = 1$ into PP'. Similarly, the nodal points NP and NP' are defined by $\gamma' = 1$. A ray intersecting the optical axis at the point NP thus intersects the optical axis at NP' at the same angle. In contrast to the previous two types of cardinal points the focal points FP and FP' are not optically correlated. The object space focal point is imaged to infinity. Any object space ray intersecting the optical axis at the point FP will thus be parallel to the optical axis in image space. At the same time, any image space ray intersecting the optical axis at the point FP' is parallel to the optical axis in object space. The distances of the focal points from the principal planes corresponds to the object and image space focal lengths f and f'. The focal power F' of the lens is defined as $F' = 1/f'$. The distance between the object plane and PP is denoted by s while the distance between PP' and the image plane is denoted by s'. In contrast to the paraxial model the collinear model is not restricted to small angles. Instead, the full object and image sizes as well as non-paraxial ray angles are used. The object and image distances are related to the focal lengths f and f' through the imaging equation

$$\frac{f'}{s'} + \frac{f}{s} = 1. \tag{2.64}$$

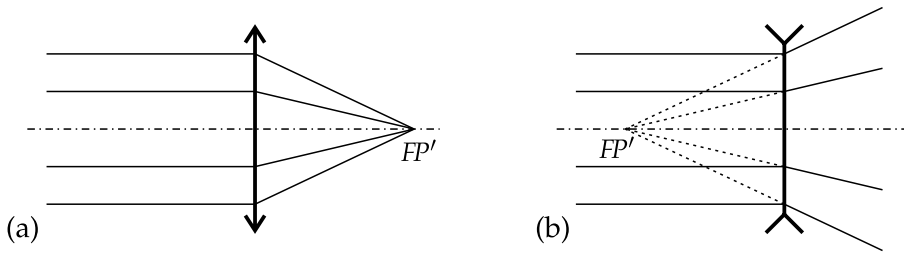

Fig. 2.8: Simplified representation of coinciding principal planes in the collinear model. (a) outside pointing arrows represent an optical system with positive focal power while (b) inward pointing arrows represent an optical system with negative focal power.

For refractive optical systems with the same media in object and image space the nodal points *NP* and *NP′* coincide with the principal planes *PP* and *PP′*, respectively. In this case the object and image space focal lengths have the same magnitude but the opposite sign ($f' = -f$). In the collinear model the rays are only deflected at the principal planes which allows for simple visual representations of complex optical systems. To further simplify the discussions within this thesis the principal planes are often assumed to coincide. Following [28, 29] they are drawn with outward and inward arrows to indicate subsystems with positive and negative focal powers, see Fig. 2.8.

Similarly to the paraxial model, the collinear model is well suited for describing the main properties of an imaging system with a set of simple parameters. Several equations like the Lensmaker's equation link the quantities of the collinear model to parameters of the optical system. The Lensmaker's equation

$$F' = \frac{1}{f'} = (n-1)\left[\frac{1}{r_1} - \frac{1}{r_2} + \frac{(n-1)s_{12}}{nr_1r_2}\right], \tag{2.65}$$

relates the collinear focal length of a lens to its radii of curvature r_1 and r_2, its refractive index n, and its vertex thickness s_{12}. The thickness of a lens is often assumed to be negligibly small. In this case Eq. 2.65 can be reduced to the thin lens equation

$$F' = \frac{1}{f'} \approx (n-1)\left[\frac{1}{r_1} - \frac{1}{r_2}\right]. \tag{2.66}$$

A detailed discussion of the collinear imaging model and the corresponding imaging equations is provided in [2]. The collinear parameters of an optical system can also be obtained from (paraxial) raytracing data. An example is the identification of *FP′*. For this purpose a ray is traced which is parallel to the optical axis in object space. The image space coordinate at which the ray intersects the optical axis corresponds to *FP′*.

The aperture stop and its images

In reality, all optical surfaces have a finite lateral extent. Typically, the ray cone emerging from the on-axis point is limited by a single surface boundary. This specific boundary is called the aperture stop. The object and image space images of the aperture stop are called the entrance pupil (EP) and the exit pupil (XP), respectively. The position and the size of the pupils are typically determined using paraxial or collinear imaging equations.

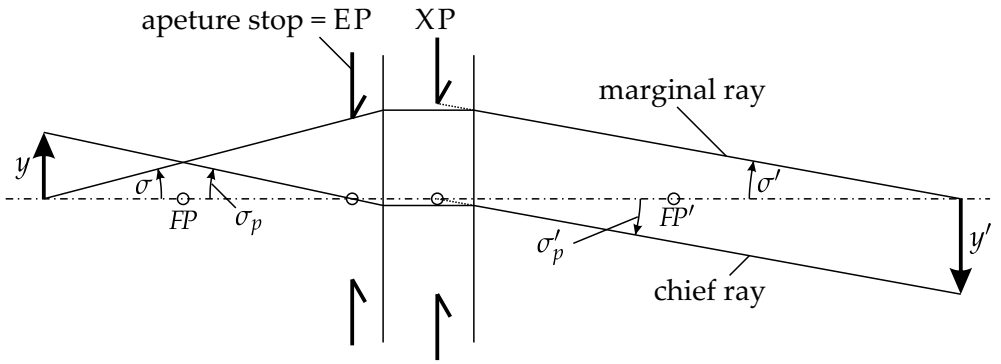

Fig. 2.9: Definition of the aperture stop and its images in the collinear model.

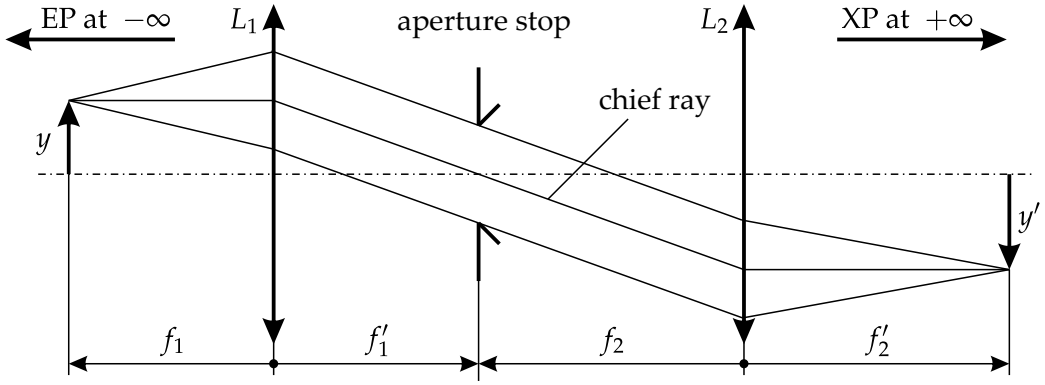

Fig. 2.10: Collinear model of a double telecentric imaging system.

The concept of the aperture stop and its images is linked to the definition of two principal rays: The marginal ray and the chief ray which are both depicted in Fig. 2.9. The marginal ray links the on-axis point of the object to the edge of the EP. It also passes the edge of the aperture stop and links the edge of the XP with the on-axis image point. The chief ray connects a specific object point (typically the outermost point of the object) to the center of the EP. It also passes the center of the aperture stop and the center of the XP. Its intersection point with the Gaussian image plane is commonly used to define the image point. The angles σ_p and σ'_p between the chief ray and the optical axis are the object and image space field angles, respectively. Similarly, the marginal ray defines the object space aperture angle σ and the image space aperture angle σ'. These values are directly related to the system's object and image space numerical apertures

$$\mathrm{NA} = n \sin\sigma, \qquad \mathrm{NA}' = n' \sin\sigma'. \tag{2.67}$$

If the system fulfills Abbe's sine condition, NA and NA′ are linked directly to the collinear lateral magnification:

$$\beta' = \frac{\mathrm{NA}}{\mathrm{NA}'}. \tag{2.68}$$

The stop position has an impact on both the aberrations and the perspective of the optical system. The perspective is related to the way in which the lateral position of the image point changes if either the object or the image plane is shifted axially. In optical metrology telecentric systems are commonly used as their lateral magnification is independent of the object and/or image distance. Fig. 2.10 shows the collinear layout of a double telecentric imaging system.

Telecentricity is obtained if the chief ray is parallel to the optical axis. Object space telecentricity is realized by placing the aperture stop at the focal point F_1'. As the focal point F_2 lies at the same position the system is also telecentric in image space. Telecentricity requirements will be used during the design of chromatic confocal line and matrix sensors.

2.3 Spectral properties of optical elements and methods for the spatial separation of spectral components

A main topic of this thesis is the encoding and decoding of information in the spectral channel. For this purpose the spectral components of a polychromatic signal are directed to different spatial positions for manipulation or evaluation. In this section dispersion and interference are discussed as two methods for separating the spectral components.

2.3.1 Spectral properties of refractive optical elements

In optics, dispersion refers to the dependence of the propagation speed of electromagnetic radiation on the wavelength λ. The reduction of the propagation speed from the value c_0 in vacuum to the value $c(\lambda)$within a dispersive medium is described by the wavelength-dependent refractive index

$$n(\lambda) = \frac{c_0}{c(\lambda)}. \tag{2.69}$$

All media used in this thesis show normal dispersion characteristics, i.e. $n(\lambda)$ decreases with growing λ. The discussion is limited to homogeneous and isotropic media whose refractive index does not depend on the spatial position, the propagation direction, or the polarization state of the electromagnetic radiation. The refractive index and the dispersion characteristics may vary significantly between different optical media. Their wavelength dependent refractive index is commonly described using empirical dispersion equations like the Sellmeier equation [30]

$$n^2(\lambda) = 1 + \frac{B_1\lambda^2}{C_1 - \lambda^2} + \frac{B_2\lambda^2}{C_2 - \lambda^2} + \frac{B_3\lambda^2}{C_3 - \lambda^2}. \tag{2.70}$$

The coefficients B_i and C_i are typically obtained from experimental data.

Dispersion leads to a wavelength dependent change of the propagation direction at the interface between neighboring media according to Snell's law of refraction (Eq. 2.45), see Fig. 2.11(a). Optical elements which deflect light according to Snell's law of refraction will be called refractive optical elements (ROEs). The amount of dispersion depends on the optical material. Fig. 2.11(b) shows the wavelength dependent refractive index for the common optical materials N-BK7, N-SF6, and SIO_2. A simple categorization of optical materials with respect to their dispersion characteristics is possible with the Abbe number. In the general version it is defined as

$$\nu_{\text{ref},\,\lambda_0} = \frac{n(\lambda_0) - 1}{n(\lambda_1) - n(\lambda_2)}. \tag{2.71}$$

In the visual range the following wavelength triples are most commonly used:

$$\begin{aligned} \nu_{\text{ref},\,d}: &\quad \lambda_0 = d = 587.56\,\text{nm}, \quad \lambda_1 = F = 486.1\,\text{nm}, \quad \lambda_2 = C = 656.3\,\text{nm}; \\ \nu_{\text{ref},\,e}: &\quad \lambda_0 = e = 546.07\,\text{nm}, \quad \lambda_1 = F' = 479.99\,\text{nm}, \quad \lambda_2 = C' = 643.85\,\text{nm}. \end{aligned} \tag{2.72}$$

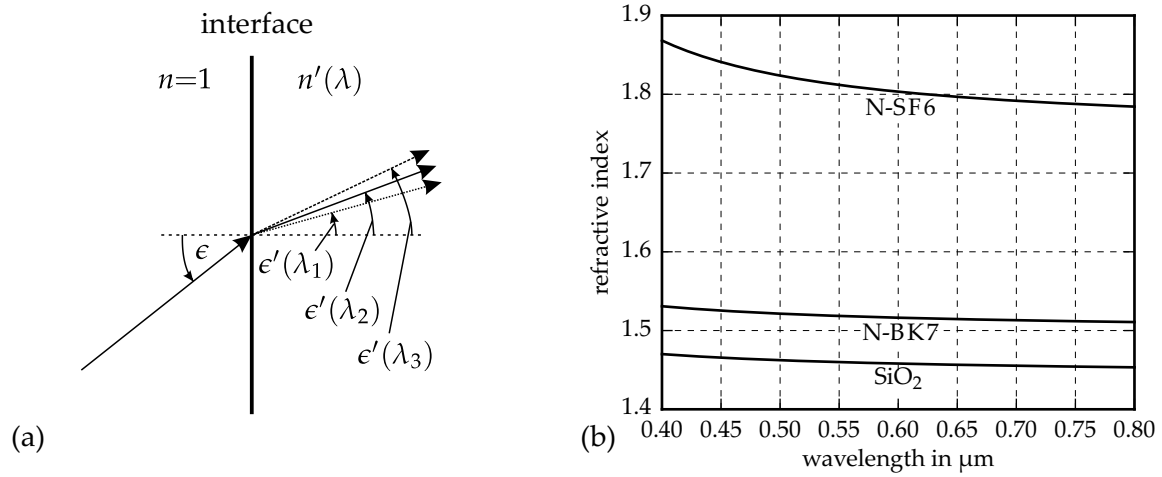

Fig. 2.11: (a) Wavelength dependent refraction of a ray at an optical interface and (b) wavelength dependence of the refractive index for three different optical materials

Typical values of $\nu_{\text{ref},\,d}$ and $\nu_{\text{ref},\,e}$ range from 20 to 95. Smaller values indicate a stronger dispersion.

Dispersion has a direct impact on the focal power and the focal length of a refractive lens. The wavelength dependent version of the Lensmaker's equations for a thin lens (Eg. 2.66) is given by

$$F'(\lambda) = \frac{1}{f'(\lambda)} = (n(\lambda) - 1)\left[\frac{1}{r_1} - \frac{1}{r_2}\right] = F'(\lambda_0)\frac{n(\lambda) - 1}{n(\lambda_0) - 1}. \tag{2.73}$$

2.3.2 Spectral properties of diffractive optical elements

A second mechanism for separating the spectral components of a polychromatic signal is multiple beam interference caused by diffractive optical elements (DOEs). DOEs lead to local modifications of the amplitude or phase of an incident wavefront. In both cases specific propagation directions exist for which the generated sub-wavefronts add constructively. These specific propagation directions are called diffraction orders and contain most of the incident power. For an ideal grating which has a period p_g and is illuminated by a plane wave, the direction of the m-th diffraction order can be determined from the grating equation [31]:

$$\sin\epsilon' = \frac{m\lambda}{p_g} \pm \sin\epsilon. \tag{2.74}$$

This equation is illustrated in Fig. 2.12(a). The plus sign accounts for a transmission grating and the minus sign for a reflection grating. ϵ and ϵ' are the angles of incidence and exitance. According to Eq. 2.74 $\sin\epsilon'$ depends linearly on the wavelength. Gratings with small periods may thus enable a much stronger separation of the spectral components than a dispersive prism.

Similarly to the vectorial law of refraction, a vectorial version of the grating equation is available [25, Eq. 47]. Although diffraction can only be explained with the wave optical model, its effects on the direction of a ray can also be considered in a ray tracing model. To generalize [25, Eq. 47] to DOEs with spatially variant grating periods and orientations, the DOE structure is approximated locally (i.e. at the intersection point with the ray) by a linear

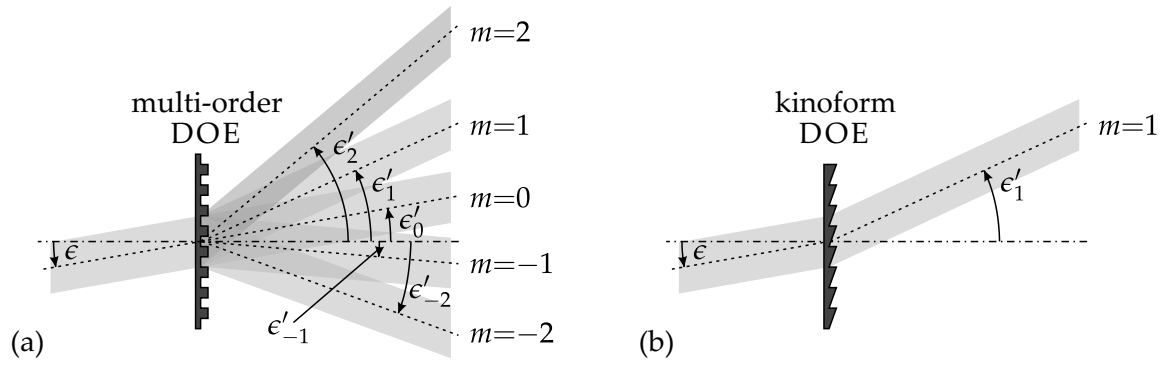

Fig. 2.12: Diffraction of an incident wavefront by (a) a multi-order DOE and (b) a kinoform DOE optimized for the first diffraction order.

grating. Although this model neglects diffraction effects caused by apertures, it enables the efficient raytracing-based optimization of optical systems containing DOEs.

If reflection losses and birefringent materials are neglected, ROEs deflect a monochromatic ray into one specific direction. In contrast, DOEs can be regarded as multiple beam splitters. This is especially the case for amplitude DOEs which distribute the incident power across multiple diffraction orders (Fig 2.12(a)). In contrast, phase DOEs can be designed to redirect most of the incident power into a single diffraction order (Fig 2.12(b)). Such phase DOEs are called kinoform elements and can be fabricated using various methods like diamond turning, grey-tone lithography or the local variation of the refractive index of a transparent substrate [31, 32].

The elements used in this thesis are fabricated using a multi-step lithographic process with binary masks. It is based on the local removal of material from the unmasked regions of a SiO_2-wafer. The sawtooth profile required for an ideal kinoform element is approximated by a staircase profile. This approximation leads to a reduction of the power within the intended diffraction order. Dammann derived a scalar model for the wavelength dependent power distribution across the different diffraction orders of a multi-level phase DOE [33]. If the DOE is optimized for the first diffraction order and the reference wavelength λ_0, the scalar, wavelength dependent diffraction efficiency of the m-th order will be given by [33]

$$\eta_m(\lambda, p_l) = \left[\frac{\sin\left(\pi\frac{m}{p_l}\right)}{\pi\frac{m}{p_l}}\right]^2 \left[\frac{\sin\left(p_l\left(\frac{\pi\lambda_0}{p_l\lambda}\frac{n(\lambda)-1}{n(\lambda_0)-1}-\pi\frac{m}{p_l}\right)\right)}{p_l\sin\left(\frac{\pi\lambda_0}{p_l\lambda}\frac{n(\lambda)-1}{n(\lambda_0)-1}-\pi\frac{m}{p_l}\right)}\right]^2 \tag{2.75}$$

p_l defines the number of phase levels while $n(\lambda)$ and $n(\lambda_0)$ are the refractive indices of the substrate at the wavelengths λ and λ_0. The substrate is assumed to be surrounded by air or vacuum. This model is valid for normal incidence and neglects both fabrication errors and rigorous diffraction effects like shadowing losses. It provides a best case estimation and is only valid for ideal elements with grating periods significantly larger than the wavelength. For smaller grating periods the accuracy of the model decreases and the fabricated element shows a significantly lower diffraction efficiency of the main diffraction order. The range of grating periods for which the scalar model is valid is discussed in [31, 34]. The scalar diffraction efficiency according to Eq. 2.75 is illustrated in Fig. 2.13 for the case that the dispersion of the substrate is neglected, i.e. $[n(\lambda)-1] \,/\, [n(\lambda_0)-1] = 1$. In Fig. 2.13(a) the wavelength dependent power within different diffraction orders is plotted for a kinoform DOE. Fig. 2.13(b)

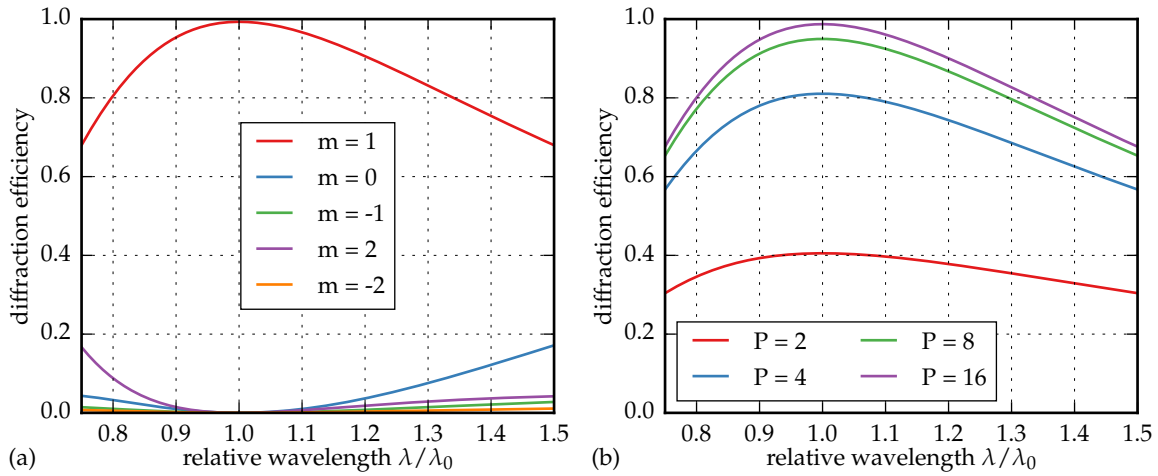

Fig. 2.13: Diffraction efficiencies according to the scalar model. (a) Wavelength dependent distribution of the incident power across the diffraction orders of a kinoform element. (b) Wavelength dependent diffraction efficiency of multi-level phase DOEs optimized for the first diffraction order.

shows the wavelength dependent influence of the staircase approximation on the diffraction efficiency. The strong dependence of the diffraction efficiency on the wavelength can be reduced by using multilayer DOEs [35–39]. A detailed analysis of this approach is provided in [39]. A high diffraction efficiency over a large wavelength range can also be achieved with DOEs containing sub-wavelength structures [32, 40–43].

Similarly to Eq. 2.71, an Abbe number can be defined for DOEs:

$$\nu_{\text{dif},\,\lambda_0} = \frac{\lambda_0}{\lambda_1 - \lambda_2}. \tag{2.76}$$

For the wavelength triples of Eq. 2.72 the diffractive Abbe number takes the values $\nu_{\text{dif},\,d} = -3.45$ and $\nu_{\text{dif},\,e} = -3.33$. DOEs thus have a stronger wavelength dependence than ROEs. The opposing sign is related to the different spectral characteristics: ROEs deflect rays with a short wavelength farther than rays with a long wavelength. On the other hand, DOEs deflect rays with a long wavelength farther than rays with a short wavelength. These aspects are illustrated in Fig. 2.14.

Rotationally symmetric DOEs are composed of a multitude of concentric annular zones which deflect the corresponding sections of an incident wavefront towards a common focal point. To obtain constructive interference at the focal point, the optical path length difference between neighboring zones has to be an integer multiple of the wavelength λ. The assumption of an optical path difference of λ between neighboring zones leads to the following equations for the radius r_{z1} of the first zone [31]:

$$r_{z1}^2 + f'^2 = \left(f' + \lambda\right)^2 \quad \rightarrow \quad r_{z1}^2 = 2f'\lambda + \lambda^2 \approx 2f'\lambda. \tag{2.77}$$

As r_{z1} is a constant, a variation of λ results in a change of $f'(\lambda)$. The approximation $r_{z1}^2 = 2f'\lambda$ leads to the equations

$$f'(\lambda) = f'(\lambda_0)\frac{\lambda_0}{\lambda} \quad \text{and} \quad \text{FP}(\lambda) = \text{FP}(\lambda_0)\frac{\lambda}{\lambda_0}. \tag{2.78}$$

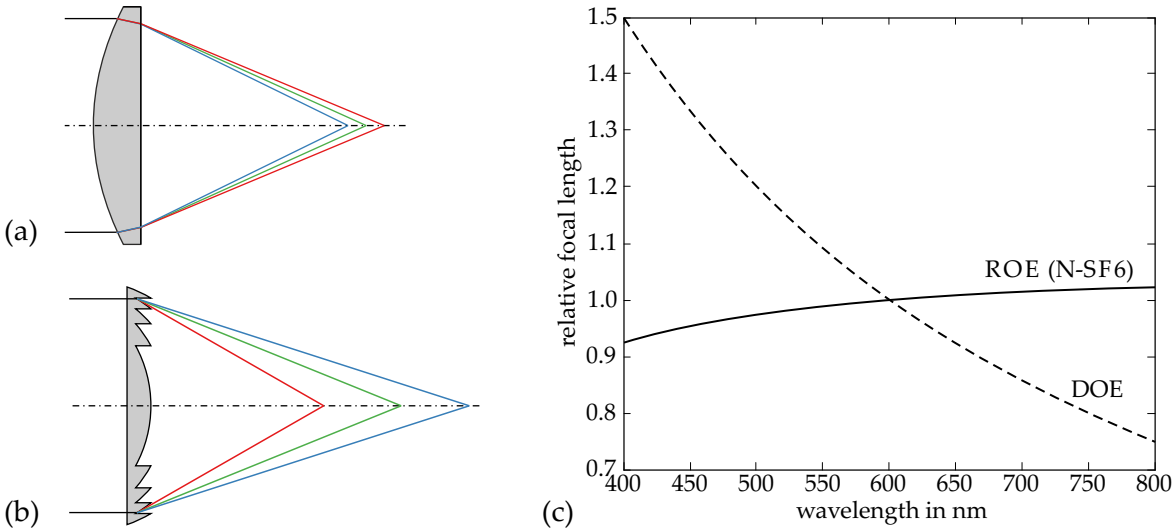

Fig. 2.14: Opposing spectral characteristics of (a) a ROE and (b) a DOE. (c) While the focal length of a ROE increases with wavelength, the focal length of a DOE decreases. $\lambda_0 = 600\,\text{nm}$ is used as the reference wavelength.

These equations describe the wavelength dependence of the DOE's focal length and focal power.

2.3.3 Longitudinal and transversal chromatic aberration in rotationally symmetrical systems

Snell's law and the grating equation are suitable for modeling the deflection of rays at general optical surfaces. Most of the systems presented in this thesis are rotationally symmetric and can be analyzed with the paraxial and the collinear model. Both models are well suited for an approximate description of the spectral properties of rotationally symmetrical systems. In classical imaging systems the separation of the spectral components is considered an aberration. The two types of chromatic aberration are the longitudinal (axial) chromatic aberration (LCA) and the transversal (lateral) chromatic aberration (TCA). Both types are commonly evaluated with the help of the chief ray and the marginal ray.

In a system with LCA the distance at which the marginal ray intersects the optical axis depends on the wavelength. Consequently, the image plane position varies with wavelength, see Fig. 2.15(a). According to classical aberration theory [2, Eq. 2.117] the LCA of a system of n thin lenses is given by

$$\Delta s'(\lambda_1,\lambda_2) = s'_n(\lambda_1) - s'_n(\lambda_2) = -\frac{s'^2_n(\lambda_0)}{\omega^2_n(\lambda_0)} \sum_{i=1}^{n} \frac{F'_i(\lambda_0)\omega^2_i(\lambda_0)}{\nu_{\lambda_0,i}(\lambda_1,\lambda_2)}. \tag{2.79}$$

$F'_i(\lambda_0)$ are the focal powers of the thin lenses. The spectral characteristics of these lenses are determined by the diffractive or refractive Abbe numbers $\nu_{\lambda_0,i}(\lambda_1,\lambda_2)$ which were defined in Eqs. 2.71 and 2.76. $s'_n(\lambda_0)$ is the distance between the last lens and the collinear image plane. Finally, the height ratios $\omega_i(\lambda_0) = h_{m,i}(\lambda_0)/h_{m,n}(\lambda_0)$ specify the intersection heights of the marginal ray with the thin lenses of the system. All values have to be provided at the reference wavelength λ_0. In the derivation of Eq. 2.79 several approximations are made. It is based on

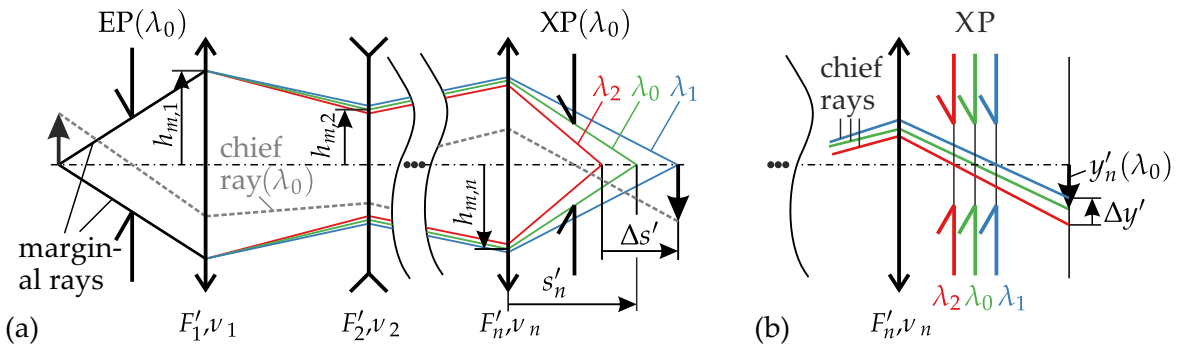

Fig. 2.15: Interpretation of (a) the longitudinal chromatic aberration $\Delta s'$ and (b) the transversal chromatic aberration $\Delta y'$ as wavelength dependent deviations of (a) the marginal ray and (b) the chief ray from their nominal path.

the assumption that the lenses have an infinitesimal thickness and are surrounded by vacuum or air. The lenses are described by the collinear focal power and the Abbe number.

Eq. 2.79 enables the selection of suitable combinations of lens materials and focal powers for the minimization of LCA. If the resulting system has the same focal power for two or three different wavelengths it is called dichromatic or trichromatic, respectively. If these systems are also corrected for spherical aberration they are called achromatic or apochromatic, respectively. In Chap. 5.1.3 the design of hyperchromatic lenses with a specific LCA is discussed. For this purpose Eq. 2.79 is used extensively.

In contrast to the LCA which does not depend on the chief ray, the TCA is dependent on the chief ray and the position of the stop. Fig. 2.15(b) shows the image space of a system with TCA. Both the position of the exit pupil and the orientation of the chief ray vary with wavelength. In consequence, the intersection height between the chief ray and a fixed image plane is wavelength dependent. It is equivalent to a wavelength dependent change of the lateral magnification of the optical system. According to [2, Eq. 2.161] the TCA of a system of n thin lenses is given by

$$\Delta y'(\lambda_1,\lambda_2) = y'_n(\lambda_1) - y'_n(\lambda_2) = -y'_n(\lambda_0)\sum_{i=1}^{n}\frac{c_i F'_i}{\nu_{\lambda_0,i}(\lambda_1,\lambda_2)}, \tag{2.80}$$

with

$$\frac{1}{c_i} = n_i\left(\frac{1}{a_i} - \frac{1}{a_{p,i}}\right). \tag{2.81}$$

The parameter c_i has to be evaluated in the local object space of each thin lens. There, a_i specifies the distance to the local object plane while $a_{p,i}$ corresponds to the local pupil distance. n_i is the refractive index of the thin lens.

2.3.4 Spectral and radiometric quantities

Table 2.1 provides an overview of the most common radiometric quantities. These quantities are defined according to DIN 5031 [44] and DIN EN ISO 80000-7:2008 [45]. The spectral and the integral quantities are linked through the relations [44, 46]:

$$X_\lambda = \frac{\mathrm{d}X(\lambda)}{\mathrm{d}\lambda} \approx \frac{\Delta X(\lambda)}{\Delta\lambda} \qquad \text{or} \qquad \mathrm{d}X(\lambda) = X_\lambda\,\mathrm{d}\lambda \tag{2.82}$$

Table 2.1: Definition of radiometric quantities [44, 45]

Quantity	Symbol	SI unit	Relation	Description
Radiant energy	Q	$\mathrm{W\,s}$		radiant energy
Radiant power	Φ_e	W	$\Phi_e = \frac{Q}{t}$	radiant energy per unit time
Spectral power	$\Phi_{e,\lambda}$	$\mathrm{W\,m^{-1}}$	$\Phi_{e,\lambda} = \frac{\mathrm{d}\Phi_e}{\mathrm{d}\lambda}$	radiant power per wavelength
Radiant intensity	I_e	$\mathrm{W\,sr^{-1}}$	$I_e = \frac{\Phi_e}{\Omega_1}$	radiant power per unit solid angle
Spectral intensity	$I_{e,\lambda}$	$\mathrm{W\,sr^{-1}\,m^{-1}}$	$I_{e,\lambda} = \frac{\mathrm{d}I_e}{\mathrm{d}\lambda}$	radiant intensity per wavelength
Radiance	L_e	$\mathrm{W\,sr^{-1}\,m^{-2}}$	$L_e = \frac{\Phi_e}{\Omega_1 A_1}$	radiant power per unit solid angle per unit projected source area
Spectral radiance	$L_{e,\lambda}$	$\mathrm{W\,sr^{-1}\,m^{-3}}$	$L_{e,\lambda} = \frac{\mathrm{d}L_e}{\mathrm{d}\lambda}$	radiance per wavelength
Irradiance	E_e	$\mathrm{W\,m^{-2}}$	$E_e = \frac{\Phi_e}{A_2}$	radiant power per unit projected detection area, sometimes called intensity
Spectral irradiance	$E_{e,\lambda}$	$\mathrm{W\,m^{-3}}$	$E_{e,\lambda} = \frac{\mathrm{d}E_e}{\mathrm{d}\lambda}$	irradiance per wavelength
Radiant emittance	M_e	$\mathrm{W\,m^{-2}}$	$M_e = \frac{\Phi_e}{A_1}$	radiant power per unit projected source area
Spectral radiant emittance	$M_{e,\lambda}$	$\mathrm{W\,m^{-3}}$	$M_{e,\lambda} = \frac{\mathrm{d}M_e}{\mathrm{d}\lambda}$	radiant emittance per wavelength

and

$$X = \int X_\lambda \,\mathrm{d}\lambda \approx \sum X_\lambda \Delta\lambda. \tag{2.83}$$

The absorption and the reflectivity of the optical elements as well as the sensitivity of the detector vary with the wavelength. These effects are incorporated in the mathematical description through the sensitivity function $s(\lambda)$ [46]:

$$X_{\lambda s} = X_\lambda s(\lambda) \qquad \text{or} \qquad X_s = \int X_\lambda s(\lambda)\,\mathrm{d}\lambda. \tag{2.84}$$

Most of the discussions presented in this thesis are not limited to light, i.e. to the visual part of the electromagnetic spectrum. Hence, the more general term "radiation" is used.

In both the wave optical and the geometrical model the energy flow within an optical system is described by the Poynting vector [5]. Its direction corresponds to the direction of the energy flow while its time average is equivalent to the irradiance E_e on a surface element oriented perpendicularly to the Poyting vector. Using the time average of the Poynting vector, Haferkorn derives the following relation between the complex amplitude u^z of the wave optical model and the irradiance E_e [3, Eq. 2.15]:

$$E_e = \frac{\epsilon_r \epsilon_0 c}{2} u^z u^{z*}, \tag{2.85}$$

with the vacuum permittivity ϵ_0, the relative static permittivity ϵ_r, and the speed of light c. u^{z*} is the complex conjugate of u^z.

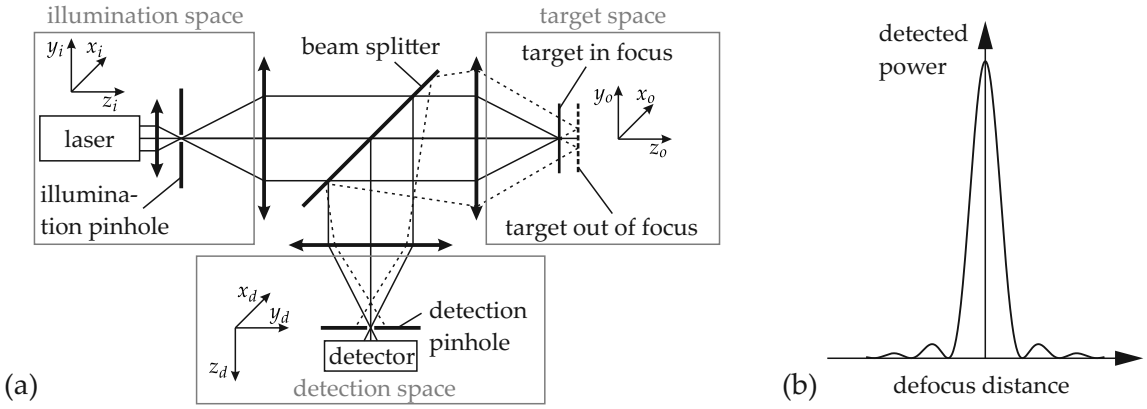

Fig. 2.16: (a) Schematic of a point scanning confocal microscope and (b) detected signal for a z-scan of an ideally reflecting mirror.

2.4 Confocal microscopy

2.4.1 Basic principle of confocal imaging

The spectral information coding principles discussed in this thesis are mainly based on spatial filtering of spectral components which are separated in the axial direction. The optical systems are closely related to those of confocal microscopes. Confocal microscopy is used extensively for the non-destructive, three-dimensional evaluation of technical surfaces and biological specimens [47, 48]. In order to avoid confusion regarding the term "object" all types of specimens or technical surfaces will be called target. The term "object" is used exclusively in the general description of an imaging system which transforms an object into an image. The space containing the target is called target space. The basic idea of confocal microscopy is attributed to Minsky [49]. A schematic of a confocal system operating in reflection mode (epi-illumination mode) is illustrated in Fig. 2.16(a). A quasi-point source, most commonly a laser beam, is imaged into target space by a microscope objective. In target space, the beam interacts with the target. A part of the radiation is reflected back into the microscope objective and is directed into detection space. The expression confocal microscope was first used in [50] to indicate that the illumination pinhole, the detection pinhole and the focal spot in target space all lie in optically conjugate planes. The part of the radiation which is focused on the target is also focused on the detection pinhole plane and passes the detection pinhole with minimum attenuation. Parts of the radiation which are out-of-focus in target space are spread across a large area of the detection pinhole plane and contribute minimally to the signal passing the detection pinhole, see Fig. 2.16(b). The resulting property of excellent background rejection makes confocal microscopy an indispensable tool for the evaluation of biological specimens. To acquire a two-dimensional image of the target with the system proposed by Minsky, the target has to be scanned in x and y directions. During the movement the detector records the local reflectivity of the target at the current focal point. The evaluation of a three-dimensional volume requires a scan of the target in x, y, and z directions.

2.4.2 Confocal microscopes - state of the art

Over the past fifty years many types of confocal microscopes were proposed. The resulting systems can be grouped in the following manner:

- Stage scanning systems [51–54] follow the original principle proposed by Minsky. The specimen is placed on a stage which is scanned in x, y, and z directions. As only the on-axis focus point is used, stage scanning systems image all points of the specimen with the same PSF. At the same time the field of view is only limited by the stage and not by the maximum field angle of the objective lens. These advantages are opposed to a frame rate which is significantly lower than the one obtainable with other scanning approaches.
- In laser scanning confocal microscopes the lateral movement of the specimen is replaced by a two-dimensional scan of the laser beam. In some of the first systems the scan is realized through a lateral shift of the microscope objective [55]. Later microscopes are based on the movement of an optical fiber [56, 57] or on galvanometer mirrors [58–61]. Laser scanning systems are faster than stage scanning systems but typically possess a field dependent PSF [62].
- Spinning disk confocal microscopes illuminate multiple lateral points in parallel and reach frame rates suitable for live view. For this purpose a modified Nipkow-disk [63] is used. It contains thousands of pinholes which are distributed in spirals across the diameter of the disk. When the disk rotates, the pinhole images illuminate the full field of view homogeneously. Reflections from the illumination space side of the spinning disk have to be kept from entering the detection system. The first systems use opposite sides of the disk for the illumination and detection paths [64, 65]. They require precise alignment and a high stability of the opto-mechanical system. By using the same part of the disk in double pass Xiao and Kino [66] avoid the stability problems at the cost of having to minimize the reflection caused by the spinning disk. For this purpose they use polarization optical components, tilt the spinning disk and add anti-reflection structures to it. All these systems suffer from low optical efficiency as most of the illumination power does not pass the pinholes. The efficiency can be boosted by the use of microlens arrays which transform the illumination beam into a lateral array of foci [67–70]. Earlier, a laterally static microlens array working with single illumination and detection pinholes was proposed in [71–73].
- Programmable array microscopes possess imaging properties similar to spinning disk systems [74–80]. Instead of rotating a disk with discrete pinholes, a spatial light modulator (SLM) like a digital mirror device (DMD) is used. To obtain confocal background rejection the bright pixels have to be well separated. The discrete pixels of the two-dimensional pixel matrix are switched on and off in a consecutive pattern to obtain the information associated with all pixels of the array.
- In slit microscopes the illumination pinholes, the detection pinholes, or both are replaced by slits. The main goal is to increase the signal-to-noise-ratio (SNR) and/or the acquisition speed at the expense of a reduced confocal discrimination of out-of-focus planes. In one of the first systems a slit was projected onto the target and the signal from the target is detected with photographic film behind the slit. To acquire a confocal image of one plane, the target and the film are moved simultaneously in opposite directions [81]. The application of slits in stage scanning confocal microscopes is analyzed in [82]. A one-dimensional scan of the slit is presented in [83–86]. In further systems the scan of the slit in the two lateral directions is implemented with galvanometric scan mirrors [87, 88]. Botcherby et al. present a special microscope for the imaging of a planes which contain the optical axis [89]. Also, spinning disk systems with slits instead of pinholes

are used [90, 91]. Further discussions are provided in [62, Chap. 2.4], [91], and [92, Chap. 9].

- Fiber-based systems may possess a simplified optical structure and a higher stability, especially if fiber couplers are used as replacement for the beam splitter. The fibers do not only guide the light but also act as pinholes [93, 94]. In endoscopic systems fiber bundles may be used to implement an array of lateral channels [85, 95–97]. In these systems the fiber bundles are used to link a miniaturized microscope objective to a remote detection and illumination system.

In this overview only some of the first papers on the specific system types were cited. Much more extensive lists of references can be found in dedicated books of confocal microscopy [48, 62, 98]. An overview of the historical background of confocal microscopy and a speed estimation of the main implementations are provided in [99] and [62, Chap. 1.3.5].

2.4.3 Signal models for confocal microscopes - state of the art

The advance of confocal microscopy as an imaging technology was accompanied by the development of signal generation models. In this section an overview of the most important literature on this topic is presented. Owing to the large number of publications only selected papers are referenced. Further references are given in [48, 62, 98, 100].

In the ideal case, confocal systems use an objective lens without aberrations and pinholes which are infinitesimally small. The corresponding signal models evaluate the axial intensity at the detection pinhole plane for different out-of-focus positions of the specimen. Both paraxial [50, 101] and non-paraxial [102–104] models were derived. The basic models were extended successively to include lens aberrations [105–109] and pinholes of finite size [110–115]. To describe the imaging of three dimensional targets in a mathematically concise way, three dimensional transfer functions were used [98, 116–119]. The influence of the shape of the surface under test on the sensor signal was studied in [120]. Further models considered fluorescence microscopy [121–124] and fiber-based setups [117, 125–127]. Additionally, various authors investigated the possibility of increasing the resolution of confocal systems by shaping the pupil function [128–134]. To explain the specific imaging properties of systems with line and slit apertures, adapted signal models were developed [82, 112, 122, 135–138]. Similarly, systems based on pinhole arrays were covered by specific models which take cross talk effects between neighboring pinholes into account [139–143].

The two most common targets used in analytical evaluations of confocal systems are the plane reflector (e.g. a mirror) and the point reflector (e.g. a separate group of molecules). Both cases are compared in [62, Chap. 3.2 and 3.3]. The comparison includes paraxial and non-paraxial models and covers infinitesimally small pinholes as well as pinholes of finite size.

If infinitesimally small pinholes are assumed, only the on-axis intensity distribution at the detection pinhole plane will have to be determined. In the paraxial approximation a direct analytical equation for the on axis intensity at out of focus planes is available. The combination of both assumptions leads to two simple analytical equations for the axial response of confocal systems. These are

$$E_e(\Delta z)_{\text{plane}} = \left[\frac{\sin\left[kn\Delta z\left(1-\cos\sigma\right)\right]}{kn\Delta z\left(1-\cos\sigma\right)}\right]^2 \tag{2.86}$$

for the plane reflector [62, Eq. 3.9], and

$$E_e(\Delta z)_{\text{point}} = \left[\frac{\sin\left[\frac{kn\Delta z}{2}\left(1-\cos\sigma\right)\right]}{\frac{kn\Delta z}{2}\left(1-\cos\sigma\right)} \right]^4 \tag{2.87}$$

for the point reflector [62, Eq. 3.16]. $k = 2\pi/\lambda$ is the wave number, n is the refractive index, and σ is the angle between the marginal ray and the optical axis. Δz specifies the distance between the paraxial focal point and the plane or point reflector. All values have to be given in target space. The point reflector model is well suited to describe the confocal signal discrimination for biological specimens. On the other hand, the plane reflector model provides a good starting point for determining the confocal signal which is caused by reflecting technical surfaces like silicon wafers.

In reality, the illumination and detection pinholes are of finite size and play significantly different roles in the imaging process [114]. The detection pinhole is essential to the confocal setup and the influence of its size on the discrimination of out-of-focus signals has been analyzed in various publications. The corresponding models are based on integrating the intensity at the detection pinhole plane over the pinhole area. This additional integration and the requirement for evaluating the field at off-axis positions lead to significantly more complex signal models [62, Chap. 3.3.2], [98, Chap. 4.1, 4.4]. Often, no analytical solution is available and the integrals have to be solved numerically. While larger pinhole diameters enhance the strength of the detector signal, they also lead to reduced lateral and axial resolution. It is thus an important goal to determine a good balance between the signal level and the resolution.

If a laser is used as the source, the illumination pinhole acts as a spatial filter and truncates the incident laser beam [114]. The amount of truncation has an effect on the field distribution at the pupil of the objective lens. Hence, the focus distributions in target space and in detection space are altered. In [62, Chap. 3.3.2] the size of the illumination pinhole is discussed from the perspective of diffraction angles. The optimum illumination pinhole diameter is reached if the diffraction angle matches the numerical aperture of the succeeding optical system. Various publications ignore these effects and combine a point source model with finite detection pinholes (e.g., [112, 144]).

The role of the illumination pinhole will change if an incoherent light source is used. In this case the points within the illumination pinhole act as independent point sources and the diameter of the illumination pinhole has a direct impact onto the size of the focal spot in target space. Drazic, Sheppard, and Gu reported that the influence of the finite illumination pinhole can be considered through a convolution operation ([113, 114], [98, Chap. 5.6]). Their analysis for incoherent illumination will be used in Chap. 4 as the starting point of the signal models for chromatic confocal systems.

2.5 Chromatic confocal distance sensing

2.5.1 Basic principle of chromatic confocal distance sensing

The mechanical z-scan required in confocal microscopy can be avoided in chromatic confocal systems [145, 146]. For this purpose the microscope objective is replaced with a hyperchromatic lens which has a well defined amount of longitudinal chromatic aberration. A schematic of the chromatic confocal setup is shown in Fig. 2.17(a). In target space each wavelength of a

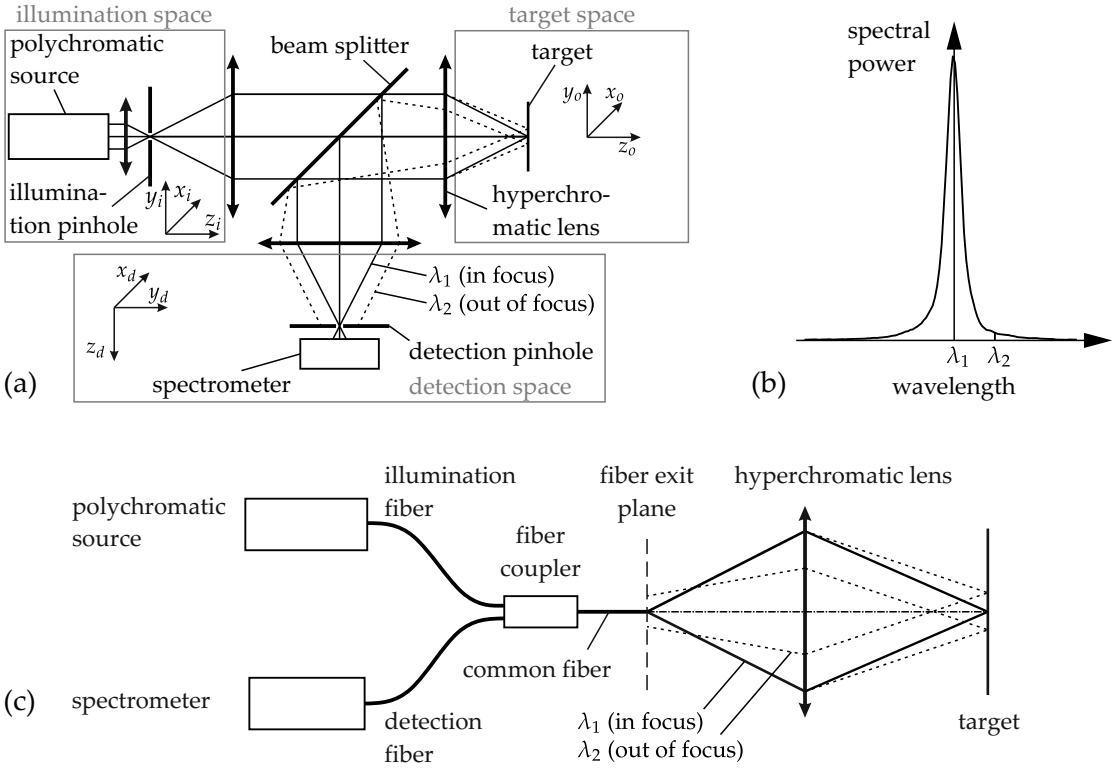

Fig. 2.17: Schematics of (a) a chromatic confocal point sensor, (b) the resulting spectral peak, and (c) a fiber-based version of the chromatic confocal point sensor.

polychromatic source is focused at a different axial distance. The axial measurement range is determined by the maximum and minimum wavelengths of the source and the longitudinal chromatic aberration of the hyperchromatic lens. The target reflects parts of the polychromatic signal back into the hyperchromatic lens. The different spectral components which reach the detection space hit the detection pinhole plane with a wavelength dependent amount of defocus. The spectral component which is focused on the surface under test is also focused on the detection pinhole plane and passes the detection pinhole with minimum attenuation. All other spectral components are damped and the spectral power distribution behind the detection pinhole shows a spectral peak, see Fig. 2.17(b). The wavelength of the spectral peak contains the information about the axial distance between the sensor and the surface under test. The distance information is thus encoded in the spectral response of the chromatic confocal sensor head. To retrieve the distance information, the wavelength at which the spectral peak reaches its maximum is evaluated. In systems with a single lateral channel a spectrometer is most commonly used for this decoding step. By placing a mirror at different distances to a lens positioned in a confocal setup, the longitudinal chromatic aberration of this lens may be evaluated [147].

The chromatic confocal principle is mainly used in industrial environments for the metrology of technical surfaces. In ISO 25178-6 it is listed as a standard method for the evaluation of the surface texture and its properties are specified in ISO 25178-602. The main applications include the fields of 3D profilometry, thickness measurements, roughness measurements, in-line process control, velocimetry, vibrometry, and autofocus sensing. Chromatic confocal systems are also used for the evaluation of biological specimens [148–150].

2.5.2 Chromatic confocal distance sensing - state of the art

The idea of encoding depth information in the spectral channel is commonly attributed to Courtney-Pratt, Gregory, and Molesini [151, 152]. However, the combination of chromatic depth encoding with a confocal setup was already proposed in 1983 by Gross and Dähne [153]. Similar systems were described by Hutley, Picard, and Browne [145, 146, 154]. Since this time many chromatic confocal sensor systems have been developed. These systems are now discussed in three groups: Point sensors, line sensors, and matrix sensors.

Point sensors are the most common chromatic confocal sensor type and are used to determine the target distance at a single lateral channel. Typically, a spectrometer is used for evaluation of the spectral distribution of the sensor signal [145, 146, 149, 150, 155–186]. Under specific conditions the spectrometer can be replaced by a detector with spectral filters [187–189]. Alternatively, a wavelength tunable light source may be used [148, 190]. In this case the depth information is acquired sequentially. To obtain three-dimensional information, the target may be moved in the two lateral directions or beam-scanning may be implemented [191]. Fig. 2.17(c) shows the schematic of a fiber-based chromatic confocal point sensor. The beam splitter is replaced by a y-coupler and the tip of the common fiber acts as both the illumination and the detection pinhole [148, 155, 162, 167, 168, 173, 177, 184]. This way the illumination and detection system can be decoupled from the senor head. As the illumination and the detection pinholes do not have to be aligned with respect to each other, fiber-based chromatic-confocal point sensors are robust and suited for harsh industrial environments. Additionally they acquire the full axial measurement range without moving parts.

In chromatic confocal line sensors the illumination and detection pinholes are replaced by slits to record the depth information along a lateral line. In combination with a target which is moved perpendicularly to the lateral line the full three-dimensional geometry of the target can be recorded. For parallelized evaluation of all measurement points on the sensor line a matrix detector is commonly used [166, 172, 192–196]. One dimension of the detector resolves the spatial information while the second dimension is used to evaluate the spatially varying spectral information passing the detection slit. The slits may be replaced by lines of fibers to realize flexible systems which record the distance information at several discrete points along the line [197, 198]. In [199] a system is described which uses a spectral multiplexing process to transfer the distance information from multiple lateral points through a single optical fiber. This system will be discussed in more detail in Chap. 6.

A major challenge of chromatic confocal matrix sensors is the evaluation of the spectral information at the lateral detection points. To this end, multiple approaches have been proposed:

- A tunable light source [73, 200] or a set of spectral filters [71, 201, 202] may be used in combination with a monochromatic detector. In both cases the axial measurement range is evaluated sequentially.
- A parallelized evaluation can be realized with RGB detectors [68, 146, 172, 193, 203–206]. These sensors may require a target-specific calibration and may produce wrong results if the spectral characteristics of the target change [172]. To overcome this issue multiple detections with different distances between the sensor and the surface can be performed [172].
- A spectrometric evaluation is possible either by using the pixels between the monochromatic pinhole images on the matrix detector [207–212] or by using a fiber cross section

converter [213]. The cross section converter transforms a 2D grid in the detection pinhole plane to a 1D line of points which can then be evaluated in the same way as the signal in a chromatic confocal line sensor.

- A colored image may be presented to the human eye for visual inspection [214, 215].

The pinholes of the chromatic confocal matrix sensor can either be static [207–213] or dynamic [172, 193, 200, 201, 205, 206]. To increase the efficiency and the SNR of the sensor system the pinhole arrays may be combined with microlens arrays [172, 193] or may be replaced by microlens arrays [68, 73, 204].

For the generation of the required longitudinal chromatic aberration both refractive lenses (e.g., [150, 163, 169, 171]) and diffractive lenses (e.g., [145, 165, 186, 190, 201]) are used. In [215] a hyperchromatic group for converting a confocal microscope to a chromatic confocal microscope is presented. By combining refractive components with different dispersion characteristics or by combining diffractive and refractive components in hybrid systems, the longitudinal chromatic aberration can be tailored to the specific application requirements [184], see Chap. 5.1.3 for more details.

2.5.3 Signal models for chromatic confocal systems - state of the art

The signal models for chromatic confocal systems are closely related to those for confocal microscopes with a monochromatic source. As the starting point Eq. 2.86 or a version with normalized coordinates is commonly used (e.g., [146, 157, 165, 174, 179]). In these models the z-scan of the mirror is replaced by a wavelength dependent defocus distance $\Delta z(\lambda)$ according to the equation

$$\Delta z(\lambda) = z(\lambda) - z(\lambda_0). \tag{2.88}$$

Here, $z(\lambda_0)$ is the focus distance at the reference wavelength and $\Delta z(\lambda)$ describes the wavelength dependent shift of the focal plane due to the LCA of the hyperchromatic lens. The resulting model is only valid for paraxial systems with point sources and point detectors. Detection pinholes of finite size are considered in [150, 161, 180] by integrating over the area of the detection pinhole. An analysis of the imaging properties of a chromatic confocal line sensor is provided in [216]. Fleischle combines geometrical raytracing with a coherent summation of the complex amplitudes assigned to the individual rays [217–219]. The resulting model includes interference effects and is used to describe the sensor signal for diffusely scattering and curved surfaces under test. Fleischle assumes a point source and does not consider illumination pinholes of finite size which transmit spatially incoherent radiation.

Many chromatic confocal systems use spatially extended light sources like LEDs or gas discharge lamps. To obtain suitable signal levels with such sources, illumination pinholes of finite size have to be used. Extended illumination and detection pinholes are considered in [172]. This analysis is based on a wave optical model without the consideration of aberrations. Extended signal models for aberrated chromatic confocal systems with pinholes of finite size will be the topic of Chap. 4.

2.5.4 Main performance criterion for chromatic confocal systems - the spectral peak

The resolution, the measurement accuracy, and the measurement uncertainty are among the most important performance criteria of sensor systems. A detailed discussion of the

measurement uncertainty and related parameters is provided in the "Guide to the expression of uncertainty in measurement" [220]. The "International vocabulary of metrology" [221] lists the following definitions relevant to this thesis:

Measurement: Process of experimentally obtaining one or more quantity values that can reasonably be attributed to a quantity.

Measurand: Quantity intended to be measured.

(Measurement) Accuracy: Closeness of agreement between a measured quantity value and a true quantity value of a measurand.

(Measurement) Uncertainty: Non-negative parameter characterizing the dispersion of the quantity values being attributed to a measurand, based on the information used.

(Measurement) Error: Measured quantity value minus a reference quantity value.

Resolution: Smallest change in a quantity being measured that causes a perceptible change in the corresponding indication.

Ruprecht [172], Fleischle [219], and Lyda [222] analyzed chromatic confocal imaging systems from the perspective of optical metrology and discussed these parameters in detail. Such analyses have to include aspects like the accuracy of the used peak finding algorithm. In the simplest case only the detector pixel with maximum intensity is determined and related to an axial distance. More advanced peak finding algorithms are e.g. based on the detection of the center of mass or on the fitting of the measured values with an analytical function like a parabolic or Gaussian function. [47, 172, 223].

In contrast, this thesis is focused on the lens design aspects of chromatic confocal systems and does not include an analysis of signal evaluation algorithms. A detailed discussion of parameters like the measurement accuracy is thus not provided. Instead, the shape and width of the spectral peak are used as primary performance criteria. These parameters are available from the signal models described in Chap. 4 and show the influence of aberrations and field dependent vignetting effects. At the same time the width and the shape of the spectral peak can be easily determined in experiments by evaluating the sensor signal with a spectrometer.

The spectral peak can be used as an intermediate value in the calculation of both the axial resolution and the measurement uncertainty. According to [223, p. 691] two different application scenarios have to be considered. In the first scenario the axial distance to a non-transparent reflecting surface is determined. The axial resolution can then be defined as the minimum step height of the sample which can be measured [221]. The obtainable axial resolution depends not only on the optical system but also on the resolution of the spectrometer and the peak finding algorithm.

The second scenario is concerned with measuring the thickness of transparent layers [224]. In this case the spectral signal consists of two peaks and the thickness is determined from the spectral distance of the peaks. The thickness can only be measured if the two spectral peaks are separable. If an incoherent summation of the two peaks is assumed, the condition for separability of the peaks is closely related to the classical two point resolution criteria of incoherent imaging [225, 226]. Additionally, the detection system has to be capable of resolving the two spectral peaks within the chromatic confocal signal.

Significant measurement errors may arise if the shape of the peak deviates from the analytical shape used in the peak finding algorithm. Precise knowledge of the shape of the spectral peak under all possible sensor conditions is thus essential for an accurate prediction of the

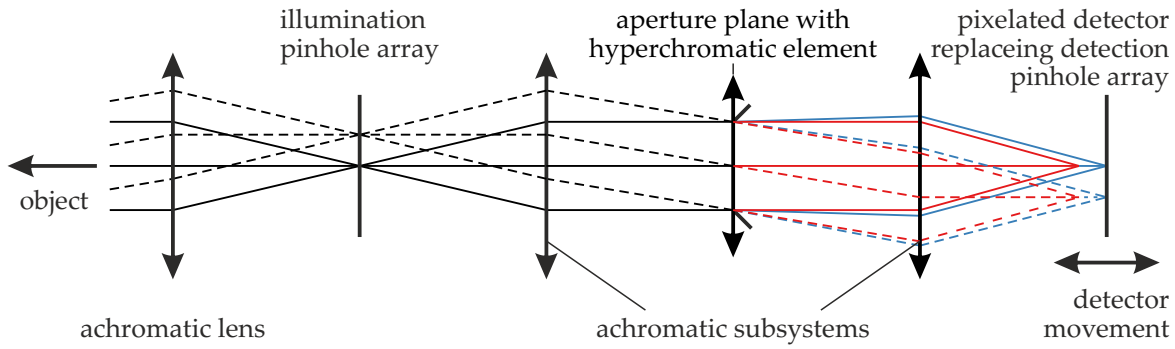

Fig. 2.18: Schematic of a chromatic confocal system for hyperspectral imaging of an object located at infinity.

measurement uncertainty. Accurate models of the spectral peak will be discussed in Chap. 4. These models can be used to analyze the effects of fabrication and alignment errors as well as field dependent aberrations.

2.6 Chromatic confocal systems for spectroscopy and hyperspectral imaging

Chromatic confocal systems are also suitable as axial monochromators or spectrometers. While the first systems mentioned in the literature operated with a single lateral channel [227, 228], multiple lateral channels were also proposed [229–231]. Fig. 2.18 shows the schematic of a multi-channel chromatic confocal system for hyperspectral imaging. An object scene is imaged onto an illumination pinhole array which generates a polychromatic array of quasi-point sources. The illumination pinhole array is imaged by a telecentric hyperchromatic lens into image space. There, a pixelated monochromatic detector acts as the detection pinhole array. Of the recorded image only small regions are evaluated which correspond to the sharp images of the illumination pinholes. These regions may consist of several physical pixels and are called generalized detection pixels. Owing to the hyperchromatic lens only a single wavelength is in focus at the detection regions. All other wavelengths are defocused and their spectral power is spread across a larger lateral region. They thus only contribute to a minor extent to the total power recorded by the generalized detection pixels. The spectrum of the object can be read out sequentially by moving the detector axially through the focal region of the hyperchromatic lens [227, 228, 230, 232] or by varying its focal length. [233, 234]. The lateral resolution may be increased by using actuated pinhole arrays [235].

The axial tuning can be avoided in systems with matrix spectrometers which separate the spectral components in the lateral direction [236–239]. The spectral components are only spread across a small distance which covers the otherwise unused detector area between neighboring pinholes. In [239] the pinholes are replaced by slits.

2.7 Related optical principles using chromatic aberrations

The focus of this thesis is on the design of chromatic confocal imaging systems. Optical metrology is only discussed as an exemplary application field. A comparison to other optical

measurement principles like triangulation or interferometry is thus beyond the scope of this thesis. Summaries of and comparisons to alternative techniques for optical profilometry are e.g. provided in [47, 172, 219, 222, 223, 240, 241]. Similarly, many different hyperspectral imaging techniques exist. Several of these techniques are e.g. discussed in [242–244]. Listed below are different optical systems which have similarities to the chromatic confocal setup or use an axial separation of the spectral information.

Optical spectrometers are used to analyze the spectral power distribution of incident radiation. They are typically based on a lateral separation of the spectral components through a grating or prism. Fig. 2.19(a) shows a schematic of the commerical spectrometer (Ocean Optics Maya 2000 Pro) which will be used for the experimental verification of the signal models presented in Chap. 4. The input signal is first collimated by a concave mirror. The spectral components are then deflected into different directions by a planar grating. Subsequently, a second concave mirror focuses the spectral components onto different pixels of a pixelated detector line. Finally, the spectral power distribution is calculated from the power recorded by the pixels of the line detector.

Chromatic confocal distance sensors with multiple discrete wavelengths are hybrid systems which combine aspects of the confocal and of the chromatic confocal principle [245, 246]. A chromatic confocal setup with a hyperchromatic lens is used, but the broadband light source is replaced by a source with discrete wavelengths. This way discrete axial distances are probed in parallel and the speed of the sensor system is increased. At the same time an axial scan of the surface under test is still required for the evaluation of the full axial distance range. To further increase the number of axial distances which are measured in parallel, multiple fibers can be placed at different axial distances to the hyperchromatic lens [245, 247].

Chromatic confocal endoscopes [248–251] use a spectral information coding principle to transfer information from different lateral measurement points through a single optical fiber. The basic setup is shown in Fig. 2.19(b). A common fiber is used as both the illumination and the detection port. The radiation leaving the fiber is collimated by the lens L_1 and is incident on an optical element with lateral chromatic aberration like a grating or prism. This element causes a wavelength-dependent deflection of the spectral components which are then focused at different lateral positions by the lens L_2. By combining a polychromatic light source with a spectrometric detection information from all points on the lateral line can be detected in parallel. To acquire 2D information the probe can be rotated around its z-axis [252] or a galvanometric scanning mirror may be used [253]. This principle can also be combined with a fiber-based interferometric setup to record 3D information [254]. Instead of the polychromatic source a wavelength-swept source may be used [252, 253]. Typically, endoscopes with fiber bundles only retrieve information from the object areas which are imaged onto the fiber cores while the information incident on the cladding is lost. To cover the object areas corresponding to the cladding a small amount of lateral chromatic aberration may be used which directs at least one wavelength onto the neighboring fiber core [255]. By adding a reference arm to the detection setup, an interferometric signal can be generated [248]. A similar macroscopic system with interferometric signal generation was proposed by Gronle et al. [256].

Chromatic confocal triangulation sensors combine a triangulation setup with confocal slit apertures and a lateral separation of the spectral components [257]. The basic working principle is illustrated in Fig. 2.19(c). The polychromatic radiation passing an illumination slit is incident on a concave grating which focuses the spectral components to lines with different height levels $z(\lambda)$. The surface under test reflects the spectral components which then hit a second concave grating. Only the spectral components in focus on the surface under test are also

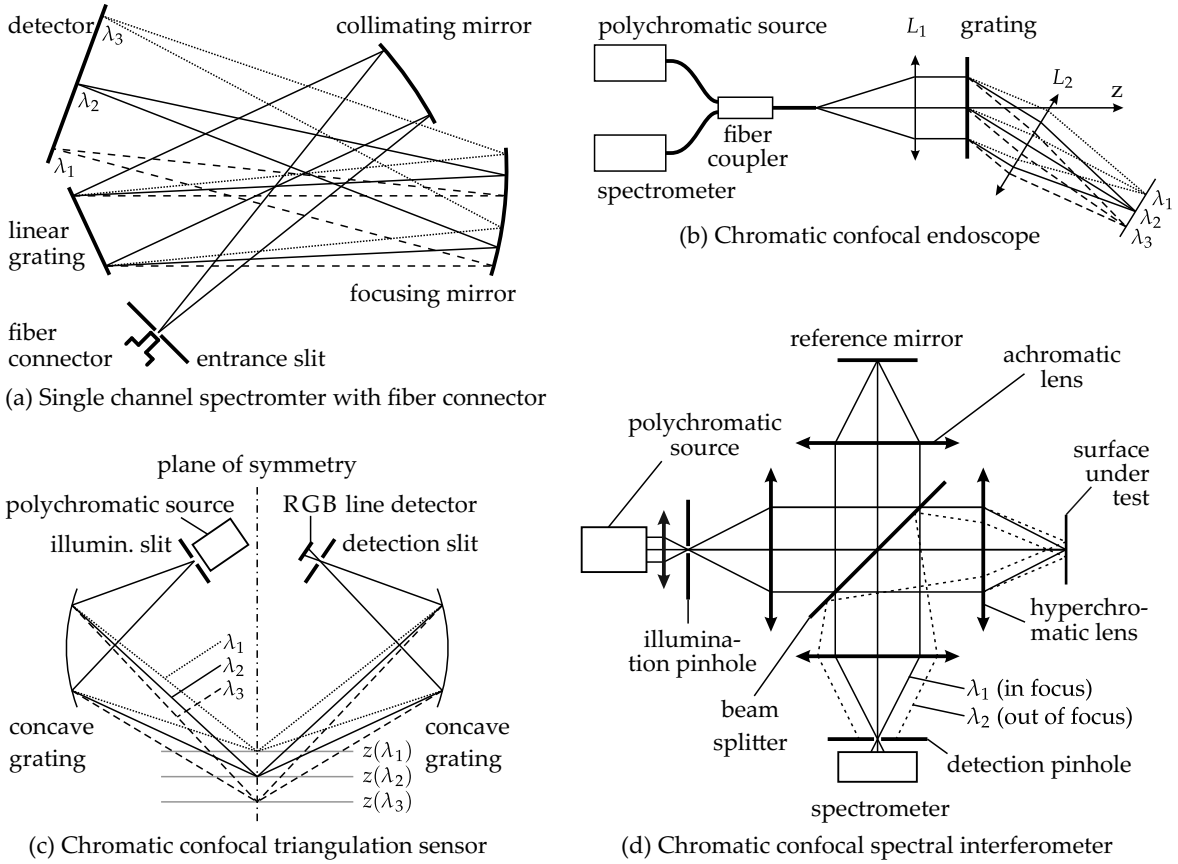

(a) Single channel spectromter with fiber connector

(b) Chromatic confocal endoscope

(c) Chromatic confocal triangulation sensor

(d) Chromatic confocal spectral interferometer

Fig. 2.19: Schematics of optical systems related to the chromatic confocal principle.

focused on the detection slit and contribute to the signal of a RGB line detector with maximum intensity. From the color coordinates of the different pixels along the RGB line detector the line profile of the surface under test is determined. An alternative spectrally coded triangulation method based on refractive components was proposed by Körner [258].

Chromatic confocal spectral interferometry (CCSI) [259–263] combines the chromatic confocal principle with a spectral interferometry setup [264–270]. For this purpose the chromatic confocal setup shown in Fig. 2.17(b) is expanded by a reference arm, see Fig. 2.19(d). The interferometric superposition of the signals from the reference and detection arms leads to a spectral interference signal which is detected by the spectrometer. The distance to the surface under test is encoded in two ways: First, in the spectral position at which the interference signal oscillates with maximum magnitude, and second, in the (spectral) oscillation frequency of the interference signal. In contrast to spectral interferometry, the measurement range of a CCSI system is not limited by the depth of field of a chromatically well corrected microscope objective. Instead, it is given by the LCA of the hyperchromatic lens [263]. In comparison to chromatic confocal sensors the CCSI system is reported to be insensitive to both self imaging effects caused by small radii of curvature of the surface under test and to an asymmetric illumination of the sensor pupil [271].

Chromatic autofocusing techniques may be used to determine the distance to an object or to increase the speed of image-based autofocus. In [272] an autofocusing technique is described which is based on the recording of multiple images at different object distances without a mechanical actuation. Using a lens with LCA the authors were able to record three images from

different object heights in parallel. They were thus able to reduce the number of mechanical movements which relates to a potential increase of autofocus speed. In [273, 274] a depth-from-defocus approach is presented which is based on the image acquisition with a hyperchromatic lens. Depth-from-defocus methods are based on the evaluation of the intensity point spread function (IPSF) at out of focus planes. If a hyperchromatic lens is used, the different channels of an RGB image contain IPSFs of different size. From these different defocus IPSFs the object distance can be determined more precisely than from a single defocus IPSF.

Single shot phase retrieval is possible with a system consisting of a hyperchromatic lens and an RGB camera [275–277]. The interaction of an electromagnetic wave with an object typically leads to a modification of both the phase and the amplitude of the electromagnetic wave. As optical detectors are only sensitive to the intensity of the incident wave field, classical imaging systems are optimized for transforming intensity information. In contrast, different applications like the imaging of transparent biological objects or the evaluation of wavefronts require the retrieval of phase information. For this purpose different approaches like phase contrast microscopy [278], interferometric techniques [279–281], Shack-Hartmann sensors [282], and phase retrieval techniques [283–285] are used. The phase retrieval techniques are based on two or more intensity measurements at different axial distances. Based on wave optical propagation equations the phase distribution leading to the intensity distributions can be determined. To avoid multiple intensity measurements at different axial distances a combination of a hyperchromatic lens and an RGB camera can be used [275–277]. In this case each spectral channel corresponds to a different propagation distance and a single RGB image contains sufficient information to determine the phase with a single measurement.

Increased depth of field and multi-plane imaging can be realized with an optical system which consists of a hyperchromatic lens and a fixed image plane. The hyperchromatic lens spans a range of depth levels in object space. As observed by Courtney-Pratt, Molesini, and Quercioli, the depth information is spectrally coded in the image recorded by the detector or the human eye [151, 286]. For each depth level one specific spectral component is imaged sharply onto the image plane. Recently, various authors reported that LCA may thus be used for increasing the depth-of-field of an imaging system. Different post-processing algorithms have been proposed for evaluating both gray-scale and colored objects [287–292]. The idea of many of these approaches is summarized in the following sentences [287]: “When employing multiple color channels, the optical system for a grayscale image need not provide high quality images across the entire range of wavelengths, but the collection of color channels must provide all information needed to reconstruct the grayscale image. [...] This approach thus relaxes the traditionally expensive constraints on optical subsystem performance and enables new classes of imaging systems.”

2.8 Summary of Chapter 2

In this chapter the required models of optical imaging were explained and it was shown how spectral information can be separated using refractive and diffractive optical elements. The basic working principle of confocal and chromatic confocal imaging systems were described and an overview of the state of the art in these fields was provided. The shape and width of the spectral peak were introduced as the main performance criteria. Additionally, overviews of existing signal models for confocal and chromatic confocal systems as well as related sensor principles were presented.

3 Advanced methods for focal field calculations

This chapter provides an overview of advanced techniques for the non-paraxial calculation of the field in the focal region. These techniques are essential to the wave optical signal model which will be presented in Chap. 4 and have to be compatible with the raytracing approaches used throughout this thesis. At the same time they have to give accurate results for large defocus distances within a reasonable time.

First, the calculation framework is explained which combines raytracing to the exit pupil with a wave optical propagation to the focal region. Second, an overview of existing wave optical calculation methods is given. Then, two well suited methods are discussed in detail. These methods are the Extended Nijboer-Zernike (ENZ) theory and the FFT-based calculation of the first Rayleigh-Sommerfeld diffraction integral (RS_I). For the FFT-based methods new sampling schemes and an efficient tiling technique are introduced. Subsequently, an accuracy comparison is presented and the methods most suitable for the intended focal calculations are determined.

3.1 Combination of raytracing and a wave optical propagation step

Fig. 3.1 illustrates the wave optical focal field calculation approach used within this thesis. It combines the wave optical model with the geometrical model and closely follows the concepts discussed in [21] and [10, Chapters 6 and 14]. The method is limited to monochromatic fields but can be applied repeatedly to account for a polychromatic source. The analysis starts with a single point of the object plane which emits a monochromatic ray bundle. The rays of this bundle have different directions and are spread homogeneously across the EP of the optical system. Each ray represents a part of the EP and carries a specific amount of power. After passing the EP the ray is traced through the optical system to the reference plane. The raytracing is performed with the commercial lens design software ZEMAX. For each ray the optical path length and the intersection point with the reference plane are calculated. Additionally, the polarization raytrace-function provides information on the absorption and (polarization dependent) reflection losses within the optical system.

The resulting data is exported to the commercial numerical computing environment MATLAB where a complex field is generated from the raytracing data. This field is propagated to the observation plane in order to determine the intensity point spread function (IPSF) of the optical system. All subsequent operations linked to the wave optical signal model (see Chap. 4) are also performed with MATLAB.

The propagation methods discussed below require the field to be described either by a continuous function or as a homogeneously sampled grid of points. In both cases the raytracing data, which is only available at discrete points, needs to be interpolated or approximated by an analytical function. To this end two types of Zernike expansions are used. For the FFT-based methods and for the direct numerical integration the complex amplitude is described at a planar reference surface with two real-valued Zernike series. The first Zernike series approxi-

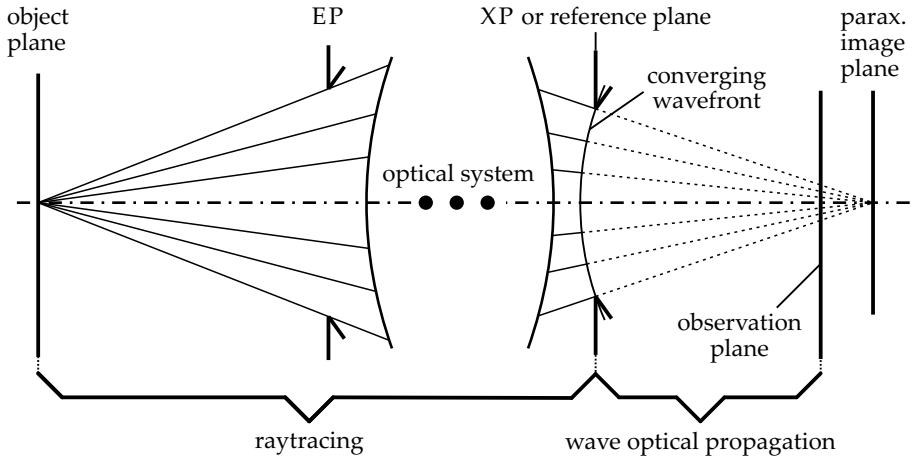

Fig. 3.1: Hybrid system model used for the wave optical calculation of the PSF at an out of focus plane.

mates the phase and the second one the amplitude. For the Extended Nijboer-Zernike theory (Chapter 3.3) a single Zernike series with complex coefficients is used to describe the deviation of the image space wavefront from a spherical reference wave. All Zernike coefficients are determined by least-square fitting of the raytracing data.

The resulting analytical functions are a representation of the geometrical wavefront in image space and do not account for diffraction effects within the optical system. Diffraction effects are only considered during the wave optical propagation step from the reference plane to the observation plane. In the Kirchhoff approximation they are all attributed to the boundary of the field u^0 at the reference plane. For an object point the boundary is assumed to be circular. If the object point lies off-axis, vignetting may be observed and the geometrical wavefront may be truncated at multiple apertures within the optical system. In this case some of the rays emerging from the object point are truncated within the optical system and do not reach the reference plane in image space. To account for these losses the convex hull of the rays reaching the reference plane is used to determine the effective lateral extent of the field u^0 (Kirchhoff approximation) or its spatial frequency extent (Debye approximation). The truncated field is then propagated to the desired observation plane using a wave optical propagation step.

Different aperture functions can be easily added to the model when generating the complex amplitude field. Radiometric effects are included in this way. They are based on the observation that an ideal optical system which fulfills Abbe's sine condition transforms an incident spherical wave into an output wave with inhomogeneous intensity distribution [8, 293–295]. Similarly, a radially varying efficiency of the DOEs may be modeled through an aperture function.

3.2 Suitable methods for the wave optical propagation step

Below, selected methods for solving the RS_I or equivalent integrals are presented. The discussion is based on the historic overviews by Born, Wolf, and Stamnes [5, 10, 296]. It includes the Fresnel and Fraunhofer approximations of the RS_I and is limited to scalar methods which are aimed at the propagation in homogeneous media:

Closed-form solutions of the RS_I are only available for a limited number of special cases like the calculation of the on-axis intensity distribution for a spherical wave which is focused on

axis [10, 297–299]. This specific case will be used as a reference for evaluating approximative calculation schemes. Further closed form solutions become available if the RS_I is reduced to the paraxial or to the far field approximation. An example is the work of Airy who demonstrated that in the paraxial approximation the lateral distribution in the focal plane of an ideal spherical wave is described by a Bessel function [300]. Born discussed the influence of small amounts of aberrations onto the intensity distribution in the Gaussian image plane [301, 302]. For this purpose he used a combination of Bessel functions. An elegant analytical solution for non-paraxial systems containing small amounts of aberrations is given by the Nijboer-Zernike theory [303–307]. There, the wavefront deviations of the optical systems are described in terms of a Zernike expansion and the contribution of the Zernike terms to the focal field is evaluated.

Semi-analytical methods are closely related to the closed form solutions but require the evaluation of infinite series to solve the diffraction integral exactly. In practice, only a finite number of terms is calculated which results in an approximate result. A prominent approach goes back to Lommel who studied the focal region of an ideal spherical wave in the paraxial approximation [308]. In the ideal focal plane Lommel's solution converges to the analytical closed-form solution of Airy [300]. A similar treatment is attributed to Struve [309] who used generalized Lommel functions to study spherial aberration [310]. A powerful semi-analytical method is the Extended Nijboer-Zernike theory (ENZ) [8, 311–313]. It extents the work of Nijboer, Zernike, and Nienhuis to arbitrary amounts of defocus and large amounts of aberrations. In contrast to the original theory infinite series are required for an exact description of the field in the focal region. Similar approaches are described by Bagheri et al. [314] and Ramos-Lopez et al. [315].

The **numerical integration** of diffraction integrals was already used at a time when computers were not readily available [316–320]. Its is challenging for a number of reasons: First, the fine details of the diffraction pattern in the observation plane require many calculations of the diffraction integral. Second, the phase term within the RS_I leads to an oscillatory integrand which requires dense sampling in the reference plane. Third, the integration area is typically large with respect to the sampling intervals. In general, the numerical effort increases with growing defocus and with growing NA. It also increases with growing lateral distances between the geometric focus point and the point at which the field is calculated. Various specialized integration schemes account for the oscillatory nature of the phase term. They are typically based on the division of the integration regions into segments within which the phase function is approximated with linear [321–326] or a quadratic functions [326–329]. The segments are then evaluated analytically and the contributions from the different segments are added coherently. In mathematics, highly oscillatory quadrature is a dynamic research field, see e.g. [330–334]. Many of the resulting techniques have not yet been transferred to optical systems and focal field calculations. For small amounts of defocus the number of oscillations within the RS_I is moderate and classical quadrature schemes may be used [335, 336].

The **Boundary Diffraction Wave Theory** describes the diffracted field as the superposition of the field predicted by geometrical optics and a boundary diffraction wave [337–342]. The boundary diffraction wave is given by the ring integral along the border of the diffracting aperture. The numerical effort is reduced from a 2D integral to a 1D integral. A significantly enhanced performance may thus be obtained.

The **geometrical theory of diffraction** replaces the calculation of the 2D integral with a ray-based approach [343–346]. The rays fulfill a generalized version of Fermat's principle. Besides the direct ray from the object to the observation point, additional rays to the rim of the aperture are considered. In its original form the geometrical theory of diffraction is not suitable for

calculating the field close to the focus or in the shadow boundary region behind the aperture. It has, however, been extended to the calculation of focal fields and caustics [347–349].

Asymptotic techniques are based on the insight that large parts of the oscillatory integration area of the RS_I do not contribute to the focused field due to destructive interference [10, 350–354]. The integration can thus be reduced to small regions containing stationary points and to the boundary region of the field. At these points the integral is evaluated asymptotically. To this end the method of stationary phase is commonly used. It results in a simplified integral which can often be solved analytically. The asymptotic evaluation of the RS_I can be significantly faster than its numerical solution [10]. At the same time the identification and handling of the stationary points requires additional effort.

Fast Fourier Transform (FFT) techniques are possibly the most common approach to solving the RS_I [9, 10, 13, 14, 16]. They are used in numerical implementations of the RSC (Eq. 2.15) and the ASM (Eq. 2.20). In contrast to the other numerical calculation schemes which are used to calculate the field at a single point, FFT techniques provide the full field in the observation plane. If many points have to be calculated in the output plane, FFT-based approaches can thus be significantly faster than point-by-point methods [10]. The FFT requires discrete sampling in the space domain and in the spatial frequency domain. At the same time the fields in both domains are finite in extent and have to be stored in memory for optimum calculation performance. These special properties of the FFT lead to high hardware requirements while specific sampling conditions have to be fulfilled in order to obtain accurate results.

The **propagation of Gaussian beamlets** is a raytracing-based technique which is used by commercial simulation programs like ASAP and FRED [355, 356]. The field at the reference plane is decomposed into Gaussian beamlets. The Gaussian beamlets are propagated to the observation plane using geometrical optics [357]. In the observation plane the fields associated with the beamlets are added coherently.

The methods described above have been developed for different application scenarios. To identify the methods best suited for the signal models of this thesis, the following requirements are defined:

- Solution of the non-paraxial version of the RS_I in the Debye or Kirchhoff approximation to achieve an accurate prediction of the measurement signal.
- Compatibility with aberrated wavefronts and non-spherical pupil shapes to account for the properties of the optical system.
- Compatibility with large defocus values of more than 50 µm to cover a reasonable measurement space.
- Fast calculation of many points in the observation plane.
- Compatibility with numerical convolution methods, i.e. calculation of the points in the observation plane on a rectangular grid.
- Semi-automatic calculation without the need for manual identification of stationary points.

Based on these requirements both the ENZ and FFT-based techniques (RSC and ASM) are identified as suitable methods for performing the wave optical propagation from the exit pupil (or a general reference plane) to the observation plane. The limitations and special properties of the ENZ, the RSC, and the ASM will be discussed in more detail in the following sections. The results obtained with the three methods will be validated by comparison to a closed-form

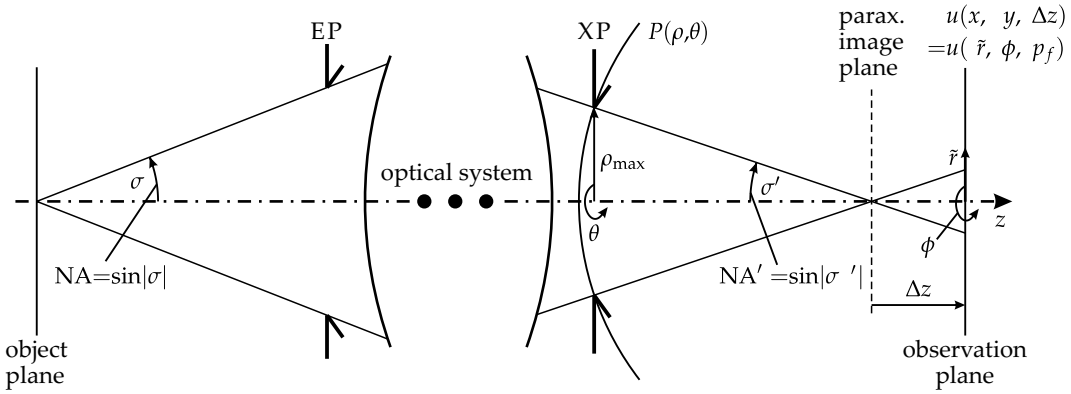

Fig. 3.2: Geometry of the ENZ calculation.

solution (primary reference) and to the results of an accurate numerical integration scheme (secondary reference).

3.3 Focal field calculations using the Extended Nijboer-Zernike theory

The ENZ solves the $\mathrm{RS_I}$ in the Debye approximation by integration over a circular pupil [8, 311–313]. For this purpose Eq. 2.29 is written in polar coordinates and adapted to the specific requirements of the ENZ calculation scheme [8, Eq. 2.39]:

$$u(\tilde{r},\phi,p_f) = \frac{-j\,\mathrm{NA}^2}{\lambda}\exp\left[\frac{-jp_f}{1-\sqrt{1-\mathrm{NA}'^2}}\right]\int_0^1\int_0^{2\pi}\mathrm{AF}\cdot\mathrm{DF}\cdot P(\rho,\theta+\pi)$$
$$\cdot\exp\left[2\pi j\rho\tilde{r}\cos(\theta-\phi)\right]\rho\,\mathrm{d}\rho\,\mathrm{d}\theta. \quad (3.1)$$

The geometry of the ENZ calculation is illustrated in Fig. 3.2. $u(\tilde{r},\phi,p_f)$ is the field in the observation plane and is calculated in normalized polar coordinates with $x = \tilde{r}\frac{\lambda}{\mathrm{NA}'}\cos\phi$, $y = \tilde{r}\frac{\lambda}{\mathrm{NA}'}\sin\phi$ and $\tilde{r} = \frac{\mathrm{NA}'}{\lambda}\sqrt{x^2+y^2}$, see [8, Eq. 2.40]. The non-normalized coordinates at the reference plane are $x^0 = -\rho r_{\mathrm{AP}}\cos\theta$ and $y^0 = -\rho r_{\mathrm{AP}}\sin\theta$, with r_{AP} being the physical aperture radius. The z-position of the observation plane is described relative to the center point of the reference sphere (defocus distance Δz) through the defocus parameter p_f:

$$p_f = -\frac{2\pi\Delta z}{\lambda}\left(1-\sqrt{(1-\mathrm{NA}'^2)}\right). \quad (3.2)$$

ρ and θ are the normalized polar coordinates in the reference plane. The input field is defined by the generalized pupil function $P(\rho,\theta) = A(\rho,\theta)\exp[j\phi(\rho,\theta)]$ which describes the deviations from a spherical reference wave. AF is an algebraic factor which accounts for radiometric effects. For a finite object distance it is given by

$$\mathrm{AF}_{\mathbf{finite}} = \frac{\left(1-\mathrm{NA}'^2\rho^2\right)^{1/2}+\left(1-\mathrm{NA}^2\rho^2\right)^{1/2}}{\left(1-\mathrm{NA}'^2\rho^2\right)^{1/4}\left(1-\mathrm{NA}^2\rho^2\right)^{3/4}}. \quad (3.3)$$

The influence of the defocus parameter p_f is considered through the defocus factor DF:

$$\mathrm{DF} = \exp\left[\frac{jp_f}{1-\sqrt{1-\mathrm{NA}'^2}}\left(1-\sqrt{(1-\mathrm{NA}'^2\rho^2)}\right)\right]. \tag{3.4}$$

To solve Eq. 3.1, the generalized pupil function as well as the algebraic factor and the defocus factor are expanded in complex Zernike series. The Zernike expansion of the generalized pupil function is given by

$$P(\rho,\theta) = \sum_{n_p,\, m_p} \beta_{n_p}^{m_p} R_{n_p}^{|m_p|}(\rho)\exp\left[jm_p\theta\right]. \tag{3.5}$$

$\beta_{n_p}^{m_p}$ are the complex Zernike coefficients. The radial polynomials R_n^m were defined in Eq. 2.49. Using the advanced techniques described in [313], the product of a single Zernike term of the pupil function and the Zernike expansions of AF and DF is converted into a single Zernike series with coefficients $\beta_{n_c}^{m_c}$. This way Eq. 3.1 can be rewritten as

$$\begin{aligned} u(\tilde{r},\phi,p_f) = \frac{-j\,\mathrm{NA}^2}{\lambda}\exp\left[\frac{-jp_f}{1-\sqrt{1-\mathrm{NA}'^2}}\right]\cdot \\ \sum_{n_p,\, m_p}\beta_{n_p}^{m_p}\left\{\sum_{n_c,\, m_c}\beta_{n_c}^{m_c}\int_0^1\int_0^{2\pi} R_{n,c}^{|m_c|}\exp\left[2\pi j\rho\tilde{r}\cos(\theta-\phi)\right]\exp[jm_c\theta]\rho\,\mathrm{d}\rho\,\mathrm{d}\theta.\right\} \end{aligned} \tag{3.6}$$

The individual integrals can be solved analytically [303, 313]:

$$\int_0^1\int_0^{2\pi} R_n^{|m|}\exp\left[2\pi j\rho\tilde{r}\cos(\theta-\phi)\right]\exp[jm\theta]\rho\,\mathrm{d}\rho\,\mathrm{d}\theta = 2\pi j^n\frac{J_{n+1}(2\pi\tilde{r})}{2\pi\tilde{r}}\exp[jm\phi], \tag{3.7}$$

with J_i being the Bessel function of the first kind and of order i.

The exact analytical description of the functions AF and DF with Zernike series requires an infinite number of Zernike coefficients. Van Haver and Janssen provide truncation rules which enable the fast calculation of Eq. 3.1 with minimum loss of accuracy [358]. In many cases the required number of coefficients and the numerical effort increase with growing defocus values.

While the ENZ solves the $\mathrm{RS_I}$ in the Debye approximation, the approach can be modified to generate results which closely resemble those of the $\mathrm{RS_I}$ in the Kirchhoff approximation, see [359] and [313, Chapter 4.5.2]. To this end the parameters $\tilde{r}$ and p_f of Eq. 3.6 are replaced by the modified parameters [313, Chapter 4.5.2]

$$\tilde{r}' = \frac{\tilde{r}}{1-\frac{\lambda p_f}{\pi\mathrm{NA}^2 z_f}\sqrt{1-\mathrm{NA}^2}}, \qquad p_f' = \frac{p_f}{1-\frac{\lambda p_f}{\pi\mathrm{NA}^2 z_f}\sqrt{1-\mathrm{NA}^2}}. \tag{3.8}$$

Finally, the output values have to be multiplied with the factor jz_f/z to obtain the correct magnitude and phase. The depicted approach is only a low order approximation. For an even better agreement between the modified ENZ approach and the results of the $\mathrm{RS_I}$ in the Kirchhoff approximation higher order terms may be included in the calculation, see [359].

3.4 FFT-based focal field calculations I: general approach

The field at a rectangular grid of points in the observation plane can be determined efficiently using FFT-based techniques. For this purpose the analytical forward and inverse Fourier transforms are replaced by discretized versions which are given by

$$\tilde{B} = \mathrm{FFT}\left\{\tilde{b}\right\} \Delta x \Delta y, \tag{3.9}$$

and

$$\tilde{b} = \mathrm{FFT}^{-1}\left\{\tilde{B}\right\} / \left(\Delta x \Delta y\right), \tag{3.10}$$

with the standard FFT expressions [360]

$$\mathrm{FFT}\left\{\tilde{b}\right\} = \sum_{n_x=0}^{N_x-1} \sum_{n_y=0}^{N_y-1} \tilde{b} \exp\left[-2\pi j \left(\frac{n_x n_{\nu x}}{N_x} + \frac{n_y n_{\nu y}}{N_y}\right)\right] \tag{3.11}$$

and

$$\mathrm{FFT}^{-1}\left\{\tilde{B}\right\} = \frac{1}{N_x N_y} \sum_{n_{\nu x}=0}^{N_x-1} \sum_{n_{\nu_y}=0}^{N_y-1} \tilde{B} \exp\left[2\pi j \left(\frac{n_x n_{\nu x}}{N_x} + \frac{n_y n_{\nu y}}{N_y}\right)\right]. \tag{3.12}$$

In comparison to the analytical Fourier transform integrals of Eqs. 2.13 and 2.14 the discretized versions are limited to arrays of finite extent. Both the space domain and the spatial frequency domain fields contain $N_x \cdot N_y$ points spaced at sampling intervals Δx and Δy. The tilde-symbol indicates discretely sampled fields. For space domain fields lower case letters are used while spatial frequency domain fields are expressed by uppercase letters. The continuous coordinates x, y, ν_x and ν_y are replaced by the discrete positions

$$x = n_x \Delta x, \;\; y = n_y \Delta y, \;\; \nu_x = n_{\nu x} \Delta \nu_x, \;\; \nu_y = n_{\nu y} \Delta \nu_y, \tag{3.13}$$

with

$$n_x,\, n_{\nu x} = 1 \ldots N_x, \quad \text{and} \quad n_y,\, n_{\nu y} = 1 \ldots N_y. \tag{3.14}$$

To describe the numerical extent of the discretely sampled fields, the *LN*-operator is introduced. The numerical extent of the space domain field $\tilde{b}(n_x, n_y)$ is given by

$$LN(\tilde{b}) = LN(\tilde{b}, n_x) \cdot LN(\tilde{b}, n_y), \tag{3.15}$$

with

$$LN(\tilde{b}, n_x) = N_x \cdot \Delta x, \text{ and } LN(\tilde{b}, n_y) = N_y \cdot \Delta y. \tag{3.16}$$

The numerical extent of the spatial frequency domain field $\tilde{B}(n_{\nu x}, n_{\nu y})$ is given by

$$LN(\tilde{B}) = LN(\tilde{B}, n_{\nu x}) \cdot LN(\tilde{B}, n_y), \tag{3.17}$$

with

$$LN(\tilde{B}, n_{\nu x}) = N_x \cdot \Delta \nu_x, \;\; LN(\tilde{B}, n_{\nu y}) = N_y \cdot \Delta \nu_y. \tag{3.18}$$

The FFT operations require that the sampling intervals in the space domain and in the spatial frequency domain are linked through the equations

$$1/N_x = \Delta x \Delta \nu_x, \qquad 1/N_y = \Delta y \Delta \nu_y. \tag{3.19}$$

The FFT implementations of the ASM and the RSC propagations are given by

$$\tilde{u}^z = \begin{cases} \mathrm{FFT}^{-1}\left\{\mathrm{fftshift}\left\{\tilde{H}\right\}\mathrm{FFT}\left\{\tilde{u}^0\right\}\right\} & \text{for AS} \\ \mathrm{FFT}^{-1}\left\{\mathrm{FFT}\left\{\mathrm{fftshift}\left\{\tilde{h}\right\}\right\}\mathrm{FFT}\left\{\tilde{u}^0\right\}\right\}\Delta x\Delta y & \text{for RSC.} \end{cases} \tag{3.20}$$

The factor $\Delta x\Delta y$ is included to implement the correct intensity scaling according to Eqs. (3.9) and (3.10). The "fftshift" operation realizes the correct indexing of the arrays, see Ref. [12] for more detail.

To retrieve the high-frequency details of the diffracted field, dense sampling of the output plane is often required. If the ASM and the RSC are implemented according to Eq. 3.20 the sampling intervals in the observation plane are identical to those in the reference plane. The requirement for a high sampling rate in the observation plane thus leads to an undesirably dense sampling in the reference plane and to a large computational load. Two different techniques are thus implemented which allow for the observation plane to be sampled at smaller intervals than the input plane.

The first technique will be called sub-pixel sampling technique (SST) and was proposed by Zhang et al. [361]. It is based on the Fourier shift theorem which implies that the multiplication with a linear phase in the spatial frequency domain leads to a lateral shift by s_x and s_y in the space domain [9]:

$$b(x-s_x, y-s_y) = \mathcal{F}^{-1}\left\{B(\nu_x,\nu_y)\exp\left[-j2\pi\left(\nu_x s_x + \nu_y s_y\right)\right]\right\} \tag{3.21}$$

This way the field in the observation plane can be shifted by a sub-pixel value and information at points between those of the normal sampling grid can be retrieved. To obtain a denser sampling grid in the observation plane the shift theorem and the consecutive inverse Fourier transform have to be applied repeatedly with different linear phase terms. Each linear phase term corresponds to one of the desired sub-pixels positions. A four times denser sampling in the observation plane requires $4 \cdot 4$ multiplications with different linear phase terms and $4 \cdot 4$ inverse Fourier transforms.

Eq. 3.21 may also be used to shift the output field by a macroscopic value [14, 362]. This approach is e.g. helpful in off-axis imaging cases in which the geometrical focus does not lie within the central output window of the FFT calculation. The center of the output window can then be shifted to the point (x_c, y_c) by multiplying the spatial frequency signal with the field $\exp\left[j2\pi\left(\nu_x x_c + \nu_y y_c\right)\right]$.

The second technique which allows for different sampling intervals and field sizes in the reference plane and the observation plane is the chirp z transform (CZT) [363–371]. The CZT can be considered an alternative to the normal FFT and does not require fulfillment of Eq. 3.19. To modify the sampling of the field in the observation plane either the forward FFTs of $\tilde{u}^0$ and $\tilde{h}$ or the inverse FFT of $\tilde{U}^z$ can be replaced by a CZT. Below, the operation $\mathrm{FFT}^{-1}\left\{\tilde{U}^z\right\}$ is replaced by a CZT according to [368]. With $a_x = \Delta x/\Delta\nu_x$ and $a_y = \Delta y/\Delta\nu_y$ a set of scaling factors is used in combination with new coordinates $w_x = a_x\nu_x$ and $w_y = a_y\nu_y$. These steps are linked to new sampling intervals $\Delta w_x = \Delta x = a_x\Delta\nu_x$ and $\Delta w_y = \Delta y = a_y\Delta\nu_y$. The CZT-replacement of the inverse FFT operation (Eq. 3.12) is given by [368]:

$$\tilde{u}^z = \mathrm{CZT}(\tilde{U}^z) = \Delta w_x\Delta w_y\tilde{D}_1\left(\frac{\tilde{U}^z\cdot\tilde{D}_3}{a_x a_y}\otimes\tilde{D}_2\right). \tag{3.22}$$

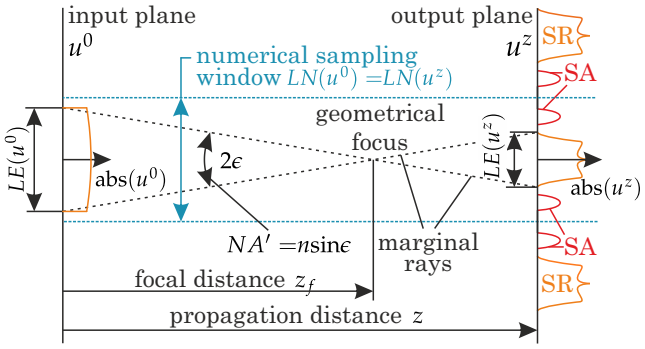

Fig. 3.3: Propagation of a focusing field u^0 from the input plane $z = 0$ to the output plane z. The discrete sampling leads to spatial replicas (SR) and may also cause spatial artifacts (SA). The effective extents of u^0 and of the output field u^z are given by $LE(u^0)$ and $LE(u^z)$ [20].

The three arrays $\tilde{D}_1$, $\tilde{D}_2$, and $\tilde{D}_3$ are discretized versions of the three chirp functions

$$D_1 = \exp\left[j\pi\left(x^2/a_x + y^2/a_y\right)\right], \tag{3.23}$$

$$D_2 = \exp\left[-j\pi\left(w_x^2/a_x + w_y^2/a_y\right)\right], \tag{3.24}$$

$$D_3 = \exp\left[j\pi\left(w_x^2/a_x + w_y^2/a_y\right)\right]. \tag{3.25}$$

The CZT includes a convolution which is indicated by the $\otimes$-operator. This convolution is performed efficiently using FFTs.

3.5 FFT-based focal field calculations II: sampling considerations

The discrete sampling used for performing the ASM and the RSC according to Eq. 3.20 leads to the appearance of replicas and artifacts [10, 360, 372, 373]. An important part of the simulation techniques introduced in this thesis consists in the development of sampling strategies which enable the calculation of focal fields with an optimum balance between accuracy and numerical effort. The results of this analysis are published in [20]. Below the main findings are summarized. To facilitate the discussion, the field at the reference plane will be called “input field" while the field at the observation plane will be called “output field."

Sampling criteria for the ASM and the RSC have been discussed by various authors [19, 367, 374–383]. In many of these publications (e.g. [19, 367, 374]) the Nyquist-Shannon sampling theorem is applied to the chirp functions h and H of the ASM and the RSC to determine propagation regions within which the two methods give accurate results. Based on this concept several modified versions of the ASM and the RSC with extended ranges of validity are introduced [367, 375, 376]. Several authors report that not only the chirp functions h and H but also the input field have to be included in the sampling considerations [367, 383]. Other authors discuss sampling criteria from the perspective of the Wigner distribution and of the space-bandwidth product [377, 379–382].

In [20] samples of focal field calculations are shown which give erroneous results although the Nyquist sampling criterion is fulfilled for both the input field and the propagation kernel. The cause of these errors is that the two fields are analyzed independently. The sampling

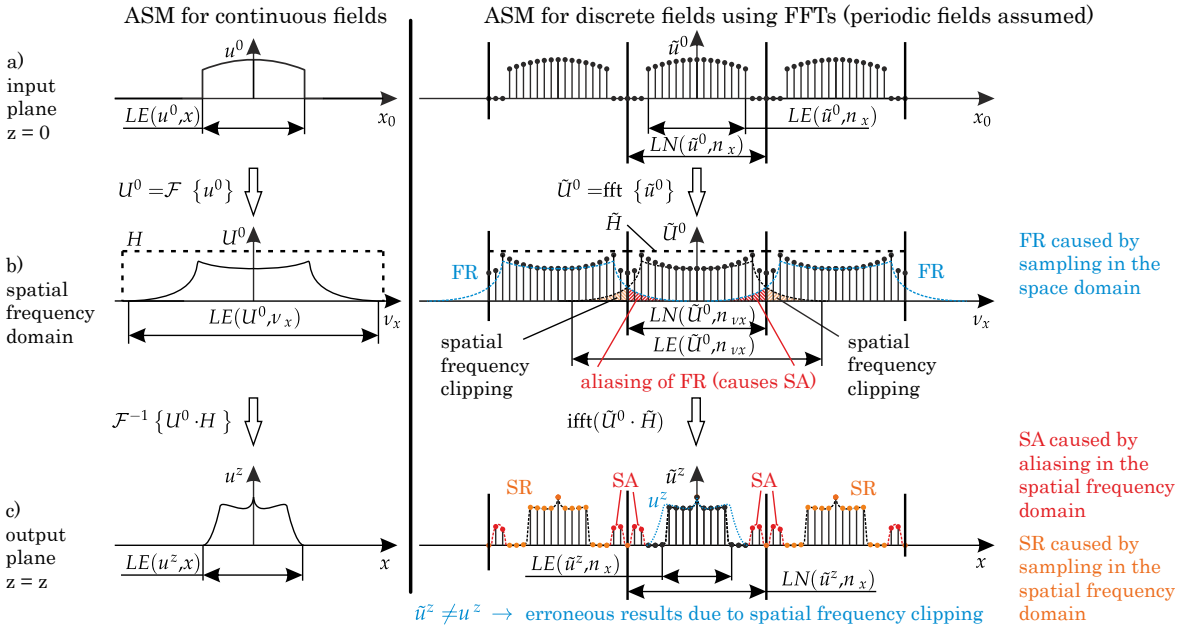

Fig. 3.4: Schematic of the ASM for the propagation of continuous and discretely sampled fields. a) spatial distribution of the input field, b) spatial frequency distribution of the input field and of the propagation kernel, and c) spatial distribution of the propagated field [20].

criteria developed below are thus based on a combined analysis of the input field and of the chirp functions h and H. They differ significantly from those found in the literature. The sampling discussion is based on the general setup depicted in Fig. 3.3. To describe the effects of discrete sampling the concept of two types of artifacts is used. The first type is called spatial replicas (SR) and is caused by discrete sampling in the spatial frequency domain. The second type is called spatial artifacts (SA) and results from aliasing (i.e. signal overlapping) in the spatial frequency domain. One of the main goals of the following sampling criteria is to keep both SA and SR from overlapping with the central region of the output field which contains the relevant information ($LE(u^z)$ in Fig. 3.3). A second goal is to ensure that none of the spatial frequencies contributing to the central region of the output field is truncated during the propagation.

The left hand columns of Figs. 3.4 and 3.5 illustrate the implementations of the ASM and the RSC with continuous Fourier transforms. From a mathematical perspective both implementations are equivalent. Differences arise when the two algorithms are implemented numerically using FFTs and discrete sampling. These differences are visualized in the right hand columns of Figs. 3.4 and 3.5 which also illustrate the origins of numerical artifacts and replicas.

In Eqs. 3.15 to 3.18 the numerical extent of space domain and spatial frequency domain fields was defined. The extent of the numerical field may differ significantly from the physical field size which can be infinite in extent. Typically, most of the power of the physical field is contained within a finite region [382, 384, 385]. To describe this region, the effective size LE of the physical field is used. The effective size of the space domain field $\tilde{b}(n_x, n_y)$ is given by

$$LE(\tilde{b}) = LE(\tilde{b}, n_x) \cdot LE(\tilde{b}, n_y). \tag{3.26}$$

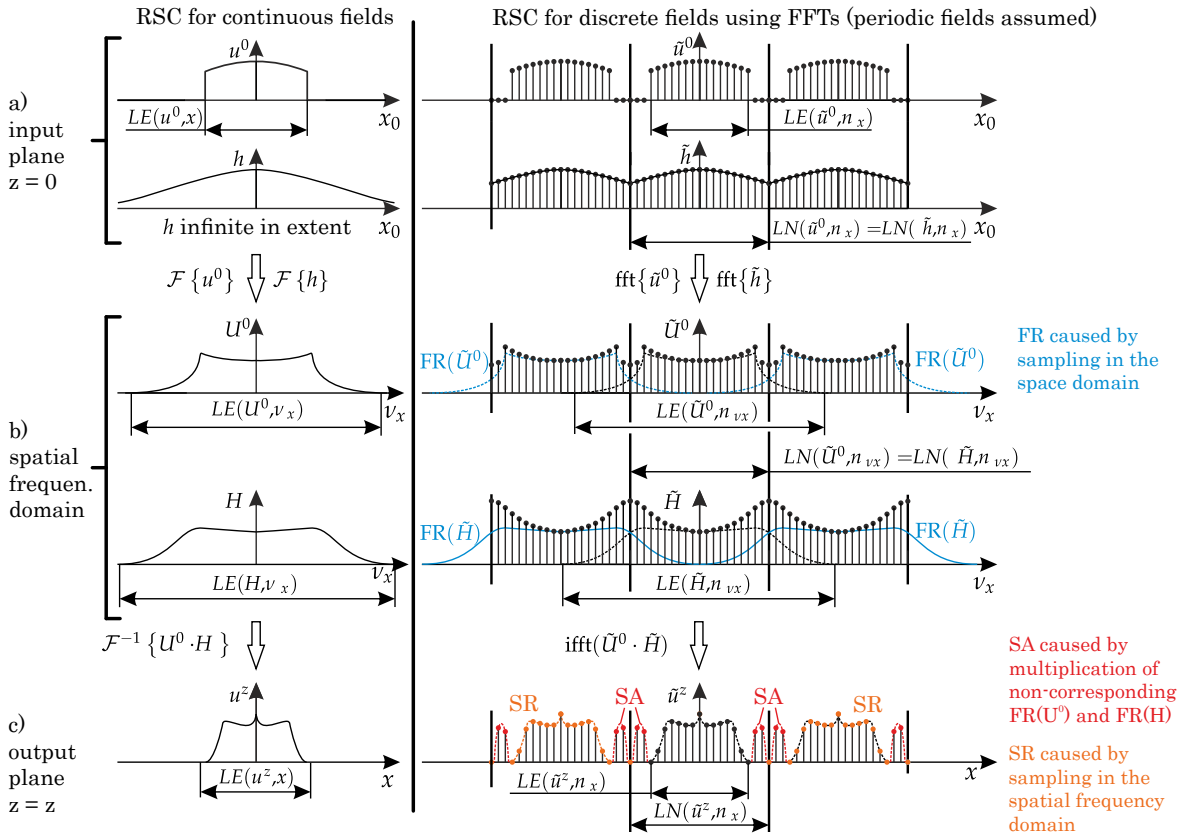

Fig. 3.5: Schematic of the RSC for the propagation of continuous and discretely sampled fields. a) spatial distribution of the input field and the propagation kernel, b) spatial frequency distribution of the input field and of the propagation kernel, and c) spatial distribution of the propagated field [20].

Similarly, the effective extent of the spatial frequency domain field $\tilde{B}(n_{\nu_x}, n_{\nu_y})$ is given by

$$LE(\tilde{B}) = LE(\tilde{B}, n_{\nu_x}) \cdot LE(\tilde{B}, n_{\nu_y}). \tag{3.27}$$

The spatial replicas (SR) shown in Fig. 3.3 are a consequence of the discrete sampling in the spatial frequency domain [360]. Their distance is given by

$$1/\Delta\nu_x = LN(\tilde{b}, n_x) \quad \text{and} \quad 1/\Delta\nu_y = LN(\tilde{b}, n_y). \tag{3.28}$$

Discrete sampling in the space domain leads to replicas in the spatial frequency domain which will be called Fourier Replicas (FRs) [360]. These replicas are separated by

$$1/\Delta x = LN(\tilde{B}, n_{\nu_x}) \text{ and } 1/\Delta y = LN(\tilde{B}, n_{\nu_y}). \tag{3.29}$$

3.5.1 Effects of discrete sampling in the space domain

In both the ASM and the RSC the input field $\tilde{u}^0$ is defined in the space domain. Thus, the spatial frequency domain shown in Figs. 3.4(b) and 3.5(b) contains an infinite series of FR($\tilde{U}^0$). If the input field is sampled below the Nyquist rate, its spatial frequency extent $LE(\tilde{U}^0)$ will

exceed the size of the numerical sampling window $LN(\tilde{U}^0)$. The consequences differ between the ASM and the RSC:

In case of the ASM the propagation kernel H is only defined within $LN(\tilde{H}) = LN(\tilde{U}^0)$. The spatial frequency components of U^0 which exceed $LN(U^0)$ are clipped (spatial frequency clipping in Fig. 3.4(b)). It is assumed that these spatial frequencies contribute to the relevant region $LE(\tilde{u}^0)$ of the output field. In this case the numerical output field $\tilde{u}^z$ differs from the correct output field u^z. Spatial frequency clipping can be avoided by requiring

$$LE(\tilde{U}^0) < LN(\tilde{U}^0). \tag{3.30}$$

Additionally, parts of neighboring $\mathrm{FR}(\tilde{U}^0)$ reach into the central Fourier window. There they are multiplied with a non-corresponding propagation kernel which leads to spatial artifacts (SAs) in the output plane (Fig. 3.4c). If Eq. 3.30 is fulfilled, SA will be avoided.

In case of the RSC not only the input field $\tilde{u}^0$ but also the propagation kernel $\tilde{h}$ is defined in the space domain. Fig. 3.5(b) illustrates that in the spatial frequency domain infinite series of replicas exist for both $\tilde{U}^z$ and $\tilde{H}$. According to the RSC calculation scheme (Eq. 3.20) both infinite series of FRs are multiplied with each other. At this point not only the matching FRs but also non-corresponding FRs are multiplied. The multiplication between non-corresponding FRs leads to SAs in the output plane. Different authors report on the position and the shape of the SAs [361, 372, 373]. In the paraxial case the SAs correspond to shifted replicas of $\tilde{u}^z$ which are spaced at distances $\lambda z/\Delta x$ and $\lambda z/\Delta y$ [361, 372]. Fig. 3.6 provides a comparison between the SAs of the paraxial and of the non-paraxial case. As observed by [361, 373] the SAs of the non-paraxial case are distorted and shifted further away from the central replica than their paraxial counterparts. The reason for this behavior is found in the slightly stronger phase slope of the non-paraxial $FR(\tilde{H})$.

The RSC is only required to give accurate results within the region $LE(\tilde{u}^z)$ of the output plane. Thus, the SAs must not contribute significantly to the numerical field within the region $LE(\tilde{u}^z)$. As the SAs of the non-paraxial RSC are spread further away from the central replica the position of the paraxial SAs can be used as the worst case estimation, see Fig. 3.7. The requirement of keeping the SAs outside of the region $LE(\tilde{u}^z)$ corresponds to the following sampling criterion:

$$\frac{\lambda z}{\Delta x} > LE(\tilde{u}^z, n_x), \qquad \frac{\lambda z}{\Delta y} > LE(\tilde{u}^z, n_y). \tag{3.31}$$

In contrast to the ASM this criterion allows for $\tilde{u}^0$ and $\tilde{h}$ to be sampled below the Nyquist rate. Again, it is assumed that the output field within the region $LE(\tilde{u}^z)$ depends on all spatial frequencies of the input field. Thus, all spatial frequencies of the input field have to be propagated to the output plane. This condition leads to another sampling criterion for the RSC:

$$LE(\tilde{U}^0) < LE(\tilde{H}). \tag{3.32}$$

3.5.2 Effects of discrete sampling in the spatial frequency domain

So far, only the effects of sampling in the space domain were discussed. The focus is now shifted to sampling in the spatial frequency domain. Generally, sampling in the spatial frequency domain with intervals $\Delta\nu_x$ and $\Delta\nu_y$ leads to SRs in the space domain which are separated by $1/\Delta\nu_x = LN(\tilde{u}^z, x)$ and $1/\Delta\nu_y = LN(\tilde{u}^z, y)$. In case of the ASM the following condition

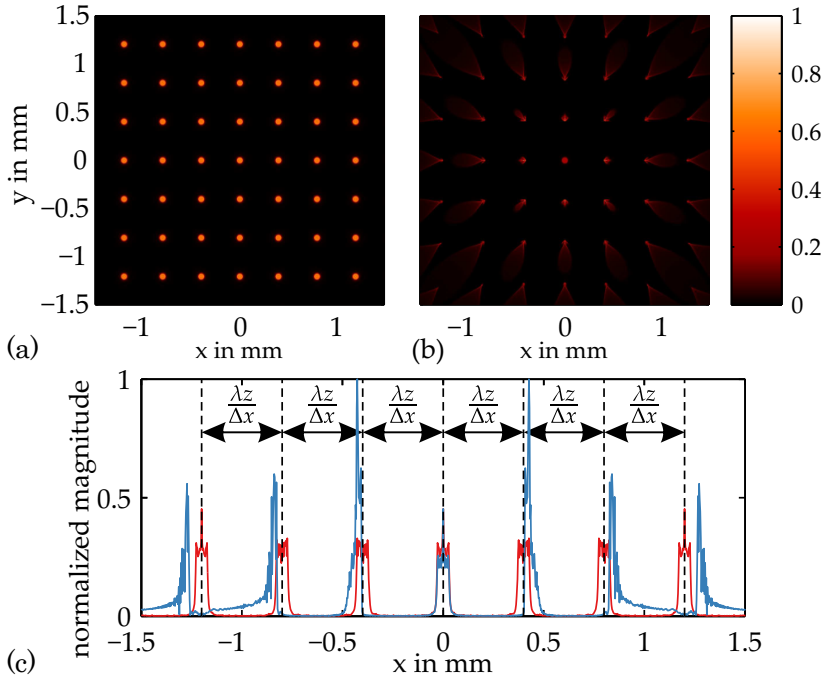

Fig. 3.6: SAs in the RSC output plane due to aliasing in the spatial frequency domain. a) In case of a paraxial propagation the SAs are evenly spaced and represent shifted replicas of the correct output field. b) For a non-paraxial propagation the SAs are distorted. c) Cross sections of the fields shown in a) (red) and b) (blue) along the line $y = 0$ [20].

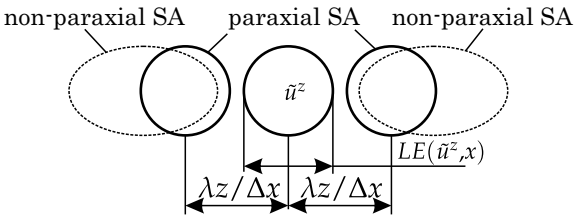

Fig. 3.7: Schematic for avoiding the appearance of SAs within the region $LE(u^z)$ [20].

ensures that neighboring SRs do not overlap with the relevant region $LE\left(\tilde{u}^z\right)$ of the output field:

$$LE\left(\tilde{u}^z\right) < LN\left(\tilde{u}^z\right). \tag{3.33}$$

The RSC implements a convolution between the input field $\tilde{u}^0$ and the propagation kernel $\tilde{h}$. Owing to the properties of the linear convolution a single SR has a maximum extent of [386]

$$LN(SR) = LN(SR, n_x) \cdot LN(SR, n_y) \tag{3.34}$$

with

$$\begin{aligned} LN(SR, n_x) &= LN(\tilde{u}^0, n_x) + LN(\tilde{h}, n_x), \\ LN(SR, n_y) &= LN(\tilde{u}^0, n_y) + LN(\tilde{h}, n_y) \end{aligned} \tag{3.35}$$

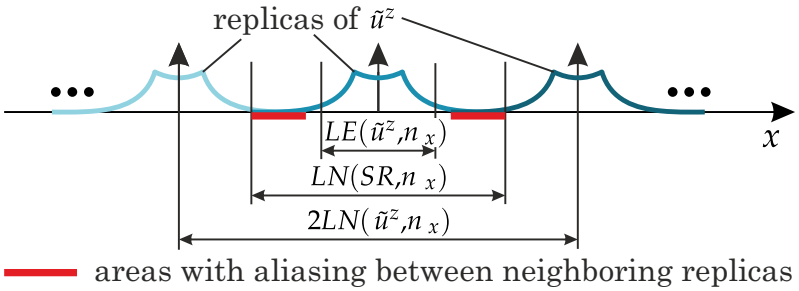

Fig. 3.8: Illustration of Eqs. 3.34 to 3.36. The $SR(\tilde{u}^z)$ given by the cyclic convolution of $\tilde{u}^0$ and $\tilde{h}$ have a finite extent $LN(SR) \leq 2LN(\tilde{u}^z)$. Thus, areas of size $2LN(\tilde{u}^z) - LN(SR)$ are free of spatial aliasing. These areas should be larger than $LE(\tilde{u}^z)$ [20].

As depicted in Fig. 3.8, the following sampling criteria ensure that neighboring SRs do not add to the relevant output region $LE(\tilde{u}^z)$:

$$\begin{aligned} LE(\tilde{u}^z, n_x) < 2LN(\tilde{u}^z, n_x) - LN(SR, n_x) = \\ LN(\tilde{u}^z, n_x) - LE(\tilde{u}^0, n_x), \\ LE(\tilde{u}^z, n_y) < 2LN(\tilde{u}^z, n_y) - LN(SR, n_y) = \\ LN(\tilde{u}^z, n_y) - LE(\tilde{u}^0, n_y), \end{aligned} \tag{3.36}$$

with $LN(\tilde{u}^z) = LN(\tilde{u}^0) = LN(\tilde{h})$. An in depth discussion of the background behind these equations is provided in [386, Chap. 8.7]. These conditions also ensure that $LE(\tilde{H}) \geq LE(\tilde{U}^0)$ and that all relevant spatial frequencies of the input field are propagated.

3.5.3 Summary of general sampling rules for the ASM and the RSC

The previous sampling discussions can be summarized in the following set of sampling criteria which ensure that both the ASM and the RSC provide a good approximation of the real physical field at the output plane.

Sampling criteria for the ASM:

$$\text{ASM-1:} \qquad LE\left(\tilde{U}^0\right) < LN\left(\tilde{U}^0\right) \tag{3.37a}$$

$$\text{ASM-2:} \qquad LE\left(\tilde{u}^z\right) < LN\left(\tilde{u}^z\right) \tag{3.37b}$$

Sampling criteria for the RSC:

$$\begin{aligned} \text{RSC-1:} \qquad & LE(\tilde{u}^z, n_x) < \lambda z/\Delta x, \\ & LE(\tilde{u}^z, n_y) < \lambda z/\Delta y. \end{aligned} \tag{3.38a}$$

$$\begin{aligned} \text{RSC-2:} \qquad & LE(\tilde{u}^0, n_x) + LE(\tilde{u}^z, n_x) < LN(\tilde{u}^0, n_x), \\ & LE(\tilde{u}^0, n_y) + LE(\tilde{u}^z, n_y) < LN(\tilde{u}^0, n_y). \end{aligned} \tag{3.38b}$$

It is important to note that the field $LE\left(\tilde{u}^z\right)$ which appears in several of these sampling criteria is determined by the product of the $\tilde{U}^0$ and $\tilde{H}$. Thus, these two fields have to be considered in a combined manner in order to determine suitable sampling intervals and numerical field sizes for the specific diffraction problem. A derivation of similar sampling criteria for the chirp-z implementations of the ASM and the RSC is presented in [20].

3.5.4 Sampling criteria for focal field calculations

Above, a general set of sampling criteria for the ASM and the RSC was developed. The efficient selection of appropriate numerical field sizes and sampling intervals requires knowledge about the effective field extents $LE\left(\tilde{U}^0\right)$ and $LE(\tilde{u}^z)$. In Chapter 3.1 raytracing was introduced as an efficient way of determining the field at the exit pupil of an imaging optical system. Moreover, raytracing can provide a-priori knowledge about the effective field sizes $LE\left(\tilde{u}^0\right)$, $LE\left(\tilde{U}^0\right)$, and $LE\left(\tilde{u}^z\right)$. To this end a localized spatial frequency model is used [9, 387]. It is based on the assumption that the geometrical wavefront behind the optical system is equivalent to the wave optical wavefront. The localized spatial frequency model implies that the ray direction at a specific point of the wavefront corresponds to the direction of the local wave vector. This model is discussed in [387] from the perspective of a first order Taylor expansion at a specific point of the wavefront. The first order Taylor expansion corresponds to a local approximation of the wavefront with a plane wave. The components of the wave vector and the spatial frequencies are given by the following equations [9, 387]:

$$\nu_x = \frac{k_x}{2\pi} = \frac{1}{2\pi}\frac{\partial\phi(x,y)}{\partial x}, \qquad \text{and} \qquad \nu_y = \frac{k_y}{2\pi} = \frac{1}{2\pi}\frac{\partial\phi(x,y)}{\partial y}, \tag{3.39}$$

with $\phi(x,y)$ being the phase function of the wavefront. It is important to note that the localized spatial frequency model is only valid for an infinitesimally small wavelength and does not account for diffraction effects. For the finite wavelengths it has an approximative character which is discussed e.g. in [9, 388, 389].

Used with caution, the localized spatial frequency model provides an efficient means for determining $LE\left(\tilde{U}^0\right)$ which is required for both the ASM and for chirp-z implementations of the RSC [20]. The necessary sampling intervals in the input plane can then be determined using the Nyquist-Shannon sampling condition [360]:

$$\begin{aligned} LE(\tilde{U}, n_{\nu_x}) &\leq LN(\tilde{U}, n_{\nu_x}) = 1/\Delta x \\ LE(\tilde{U}, n_{\nu_y}) &\leq LN(\tilde{U}, n_{\nu_y}) = 1/\Delta y \end{aligned} \tag{3.40}$$

In contrast to the discussion in [19, 374] these conditions are applied to the input field and not to the propagation kernel. As pointed out in the previous section this sampling condition is not required for the RSC. Fig. 3.9 illustrates the approximative nature of the localized spatial frequency model for a truncated spherical wave with $\mathrm{NA}' = 0.30$ and with a wavelength of 500 nm. The localized spatial frequency model predicts maximum spatial frequencies of

$$|\nu_x|_{\max} = |\nu_y|_{\max} = \mathrm{NA}'/\lambda = 6 \cdot 10^5\ \mathrm{m}^{-1}. \tag{3.41}$$

In this equation the relation $|\alpha|_{\max} = |\beta|_{\max} = \cos(\pi/2 - \sigma) = \sin\sigma = \mathrm{NA}'$ is used which is only valid for on-axis focal points in air.

The effective sizes of the input and output fields can be derived directly from a raytracing analysis or from a collinear model of the optical system. $LE(\tilde{u}^0)$ corresponds to the diameter of the exit pupil and $LE(\tilde{u}^z)$ is approximated by the size of the spot in the observation plane. If Δz corresponds to the axial distance between the observation plane and the geometrical focus point, the collinear model predicts values of $LE(\tilde{u}^z, x) = LE(\tilde{u}^z, y) = 2\,|\Delta z|\,\tan[\arcsin(\mathrm{NA}')]$ for the on axis imaging case. Again, it is important to note that the geometrical circle of confusion at the observation plane does not account for diffraction effects and that slightly larger values (e.g. by a factor of 1.2) should be used for the actual calculation.

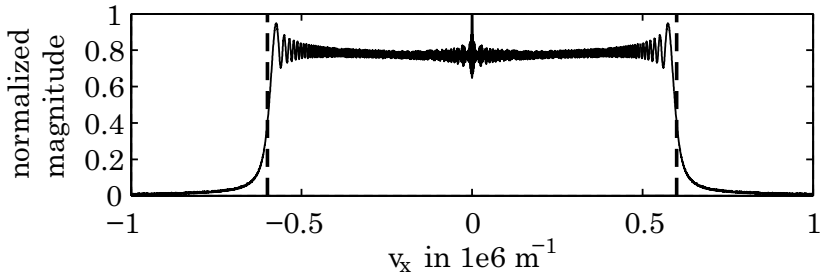

Fig. 3.9: Spatial frequency extent of a spherial wave (continuous line) in comparison to the geometric optics approximation (dashed vertical lines). Simulation parameters: $\lambda = 500$ nm, $NA' = 0.30$, $z_f = 2.0$ mm. The geometric estimation is given by $\nu_{x,\max} = 6 \cdot 10^5$ m^{-1}.

In [20] these sampling criteria are used for the calculation of several focal fields. The corresponding FFT-based calculations are in good agreement with the results of a highly accurate Gauss-Kronrod integration of the RS_1.

3.6 FFT-based focal field calculations III: summed field method

The exit pupil of an imaging system often has a diameter of several cm. In this case the sampling criteria discussed in the previous section result in large numerical fields. These fields can easily exceed the random-access memory (RAM) of current personal computers and are linked to a high computational load. Various approaches to the propagation of large fields are proposed in the literature. In [378, 390, 391] the input field is separated into tiles which are propagated individually and are recombined at the output plane. A tile represents a spatial subregion of a larger field. Various techniques aim at digital holography where a densely sampled object field is retrieved from the data recorded with a coarsely sampled detector [392–395]. These techniques are based on an additional interpolation step. In [395] the interpolation is realized through a modified convolution kernel. Kanka et al. performed the interpolation both in the space domain [392] and in the spatial frequency domain [393, 394]. The inverse problem, i.e. the propagation from a densely sampled object to a coarsely sampled detector region is described in [396].

In this section an advanced method for calculating focal fields is introduced. It is an extension of the tile-superposition technique by Kanka et al. [392] and enables focal field calculations with significantly reduced memory requirements and with low numerical effort. This technique is called summed field method (SFM) and has been published in [371]. Below, a summary of the main findings is given.

The SFM makes use of specific properties of the FFT (or equivalently the discrete Fourier transform) which is used to perform the ASM and the RSC. The numerical concept of the SFM is illustrated in Fig. 3.10 for an ASM-based focal field calculation. A quadratic, discretely sampled input field $\tilde{u}^0$ with $N \cdot N$ sampling points is assumed. First, this field is divided into $T \cdot T$ tiles with $V \cdot V$ sampling points per tile ($N = T \cdot V$). Second, the complex fields of the tiles are added coherently which gives the summed field $\tilde{u}^0_\Sigma$ with the size of a single tile. Third, the FFT of $\tilde{u}^0_\Sigma$ is calculated. Forth, the resulting field $\tilde{U}^0_\Sigma$ is multiplied with a coarsely sampled version of the ASM propagation kernel H. Fifth, the inverse FFT of the product $\tilde{u}^0_\Sigma \cdot H$ is calculated and gives the field $\tilde{u}^z_\Sigma$ in the output plane. The same result is obtained by

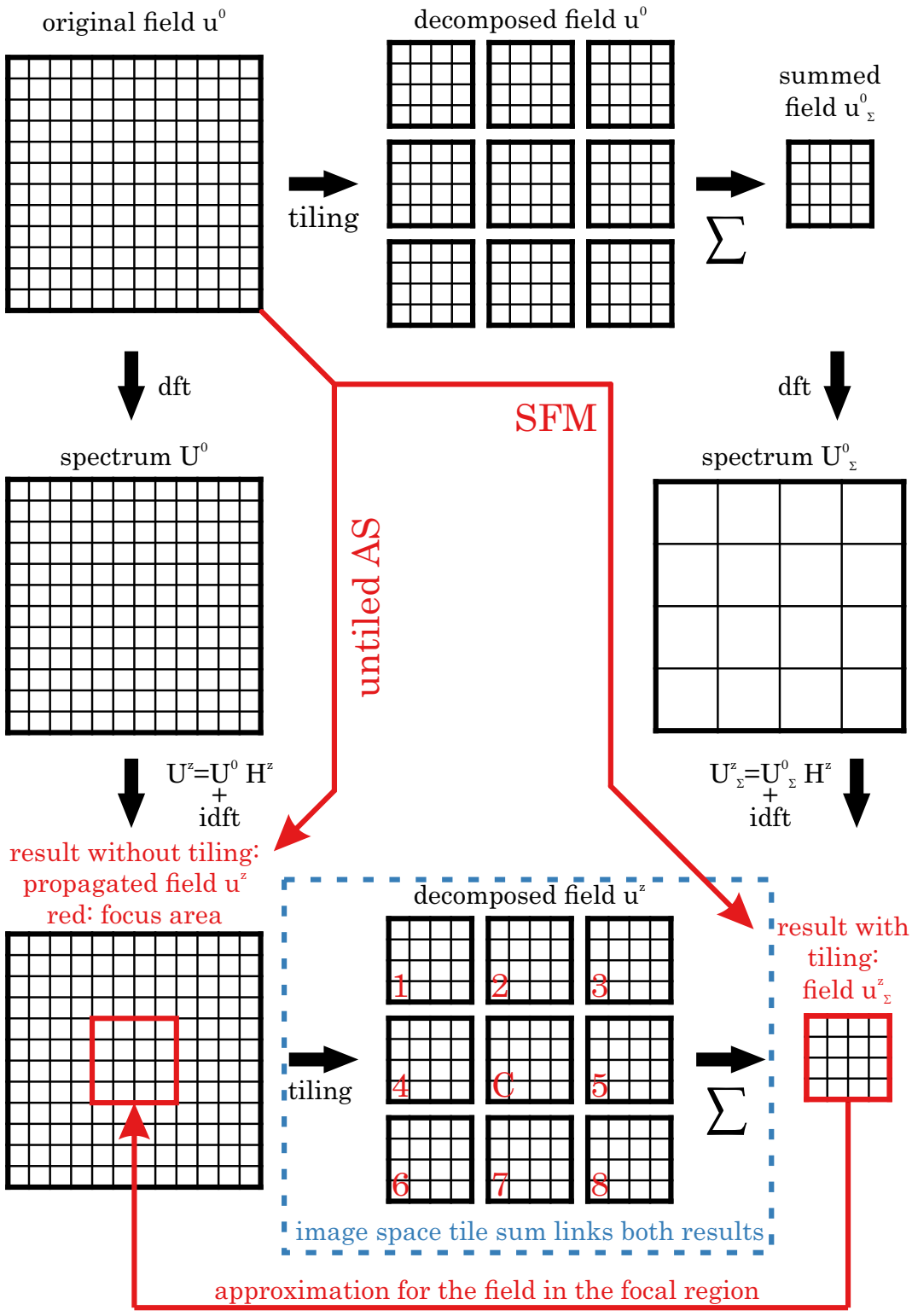

Fig. 3.10: Schematic of the SFM, the untiled ASM and of an alternative method for calculating the summed field at the observation plane [371].

performing the ASM for the untiled input field, by separating the output field into tiles and by summing these tiles (see Fig. 3.10).

This identity can be proven by rewriting the FFT equations 3.11 and 3.12 to incorporate the tiling. Therefor, a new indexing scheme is introduced in the space domain: $n_x = t_x V + v_x$ and $n_y = t_y V + v_y$ with $t_x,\ t_y = 0, 1, \ldots, T-1$ and $v_x,\ v_y = 0, 1, \ldots, V-1$. In the spatial frequency domain the distance between neighboring sampling points is increased by a factor of T: $\Delta\nu_{Tx} = T\Delta\nu_x$ and $\Delta\nu_{Ty} = T\Delta\nu_y$. To address the corresponding sampling points in the spatial frequency domain, the indices v_{vx} and v_{vy} with $v_{vx}, v_{vy} = 0, 1, \ldots, V-1$ are used. For these new spatial frequencies Eq. 3.11 can be written as

$$B_{Tv_{vx},\,Tv_{vy}} = \sum_{v_x=0}^{V-1}\sum_{v_y=0}^{V-1}\sum_{t_x=0}^{T-1}\sum_{t_y=0}^{T-1} b_{(t_xV+v_x),,(t_yV+v_y)} \cdot \exp\left[-2\pi j \frac{Tv_{vx}\left(t_xV+v_x\right) + Tv_{vy}\left(t_yV+v_y\right)}{VT}\right]. \tag{3.42}$$

With $\exp\left[-j2\pi l\right] = 1$ for arbitrary integers l the observation

$$\frac{Tv_{vx}\left(t_xV+v_x\right) + Tv_{vy}\left(t_yV+v_y\right)}{VT} = v_{vx}t_x + v_{vy}t_y + \frac{v_{vx}v_x + v_{vy}v_y}{V} \tag{3.43}$$

leads to

$$B_{Tv_{vx},\,Tv_{vy}} = \sum_{v_x=0}^{V-1}\sum_{v_y=0}^{V-1}\left[\sum_{t_x=0}^{T-1}\sum_{t_y=0}^{T-1} b_{(t_xV+v_x),\,(t_yV+v_y)}\right] \cdot \exp\left[-2\pi j \frac{v_{vx}v_x + v_{vy}v_y}{V}\right]. \tag{3.44}$$

According to this mathematical derivation the spectrum of the summed field $\tilde{u}^0_\Sigma$ contains only a subset ($V \cdot V$ discrete values) of the spatial frequencies associated with the original field u^0 ($N \cdot N$ discrete values). The SFM thus leads to a T-fold increase of the sampling intervals between successive sampling points in the spatial frequency domain. The propagation kernel H is only calculated at these new spatial frequency domain sampling points. After the multiplication of the fields FFT $\left\{\tilde{u}^0_\Sigma\right\}$ and H an inverse FFT operation is performed. For the inverse FFT a similar set of equations can be formulated. The output field of the SFM thus corresponds to the sum of tiles in the output plane which are shown in the dashed blue box at the bottom of Fig. 3.10. If all power of the output field was concentrated on the region of the central tile C the outer tiles 1-8 would not contribute to the summed field. In this case the result of the SFM would be identical to the center of the field within the red box highlighted in the lower left corner of Fig. 3.10. An optical field can have a finite extent in only one optical plane [397]. In focal field calculations the optical field is typically assumed to have a hard boundary at the exit pupil plane (Kirchhoff approximation). In consequence, the field at any other plane is infinite in extent and the SFM can only provide an approximation of the exact field. At the same time most of the power is spread across a finite spatial region. Outside of this region the intensity drops to very low values which can often be neglected. As long as nearly all power of the output field is spread across a single tile, the summed field $\tilde{u}^z_\Sigma$ is a good approximation of the exact focal field. To guarantee that the converging wave is focused on a single tile the output field may be shifted using Eq. 3.21 [14, 362].

The errors of applying the SFM to fields of infinite extent can be viewed from two different perspectives. Both perspectives are discussed using the example of a converging spherical wave with NA $= 0.50$, $\lambda = 500\,\text{nm}$ and exit pupil to focus distance of 5 mm. The input field contains $N \cdot N = 25600^2$ sampling points at sampling intervals of $\Delta x = \Delta y = 250\,\text{nm}$. It covers an area of $6.4 \cdot 6.4\ \text{mm}^2$ while the aperture has a diameter of 5.8 mm. The SFM is used

with $25 \cdot 25$ tiles to calculate the output field $-50\,\mu m$ and $-250\,\mu m$ in front of the ideal focus point. For $\Delta z = -50\,\mu m$ most of the power of the output field coincides with the central tile. For $\Delta z = -250\,\mu m$ the output power is spread across multiple tiles and the SFM is expected to provide erroneous results.

First, the errors of the SFM are discussed from the perspective that the two calculation paths (tiling at the input plane vs. tiling at the output plane) of Fig. 3.10 are equivalent. The SFM is thus assumed to produce the same results like an untiled ASM propagation which is followed by tiling and summation of the output field. This approach is illustrated in Fig. 3.11. Subfigs. 3.11(a) and 3.11(e) show reference calculations for the field at the output plane which were performed using the normal ASM without tiling. Only the central region of the field which corresponds to a single tile is depicted. This area corresponds to the one highlighted by the red box in the lower left part of Fig. 3.10. Subfigs. 3.11(b) and 3.11(f) show the coherent sums of the outer tiles (tiles 1-8 depicted at the bottom center of Fig. 3.10) but do not include the contribution of the central tile. The resulting sum of tiles 1-8 correspond to the error of the SFM. Again, these fields were calculated using the untiled ASM path presented in Fig. 3.10. For $\Delta z = -50\,\mu m$ the power spread across the outer tiles is small and a good accuracy of the SFM is expected. In the second case with $\Delta z = -250\,\mu m$ a significant amount of power is spread across the outer tiles and the SFM is expected to give erroneous results in the regions where the summed field possesses high intensity. These expectations are met by Subfigs 3.11(c) and 3.11(g) which show the result of the SFM calculation. For the small defocus value the result of the SFM agrees very well with the reference field of Subfig 3.11(a) while the result of the (g) is erroneous in exactly the regions where Subfig. 3.11(f) showed high intensity values. According to the previous discussions the field of Subfig 3.11(c) is the coherent addition of the fields shown in Subfigs. 3.11(a) and 3.11(b). To test this perspective Subfig 3.11(d) shows the difference field $(\mathrm{d}) = (\mathrm{c}) - [(\mathrm{a}) + (\mathrm{b})]$. In the same way Subfig (h) shows the difference field $(\mathrm{h}) = (\mathrm{g}) - [(\mathrm{e}) + (\mathrm{f})]$. Relative differences of less than 10^{-11} indicate that the two calculation paths for the summed field which are shown in Fig. 3.10 are indeed identical.

An alternative explanation of the errors of the SFM method can be given from the perspective of aliasing between neighboring SR. In case of the untiled ASM the replicas in the output plane are spaced at distances of $1/\Delta\nu_x$ and $1/\Delta\nu_y$ [360]. If the SFM is used with $T \cdot T$ tiles, the distance between the spatial frequency domain sampling points is increased by the factor T and the distance between the SR in the output plane is reduced to $1/(T\Delta\nu_x)$ and $1/(T\Delta\nu_y)$. Only if the effective extent of the focal field is smaller than the distance between neighboring SR, the SFM will give accurate results. This perspective is illustrated in Fig. 3.12.

Both kinds of error analysis lead to the conclusion that the SFM is limited to calculations where the effective extent of the output field is smaller than the tile size. If this condition is violated, neighboring tiles will contain a significant amount of the total power and the summation of the tiles in the output plane will lead to aliasing effects. If the condition is fulfilled, the SFM will offer significant speed advantages while the memory requirements will decrease by a factor equal to the number of tiles. Above, the SFM was mainly discussed for the ASM. The same methods can also be applied to the RSC. In this case the tiling operation has to be performed for both the input field $\tilde{u}^0$ and for the space domain propagation kernel h.

Often, the sampling criteria discussed in the previous section allow for sampling intervals in the input plane which are much larger than the desired sampling grid at the output plane. To realize denser sampling in the output plane the SFM can be combined with the two sub-pixel sampling techniques which were introduced in Chapter 3.4. The combination of the SFM with the SST or a CZT is discussed in detail in [371]. In both cases the additional operations

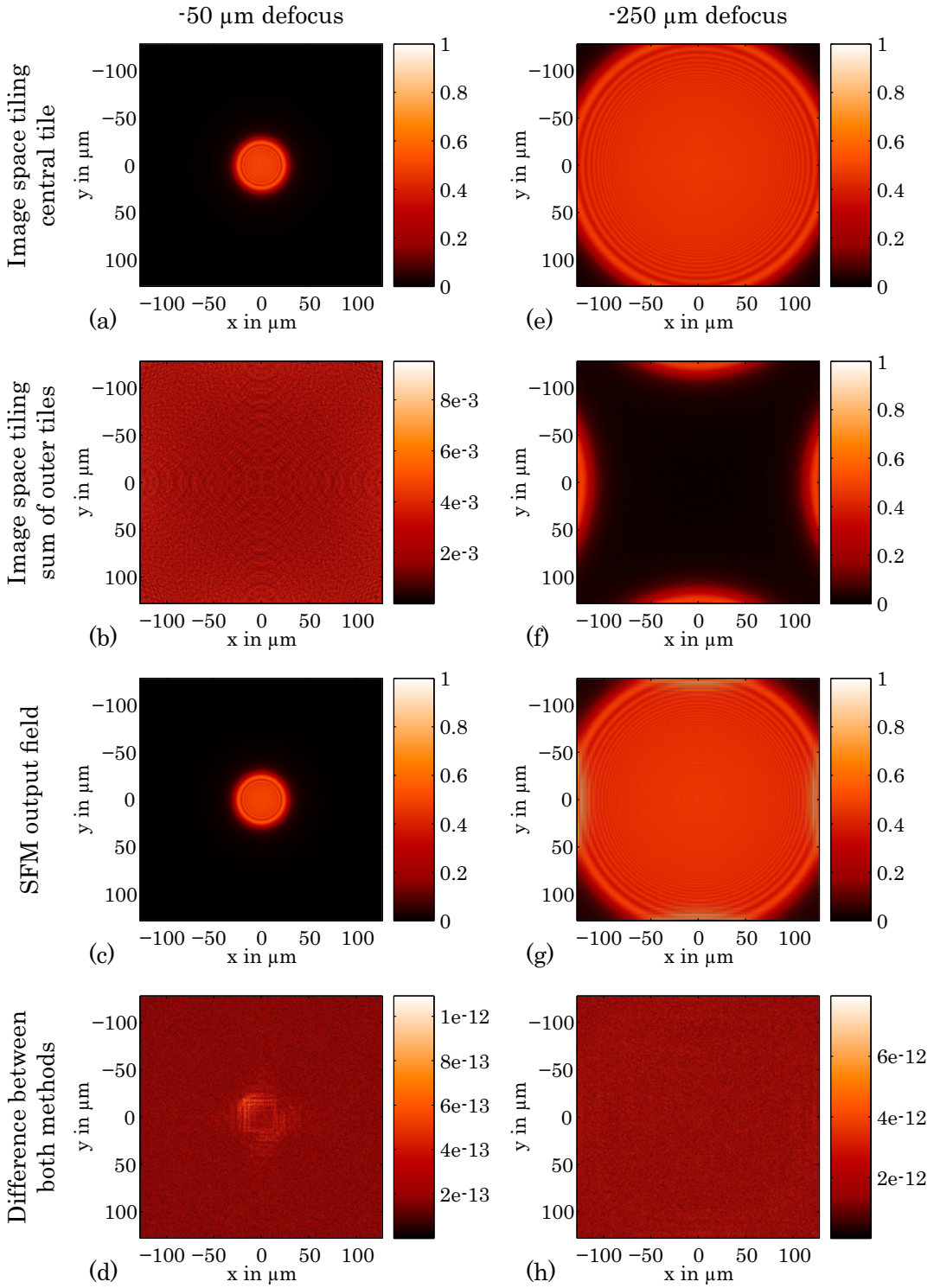

Fig. 3.11: Error analysis of the SFM for the AS propagation of a spherical wave to out of focus planes with defocus distances −50 µm and −250 µm. Comparison between the SFM implementation of the AS and an untiled AS. The fields show the magnitude in the output plane and are normalized with respect to the maximum magnitude in this plane for the SFM-cases (c) and (g) [371].

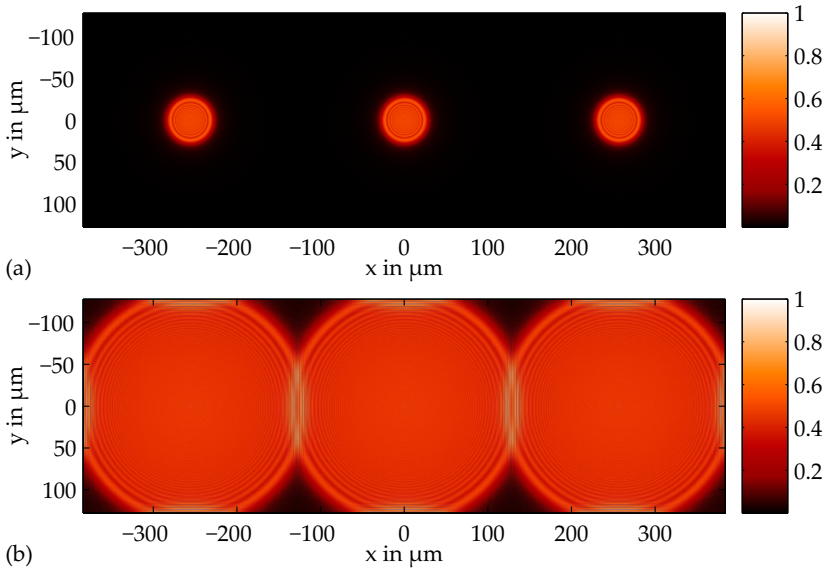

Fig. 3.12: Errors of the SFM from the perspective of aliasing between neighboring replicas. The output plane lies (a) 50 µm and (b) 250 µm in front of the geometrical focus; During the AS propagation two zeros have been inserted in x-direction between each value of $\mathcal{F}\left\{u_{\Sigma}^{0}\right\} H_{\Sigma}^{z}$ before performing the inverse DFT to increase the output field size in x-direction [380]. The fields show the magnitude in the output plane and are normalized with respect to the maximum magnitude in this plane [371].

required by the SST and the CZT are only performed for a single tile. For large numbers of tiles the additional time requirements of the SST and CZT operations can thus often be neglected in comparison to the time required for the calculation of the input field.

In [371] the possible speed improvements and the numerical accuracy of the combined methods are analyzed on the example of a converging spherical wave. The spherical wave has a wavelength of 500 nm and is propagated 9.99 mm from the exit pupil to an observation plane 10 µm in front of the focal point. It has a NA of 0.50 which corresponds to an exit pupil diameter of 11.6 mm. The input field is sampled with 32768^2 points at a distance of 400 nm. For the output field sampling intervals of 25 nm are required. The SFM is performed with $32 \cdot 32$ tiles and is combined with the SST or a CZT. In comparison to a normal ASM which would require the input field to be sampled at intervals of 25 nm, a speed improvement of approx. 800x is obtained in both cases. At the same time the memory requirements are reduced by more than 99% and the relative error is kept below 0.1%. Even further speed improvements can be obtained for larger input fields. If many tiles are used, most of the calculation time will be required for the generation of the input field. In comparison, the propagation to multiple observation planes can be performed very quickly. The calculation of the 3D intensity distribution of the focal region can thus be performed very efficiently.

3.7 Validation of the implemented numerical calculation algorithms

In this section the accuracy of the numerical focal field calculation methods is evaluated. Two specific test cases are used which are both based on converging spherical waves with a wavelength of 500 nm and a distance of 20 mm between the focal point and the truncating circular aperture. The two test cases only differ in the used NA′ of 0.20 and 0.50. The calculation of

converging spherical waves is selected because the numerical results for the on-axis irradiance can be compared to a closed-form solution of the RS_I in the Kirchhoff approximation. The on-axis complex amplitude behind a converging spherical wave with an on-axis focus is given by [10, 297–299]

$$u(0,0,z) = \frac{z \exp\left[jk\left(R - R_f\right)\right]}{\sqrt{z^2 + r^2}} - \frac{\exp\left[jk\left(z - z_f\right)\right]}{z - z_f}, \tag{3.45}$$

with

$$R = \sqrt{z^2 + r^2} \qquad R_f = \sqrt{z_f^2 + r^2}. \tag{3.46}$$

$r = z_f \cdot \tan\left(\arcsin \mathrm{NA}'\right)$ is the radius of the circular aperture while z and z_f are the axial distances to the observation point and to the focal point, respectively. The field at the focal point is given by [10, Eq. 4.54a]

$$u(0,0,z_f) = -jk\left(1 - \cos\sigma'\right) + \frac{\sin^2\sigma'}{2z_f}, \qquad \text{with} \qquad \sin\sigma' = \mathrm{NA}'. \tag{3.47}$$

To determine the irradiance from the complex amplitude, Eq. 2.85 is used. The focal point irradiance is thus given by

$$E_{\text{focus}} = \frac{\epsilon_r \epsilon_0 c}{2} u(0,0,z_f) \cdot u^*(0,0,z_f) \tag{3.48}$$

and will be used as the normalization value in all calculations. All methods are implemented quantitatively and give absolute output values. For better comparability between the two test cases the results are normalized in the last calculation step.

Within this section the following methods are compared:

- Analytical: calculation of the on-axis intensity distribution according to Eq. 3.45.
- DNI: point-by-point direct numerical integration of the RS_I in the Kirchhoff approximation (Eq. 2.27) using a Gauss-Kronrod integration function [335].
- Paraxial: point-by-point numerical integration of the paraxial RS_I in the Kirchhoff approximation (Eq. 2.36) using a Gauss-Kronrod integration function [335].
- ENZ (Debye): ENZ calculation in the Debye approximation (Eq. 3.6). Automatic truncation of the series according to [358].
- ASM: FFT-based angular spectrum method (Eq. 3.20) using tiling and a CZT.
  Parameters for NA = 0.20: $N_x = N_y = 16384$, $T_x = T_y = 8$, $\Delta x = \Delta y = 600\,\mathrm{nm}$, CZT zoom factor = 15;
  Parameters for NA = 0.50: $N_x = N_y = 65536$, $T_x = T_y = 32$, $\Delta x = \Delta y = 400\,\mathrm{nm}$, CZT zoom factor = 10;
- RSC: FFT-based Rayleigh-Sommerfeld convolution, see Eq. 3.20.
  Parameters for NA = 0.20: $N_x = N_y = 16384$, $T_x = T_y = 8$, $\Delta x = \Delta y = 600\,\mathrm{nm}$, CZT zoom factor = 15;
  Parameters for NA = 0.50: $N_x = N_y = 65536$, $T_x = T_y = 32$, $\Delta x = \Delta y = 400\,\mathrm{nm}$, CZT zoom factor = 10;
- ZEMAX FFT: FFT-based IPSF calculation with 8192^2 output plane sampling points in ZEMAX.

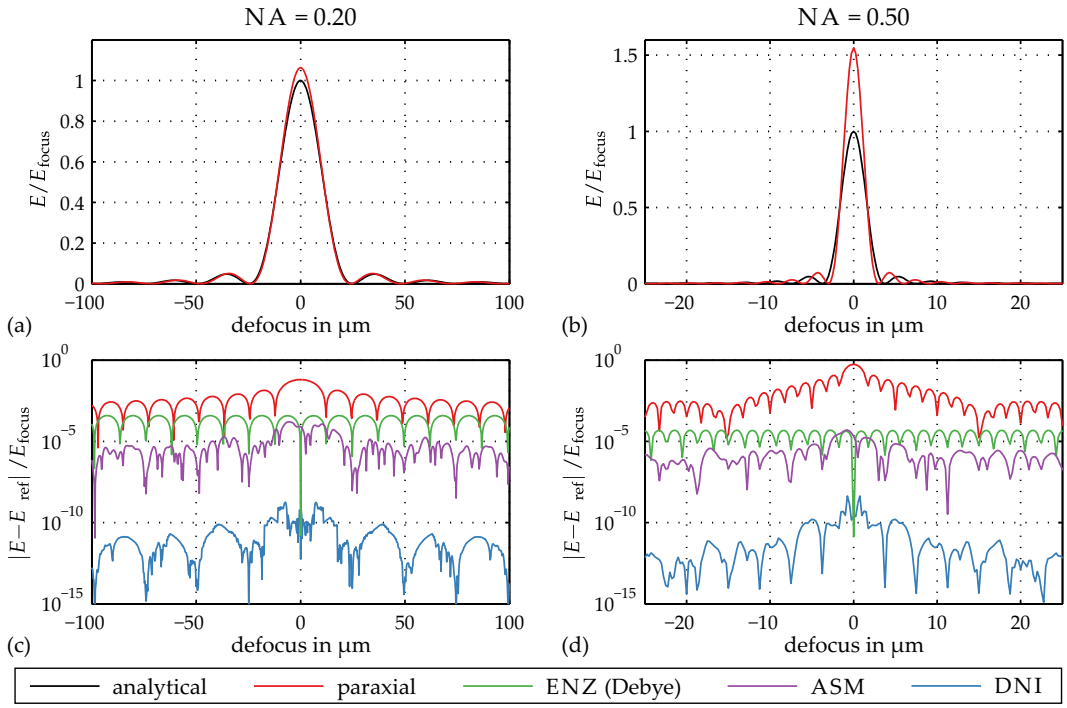

Fig. 3.13: Axial irradiance distributions for NAs of (a) 0.20 and (b) 0.50 and normalized differences to the analytical solution ((c): NA = 0.20; (d): NA = 0.50). The ENZ, the ASM, and the DNI provide result which are nearly identical to the analytical solution. These methods are thus excluded from (a) and (b).

- ZEMAX Huygens: IPSF calculation in ZEMAX using the Huygens PSF analysis function with 2048^2 pupil plane sampling points.

Fig. 3.13 visualizes the on-axis irradiance distribution for selected propagation methods. The analysis was limited to methods with a total calculation time of less than 30 minutes. Except for the paraxial calculation the results are nearly indiscernible. Thus only the analytical and paraxial results are shown in Subfigs. 3.13(a) and 3.13(b). The deviations of the numerical results from the analytical reference are depicted in Subfigs. 3.13(c) and 3.13(d). The results of the direct numerical integration (DNI) are in very good agreement with the analytical reference. The DNI is thus used as the reference for the evaluation of lateral irradiance distributions for which no analytical reference is available. The reason for the limited accuracy of the ENZ is that it operates in the Debye approximation while the other methods are based on the Kirchhoff approximation.

Fig. 3.14 shows the numerically calculated irradiance distributions along radial lines in defocused observation planes. Defocus values of $-50\,\mu m$ and $-25\,\mu m$ are used for the first test case (NA = 0.20) and the second test case (NA = 0.50), respectively. Subfigs. 3.14(a) and 3.14(b) only show results which deviate significantly from the DNI while Subfigs. 3.14(c) and 3.14(d) show the relative errors of all methods. The results indicate that neither the paraxial approximation of the RS_I nor the ZEMAX IPSF calculation methods provide valid results for the NA = 0.50 case and for large defocus values. The paraxial methods also fail in predicting the in-focus irradiance in the high-NA case. On the other hand, both the ASM and the RSC provide results which are nearly indiscernible from the DNI even if the SST is used. Without

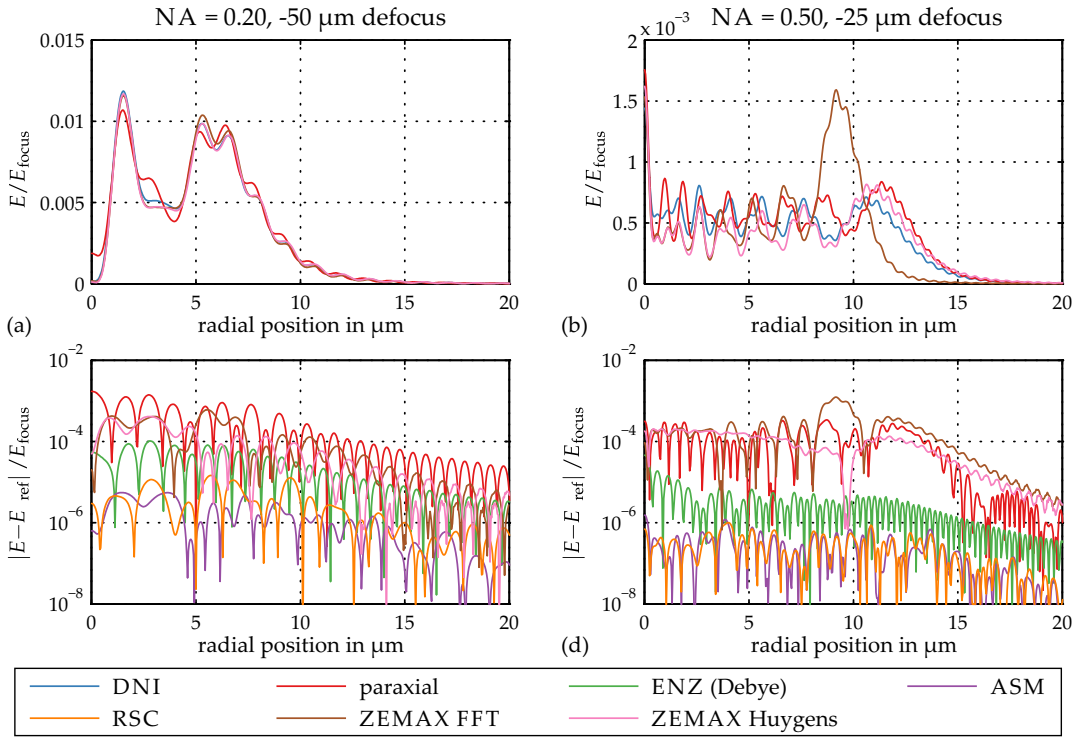

Fig. 3.14: Lateral irradiance distributions for NAs of (a) 0.20 and (b) 0.50 and normalized differences to the DNI ((c): NA = 0.20; (d): NA = 0.50). The ASM, RSC, and ENZ results are nearly identical to those of the DNI. They are omitted in (a) and (b).

the SST both methods deliver an even better numerical accuracy at the expense of increased calculation times and RAM requirements.

In Chap. 2.2.1 the Kirchhoff approximation and the Debye approximation were introduced as two models for describing the interaction between the propagating field and the diffracting aperture. For small distances between the focus and the diffracting aperture and for small Fresnel numbers the Kirchoff approximation is considered to be more accurate [8, 10, 23, 24]. The discrepancy between the two models increases with decreasing distances between the aperture and the focus and with decreasing NA [8]. The region for which the Debye approximation provides accurate results is analyzed in Fig. 3.15. For aperture to focus distances larger than 100 mm the two approximations are in very good agreement. For small propagation distances the results of the Debye approximation deviate significantly from the more accurate predictions of the Kirchhoff approximation.

In its original version the ENZ is based on the Debye approximation and is not suitable for modeling systems with a small Fresnel number and a small distances between the exit pupil and the geometric focus. However, the ENZ can be modified to give results which closely resemble those obtained with the Kirchhoff approximation. The required approach was discussed in Chap. 3.3. In the simplest case the ENZ calculation has to be performed with the scaled coordinates defined in Eq. 3.8. In the example shown in Fig. 3.16, this simple step corresponds to a reduction of the differences between Kirchhoff and Debye approximation by one to two orders of magnitude. This leads to the conclusion that the modified ENZ method may also be used for aperture to focus distances significantly smaller than 100 mm.

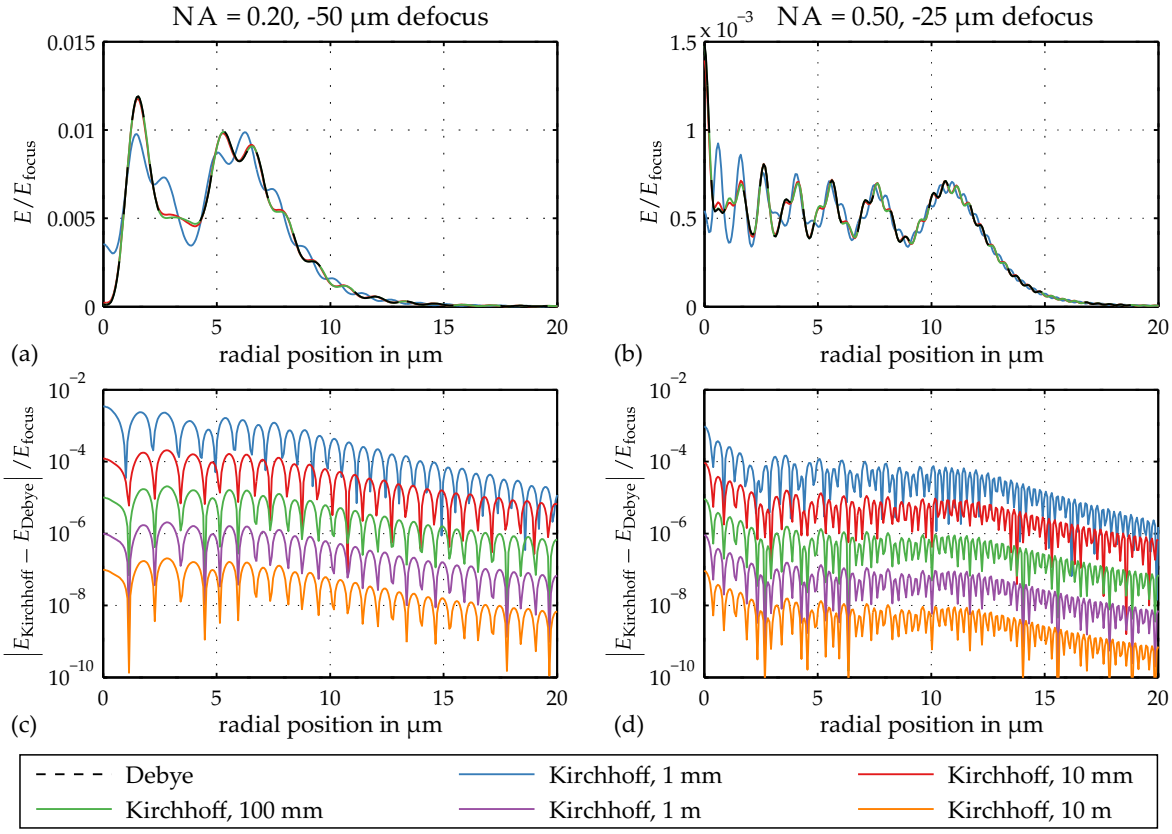

Fig. 3.15: Differences between the Kirchhoff and Debye approximations of the RS_I for different propagation distances. Subfigs (a) and (b): Radial irradiance distributions for NAs 0.20 and 0.50. Subfigs (c) and (d): Irradiance differences.

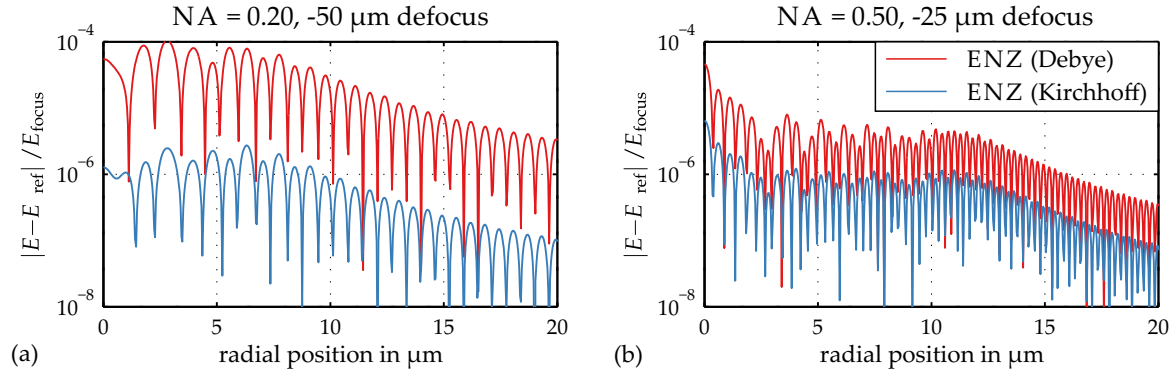

Fig. 3.16: Enhanced accuracy of the ENZ in the Kirchhoff modification for an aperture to focus distance of 20 mm and for numerical apertures of (a) 0.20 and (b) 0.50. The reference field E_{ref} is given by the RS_I in the Kirchhoff approximation. This reference field is approximated more accurately by The ENZ with the Kirchhoff modification (blue) than by the ENZ in the original Debye version (red).

3.8 Application-specific selection of the propagation algorithm

The ENZ is a semi-analytical method which solves the RS_I in the Debye approximation. As shown in Fig. 3.16, it can be easily modified to provide the solution to the RS_I in the Kirchhoff approximation. For a NA > 0.20 and for aperture to focus distances larger than 100 mm the Debye and Kirchhoff approximations lead to practically identical results. The normal ENZ calculation is well suited for the simulation of optical systems with a large aperture to focus distance. This includes systems with image space telecentricity where the exit pupil is located at infinity. Based on the results of [358] the number of terms of the internal Zernike series can be determined automatically which makes the ENZ easy to use. Furthermore, the ENZ framework is not limited to scalar calculations but also covers vectorial focal field calculations. While vectorial analyses are excluded from this thesis they may be of interest to the reader.

At the same time the method is currently limited to elliptical or annular pupils. In principle, it is possible to implement non-circular aperture shapes by a Zernike expansion with a high number of complex Zernike coefficients. This step, however, leads to a high numerical load and increased calculation times. In contrast, the RSC and ASM operate independently of the aperture shape. Both methods are based on FFT calculations and are prone to numerical artifacts and sampling issues. The user of these techniques typically faces two important obstacles: First, appropriate field sizes and sampling intervals have to be selected. Second, correct sampling may lead to very large fields which exceed the computers RAM and are related to high numerical loads. Both issues were addressed in Chaps. 3.5 and 3.6. In Chap. 3.5 a set of simple sampling rules was introduced which leads to an optimum balance between accuracy and numerical effort. Additionally, the summed field method discussed in Chap. 3.6 can be used to reduce the RAM requirements by several magnitudes while the calculation speed can be multiplied.

Together, these methods provide a fast and flexible platform for wave optical focal field calculations. The selection of the most suitable methods depends mainly on the distance between the aperture and the focus point, the amount of defocus, and the shape of the aperture. The ENZ is well suited for large aperture to focus distances in combination with elliptical or annular apertures. For small aperture to focus distances and for complex aperture shapes the RSC and the ASM may be favored.

3.9 Summary of Chapter 3

The goal of this chapter was to identify suitable numerical methods for the wave optical signal models of Chap. 4. With the ASM, the RSC, and the ENZ three viable options were discussed. They may be used to propagate a complex field from the exit pupil of an optical system to the desired observation plane. To determine the field at the exit pupil, the methods are combined with geometrical optics raytracing of the optical system. All three methods are based on the non-paraxial RS_I and account for aberrations of the optical system as well as an inhomogeneous intensity distribution across the exit pupil. Together, they cover all simulation cases which are relevant in this thesis. For the ENZ calculation an existing algorithm is used. For the fast and accurate calculation of focal fields with either the ASM or the RSC a new set of sampling conditions and a tiling technique were developed and published.

4 Signal models for chromatic systems

The methods introduced in the previous chapters are now used to derive signal models for chromatic confocal systems. These signal models have several important applications: First, they enable the optical engineer to predict the performance of the sensor system at all stages of the lens design process. At the collinear pre-design stage they may be used to quickly identify suitable combinations of optical components which are capable of fulfilling the specifications. During the optimization process the signal models can be used to analyze the influence of aberrations on the system's performance and to define corresponding error limits. Second, the influence of alignment errors on the sensor signal can be simulated. The resulting knowledge of how different types of misalignment influence the sensor signal may then be used to speed up the alignment process. Third, signal models play an essential part in model-based optical metrology. There, a priori knowledge about the system's response to different types of test objects enhances the interpretation of the sensor signal.

In Chapters 2.4.3 and 2.5.3 the state of the art of signal models for confocal and chromatic confocal was discussed. Below, extended signal models are presented which are published in [398]. These models describe the spectral distribution of the signal which passes the detection pinhole of a chromatic confocal system. The models are verified by comparison to experimental results. Additionally, it is shown how they can be extended to spectrometers and hyperspectral imaging systems.

In many commercial chromatic confocal systems inexpensive sources like light emitting diodes (LEDs) or gas discharge lamps are used. In contrast to lasers, these sources are neither spatially nor temporally coherent and have a relatively low radiance. To obtain a strong sensor signal and a high signal to noise ratio (SNR) pinholes of finite size are required. These pinholes cannot be modeled as point sources. At the same time the sensor systems may exhibit residual aberrations and field dependent vignetting effects. Additionally, the sensor signal may depend strongly on the reflection characteristics of the target. All of these aspects are explicitly considered in the new signal models which are compatible with the classical lens design process.

Below, two types of signal models are presented which are both based on the assumption of an incoherent light source. First, convolution-based signal models are discussed. They calculate the intensity point spread function (IPSF) of a single object point and convolve it with the geometric projection of the illuminating aperture. Second, a signal model is considered which relies on the tracing of rays from different points of the illuminating aperture. For simplicity a single circular illumination pinhole with homogeneous radiance and a circular detector (or detection pinhole) are assumed. The concepts can be generalized to pinhole arrays. In this case cross talk effects between neighboring pinholes have to be considered, see e.g. [140, 142].

All of these methods evaluate a single wavelength at a time and use spectral quantities (see Eqs. 2.82 and 2.83). They have to be performed repeatedly with different input wavelengths to determine the system response for a broadband illumination spectrum. This aspect is discussed in Chapter 4.3.

4.1 Convolution-based signal models for the chromatic confocal subsystem

The convolution-based signal models assume that the illumination pinholes emit incoherent radiation. According to linear system theory the image space irradiance distribution is then given by the convolution of intensities (in contrast to the convolution of complex amplitudes in the coherent case) [9]. The calculation of the irradiance distribution in the observation plane consists of the following three steps: First, the IPSF at the observation plane is determined. Second, the geometric projection of the illumination pinhole is calculated. Third, both fields are convolved.

The described approach is only valid for imaging systems with local isoplanatism [2, 9, 399] within the area of the illumination pinhole. This means that the IPSF is locally space invariant and may be convolved with the geometric pinhole image. At the same time the IPSF may vary between the different pinholes of a pinhole array.

In the following subsection different ways of approximating the IPSF are introduced. They are based on the collinear, the geometrical, and the wave optical model. Both, diffusely and specularly reflecting targets are considered and it is shown that these two cases require different imaging models. The discussion is limited to planar targets whose normal is parallel to the optical axis of the chromatic confocal sensor. For the effects of curved surfaces the reader is referred to [120] while tilted targets are addressed in the Chapter 5.

4.1.1 Approximations of the intensity point spread function

The IPSF corresponds to the irradiance distribution at the (possibly defocused) observation plane which is caused by a point source in object space. Depending on the signal model the observation plane is placed either on the target or on the detection pinhole. Its position is fixed while other properties, especially the focal length of the hyperchromatic lens, vary with the wavelength and lead to a wavelength dependent IPSF in the observation plane. The main goal is to derive approximations for the wavelength dependent IPSF.

In the literature, the IPSF is approximated

- as a circular disc of homogeneous radiant emittance (collinear model) [10, 400–404].
- with a normal irradiance distribution [403, 405].
- through the spot diagram (geometrical optics model), e.g. [2].
- wave optically [8, 10, 62, 98, 100, 400–402].

Below, the collinear, the geometrical, and the wave optical approximation of the IPSF are discussed based on the geometry depicted in Fig. 4.1(a). The corresponding IPSF approximations are illustrated in Fig. 4.1(b) to (d). The defocus distance $\Delta s'(\lambda)$, the marginal ray angle $\sigma(\lambda)$, the exit pupil radius $h_{XP}(\lambda)$, and the propagation distance $z(\lambda)$ (i.e. the exit pupil position) are all expected to vary with the wavelength.

In the collinear approximation the IPSF is described by a circular disk with homogeneous irradiance distribution:

$$\mathrm{IPSF}_\lambda(x,y) = \frac{\Phi_{e,\lambda}}{r_g^2(\lambda)\pi}, \tag{4.1}$$

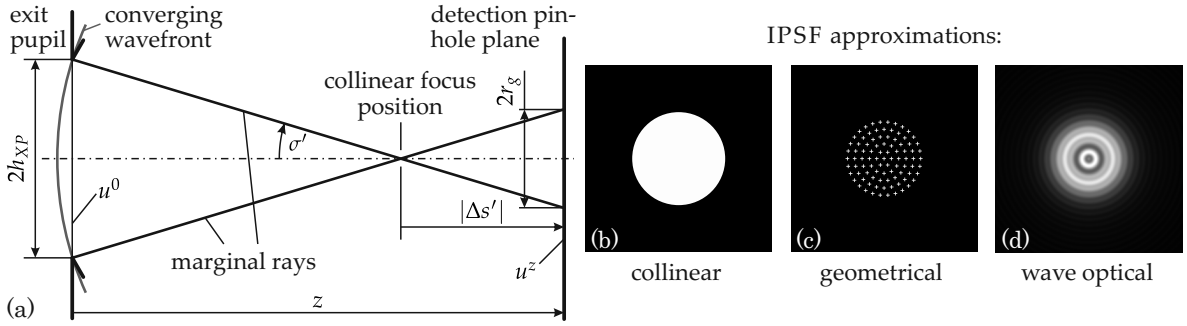

Fig. 4.1: a) Basic geometry for the IPSF calculations. IPSF in the detection plane for b) the collinear, c) the geometrical, and d) the wave optical approximation [398].

with

$$r_g(\lambda) = \left|\Delta s'(\lambda)\right| \tan \sigma'(\lambda). \tag{4.2}$$

$\Phi_{e,\lambda}$ is the spectral power passing the exit pupil. All parameters can be determined with the methods introduced in Chaps. 2.2 and 2.3. The collinear approach accounts neither for monochromatic aberrations nor for vignetting or diffraction effects.

The geometrical IPSF approximation is significantly more complex but accounts for both monochromatic aberrations and vignetting effects. It is based on the tracing of rays from the object point. All rays carry the same amount of power and sample the entrance pupil of the optical system homogeneously. In image space, the intersection points between the rays and the observation plane are determined. For optimum compatibility with the subsequent convolution operation (the next step in the calculation of the sensor signal) the observation plane is described by a grid of quadratic pixels. The pixelated irradiance distribution at the observation plane is then determined from the number of rays hitting the individual pixels. If the system is free from aberrations and vignetting effects the resulting irradiance distribution will correspond to the homogeneous circle of the collinear model. Otherwise an inhomogeneous irradiance distribution results.

The wave optical IPSF calculation is the most complex approach used in this thesis. It accounts not only for monochromatic aberrations and vignetting effects but also for diffraction effects. The basic calculation steps and their fast implementation were discussed in Chap. 3. Even without aberrations and vignetting effects the wave optical model does not lead to a homogeneous irradiance distribution in the observation plane.

4.1.2 Convolution models for diffusely and specularly reflecting targets

The selected method of calculating the signal of a chromatic confocal system is closely related to the one discussed in [114] and [98, Chap. 5.6]. It is based on the convolution of the IPSF with the geometric projection of illumination pinhole onto the observation plane, see [2, 9, 399]. This method requires local isoplanatism within the area of the illumination pinhole. Fig 4.2 depicts the basic calculation procedure.

First, the IPSF at the (possibly defocused) observation plane is calculated for the central point of the illumination pinhole. Here, the normalized version

$$\overline{\mathrm{IPSF}}(x', y', \lambda) = \frac{\mathrm{IPSF}(x', y', \lambda)}{\int\int_{-\infty}^{\infty} \mathrm{IPSF}(x', y', \lambda)\, \mathrm{d}x'\, \mathrm{d}y'} \tag{4.3}$$

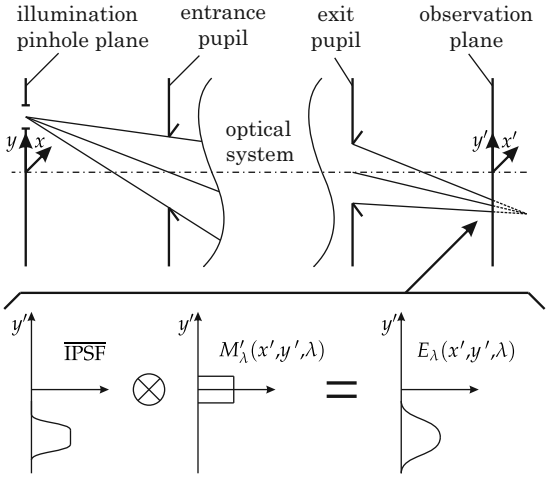

Fig. 4.2: Calculation of the image space irradiance for an extended illumination pinhole [398].

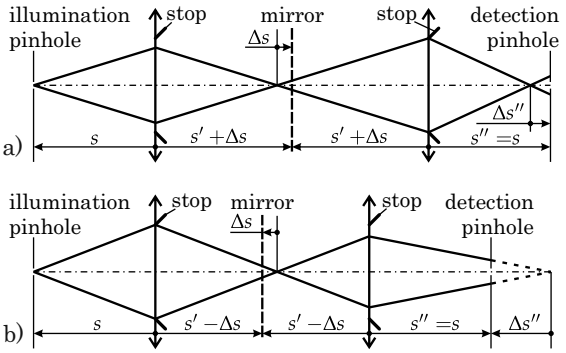

Fig. 4.3: Unfolded layout of the double pass system with a specularly reflecting surface under test. In both cases, a mirror shift (a) away from and (b) towards the sensor, the physical stop affects the light rays only once [398].

is used to obtain the correct physical units and the correct output power from the convolution with the geometric projection of the illumination pinhole. Second, the geometric projection $M'_\lambda(x', y', \lambda)$ of the object space spectral radiant emittance $M_\lambda(x, y, \lambda)$ is calculated:

$$M'_\lambda(x', y', \lambda) = \frac{\delta_{\text{comp}}(\lambda)}{|\beta'^2(\lambda)|} M_\lambda \left(\frac{x'}{\beta'(\lambda)}, \frac{y'}{\beta'(\lambda)} \right). \tag{4.4}$$

$\beta'(\lambda)$ is the lateral magnification of the defocused imaging system. It links the extents x and y of the object to those of the geometric projection in the observation plane: $x' = \beta'(\lambda)x$ and $y' = \beta'(\lambda)y$. β', x', and y' are determined by tracing a paraxial chief ray from the object plane to the observation plane. Wavelength dependent losses within the imaging system are considered through the function $\delta_{\text{comp}}(\lambda)$. In the third calculation step the two fields $\overline{\text{IPSF}}(x', y', \lambda)$ and $M'_\lambda(x', y', \lambda)$ are convolved. The resulting field

$$E_\lambda(x', y', \lambda) = M'_\lambda(x', y', \lambda) \otimes \overline{\text{IPSF}}(x', y', \lambda), \tag{4.5}$$

describes the spectral irradiance in the observation plane.

The convolution approach is the foundation for the two signal models depicted in Fig. 4.4. The first model shown on the left of Fig. 4.4(a) is suited for single pass systems and for double pass systems with a specularly reflecting target. A double pass system with a specularly reflecting target is treated as a single pass system with an effective IPSF, see [62]. To explain this approach the unfolded system is depicted in Fig. 4.3. Fig. 4.3(a) illustrates the case that the target lies in front of the collinear focus. In Fig. 4.3(b) the target lies behind the geometrical focus. In both cases the marginal ray hits the physical stop only once, either during the forward or during the backward propagation. The diffraction effects of the unfolded system can thus be attributed to a single physical stop within the optical system. Hence, the double pass system is treated like a single pass system with the effective defocus distance $\Delta s''$.

A different approach has to be used for the double pass system with a diffusely reflecting target. Here, the incident light field is scattered at the target and all illuminated points of the target are considered secondary sources. To account for this effect of the target, a two

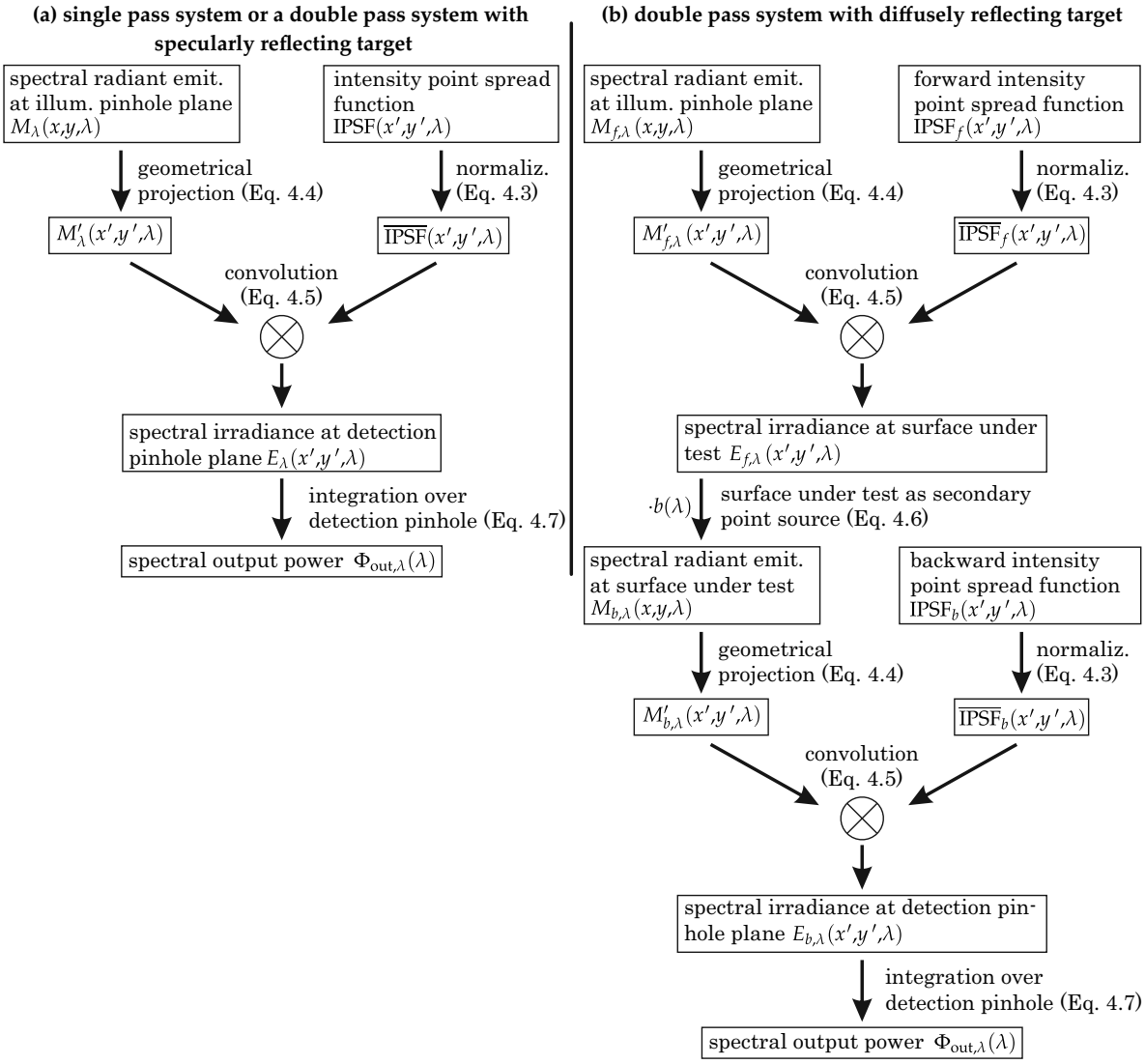

Fig. 4.4: Calculation steps for the spectral signal of a chromatic confocal sensor. (a) Single pass system or a double pass system with specularly reflecting target. (b) Double pass system with diffusely reflecting surface [398].

step approach is used which is depicted in Fig. 4.4(b). The first step is the same as for the single pass system. An intermediate observation plane is placed on the surface of the target and the irradiance distribution in this plane is calculated. During the second calculation step the illuminated target region is considered the source (i.e. the illumination pinhole) for the backward propagation through the optical system. The spectral radiant emittance of the target is modeled through the equation

$$M_{b,\lambda}(x,y,\lambda) = \delta_t(\lambda) E_{f,\lambda}(x',y',\lambda). \tag{4.6}$$

$E_{f,\lambda}(x',y',\lambda)$ is the spectral irradiance on the target while $\delta_t(\lambda)$ describes its spectral reflection characteristics. Eq. 4.6 is based on the assumption that the angular scattering characteristics do not vary with wavelength.

The second calculation step is performed in the same way as the first step. This time the system is modeled in the backward direction and the propagation from the target to the detection

pinhole plane is analyzed. In Fig. 4.4(b) the subscripts f and b are used to label the forward and backward propagations. Also for the backward propagation local space invariance of the IPSF is assumed.

The last step is the same for both models and consists of integrating the spectral irradiance in the detection pinhole plane over the area A_{Det} of the detection pinhole:

$$\Phi_{\mathrm{out},\lambda}(\lambda) = \iint\limits_{A_{\mathrm{Det}}} E_{\lambda}(x', y', \lambda)\,\mathrm{d}x\,\mathrm{d}y. \tag{4.7}$$

$\Phi_{\mathrm{out},\lambda}(\lambda)$ is the spectral power passing the detection pinhole and $E_{\lambda}(x', y', \lambda)$ is the spectral irradiance incident upon the detection pinhole plane.

4.2 Raytracing-based signal model for the chromatic confocal subsystem

In this section an alternative, raytracing-based signal model is introduced. In contrast to the models discussed above it requires neither the calculation of the IPSF nor a convolution with the collinear image of the illumination pinhole. Instead, an extended source object is used which is sampled with numerous rays. The rays represent the spectral radiance of the source through different starting positions and directions. The rays are traced from the source through the optical system to the target and then from the target to the detector. If only the signal passing the detection pinhole of a chromatic confocal point sensor has to be modeled, a single detection pixel with the shape of the detection pinhole will be sufficient. Alternatively, a multi-pixel detector can be used to simulate more complex systems like a hyperspectral imaging system with an array detector. In both cases the spectral power at the detection plane is derived from the relative number of rays hitting the detector pixel(s).

This approach is compatible with many commercial raytracing programs and has been implemented successfully in the non-sequential mode of ZEMAX. It is compatible with both specularly and diffusely reflecting targets and can also be used for the analysis of non-planar targets. In addition to the two extreme cases of ideal specular reflection and ideal diffuse reflection other scattering characteristics can be assigned to the target.

In case of a single pass system with a circular detector, a simplified calculation can be performed in the sequential mode of ZEMAX. It is based on the Extended Source Encircled Energy Analysis function and evaluates the relative power within a circle around a reference point in the observation plane. If the object distribution is set to a homogeneously emitting circle this analysis gives results which closely resemble those of a non-sequential raytracing analysis. In Chap. 4.1.2 it was shown that a double pass system with a specularly reflecting target can be treated in the same way as a single pass system. This concept is also applicable to the analysis in the sequential mode of ZEMAX which is much faster than a full non-sequential analysis. It often requires only a few ms for a single calculation and will thus be used extensively for the analyses discussed in Chap. 5.

In contrast to the convolution model with the wave optical IPSF, the raytracing models of this section do not account for diffraction effects. However, they incorporate monochromatic aberrations and vignetting effects. Additionally, they enable the modeling of systems whose IPSF varies across the area of a single pinhole. The raytracing based models are thus suited for optical systems whose performance is dominated by monochromatic aberrations.

4.3 System properties beyond the chromatic confocal module

A chromatic confocal sensor system is composed of three modules: the illumination module, the chromatic confocal module with the hyperchromatic lens, and the detection module. Above, only the chromatic confocal module was discussed. At the same time, both the illumination module and the detection module can have a significant impact on the sensor signal: First, the spectral power of the light source varies with the wavelength. Similarly, a spectrometric detection system typically has a wavelength dependent sensitivity and a limited spectral resolution. It records a monochromatic input signal as a peak of finite spectral extent. In consequence, the spectral signal shown by the spectrometer will be broader than the signal produced by the chromatic confocal system. Many other aspects like an angled fiber tip (FC/APC connector) or ghost images caused by the reflections at the beam splitter or the fiber optical y-coupler further degrade the quality of the sensor signal.

A detailed analysis of these aspects is beyond the scope of this thesis. However, some of them can be easily included in the existing signal models. The discussion of Chaps. 4.1 and 4.2 were limited to a single wavelength. To compute the sensor response to a polychromatic spectrum, the light source spectrum is sampled with a set of discrete wavelengths. For each wavelength the detected spectral power is calculated. At this point the spectral properties of the source, of the detector, and of the components which link the different sensor modules can be considered. To this end multiplicative spectral factors $\delta(\lambda)$ are used:

$$\Phi_{\lambda,\,\mathrm{sensor}} = \Phi_{\lambda,\mathrm{CC}} \cdot \delta_{\mathrm{comp}} \cdot \delta_d. \tag{4.8}$$

$\Phi_{\lambda,\,\mathrm{sensor}}$ is the spectral power distribution detected by the full sensor system while $\Phi_{\lambda,\,\mathrm{CC}}$ is the spectral power distribution passing the detection pinhole. δ_{comp} accounts for the influence of the sensor's optical components while δ_d describes the spectral sensitivity of the detector. The spectral characteristics of the source is included in $\Phi_{\lambda,\mathrm{CC}}$, see Eq. 4.6.

4.4 Experimental verification

To verify the signal models experimentally a fiber-based chromatic confocal point sensor is chosen. The sensor layout is shown in Fig. 4.5. For the illumination and the detection a LED-based light source (Thorlabs MWWHF1) and a commerical single channel spectrometer (Ocean Optics Maya2000) are used. The hyperchromatic system consists of two off-the-shelf hyperchromatic lenses (Quioptiq G033101000, $f'(\lambda_0) = 50\,\mathrm{mm}$) and is depicted in Fig. 4.5 with the relevant distance data. At the reference wavelength $\lambda_0 = 550\,\mathrm{nm}$ the system possesses a lateral magnification $\beta' = -1$ and image- and object space numerical apertures $\mathrm{NA}' = \mathrm{NA} = 0.176$. The illumination and detection pinholes are given by a GRIN fiber with a core diameter of 50 µm and a NA of 0.22 which is used in double pass. The higher NA of the fiber in comparison to the systems NA reduces the influcence of the angled fiber tip (FC/APC connector) at the expense of significant power losses. Together, the two hyperchromatic lenses generate a total LCA of $\Delta s'(\lambda_1, \lambda_2) = 6.6\,\mathrm{mm}$ between the two wavelengths $\lambda_1 = 450\,\mathrm{nm}$ and $\lambda_2 = 650\,\mathrm{nm}$. This distance corresponds to the measurement range of the sensor.

The hyperchromatic lens is corrected for spherical aberration. In double pass it shows an on-axis Strehl ratio of 0.7. It is, however, not optimized for off-axis imaging. When imaging off-axis points, the Strehl ratio drops to a value below 0.1 for object heights of 1 mm and larger. At the same time, significant vignetting effects can be observed at off-axis field points. These

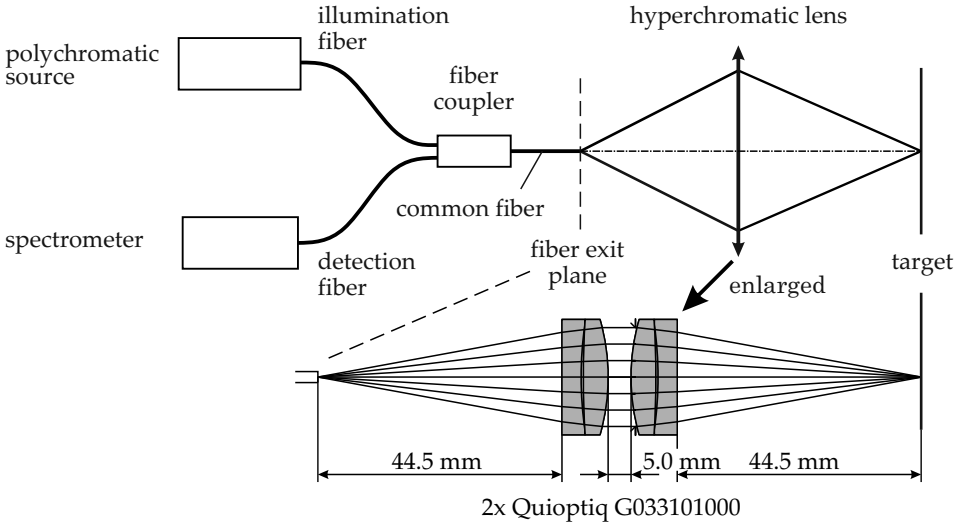

Fig. 4.5: Layout of the hyperchromatic lens used in the experimental setup.

effects are more severe in case of the specularly reflecting target where a part of the reflected light cone is diverted away from the system. The imaging of on-axis and off-axis field points is thus used to test the validity of the signal models in the presence of both small and strong aberrations.

The main results of the experimental analysis are presented in Fig. 4.6 for both a diffusely and a specularly reflecting target. These results represent the response of the full sensor system including the illumination module, the chromatic confocal module, and the detection module. They are compared to different signal models for the chromatic confocal system. The effects of the illumination module and of the detection module are thus excluded from the simulations. The following signal models are evaluated for both a diffusely and a specularly reflecting target:

- Convolution-based model with a collinear approximation of the IPSF.
- Convolution-based model with a wave optical approximation of the IPSF.
- Raytracing-based model implemented in the non-sequential mode of ZEMAX. For the diffusely reflecting target a Lambertian scattering characteristics is assumed.

In Fig. 4.6(a) the results for a specularly reflecting target (first surface mirror) are shown. For the on-axis case monochromatic aberrations are low and all three models give nearly identical results which are in good agreement with the experiment. For the two off-axis cases with lateral displacements of the fiber by 2 mm and 4 mm the predictions of both the geometrical and the wave optical model are in very good agreement with the experimental results. Owing to field curvature, the spectral peak position is slightly shifted towards longer wavelengths.

The experiments with diffuse reflection were performed with two different targets. First a Spectralon diffuse reflection standard with a peak-to-valley surface roughness of more than 50 µm was used. In Fig. 4.6(b) the experimental results are compared to those of the three signal models. For all field positions the experimental peak is broader than the predictions of the signal models. The differences are expected to be caused by the high surface roughness of the Spectralon diffuse reflection standard. The experiment was thus repeated with a sand-blasted aluminum target (Qioptiq alignment target G061680000). The results are in very good agreement with the geometrical and wave optical models. Small deviations of the peak

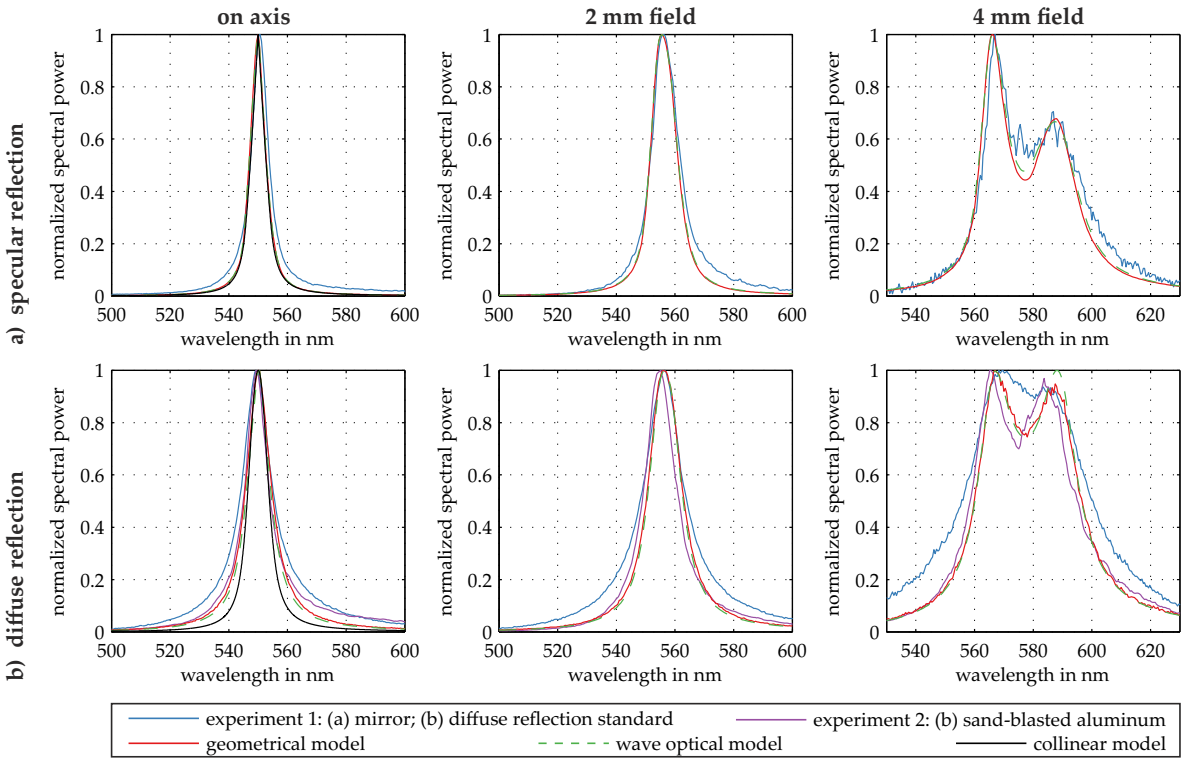

Fig. 4.6: Comparison of the different signal generation models and experimental results for (a) a specularly and (b) a diffusely scattering surface under test. The collinear model does not take aberrations or vignetting effects into account. It gives the same result independently from the object position and is only shown for the on-axis case. Intermediate results published in [398].

positions may be attributed to a slightly tilted target. At the same time the spectral peak of the collinear model is narrower than both the experimental results and the results of the other signal models.

The comparison of the signal models leads to the following conclusions:

1. As the convolution-based model with the collinear IPSF approximation does not account for aberrations it is only suited for modeling well corrected systems. In the presence of aberrations it gives inaccurate results.
2. The convolution-based model with the wave optical IPSF approximation is in very good agreement with the experimental results for all tested cases. It includes aberrations as well as vignetting and diffraction effects. Without proof, it is also considered suitable for systems with a low numerical aperture which are dominated by diffraction effects. The drawbacks of this model are a high computational load, a relatively complex calculation procedure, and the requirement of local isoplanatism.
3. For the analyzed system the raytracing model gives results which are nearly identical to those of the convolution-based model with the wave optical IPSF approximation. It accounts for aberrations and vignetting effects but does not include diffraction. It may thus give erroneous results for systems with small NA. At the same time it does not require local isoplanatism.

4. The raytracing model is favored due to the simplistic approach and the possibility of performing all calculations within ZEMAX or alternative lens design programs. It will be used extensively in Chap. 5 for the discussion of various design aspects.
5. In experiments with confocal sensors Corle [62, Chapter 3.3] did not notice a significant impact of the surface properties of the target onto the sensor response. In contrast, the experiments and simulations presented in Fig. 4.6 both show a clear difference between a diffusely and a specularly reflecting target. These findings lead to the recommendation to include the targets scattering characteristics in signal models for chromatic confocal sensor systems with finite illumination pinholes.
6. In the experiments with diffusely scattering targets significant differences in the sensor signal were observed between the Spectralon diffuse reflection standard (high surface roughness) and the sand blasted aluminum target (lower surface roughness). In the signal models volumetric effects caused by the surface roughness are not considered and all scattering effects are attributed to a single plane. The spectral peaks obtained with targets of high roughness are thus expected to be broader than the predictions from the simulations.
7. Although the simulations are only performed for the chromatic confocal system they agree very well with the experimental results for the full sensor system. This indicates that the spectrometer has a high spectral resolution and a low impact on the spectral distribution of the recorded sensor signal.

4.5 Extension of the signal models to systems with pixelated detectors

The signal models described above can be easily extended to other types of chromatic systems including those discussed in Chap. 2.7. In this section the extension of the signal models to other applications is presented for two selected examples: The chromatic confocal hyperspectral imaging (HSI) system shown in Fig. 4.7 and the spectrometer shown in Fig. 4.8. As quantitative simulations and their verification by experimental results are beyond the scope of this thesis, only the general approach is outlined. Both examples can be reduced to a common pattern:

1. Broadband radiation is incident upon an illumination aperture of finite size. In case of the spectrometer the aperture corresponds to an entrance slit. In case of the HSI system an array of circular pinholes is used.
2. The radiation passing the illumination aperture(s) is imaged onto a pixelated detector by an optical systems whose imaging properties vary with wavelength. In the spectrometer each wavelength is imaged to a different lateral position. In the HSI system each wavelength is focused at a different axial position.
3. The spectral distribution of the input signal is determined from the irradiance distribution on the pixelated detector. The spectrometer uses a static detector and determines the spectral distribution of the input signal from the spatial irradiance distribution. The HSI system uses an actuated detector and determines the spectral distribution of the input signal from the temporal irradiance distribution.

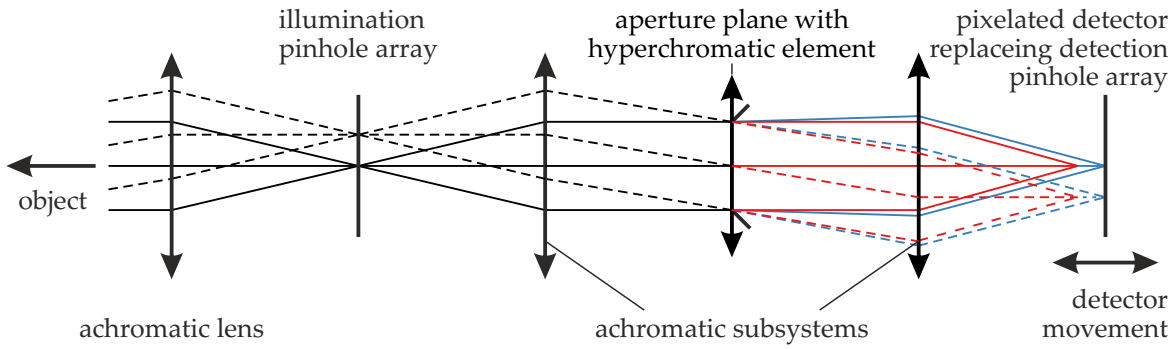

Fig. 4.7: Example of a chromatic confocal hyperspectral imaging system. Copy of Fig. 2.18, see Chap. 2.6 for further details.

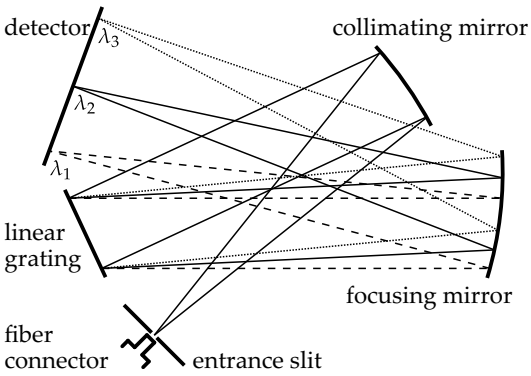

Fig. 4.8: Example of a single channel spectrometer. Copy of Fig. 2.19, see Chap. 2.7 for further details.

The signals of the two sensor systems can be simulated using the following steps:

1. The polychromatic input signal is sampled resulting in a discrete set of wavelengths.
2. For each discrete wavelength and for the central point of the illumination aperture the IPSF on the detector plane is determined.
3. Additionally, the geometric projection of the illumination aperture onto the detector is calculated.
4. The IPSF is convolved with the geometric projection of the illumination aperture. The convolution operation gives the spectral irradiance distribution on the detector which may span several pixels.
5. The spectral irradiance distribution is multiplied with the spectral sensitivity of the detector. The product gives the contribution of the selected wavelength to the detected irradiance.
6. The irradiance distribution is integrated over the areas of the relevant pixels. The integration gives the contribution of the wavelength to the power detected by the pixels.
7. Steps 2 to 6 are performed repeatedly for all wavelength bands of the sampled spectrum. The contributions of the wavelengths are added and give the power incident on the specific pixels.

These steps model the response of the spectrometer to a specific illumination spectrum. Similarly, they give the power distribution on the pixelated detector of a HSI system for a static detector position. In order to evaluate the spectral filtering characteristics of the HSI system, the detector has to be shifted to different axial positions and the calculation procedure has to be performed for all positions. Cross talk effects between neighboring channels of the HSI system can be considered by evaluating how much power from an illumination pinhole falls on the detection area assigned to a neighboring pinhole.

4.6 Summary of Chapter 4

In this chapter a new set of signal models for chromatic confocal sensor systems was presented. They differ from the state of the art in several important points: First, the assumption of an incoherent source is combined with the concept of finite illumination and detection pinholes. Second, aberrations and vignetting effects are explicitly included. Third, the models for double pass systems distinguish between specularly and diffusely reflecting targets. The resulting signal models are of two different types. The first type is based on a convolution between the image of the illumination pinhole and the IPSF. To this end different IPSF approximations are discussed which use a collinear, a geometrical, or a wave optical approach. The second type is based on the tracing of rays from different points of a spatially extended source geometry.

Both, the convolution-based signal model with the wave optical IPSF approximation and the raytracing-based signal model agree very well with experimental results. The two examples of a hyperspectral imaging system and of a fiber-based spectrometer show that the models can also be used for the simulation of other types of chromatic imaging systems.

5 Application-specific design of chromatic confocal imaging systems

This chapter focuses on selected design aspects of chromatic confocal sensor systems. It is based on the assumption that an imaging system is the result of a compromise - a compromise between competing constraints and performance criteria. Fig. 5.1 illustrates several conflicting fields between which the lens designer has to find a viable solution. A common example is the conflict between the wish for a small, low-cost system on the one hand and specific resolution requirements on the other hand which can only be fulfilled with a complex optical layout. It is thus not the goal of the designer to develop a perfect imaging system without aberrations. Instead, he aims at systems which fulfill the requirements at minimum cost (including size, weight and stability). Especially, he considers the assembled system which includes fabrication and alignment errors and may be used under harsh thermal and mechanical conditions.

Owing to the large number of design parameters, the lens design process is not deterministic. This means that in the majority of cases a given set of constraints and performance criteria does not lead to a single design but to a multitude of possible solutions. One reason is the high dimensionality of the solution space which is often probed with local optimization routines. Small user-defined alterations during the semi-automatic optimization process may lead to significantly different solutions. Even the results of global optimization routines depend strongly on the choice of the starting system. Hence, the quality of the final system is determined to a large part by the skills of the lens designer who selects appropriate starting systems and intervenes wisely in the optimization process.

In view of the complexity of the lens design process no universal laws for designing chromatic confocal systems can be given. Instead, rules of thumb and guidelines are proposed which may facilitate the design process. For this purpose the design process is decomposed into two steps, a pre-optimization step and the optimization step. The first part of this chapter is devoted to the pre-design stage. It is focused on the identification of suitable starting systems and is

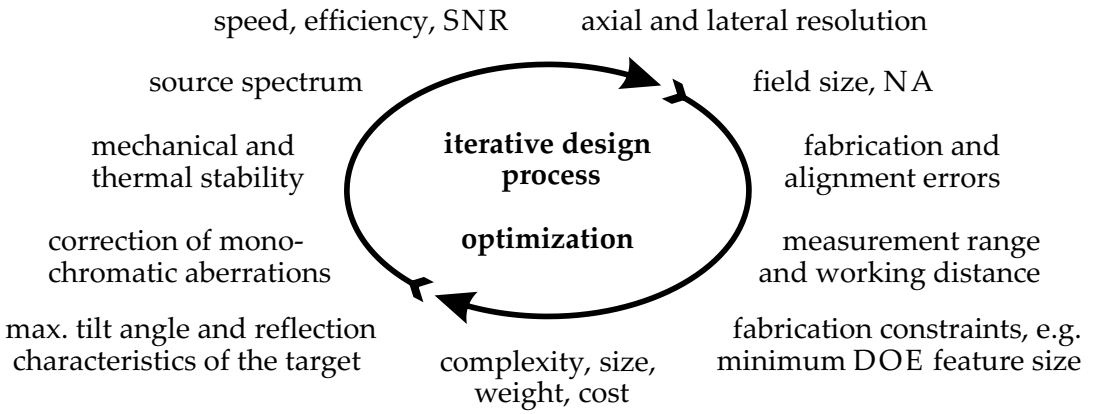

Fig. 5.1: Lens design process as a compromise between competing constraints and performance criteria.

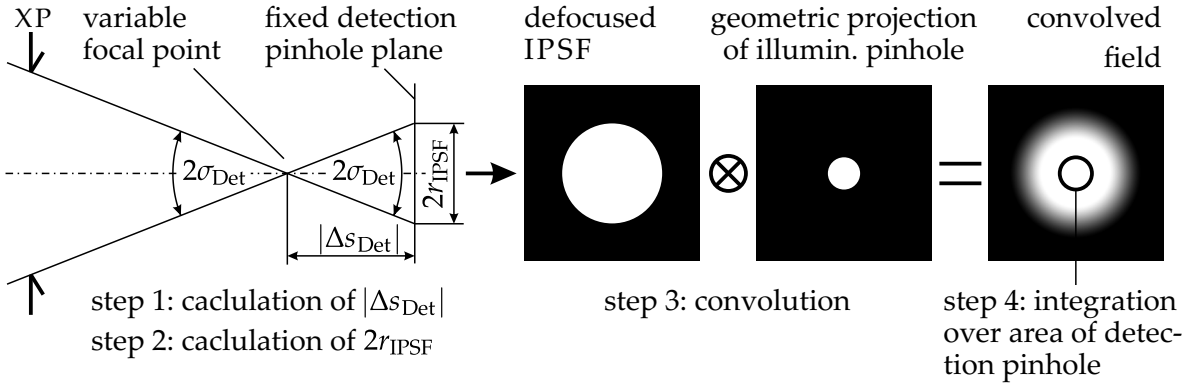

Fig. 5.2: Basic layout of the detection space of the chromatic confocal system and calculation steps of the collinear signal model.

mainly based on the collinear system model. In the second part of this chapter an aberration discussion is presented. To aid the designer during the raytracing-based optimization, the influence of different types of aberrations on the system performance is analyzed.

5.1 Collinear development of starting systems

In Chap. 2.2.4 the collinear system model was introduced as a powerful tool for describing the main properties of an optical system and for developing starting systems. Two reasons are the simple, linear imaging equations and the abstract description of optical elements by their focal powers (or focal lengths) and Abbe numbers. At the same time, many system properties can be related to the two principal rays, the chief ray and the marginal ray. The collinear model provides a very good approximation of the properties of a well corrected imaging system. Different design concepts can thus be compared very efficiently at the collinear design stage. At the same time the performance of the final optical system is determined to a large part by the collinear layout.

The main question to be answered in this section is how different collinear properties influence the spectral signal of a chromatic confocal system. As the starting point the basic ideas behind the signal models of Chapter 4 are used. To simplify the discussion, the following assumptions and simplifications are made:

- Extended illumination and detection pinholes are considered.
- A spatially and temporally incoherent source is assumed.
- The system is analyzed in the detection space which contains the detection pinhole, see Fig. 2.17.
- The IPSF is calculated in the collinear approximation, i.e. monochromatic aberrations and diffraction effects are neglected. The IPSF is described by a circular disc of homogeneous irradiance.
- The only spectral effect to be considered is the wavelength dependent amount of defocus. For simplicity reasons, the numerical aperture and the lateral magnification are assumed to be independent from the wavelength.

Under these conditions the signal passing the detection pinhole can be calculated using the following steps which are also illustrated in Fig. 5.2:

1. Calculation of the wavelength dependent amount of defocus $\Delta s_{\mathrm{Det}}(\lambda)$.
2. Calculation ot the corresponding IPSF which is given by a circular disc with radius $r_{\mathrm{IPSF}} = \Delta s_{\mathrm{Det}}(\lambda) \cdot \tan \sigma_{\mathrm{Det}}$.
3. Convolution of the IPSF with the geometric projection of the illumination pinhole onto the defocused detection plane. The geometric projection is described by the chief ray from the edge of the illumination pinhole. The intersection point of the chief ray with the detection plane defines the radius r_{Image}.
4. Integration of the convolved field over the area of the detection pinhole with radius r_{Det}.

In consequence, four detection space parameters have an influence on the output signal. These are the wavelength-dependent amount of defocus $\Delta s(\lambda)$, the aperture angle σ_{Det}, the radius r_{Image}, and the radius r_{Det}. They are analyzed in two steps. In the first step the influence of the aperture angle and the pinhole diameters is discussed for different amounts of defocus. As a performance criterion the full width at half maximum (FWHM) of the sensor signal is used. It describes the defocus distance at which the power drops to 50% of its maximum value and is a common measure for the width of a peak. The FWHM of the depth response is commonly used as a measure for the axial resolution of confocal and chromatic confocal distance sensors, see e.g. [62, Chapter 3]. In the second step the defocus values are related to the LCA of the optical system and to the spectrum of the source. At this point the detection space is also connected to the target space and aspects like the lateral magnification are taken into account. Afterwards, additional aspects like telecentricity and the maximum focal power of a DOE are discussed.

5.1.1 Influence of detection space quantities on the confocal peak

The influences of the pinhole diameter and of the numerical aperture on the confocal peak are considered in various publications on confocal microscopy, see [62, 98, 100] and the references cited therein. Typically, a finite detection pinhole is considered while the illumination pinhole is assumed to be infinitesimally small. At the same time the discussion is usually based on a wave optical analysis of the optical system. Wave optical models which take a finite illumination pinhole into account are presented in [172, Chapter 4.1.1], [114] and [98, Chap. 5.6].

Following the lines of these publications an extended, incoherently radiating illumination pinhole is assumed. However, the wave optical IPSF model is replaced by the simpler collinear model. This approach is supported by Corle and Kino who state that for large pinhole diameters geometrical optics may be used to estimate the FWHM of the confocal peak and thus the axial resolution of the sensor system [62, p. 167]. Successively, they present a simple equation [62, Eq. 3.35] for the FWHM which depends on the NA and the diameter of the detection pinhole. In the derivation of this equation an infinitesimally small illumination pinhole is assumed and the result is given in target space quantities. The target space version of [62, Eq. 3.35] is

$$s_{\mathrm{FWHM}} = 2\frac{r_{\mathrm{Det}}\sqrt{2}}{\tan \sigma_{\mathrm{Det}}} \approx 2\frac{r_{\mathrm{Det}}\sqrt{2}}{\sin \sigma_{\mathrm{Det}}} = 2\frac{r_{\mathrm{Det}}\sqrt{2}}{\mathrm{NA}_{\mathrm{Det}}}. \tag{5.1}$$

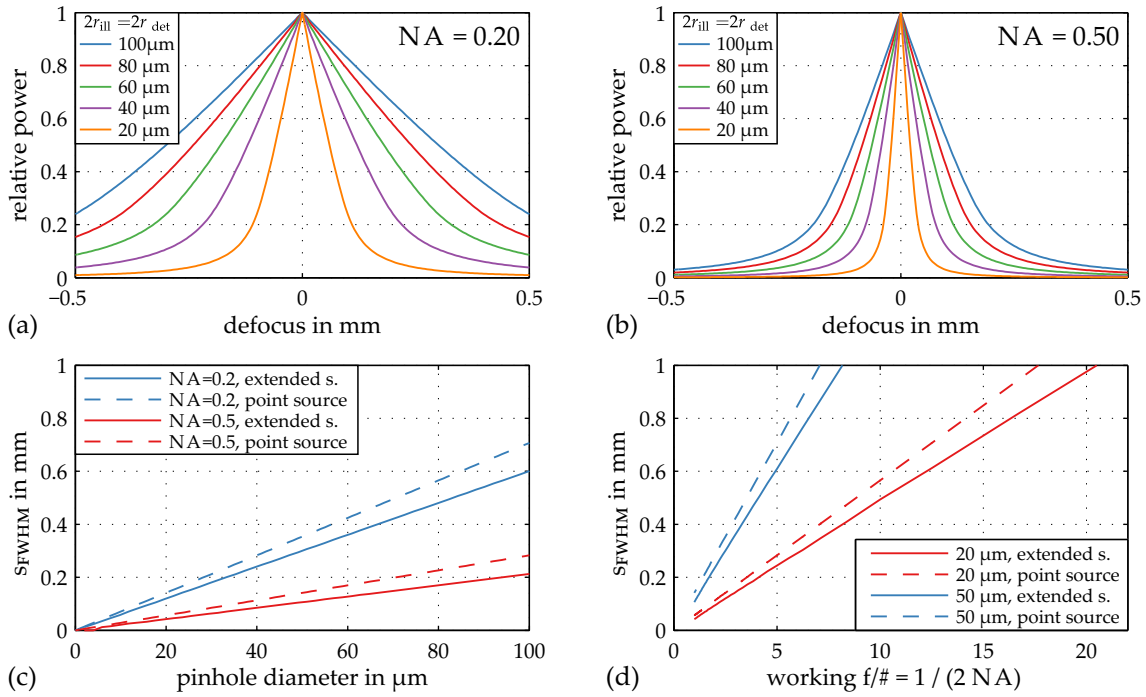

Fig. 5.3: Collinear model of the confocal peak for (a) $\mathrm{NA_{Det}} = 0.20$ and (b) $\mathrm{NA_{Det}} = 0.50$ and different pinhole diameters. Subfigs (c) and (d) indicate a linear dependence of the peak's FWHM defocus distance on (c) the pinhole diameter and (d) the working $f/\# = 1/\left(2\mathrm{NA_{Det}}\right)$. Additionally, the convolution-based model with extended illumination pinholes is compared to the point source model of Eq. 5.1.

$\mathrm{NA_{Det}} = \sin\sigma_{\mathrm{Det}}$ is the detection space numerical aperture. Eq. 5.1 can be derived from Fig. 5.2 based on the following consideration: The FWHM distance s_{FWHM} is the distance between the positive and negative defocus positions at which 50% of the incident power passes the detection pinhole, i.e. when the area of the collinear IPSF is twice the area of the detection pinhole. This condition corresponds to the requirement $r_{\mathrm{IPSF}} = \sqrt{2}r_{\mathrm{Det}}$. According to Eq. 5.1, the FWHM of the confocal peak depends linearly on the width of the detection pinhole and is inversely proportional to $\mathrm{NA_{Det}}$.

Eq. 5.1 is based on the assumption of an infinitesimally small illumination pinhole (point source model). This raises the question, whether the predictions of Eq. 5.1 hold for systems with illumination pinholes of finite size. To answer this question different combinations of defocus distances, pinhole diameters and numerical apertures are analyzed in Fig. 5.3. The corresponding calculations follow the steps depicted in Fig. 5.2 and include the assumption that the detection pinhole has the same radius as the collinear image of the illumination pinhole.

The analysis indicates that within the investigated parameter space the confocal peak depends linearly on the pinhole diameter and on the working $f/\# = 1/\left(2\mathrm{NA_{Det}}\right)$. However, the consideration of extended illumination pinholes leads to a different slope in comparison to the one predicted by Eq. 5.1. The FWHM defocus distance of the model with finite sources is smaller than the one of the less accurate point source model. It is important to note that several simplifications have been made to arrive at this result. Especially, diffraction effects, aberrations and the dependence of $\mathrm{NA_{Det}}$ on the defocus distance have been neglected. Thus, differences between experimental results and these predictions have to be expected. At the

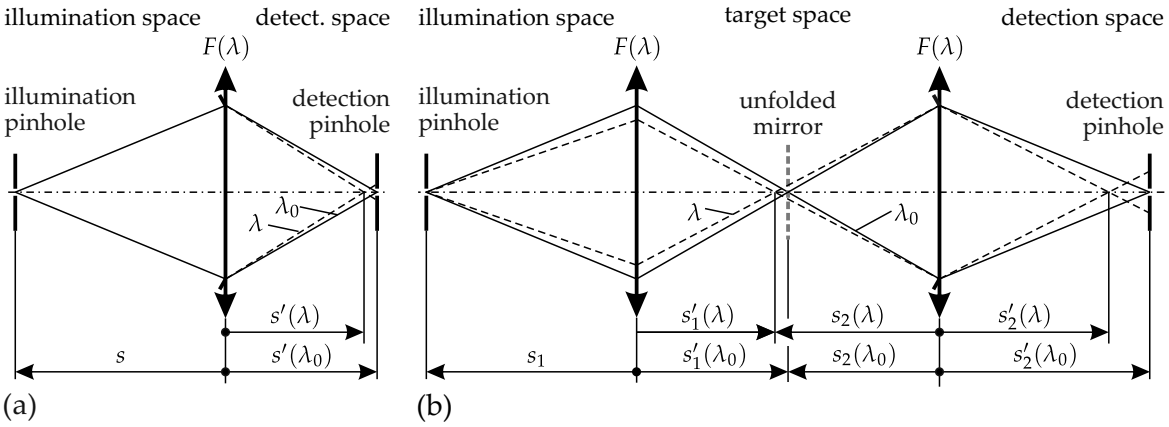

Fig. 5.4: Schematics of the considered chromatic confocal imaging systems. (a) single pass system, (b) an unfolded double pass system.

same time the designer gains valuable insight into how the width of the spectral peak is influenced by the pinhole diameter and the $\mathrm{NA}_{\mathrm{Det}}$.

5.1.2 Relation between detection and target space quantities

The findings of the previous section are based on detection space quantities. They were discussed independently from the longitudinal chromatic aberration (LCA) of the chromatic confocal system. In this section the detection space quantities are linked to the illumination and target spaces and to the LCA of the hyperchromatic lens. For this purpose the equation

$$\Delta s'(\lambda) = s'_n(\lambda) - s'_n(\lambda_0) = -\frac{s'^2_n(\lambda_0)}{\omega^2_n(\lambda_0)} \sum_{i=1}^{n} \frac{F'_i(\lambda_0)\omega^2_i(\lambda_0)}{\nu_{\lambda_0,i}(\lambda,\lambda_0)}. \tag{5.2}$$

is used which is based on Eq. 2.79. It establishes a relation between the defocus distance in detection space and the wavelength.

The goal is to calculate the shape of the spectral peak for incoherent systems with large illumination pinholes which cannot be modeled as a point source. These finite illumination pinholes have to be considered through a convolution integral for which often no simple closed form solution can be found. Hence, a heuristic approach is chosen and the influence of four common parameters is analyzed. These are: The pinhole diameter, the numerical aperture, the scaling of the imaging system, and the longitudinal chromatic aberration (LCA). The impact of these parameters varies with the type of imaging system. Here, a single pass and a double pass chromatic confocal system are analyzed. Schematics of these systems are shown in Fig. 5.4.

Single pass hyperspectral imaging system: FWHM of the spectral peak

The influence of the four parameters is first discussed for the single pass hyperspectral imaging (HSI) system. There, the FWHM of the spectral peak is used as the performance criterion which is directly related to the spectral resolution of the HSI system:

The influence of the pinhole diameter was already analyzed in Fig. 5.3(c). The width of the confocal peak was found to be proportional to the pinhole diameter . The same observation holds for chromatic confocal systems. There, the target space defocus follows Eq. 5.2.

Similarly, the influence of the numerical aperture was analyzed in 5.3(d). Again, the results can be transferred to the chromatic confocal case through Eq. 5.2. Within the analyzed parameter space the width of the spectral peak is **inversely proportional** to the numerical aperture.

The variation of the longitudinal chromatic aberration (LCA) has a linear impact on the target space defocus distance $\Delta s'(\lambda)$ assigned to a fixed wavelength difference $\lambda - \lambda_0$. The FWHM of the spectral peak is **inversely proportional** to the LCA of the hyperchromatic lens.

The scaling of the optical systems corresponds to a multiplication of all linear quantities with the factor M while the angles are not affected. Eq. 5.2 is modified as follows: $s'_n \rightarrow M \cdot s'_n$; $F'_i \rightarrow F'_i/M$, thus $\Delta s'(\lambda) \rightarrow M \cdot \Delta s'(\lambda)$. The FWHM of the spectral peak is thus **inversely proportional** to the scaling factor M.

Double pass chromatic confocal distance sensor: Measurement range

The performance of a chromatic confocal distance sensor is described by different criteria than the spectral resolution considered in case of the HSI system. Below, the measurement range and the axial two-point resolution are selected as the performance criteria. The measurement range corresponds to the target space distance $|s'_1(\lambda_{\max}) - s'_1(\lambda_{\min})|$ between the collinear image planes for the maximum and minimum wavelengths of the source. It has the following dependence on the pinhole diameter, the numerical aperture, the scaling of the imaging system, and the LCA:

The pinhole diameter has **no impact** on the measurement range.

Also, the numerical aperture has **no impact** on the measurement range.

The LCA in target space is **identical** to the measurement range of the sensor system.

Scaling of the lens by the factor M leads to the following modifications:
$s'_n \rightarrow M \cdot s'_n$; $F'_i \rightarrow F'_i/M$, thus $\Delta s'(\lambda) \rightarrow M \cdot \Delta s'(\lambda)$. The measurement range is thus **proportional** to the scaling factor.

Double pass chromatic confocal distance sensor: Axial resolution

Following the discussion in Chap. 2.5.4, the axial separability of two reflecting surfaces is used as the axial resolution criterion. Each surface leads to a peak in the spectral sensor signal. As the two surfaces are located at different axial distances to the sensor the maxima of the two spectral peaks are located at different wavelengths, see Fig. 5.5(a). The two peaks are assumed to add incoherently. The two layers of the target are considered resolvable if the peaks touch each other at a relative spectral power value of 40%, see Fig. 5.5(a). In this case the summed signal has a contrast of approx. 16%. This approach is applicable to both a reflecting target with different height levels within the region of the measurement spot (Fig. 5.5(b)) and to a semi-transparent target with multiple layers (Fig. 5.5(c)). In the latter case the equivalent

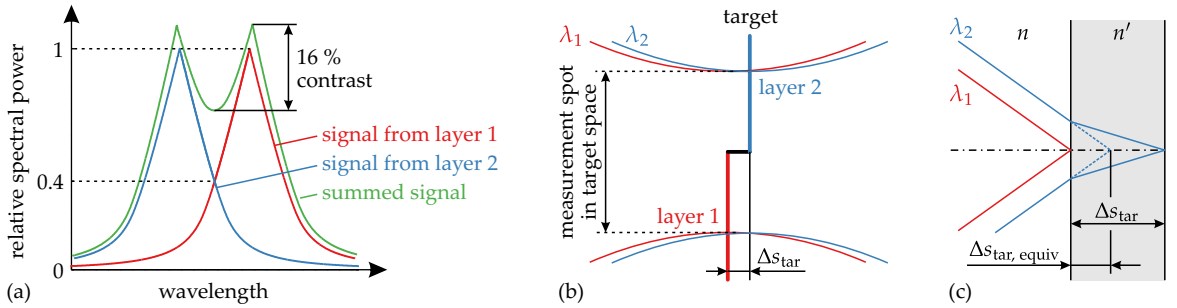

Fig. 5.5: Axial resolution criterion for the chromatic confocal distance sensor. (a) Two layers are considered resolvable if their spectral peaks intersect at relative spectral power values of 0.4 or lower. (b) Corresponding minimum profile height Δs_{tar} of a reflecting surface with two height levels which are both covered by the measurement spot. (c) Measurable thickness Δs_{tar} of (semi-) transparent target surrounded by air.

layer thickness $\Delta s_{tar,\,equiv}$ is used instead of the actual layer thickness Δs_{tar}. In the small angle approximation it is given by [3, Eq. 5.253]

$$\Delta s_{tar,\,equiv} = \frac{n}{n'} \Delta s_{tar}. \tag{5.3}$$

As no analytical expression for the axial resolution can be given, it is analyzed using numerical examples. The target is composed of two reflecting surfaces with a relative distance of 0.2 mm. The results are shown in Figs. 5.6 to 5.9 in a unified manner. They are based on the convolution of the geometric projection of the illumination pinhole with the collinear defocus IPSF; they can be interpreted as follows:

The pinhole diameter (Fig. 5.6) has no impact on the position of the spectral peaks. The width of the spectral peaks, however, depends linearly on the pinhole diameter. In consequence, the resolvable layer thickness is **proportional** the pinhole diameter. Simulation parameters: Hyperchromatic lens = DOE; $\beta' = -1$; $s = -40\,\text{mm}$; $s'(\lambda_0) = 40\,\text{mm}$; $f'(\lambda_0) = 20\,\text{mm}$; $\text{NA}_{det} = \text{NA}_{tar} = 0.20$.

The numerical aperture (Fig. 5.7) has a similar impact on the axial resolution as the pinhole diameter. A change of the NA does not alter the distance of the peaks but influences their width which is inversely proportional to the NA. The axial resolution is thus **inversely proportional** to the NA. Simulation parameters: Hyperchromatic lens = DOE; $\beta' = -1$; $s = -40\,\text{mm}$; $s'(\lambda_0) = 40\,\text{mm}$; $f'(\lambda_0) = 20\,\text{mm}$; $r_{PH} = 50\,\mu\text{m}$.

The scaling of the hyperchromatic lens (Fig. 5.8) corresponds to an increase of its focal length as well as its object and image distances by a factor M. At the same time the pinhole diameters and the NA are kept constant. Fig. 5.8 indicates that both the peak distance and the width of the peak are inversely proportional to the scaling factor M. As both effects cancel each other, the lens scaling has **no impact** on the axial resolution. Simulation parameters: Hyperchromatic lens = DOE; $\beta' = -1$; $r_{PH} = 50\,\mu\text{m}$;

The variation of the LCA (Fig. 5.9) is realized with a hybrid diffractive-refractive element, i.e. a refractive lens with a diffractive surface. This element is made of SiO_2 and has a total focal length of $f'_{total}(\lambda_0) = 20\,\text{mm}$ at the reference wavelength $\lambda_0 = 500\,\text{nm}$. To change the spectral characteristics the focal length f'_{DOE} of the diffractive surface is varied. The focal length contributed by the refractive surface is then given by $1/f'_{ROE}(\lambda_0) = 1/f'_{total}(\lambda_0) - 1/f'_{DOE}(\lambda_0)$.

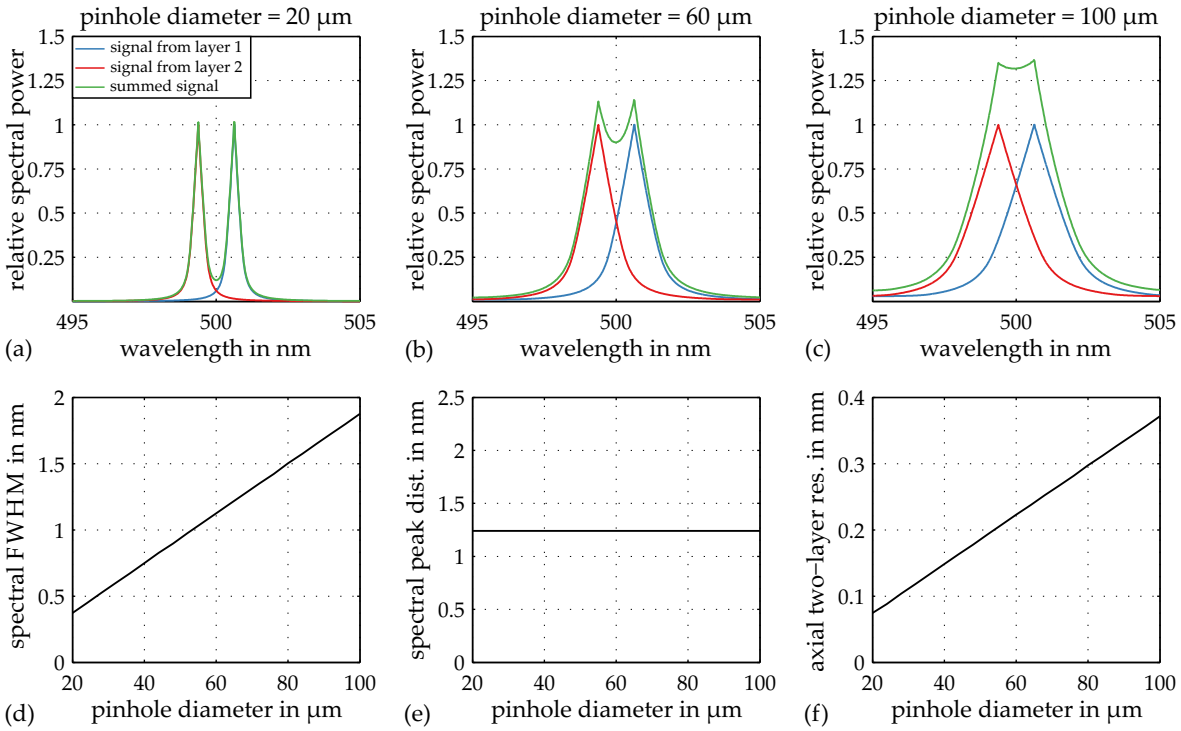

Fig. 5.6: Influence of the pinhole diameter. (a) to (c): Sensor signal for three discrete pinhole diameters. (d) to (f): Influence of the pinhole diameter on (d) the spectral FWHM of a single peak, (e) the spectral distance of the peaks, and (f) the axial resolution.

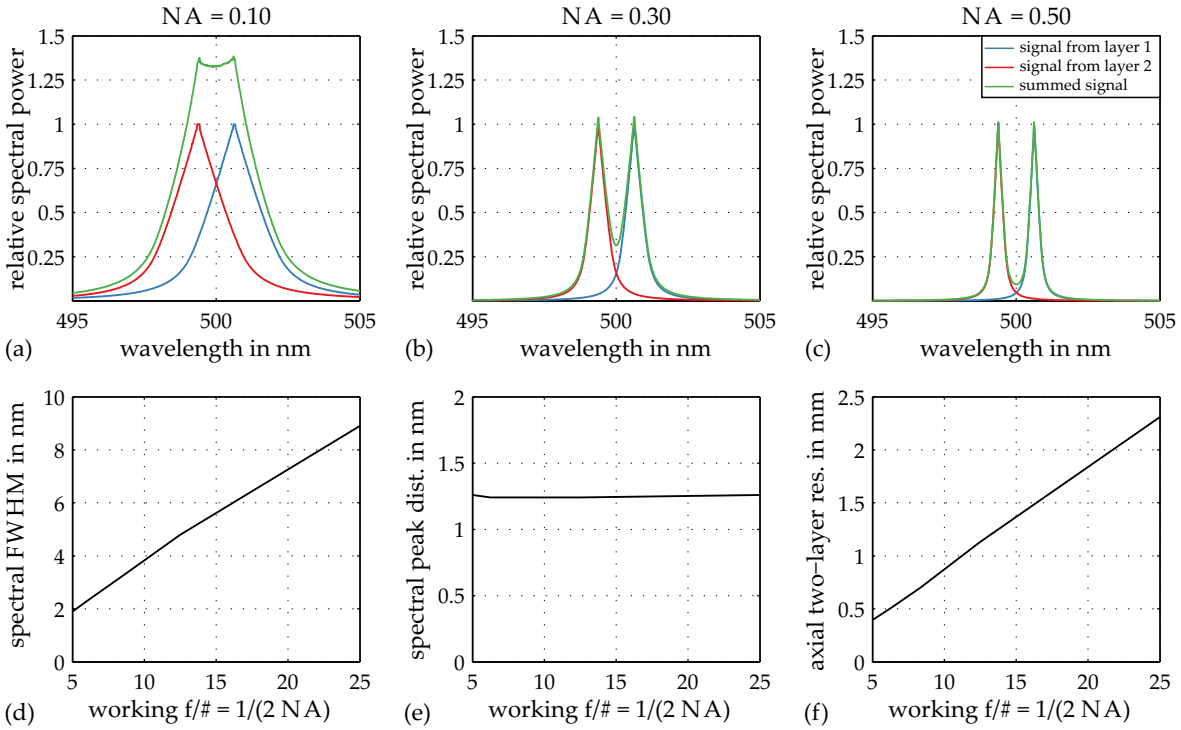

Fig. 5.7: Influence of $NA_{ill} = NA_{det}$. (a) to (c): Sensor signal for three discrete NA_{ill}. (d) to (f): Influence of NA_{ill} on (d) the spectral FWHM of a single peak, (e) the spectral distance of the peaks, and (f) the axial resolution.

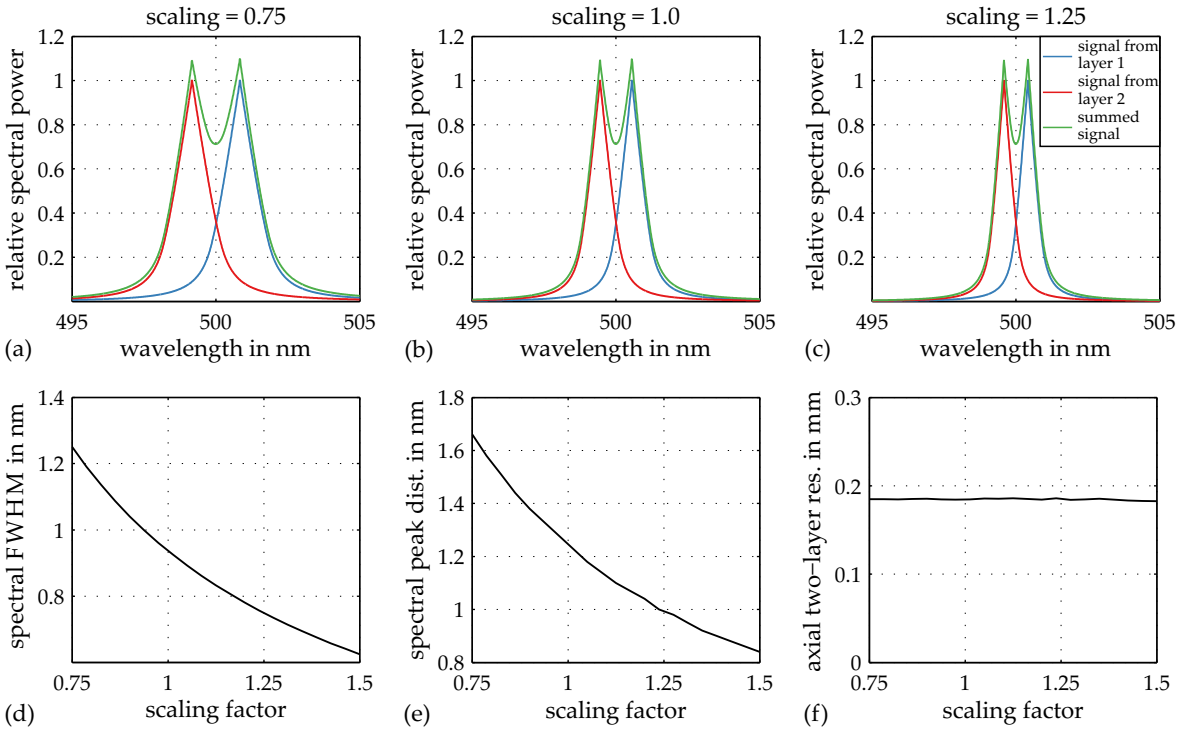

Fig. 5.8: Influence of lens scaling. (a) to (c): Sensor signal for three discrete scaling values. (d) to (f): Influence of the lens scaling on (d) the spectral FWHM of a single peak, (e) the spectral distance of the peaks, and (f) the axial resolution.

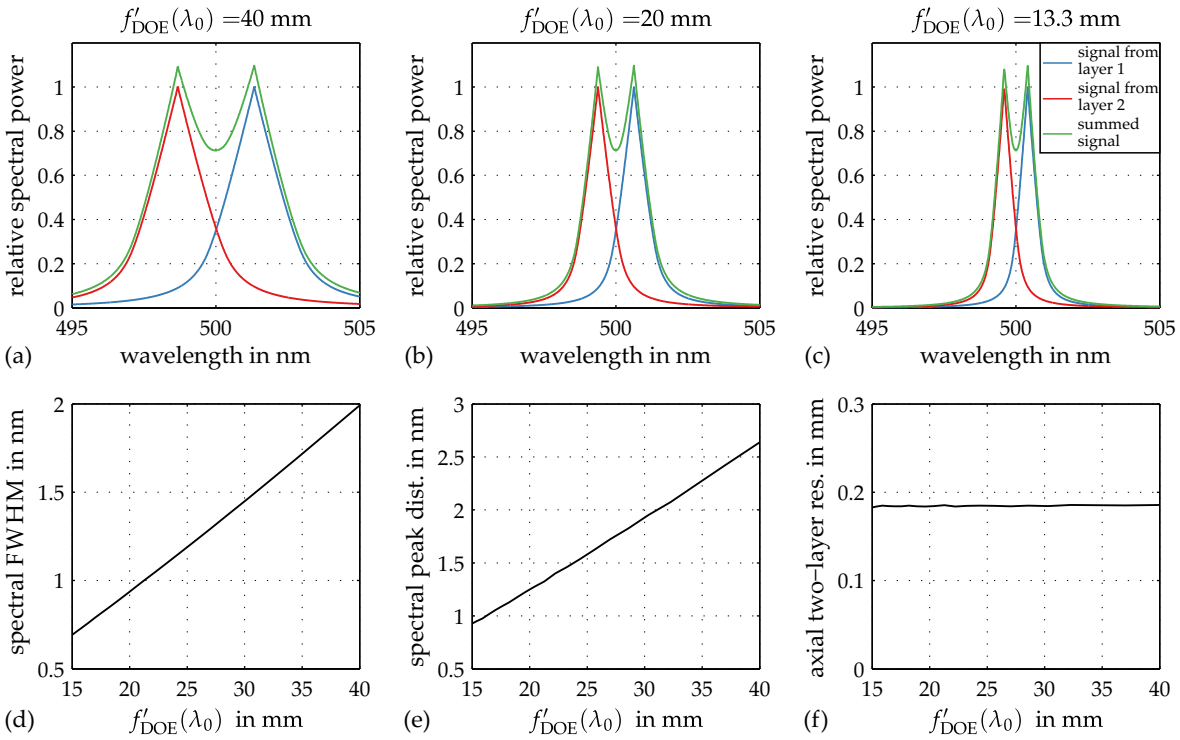

Fig. 5.9: Influence of longitudinal chromatic aberration (LCA). (a) to (c): Sensor signal for three LCA values. (d) to (f): Influence of the LCA on (d) the spectral FWHM of a single peak, (e) the spectral distance of the peaks, and (f) the axial resolution.

Table 5.1: Summary of the main parameters influencing the spectral resolution of a hyperspectral imaging system as well as the measurement range and the axial two-layer resolution of a double pass distance sensor. The indicated dependencies are of approximative nature and only valid in the collinear model.

system parameter	system type and performance criterion		
	HSI: spectral FWHM	distance sensor: measurement range	distance sensor: axial resolution Δs_{tar}
r_{PH}	$\propto r_{\text{PH}}$	-	$\propto r_{\text{PH}}$
NA	$\propto 1/\text{NA}$	-	$\propto 1/\text{NA}$
LCA	$\propto 1/\text{LCA}$	= LCA	-
scaling factor M	$\propto 1/M$	$\propto M$	-

In this combination, the LCA grows with decreasing focal lengths of the diffractive element. A variation of the LCA influences both the distances and the widths of the spectral peaks. Both values have a linear dependence on the focal length of the DOE. In consequence, the spectral characteristics of the hyperchromatic lens has **no impact** on the axial resolution. Simulation parameters: $\beta' = -1$; $s = -40\,\text{mm}$; $s'(\lambda_0) = 40\,\text{mm}$; $f'(\lambda_0) = 20\,\text{mm}$; $r_{\text{PH}} = 50\,\mu\text{m}$; $NA = 0.20$.

In conclusion, multiple parameters were discussed which influence the performance of chromatic confocal imaging systems. The impact of these parameters on the spectral selectivity (i.e. the spectral resolution) of hyperspectral imaging systems as well as the measurement range and the axial resolution of distance sensors is summarized in Table 5.1. Typically, an application-specific selection of parameter values is required as they also have an impact on other system properties like the lens diameter. Several of the identified relations are only an approximation and may not be valid under different circumstances like in systems with a small pinhole diameter or with a large NA.

5.1.3 Tailoring of the LCA to the specific application requirements

In the previous section it was shown that the LCA of the hyperchromatic lens influences both the spectral resolution of chromatic confocal HSI systems and the measurement range of chromatic confocal distance sensors. Depending on the application, the required LCA varies from a few µm [163, 192] to several mm [178, 199, 398]. The adaptation of the LCA to the requirements of the specific application is thus an essential part of the lens design process. The discussion in this section reflects the findings published in [184]. Again, Eq. 5.2 is used as the starting point. It shows that even for a fixed image distance $s'(\lambda_0)$ and for a fixed total focal power of the hyperchromatic lens [6]

$$F'_{\text{tot}}(\lambda_0) = \frac{1}{h_1} \sum_{i=1}^{N} h_i(\lambda_0) F'_i(\lambda_0) \tag{5.4}$$

the LCA may be modified by varying the focal powers $F'_i(\lambda_0)$ and the Abbe numbers $\nu_{\lambda_0,\,i}(\lambda_1,\,\lambda_2)$ of the optical elements. The Abbe numbers were defined in Eqs. 2.71 and 2.76.

In principle, it is possible to obtain a LCA of several mm with a single hyperchromatic group of two refractive lenses. However, this approach has certain constraints: First, the maximum focal power of a refractive element is limited. Second, the monochromatic aberrations of the optical system typically grow with increasing focal powers. It may thus be required to realize the desired LCA with many optical elements, a step which often leads to a large, heavy, and expensive system.

Alternatively, lens elements with different Abbe numbers may be used. According to the discussion in Chap. 2.3 the Abbe number of a DOE is at least five times smaller than the Abbe number of a ROE. By including DOEs in the optical system the same LCA can thus be generated with a reduced number of elements or with elements of lower focal power. These benefits are bought at the cost of a limited diffraction efficiency of the DOE and at the cost of multiple diffraction orders which may lead to stray light and a reduced SNR, see Chap. 2.3.2. At the same time the maximum refractive power of the DOE is limited by the minimum feature size $\mathrm{fs}_{\mathrm{min}}$ of the fabrication process. The minimum feature size $\mathrm{fs}_{\mathrm{min}}$ of a multi-level phase DOE with P phase levels is given by [31, 406]

$$\mathrm{fs}_{\mathrm{min}} = \frac{\lambda_0}{\mathrm{NA}_{\mathrm{DOE}} \cdot P}. \tag{5.5}$$

$\mathrm{NA}_{\mathrm{DOE}}$ is the image space NA of the DOE for an object at infinity. It is related to the working $f/\#$ through the relation

$$f/\# = \frac{f'}{d_{\mathrm{EP}}} = \frac{1}{2\mathrm{NA}_{\mathrm{DOE}}}. \tag{5.6}$$

Many of the DOEs used in the context of this thesis were fabricated with a minimum feature size of 700 nm to 1000 nm and with 4 phase levels. At the reference wavelength $\lambda_0 = 550\,\mathrm{nm}$ these values correspond to a maximum $\mathrm{NA}_{\mathrm{DOE}}$ of 0.14 to 0.20. To realize a larger NA, the refractive power has to be distributed among multiple DOEs. Without efficiency achromatization the wavelength dependent diffraction efficiency of each DOE drops with increasing spectral distances to the reference wavelength. A drop by 20% at the extreme wavelengths means that in a double pass system with two DOEs the total efficiency at these wavelengths is reduced by 59%. These effects may thus prohibit the use of multiple DOEs in the hyperchromatic lens.

Based on these considerations two hyperchromatic lenses for chromatic confocal distance sensors were designed and fabricated. The first system is a purely diffractive design and consists of two DOEs. It shows that a system with two DOEs is indeed feasible. The second system consists of a DOE with positive power and a ROE with negative power. By combining these two elements, a LCA is obtained which is 81% larger than the one of a single DOE with the same total focal power $\mathrm{FP}_{\mathrm{tot}} = \mathrm{FP}_{\mathrm{DOE}} + \mathrm{FP}_{\mathrm{ROE}}$. This system proofs that the LCA can be easily customized by altering the focal powers of the diffractive and refractive elements. For a detailed discussion of both systems including experimental results, see [184].

5.1.4 Telecentricity

Telecentricity was introduced in Chap. 2.2.4 as a specific system layout where the object and/or image space images of the aperture are located at infinity. Fig. 5.10 visualizes the importance of broadband telecentricity to chromatic confocal systems which image an extended field of view. In this figure three different systems are compared: a system without telecentricity,

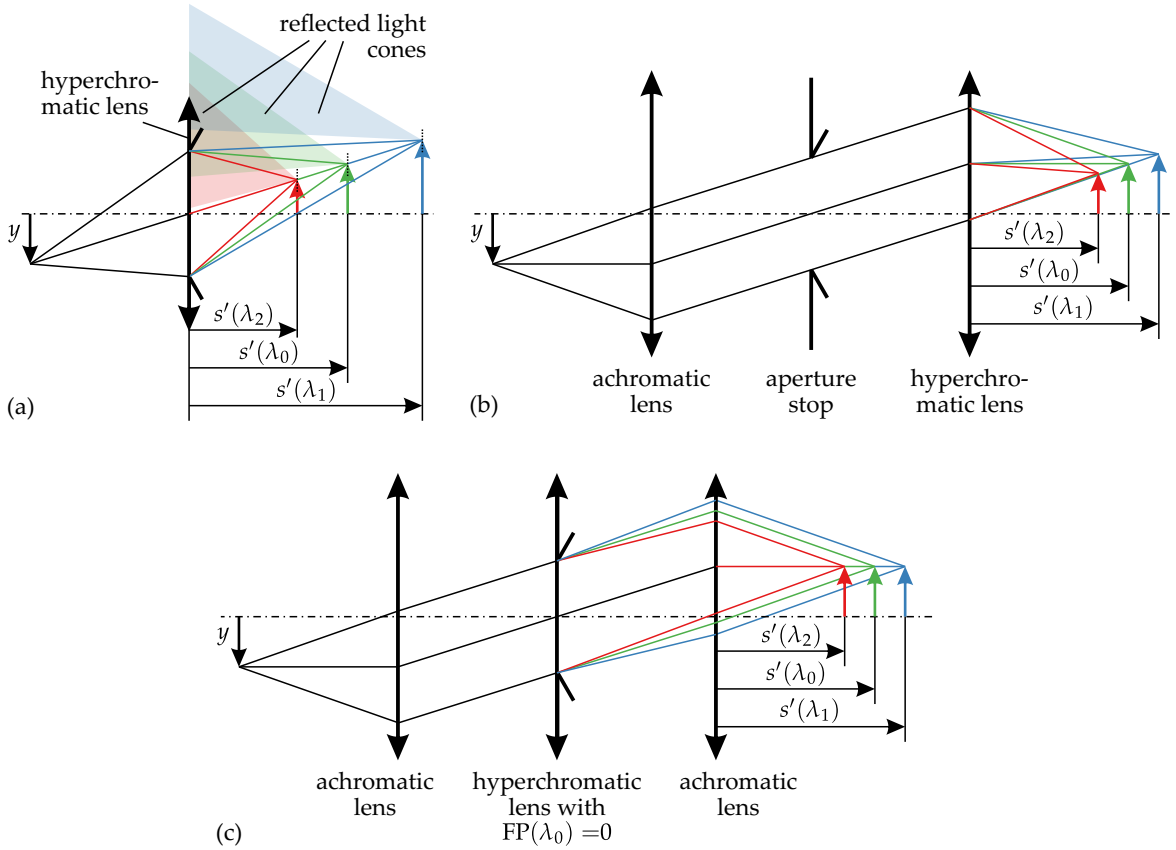

Fig. 5.10: Influence of telecentricity on the imaging properties of chromatic confocal imaging systems. (a) non-telecentric system. (b) system with telecentricity at the wavelength λ_0. (c) system with broadband telecentricity.

a system with telecentricity at the reference wavelength λ_0 and a system with broadband telecentricity.

Fig. 5.10(a) illustrates two disadvantages of chromatic confocal systems without telecentricity. First, only a part of the reflected light cone overlaps with the system aperture. In double pass setups a large part or even all the reflected radiation may not reach the detector. The losses increase with growing values of $|y|$ and $s'(\lambda)$. Second, the image points are not located on a line parallel to the optical axis. The implications of this effect depend on the type of chromatic confocal system:

- In a hyperspectral imaging system the center of a specific image space spot coincides with the center of the detection pinhole at only one wavelength. At all other wavelengths the centers have different lateral positions which leads to an erroneous signal. In principle, this effect can be compensated by replacing the detection pinhole array by a pixelated detector. In this case the system has to be calibrated to read out different detection pixels depending on the wavelength in focus.
- In a chromatic confocal distance sensor a single sensor channel does not probe the target space along a line parallel to the optical axis. Instead, the lateral detection position depends on the axial distance to the target. In principle, this effect can be compensated through a calibration of the sensor system.

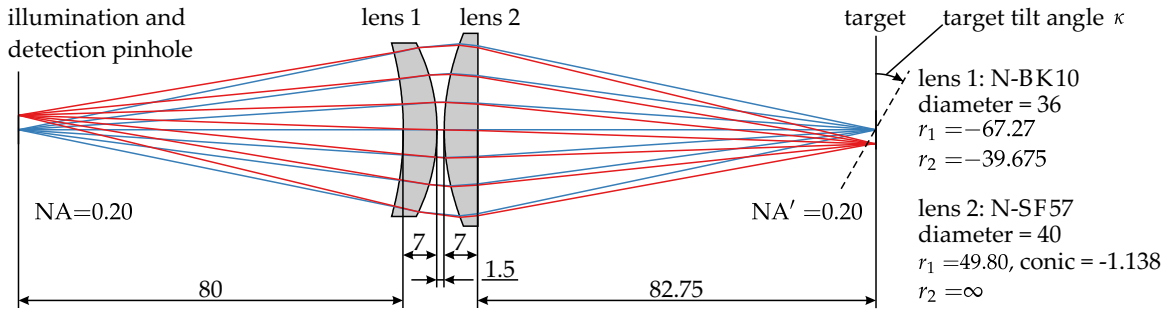

Fig. 5.11: Layout of refractive hyperchromat used for the aberration discussion. All distances and radii are given in mm.

Telecentricity is thus of general relevance in both single and double pass chromatic confocal setups. Fig. 5.10(b) shows an optical setup which realizes image space telecentricity at the reference wavelength λ_0. While this setup reduces the effects observed in Fig. 5.10(a), it is not telecentric at the wavelengths λ_1 and λ_2. A simple way of obtaining broadband telecentricity in image space is depicted in Fig. 5.10(c). It is closely related to the approaches used in [207, 210, 215]. A thin hyperchromatic lens is placed at the stop of the optical system. The lens is imaged to infinity by an achromatic lens. As the chief ray passes the nodal points of the hyperchromatic lens, its direction is not altered by the hyperchromatic lens. The chief ray is thus parallel to the optical axis in image space for all wavelengths and broadband telecentricity is achieved. In Chap. 6 an exemplary system will be discussed which is based on this approach. There, the hyperchromatic lens is composed of a diffractive and a refractive component which have focal powers of the same magnitude but of the opposite sign. At λ_0 the hyperchromatic lens group has no focal power. At all other wavelengths it acts as a positive or negative lens and influences the distance to the image point.

5.2 Aberration considerations

While a full aberration discussion is beyond the scope of this thesis, this section summarizes several aberration-related design aspects which were explored during the development of chromatic confocal imaging systems. Several of the systems were developed for industrial applications and cannot be disclosed. Instead, a simple, purely refractive system is used as the starting point for the discussion. It is shown in Fig. 5.11. This system is well corrected on axis but shows severe aberrations when imaging off-axis object points. Consequently, the effects of field dependent aberrations on the sensor performance can be studied. Two scenarios are analyzed: The use of the system in single pass and its use in double pass. Later, the results of the two scenarios are generalized and the compensation of aberrations is discussed. The chapter closes with a discussion of alignment errors, of tilted targets, and of spherical aberration which is induced by the target.

Single pass scenario

First, the chromatic confocal imaging system of Fig. 5.11 is analyzed in single pass for pinholes with a diameter of 50 µm. The results are presented in Figs. 5.12(a), 5.13(a, b) 5.14(a, b), and 5.15. These figures show that the system suffers from all third order aberrations: Spherical aberration, coma, astigmatism, field curvature, and distortion. The imaging performance

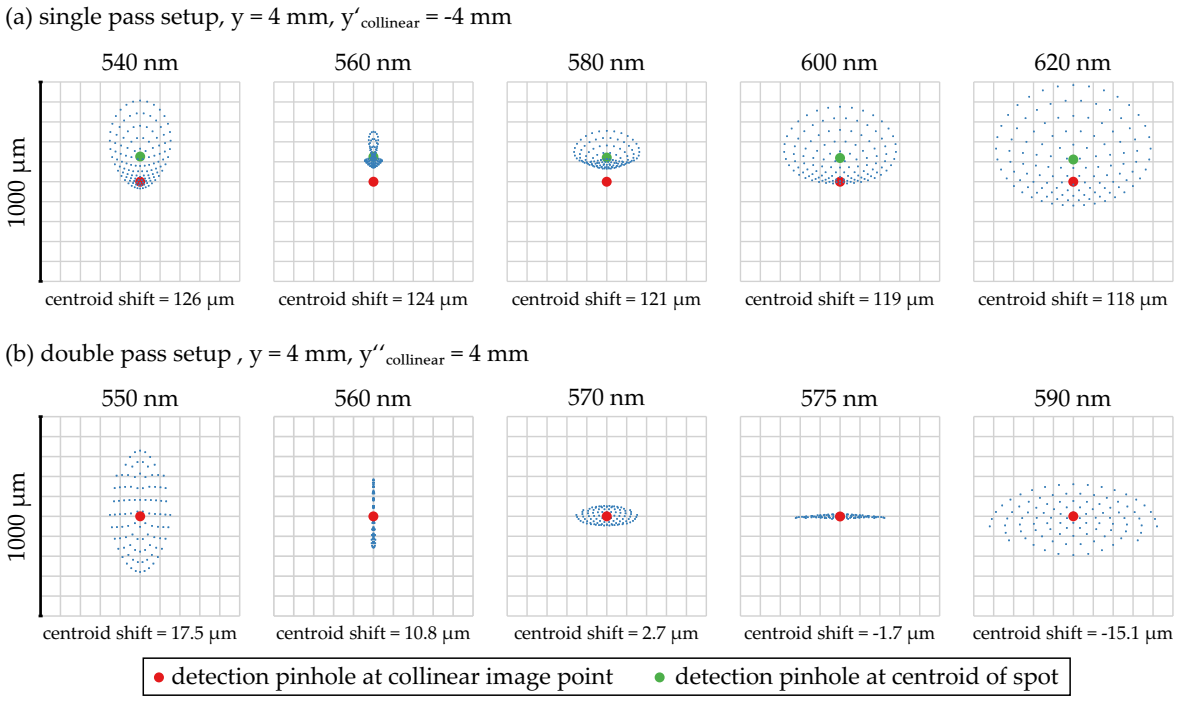

Fig. 5.12: Spot diagrams of the hyperchromatic lens in (a) single pass and (b) double pass for the field point $y = 4\,\text{mm}$.

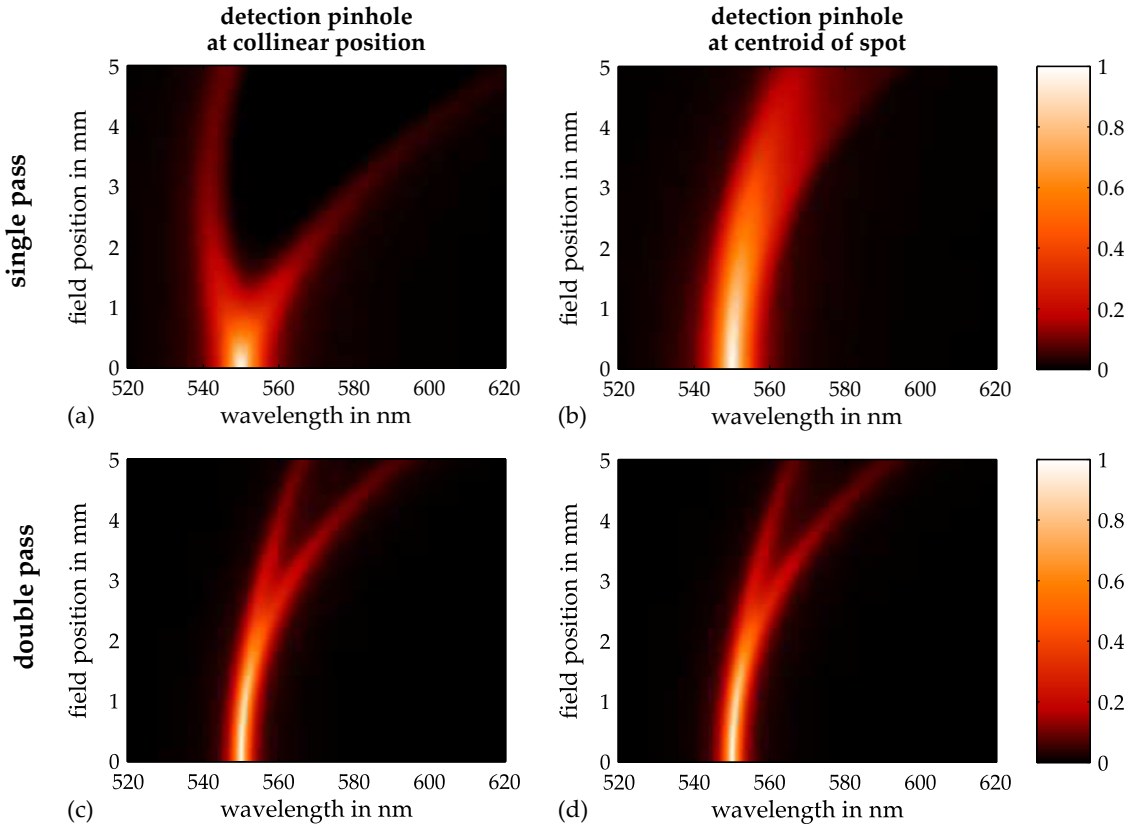

Fig. 5.13: Spectral characteristics of the hyperchromatic lens in dependence on the lateral position of the illumination pinhole. The system is analyzed in single pass (a, b) and in double pass (c, d). The detection pinhole is placed either at the collinear image point (a, c) or at the centroid of the spot (b, d).

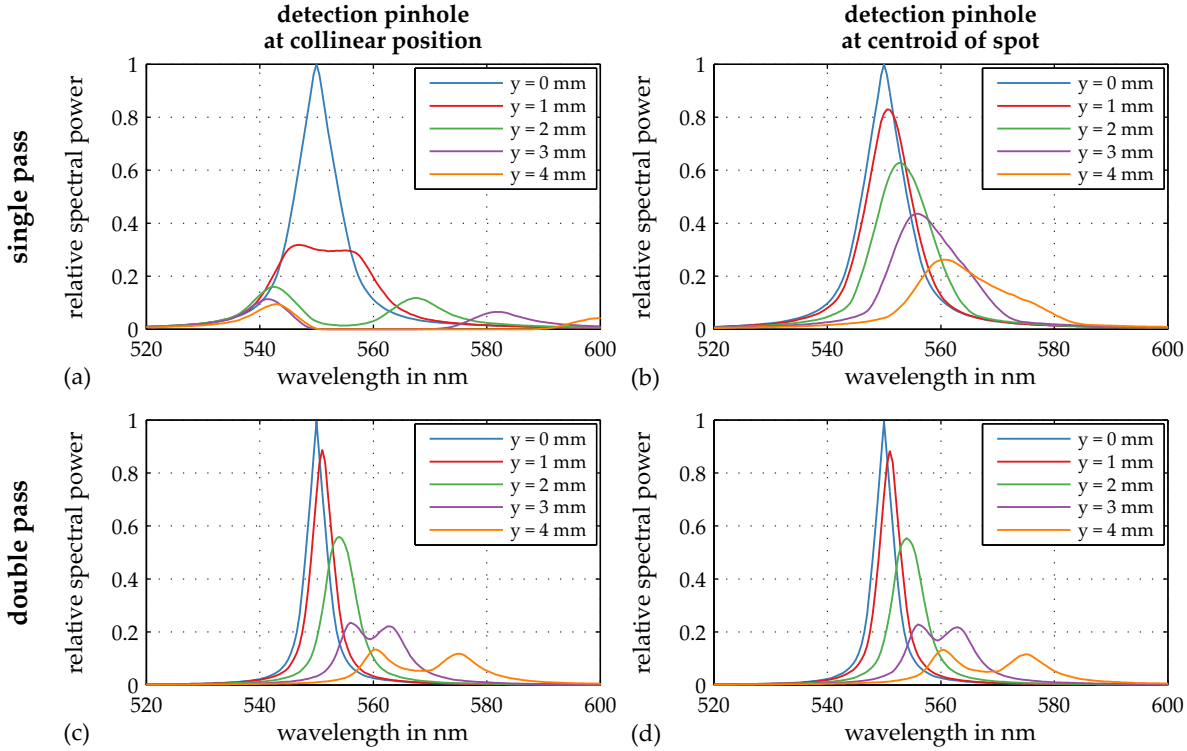

Fig. 5.14: Spectral peaks of the hyperchromatic lens in single pass (a, b) and double pass (c, d) for different lateral positions of the illumination pinhole. The detection pinhole is placed either at the collinear image point (a, c) or at the centroid of the spot (b, d).

depends strongly on the position of the detection pinhole: If the pinhole is placed at the collinear image point, the system is unusable for object heights larger than $y = 1.5\,\text{mm}$ where two peaks appear. The main reason is clearly visible in Fig. 5.12(a): Owing to distortion, the spot in the detection plane is shifted laterally with respect to the detection pinhole. For the wavelength in focus on the detection pinhole plane the spot size is smaller than the displacement. In consequence, the rays of this wavelength do not pass the detection pinhole and are missing from the sensor signal. Defocused wavelengths cause a larger spot and a few rays hit the detection pinhole. Thus, two maxima appear for wavelengths which have a focus in front of and behind the detection pinhole plane.

The system performance can be improved by moving the detection pinhole laterally from the collinear position to the center of the spot. For all considered object points a single peak is observed and the sensor may be used for object heights of up to $y = 5\,\text{mm}$. At the same time, field curvature leads to a shift of the wavelength in focus on the detection pinhole plane. The shift grows with increasing object heights y.

Double pass scenario

The imaging properties of the chromatic confocal system changes significantly when it is used in double pass. These changes are reflected by Figs. 5.12(b), 5.13(c, d) 5.14(c, d), and 5.15:

1. The spots are very well centered with respect to the collinear position of the image point. Thus, no significant differences are present between the placement of the detection pinhole at the collinear image point and at the centroid of the spot. At the same time,

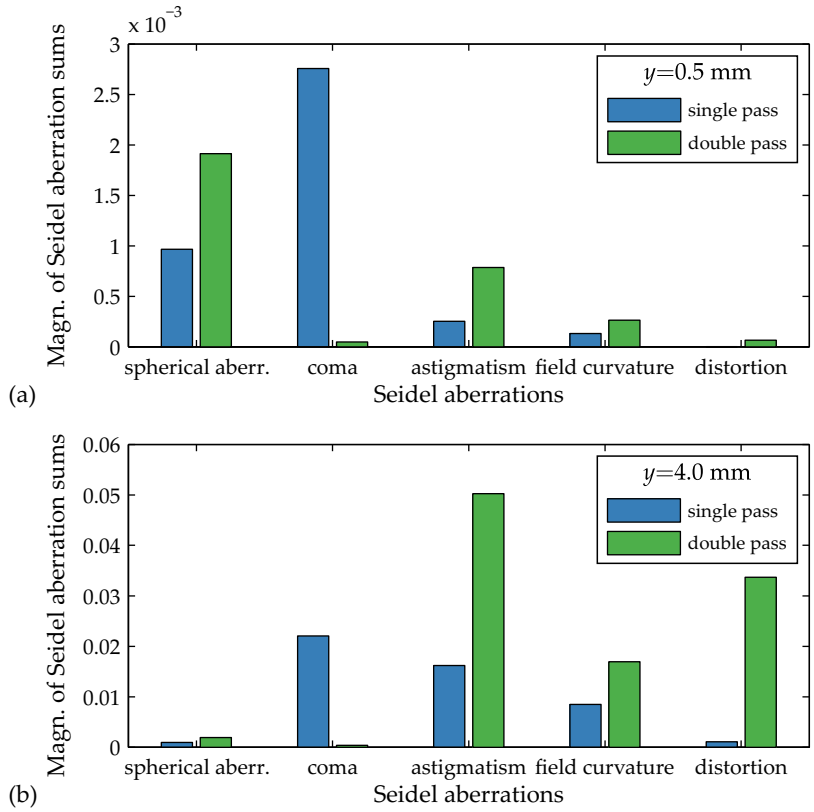

Fig. 5.15: Magnitude of the Seidel aberration sums for the hyperchromatic lens in single and double pass. The calculations were performed in ZEMAX with object heights y of (a) 0.5 mm and (b) 4.0 mm.

Fig. 5.15 indicates a significant amount of distortion which is related to the observation that the chief ray does no longer define the center of the spot in the detection pinhole plane. At $y = 4$ mm the chief ray deviates by a value of 80 µm from the position of the centroid. These self-aligning property of the double pass configuration is very useful for fiber-based point sensors where the detection pinhole corresponds to the illumination pinhole.

2. The coma contribution of the first pass is canceled by the second pass. Although the other third order aberrations increase during the second pass, the double pass system still has a better performance than the single pass system for object heights of up to $y = 3$ mm. For larger field values astigmatism begins to dominate and the imaging performance reduces.
3. For object heights $y > 3$ mm the spectral signal shows two peaks. These two peaks can be related to the wavelengths where the two astigmatic foci (sagittal and meridional) coincide with the detection plane.
4. The FWHM of the spectral peak is approx. half the FWHM value of the single pass case. This is due to the LCA of the double pass configuration being approx. twice as large as the one of the single pass setup.
5. Field curvature causes the spectral peak to shift to higher focal lengths for larger object heights y.

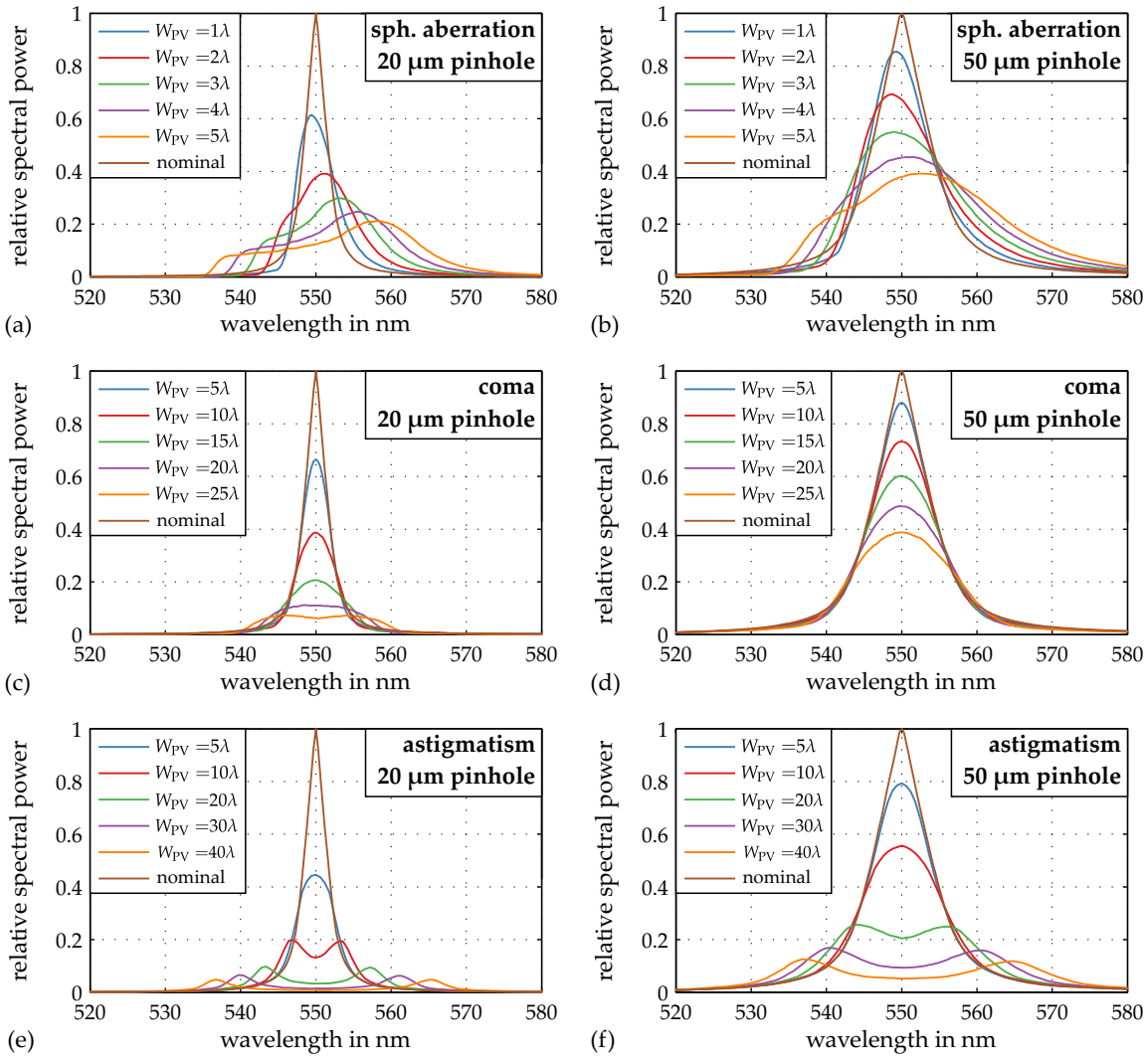

Fig. 5.16: Influence of different amounts of (a, b) spherical aberration, (c, d) coma, and (e, f) astigmatism on the performance on the hyperchromatic lens of Fig. 5.11 with pinhole diameters of (a, c, e) 20 µm and (b, d, f) 50 µm. The values W_{PV} correspond to the peak-valley wavefront errors.

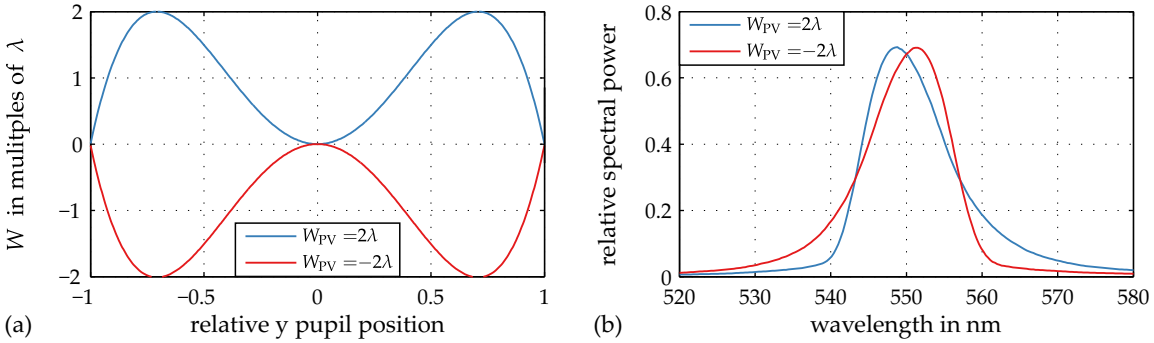

Fig. 5.17: Influence of spherical aberration of the same magnitude but the opposing sign on the spectral peak. (a) Wavefront aberration at the exit pupil. (b) Resulting shape of the spectral peak.

Generalized aberration discussion

These observations provide the starting point for a more general discussion of third order aberrations and their impact on chromatic confocal imaging systems. The impact of the aberrations is discussed for three different cases: Single pass systems, double pass systems with a specularly reflecting target and small tilts of the target, and double pass systems with a diffusely reflecting target:

Spherical aberration blurs the image of the illumination pinhole and is already present on axis. It is the main aberration in chromatic confocal point sensors with an on-axis illumination pinhole. The impact of different amounts of spherical aberration on the spectral signal is visualized in Fig. 5.16(a, b) for pinhole diameters of 20 µm and 50 µm. In these simulations the spherical aberration is balanced by defocus to keep the spectral peak at the same position. With growing amounts of spherical aberration the IPSF is spread across a larger region in the detection pinhole plane and a decreasing part of the signal passes the detection pinhole. This leads to a reduction of the height of the spectral peak. At the same time the spectral peak broadens and becomes asymmetric. The system with smaller pinhole diameter has a lower nominal peak width it is also more sensitive to spherical aberration. Fig. 5.17 shows that changing the sign of the spherical aberration leads to a spectral peak whose shape corresponds to the original one flipped about the y-axis. This opens up the possibility of determining the spherical aberration present in the optical system from the shape of the spectral peak.

Impact on single pass systems: Critical.

Impact on both types of double pass systems: Critical; the errors of the second pass add to those of the first pass.

Coma leads to both a blurring of the spot in the detection plane and to a shift of its centroid. The influence of different amounts of coma on the shape of the spectral peak are illustrated in Fig. 5.16(c, d) for pinhole diameters of 20 µm and 50 µm. Again, the system with the smaller pinhole diameter has the better nominal performance but is more sensitive to coma.

Impact on single pass systems: Critical.

Impact on double pass systems with a specularly reflecting target: Uncritical; the coma contributions of the first pass are canceled by those of the second pass.

Impact on double pass systems with a diffusely reflecting target: Critical; The blurred spot on the target is further blurred during the second pass.

Astigmatism results in separate meridional and sagittal focus planes in which the rays are aligned in meridional and sagittal lines. At these lines a high irradiance can be observed. At other planes the spot has an elliptical shape with a reduced irradiance, i.e. the power is spread across a larger region. In a chromatic confocal sensor system astigmatism causes two spectral peaks which correspond to the wavelengths for which the meridional and sagittal lines are in focus on the detection pinhole plane. Increasing astigmatism leads to a growing spectral distance between the two peaks. 5.16(e, f) illustrates the effects of astigmatism for pinhole diameters of 20 µm and 50 µm.

Impact on single pass systems: Critical.

Impact on both types of double pass systems: Critical; the errors of the second pass add to those of the first pass.

Field curvature causes the field points for a single wavelength to lie on a curved surface. In consequence, the wavelengths in focus on the detection plane vary with the field position. Thus, the position of the spectral peak varies across the field, see Figs. 5.13 and 5.14.

Impact on single pass systems: Critical, but compensable in post processing.

Impact on both types of double pass systems: Critical but compensable in post processing; the errors of the second pass add to those of the first pass.

Distortion causes the chief ray to intersect the image plane at a position which deviates from the collinear image point. Alternatively, it can also be defined as a lateral shift between the centroid of the spot and the center of the detection pinhole. The effect of distortion on the confocal signal is visible in Figs. 5.12(a) and 5.13(a). The wavelength in focus on the detection pinhole plane causes a small spot. With distortion, the spot can lie outside of the detection pinhole. In this case the wavelength which should have the strongest contribution to the output signal does not contribute at all. At the same time, defocused wavelengths are spread across a larger region and contribute to the output signal.

Impact on single pass systems: Critical, but compensable in systems where the fixed detection pinhole array is replaced by a matrix detector.

Impact on both types of double pass systems: Self-compensation, i.e. for all analyzed systems the spot on the detection pinhole plane was well aligned with the detection pinhole. At the same time the lateral position of the measurement point in target space deviates from the collinear position.

Compensation of aberrations

The optical designer has different options for dealing with monochromatic aberrations. On the one hand the aberrations can be minimized in a complex optical system with many or with aspherical surfaces. This approach typically results in large and expensive systems. The second option is linked to a more complex calibration routine but has the potential of simplifying the layout of the optical system. It is very limited in case of single pass systems with fixed detection pinhole arrays. If, however, the detection pinhole array is replaced by a matrix detector, the effects of field curvature and distortion can be compensated in post processing. In this case the detection pinholes are replaced by generalized detection pixels, i.e. groups of pixels which are binned in post processing. For each sensor setting the generalized detection pixels can be set to the best positions. These best positions are determined in a calibration process which also accounts for field curvature and for a wavelength-dependent lateral magnification.

The same approach can be used for double pass systems with matrix detectors. In fiber-based setups where the fibers are used in double pass the lateral shift of generalized detection pixels is not available. However, distortion effects were found to be insignificant for the double pass systems analyzed in this thesis. At the same time, the effects of field curvature can be compensated by an appropriate calibration routine which contains a calibration curve for each pinhole. Thus, in both single pass systems with matrix detectors and double pass systems the correction of monochromatic aberrations can be reduced to the minimization of spherical aberration and astigmatism while the other aberrations are handled in post processing. Under certain circumstances there may even be the option to reduce the effects of spherical aberration with deconvolution techniques [48].

Fabrication and alignment errors

Another important aspect of the lens design process are fabrication and alignment errors which are always present in a fabricated system. During the design of commercial sensor systems extensive tolerance simulations were performed for chromatic confocal point sensors.

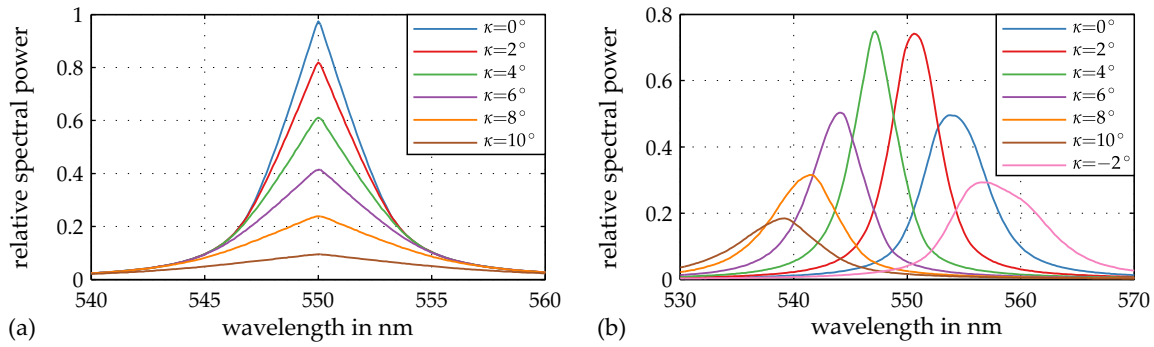

Fig. 5.18: Spectral signal of the hyperchromatic lens (Fig. 5.11) used in double pass with a 50 µm illumination and detection pinhole placed (a) on axis and (b) at $y = 2\,\text{mm}$. Different tilt angles κ of a specularly reflecting planar target are considered.

Significant differences in the sensitivity to tilt and decenter tolerances were observed between single- and double pass systems. One of the main reasons for the difference is on-axis coma, which is caused by tilted and decentered surfaces and lenses within the optical system [407, Chap. 35.5]. In classical imaging systems it is commonly reduced by laterally shifting a specific lens element of the optical system as a compensator [407, Chap. 35.5]. Above, it was shown that in a double pass setup with a specularly reflecting target the coma contributions of the first pass are canceled by those of the second pass. Similar effects were observed for misalignment-induced on-axis coma. It was found that the double pass system was much more tolerant to fabrication and alignment errors than the same system used in single pass.

Tilt of the target

In double pass systems with a specularly reflecting target, the tilt angle κ of the target has a strong impact on the width and the intensity of the spectral peak. The reason is that the reflected light cone overlaps only partially with the aperture of the hyperchromatic lens. This effect was already mentioned in the context of telecentricity (see Fig. 5.10(a)) and is analyzed in more detail in [172, 408–410]. In [410] also measurement errors which arise from an increasing non-symmetry of the peak are addressed. Fig. 5.18 shows the spectral response of the hyperchromatic system of Fig. 5.11 for an on-axis and an off-axis pinhole position and for different target slope angles κ. In the on-axis case the tilt of the target leads to a drop in signal strength and to an increase of the spectral FWHM.

In the off axis case with $y = 2\,\text{mm}$, the peaks are shifted to different wavelengths. This shift is related to the assumption that the target is tilted about an on-axis point. Hence, the distance to the surface varies with the tilt angle κ. The strongest peak is reached for a tilted target. Again, an increase of the spectral FWHM with growing $|\kappa|$ can be observed. In theory, the maximum slope angle at which a reflected signal can be measured in air is given by $\kappa = \arcsin \text{NA}'$. Then, the marginal ray hits the target at an angle of 90° and passes the system a second time while all other rays are truncated. In practice, a usable sensor signal at the maximum slope angle is only obtained for a NA′ considerably larger than $\sin(\kappa)$, e.g. $\text{NA}' \geq \sin(\kappa + 5°)$. Even then, the axial resolution and the SNR decrease with growing slope of the target.

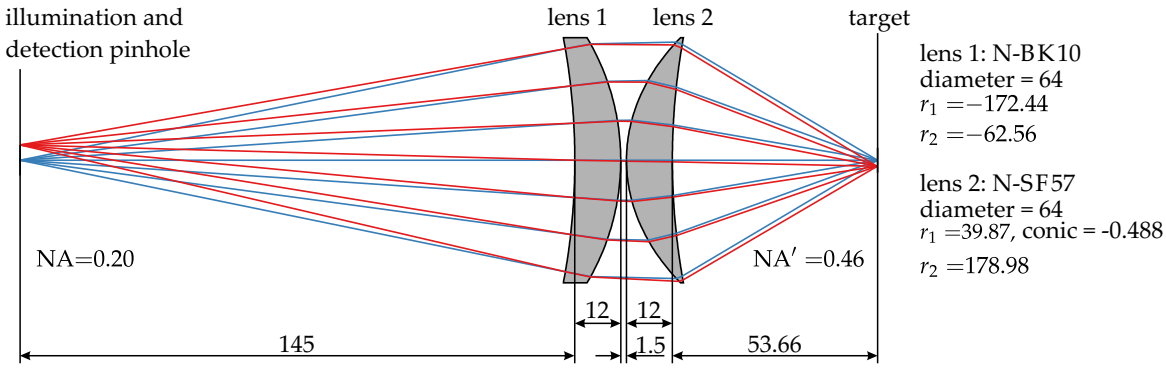

Fig. 5.19: Layout of a second refractive hyperchromat used to study the influence of the thickness of a layered target on the width of the spectral peak. All distances and radii are given in mm.

Spherical aberration induced by the target

In microscopy it is well known that a variation of the default cover slip thickness or focusing into a thick specimen causes spherical aberration, see e.g. [411, Chap. 28.3] and [412]. Similarly, in chromatic confocal sensing the spectral peaks from all but the first layer of a layered target are expected to be affected by spherical aberration. In some industrial applications, like the wall thickness measurement of jars, a layer thickness of several mm is common. The effect of a wall thickness up to 4.0 mm are thus studied for the two systems depicted in Figs. 5.11 and 5.19 which have target space NAs of 0.20 and 0.46. The simulations are performed for pinhole diameters of 20 µm and 50 µm. The results are shown in Fig. 5.20. For the first system with a target space NA of 0.20 the effects of the spherical aberration are too small to matter for most practical cases. However, at a target space NA of 0.46 spherical aberration has a significant impact on the spectral peak. The deteriorations are more pronounced in case of the 20 µm pinholes but are also clearly visible for the pinholes with a diameter of 50 µm. The effect of target-induced spherical aberration should thus be included in the design considerations for high-NA chromatic confocal wall thickness sensors.

5.3 Summary of Chapter 5

In this chapter practical design considerations for chromatic confocal imaging systems were presented. They are based on the common approach of decomposing the lens design process into two steps: the collinear development of starting systems and a raytracing-based optimization. The structure of the chapter reflects this two-step approach. First, the influence of the main system parameters like the numerical aperture, the lateral magnification, the LCA, and the pinhole diameter on the system performance were analyzed based on a collinear system model. The main results are summarized in Table 5.1. This Table shows multiple ways of adapting the system performance to the requirements of a specific application.

In the second part of the chapter aberration-related design aspects were considered with the help of two exemplary systems. The discussion provides insight into the main aberrations which arise during the design of chromatic confocal sensor systems and how they affect the sensor performance. A focus was put on the compensation of aberrations in post processing through appropriate calibration routines. It was shown how simple, light, and cost-effective

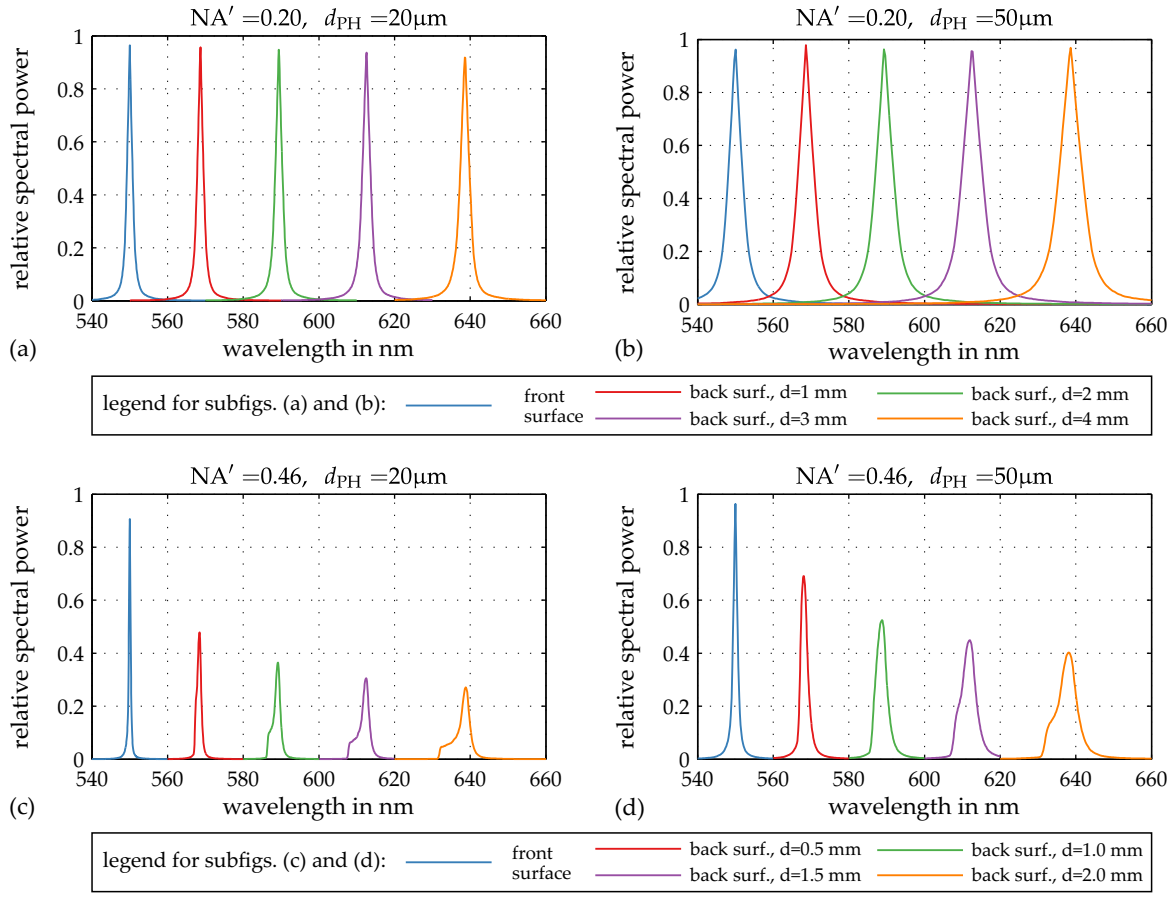

Fig. 5.20: Simulation of the spectral signals of the two refractive hyperchromats shown in Figs. 5.11 and 5.19 for pinhole diameters of 20 µm and 50 µm. Both the peaks from the front surfaces and from the back surfaces of glass plates (N-BK7) with thicknesses of 0.5-4.0 mm are calculated.

chromatic confocal imaging systems can be realized. The discussion also included aspects like the possible slope of the target or spherical aberration caused by a multi-layer target.

6 Example systems

Many of the questions discussed in the previous sections emerged during the design of chromatic confocal point sensors. Most of these sensors were developed for industrial applications and cannot be disclosed in detail. Instead, Table 6.1 lists the main parameters of these systems. All sensors were developed for macroscopic applications like wall thickness measurement of bottles and jars. They have measurement ranges of more than 10 mm and are used in fiber-based setups, see Fig. 2.17(c). The list of sensors includes refractive, diffractive, and hybrid diffractive-refractive systems which are all used in combination with an LED light source.

Chromatic confocal point sensors are discussed extensively in the literature, see Chap. 2.5.2. Here, these discussions will not be repeated. Instead, two new types of chromatic confocal multi-point sensors and two chromatic confocal hyperspectral imaging systems are presented which were developed in the context of this thesis.

Table 6.1: Overview of chromatic confocal point sensors developed in the context of this thesis. NA_{max} is the maximum target space numerical aperture and s is the working distance. N_{ROE} and N_{DOE} are the numbers of the refractive and diffractive elements, respectively. d_{max} is the maximum clear lens diameter.

NA_{max}	λ in nm	s in mm	Δs in mm	N_{ROE}	N_{DOE}	d_{max} in mm	type
0,45	430 - 630	37.3 – 52.0	14.7	8^{A}	0	56	commercial
0,29	430 - 650	51.9 – 63.2	11.3	5^{A}	0	41	commercial
0,27	460 - 640	38.6 – 51.2	12.6	2^{A}	1	24	commercial
0,27	435 - 670	64.6 – 90.6	26.0	3^{A}	1	38	commercial
0,07	550 - 640	39.4 – 66.6	27.2	1	1	8.8	research [184]
0,20	550 - 640	42.9 – 59.7	16.8	0	2	18	research [184]

[A] including protective window

6.1 Spectrally multiplexed three point sensor

Several industrial processes require the evaluation of distance or layer thickness information at a low number of lateral points but with high speed. One solution consists in the use of multiple single-point sensors. While this approach enables measurements with the speed of a point sensor, it also results in high cost as multiple sensor heads, light sources, and spectrometers are required. At the same time it is not suitable for constricted industrial environments with not enough space for multiple sensor heads. An alternative solution is to use chromatic confocal line or matrix sensors like those described in Chap. 2.5.2. However, these systems typically use a matrix detector with low frame rates. They may thus not fulfill the speed requirements

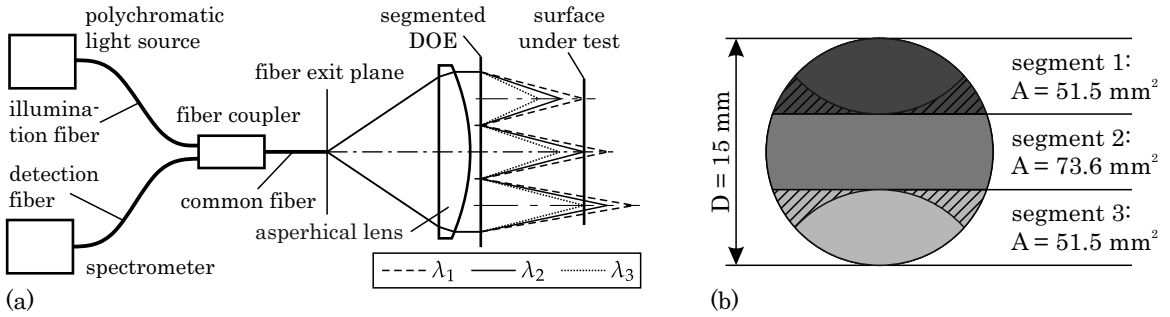

Fig. 6.1: Layouts of (a) the chromatic confocal three point sensor and (b) the segmented diffractive element which is used as a part of the hyperchromatic lens. Shaded areas do not contribute to the double pass signal [199].

of many industrial processes. In this section a new kind of spectrally multiplexed multi-point distance sensor is presented as a third solution. It is aimed at the high-speed evaluation of a low number of lateral channels (e.g. 3-5 channels) with a compact and robust system. A detailed analysis of the system is published in [199]. Below, the main results of this publication are summarized.

The layout of a spectrally multiplexed chromatic confocal sensor with three lateral channels is shown in Fig. 6.1. The sensor is closely related to the fiber-based chromatic confocal point sensor depicted in Fig. 2.17(c). It has been developed for the real-time wall thickness measurement of container glass with frame rates of up to 2 kHz. The only difference to a point sensor is that the rotationally symmetrical hyperchromatic lens is replaced by a hybrid group consisting of an aspherical lens and a segmented diffractive optical element (DOE). The layout of the DOE is shown in Fig. 6.1(b). The light cone leaving the illumination fiber is collimated by the aspherical lens. The collimated bundle is then focused at three lateral points by the three segments of the DOE. Each segment of the DOE has a different focal length. Thus, at each segment a different wavelength is in focus on a planar target. The signals reflected by the target pass the hyperchromatic lens a second time and are coupled back into the fiber which directs the signals to the spectrometer. For each lateral channel a spectral peak is generated which encodes the distance to the target. Owing to the different focal lengths of the DOE segments the three spectral peaks are centered at different wavelengths and do not overlap. They are transferred through a single fiber and are evaluated with a single-channel spectrometer.

The sensor offers several advantages: First, the sensor head does not contain any electrical or actuated parts and is linked to the illumination and detection modules through a flexible fiber. The sensor system is thus very well suited for a harsh industrial environment with small installation space. Second, as it only requires a single light source, a single fiber coupler, and a single spectrometer it can be built at the cost of a single point sensor. Third, evaluation speeds similar to those of a single-point sensor can be obtained. Fourth, the sensor is telecentric for all lateral channels. For the benefits of target space telecentricity see the discussion in Chap. 5.1.4.

A general drawback of the sensor concept is that the spectral bandwidth available for each channel is significantly lower in comparison to a single point sensor. To obtain the same measurement range with one third of the total spectral bandwidth, the LCA of the hyperchromatic lens has to be increased by a factor of 3. At the same time only one third of the spectrometer's bandwidth is available for a single channel, which can lead to a reduced axial resolution. Another restriction of the sensor concept is the reduced aperture area which is available per

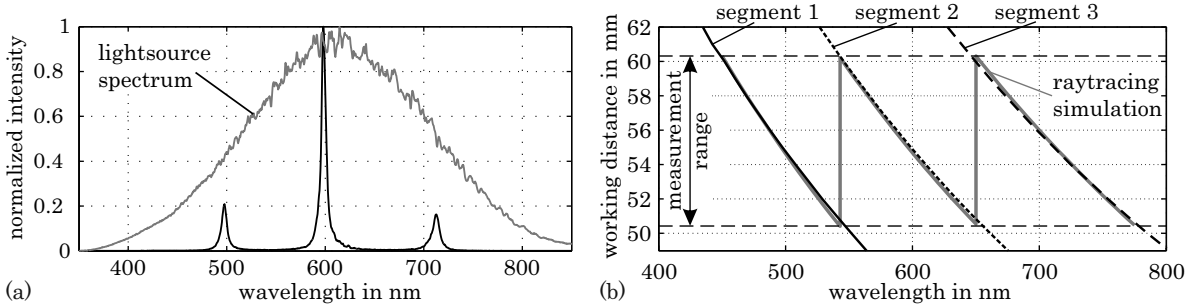

Fig. 6.2: Measurement results of the chromatic confocal three point sensor for (a) a mirror positioned at the center of the measurement range (b) a movement of the mirror through the measurement range (depth-to-wavelength coding characteristics) [199].

channel, see Fig. 6.1(b). In comparison to a single point sensor of the same diameter, the target space NA of a single channel is lower. This leads to a weaker signal and to a lower acceptable slope angle of the target.

Fig. 6.2 shows experimental results recorded with the chromatic confocal three point sensor. Fig. 6.2(a) demonstrates that the three spectral peaks are well separated. However, the outer peaks have a lower spectral power. This has four reasons: First, the area of the outer segments is smaller than the area of the central segment. Second, for a planar reflecting target perpendicular to the sensor axis a part of the reflected signal is lost, see the shaded areas in Fig. 6.1(b). Third, the outer segments use the outer parts of the light source spectrum which have a lower spectral power. Fourth, the DOE etching depth was optimized for a wavelength of 600 nm which means a lower diffraction efficiency of the outer DOE segments which operate at the outer wavelength ranges of the light source spectrum. These issues can be overcome in future sensor versions by adapting the size and shape of the DOE segments, by changing the light source, and by etching the different DOE segments individually with adapted heights. Fig. 6.2(b) illustrates the depth-to-wavelength coding characteristics of the sensor system. The experimental results agree well with the predictions of the raytracing simulations. As long as the target moves within the defined measurement range of the sensor from 50.5 mm to 60.2 mm no crosstalk between the channels can be observed.

In summary, the chromatic confocal three point sensor is a specialized tool for constricted industrial environments where a high sensor speed is essential. A reduced axial resolution and a lower signal strength are the trade-offs of the cheap, compact, robust, and flexible design. For further details on the layout or the performance parameters of the sensor system the reader is referred to [199].

6.2 Chromatic confocal matrix sensor with actuated pinhole arrays

In this section a new type of chromatic confocal matrix sensor with actuated pinhole arrays is described. The system belongs to the group of sensors with a spectrometric evaluation of the signal which is proposed in the patents [207–213]. This system type has unique features which distinguish it from the other types of chromatic confocal matrix sensors referenced in Chap. 2.5.2. On the one hand it is capable of measuring all layers of a multilayer target with a single shot. On the other hand it does not require a target-specific calibration and works independently of the reflectivity characteristics of the object.

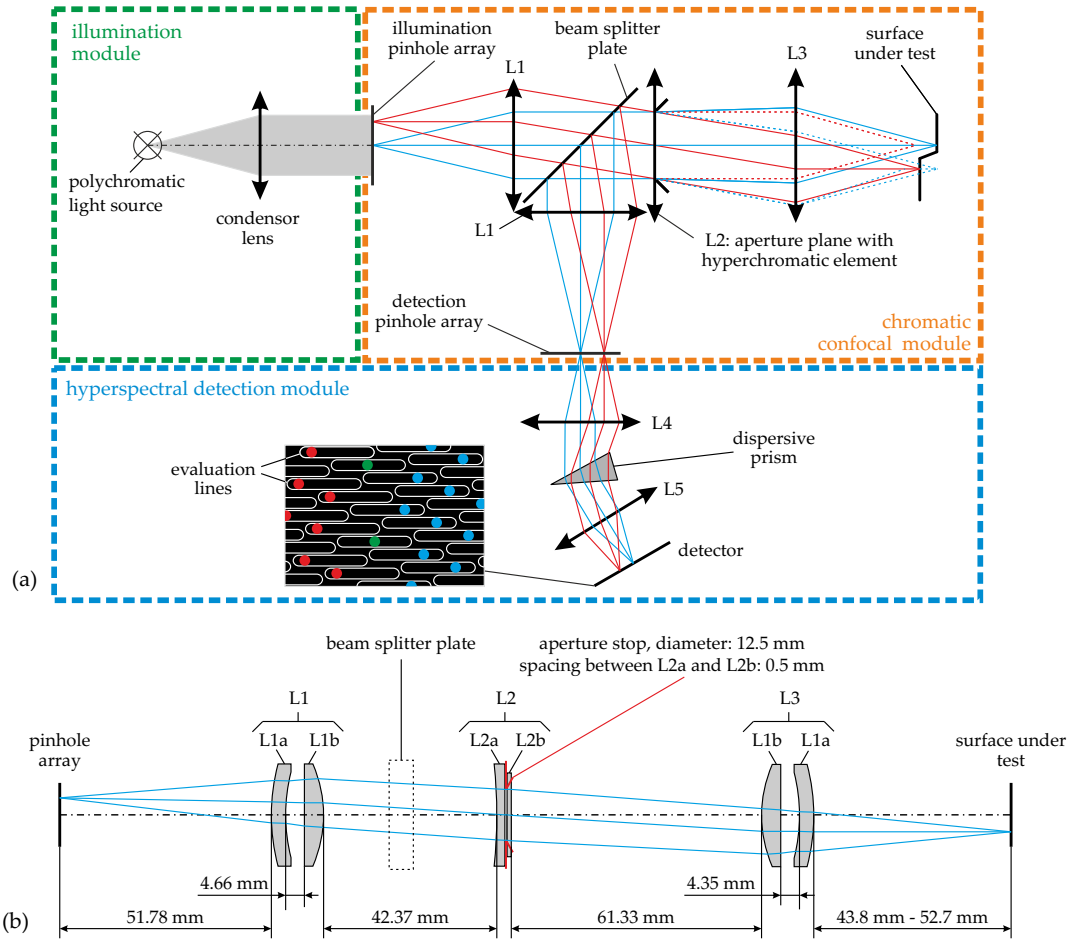

Fig. 6.3: (a) Schematic of the chromatic confocal matrix sensor and (b) detailed layout of its chromatic confocal module [235].

This section summarizes the main achievements of the system described in [235]. It is based on the observation that the systems of references [207–213] evaluate the object at a coarse grid of lateral points. The large spacing between the pinhole defining the lateral channels is required for the confocal discrimination of out of focus information. At the same time detector areas between the pinhole images are used for the lateral separation of the spectral components passing the detection pinholes. This way an array of spectrometers is implemented which enables the evaluation of the spectral distribution of the output signal. The system presented here extends the concept of [207–213] by actuated pinhole arrays. For the actuation a new kind of micromechanical inch-worm stepping drive is used. It enables a step-by-step movement of the pinhole arrays in the lateral direction to cover the areas between the original pinhole positions. After each step a frame is captured with the sensor system, thus increasing the lateral resolution at the expense of the measurement time. At any time the user is able to switch between the high-speed, low resolution snap-shot mode and the lower speed, high-resolution scanning mode. This concept opens up new fields of application and may lead to a reduced number of sensors required for process control. In industrial inspection the sensor can be used by default in the static mode for object detection. If required, it can be switched to the higher resolution scanning mode for the inspection of defects.

In [235] two sensor systems are described. The first system uses separate illumination and detection pinhole arrays. It follows the principles of the first spinning disk confocal micro-

scopes which used opposite sides of the spinning disk to realize separated illumination and detection beam paths [64, 65]. The second system implements the ideas of the spinning disk confocal microscope described in [66, 413]. It uses a single pinhole array in double pass for both, illumination and detection. Here, only the first system is discussed. It offers a better SNR at the expense of a more complex layout and small alignment tolerances. According to the layout in Fig. 6.3 the system consists of three modules: the illumination module, the chromatic confocal module, and the detection module. Detailed lens data of these modules and the paraxial system parameters are provided in [235]. Here, only the basic working principle is discussed.

The illumination module consists of a fiber bundle-based microscopy light source and realizes a homogeneous illumination of the illumination pinhole array with the required NA.

The chromatic confocal module is designed for this specific sensor system. Its elements L1b and L2a are off-the-shelf refractive lenses while the lens L1a is a custom made asphere. The lens L2a is a custom made DOE and is required for generating the LCA of the chromatic confocal module. In double pass with 50 µm pinholes the chromatic confocal module is characterized by a spectral FWHM of 7.4 - 7.8 nm across a field with maximum extent $y = 4.15\,\mathrm{mm}$. It has an axial measurement range of 8.9 mm with the minimum wavelength $\lambda_{\mathrm{min}} = 450\,\mathrm{nm}$ and the maximum wavelength $\lambda_{\mathrm{max}} = 650\,\mathrm{nm}$. To achieve target space telecentricity, the lens group L2, which contains the aperture stop, is positioned at the focal plane of the lens group L3. At λ_{ref} the two lenses L2a and L2b have focal lengths of the same magnitude but of the opposite sign. Hence, the lens group L2 has zero focal power at λ_{ref}. A similar setup is e.g. described in [207, 210, 215]. To modify the measurement range of the chromatic confocal module, the lens group L2 can be replaced by a similar group with different spectral properties. In total, four systems were designed which generate measurement ranges between 2.5 mm and 12.5 mm.

To minimize development costs, the hyperchromatic detection system is built from off-the shelf components. It uses the working principle of [208–210]. The signals passing the detection pinhole array are first collimated by the lens L4. In the second step they pass a dispersive prism which deflects the spectral components into different directions. The lens L5 then focuses the spectral components at different lateral positions on a pixelated detector. The line of possible spectral locations, which exists for each pinhole, is called evaluation line. The pixel positions are related to the wavelength of the spectral peak generated by the chromatic confocal module. Each pixel position corresponds to a specific distance between the sensor system and the surface under test. By evaluating all lines in parallel, a snapshot chromatic confocal matrix sensor with hyperspectral detection is implemented. If individual calibration curves are recorded for all lateral channels, the field curvature of the hyperchromatic lens can be compensated in post processing. To increase the allowed length of the detection lines and to fully use the detector area, the pinhole arrays can be rotated with respect to the dispersive prism and the detectors [208, 209, 414]. For quantitative experiments a monochrome camera is used. Additionally, a RGB camera is used in several qualitative experiments to visualize the spectral properties of the sensor system. The parameters of both cameras are given in [235].

To increase the lateral resolution of the sensor system, actuated pinhole arrays are included in the chromatic confocal module. They implement a displacement range of 200 µm and a step size of approx. 13 µm. To shift the pinhole arrays which have a size of $5.5 \times 7\ \mathrm{mm}^2$ a new kind of inch-worm stepping drive was developed at the Fachgebiet Mikromechanische Systeme at TU Ilmenau [415]. These actuators have a chip size of $10 \times 10 \times 0.5\ \mathrm{mm}^3$ and are well suited for future miniaturizations of chromatic confocal sensor systems. The working principle and the parameters of the actuators are provided in [235]. Here, it is sufficient to note that a single

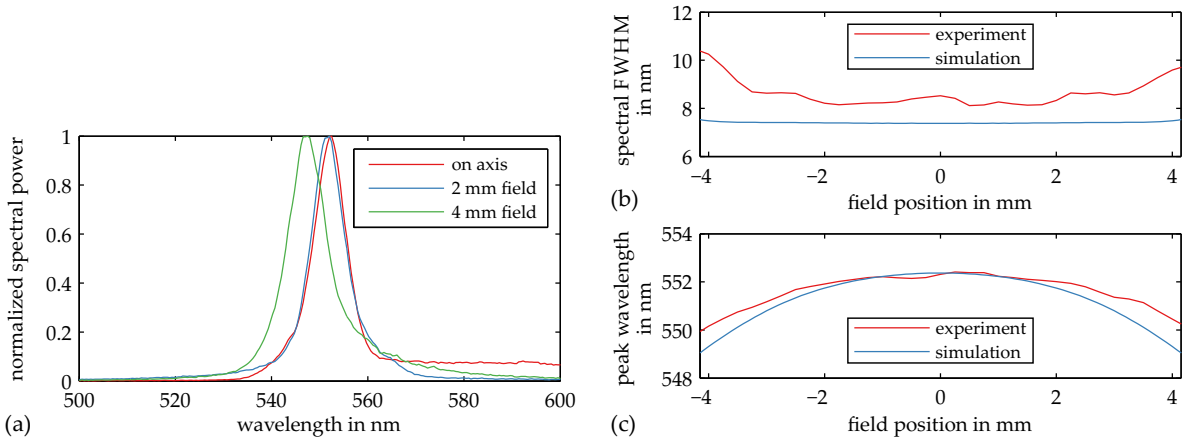

Fig. 6.4: Imaging performance of the chromatic confocal system. (a) Spectral peaks measured at different field positions. (b) Field-dependent FWHM of the spectral peak. (c) Field-dependent center wavelength of the spectral peak [235].

step is performed within 196 ms while the monochrome camera has a continuous frame rate of 3.2 frames per second. The full actuation can thus be performed during the readout times of the camera and does not affect the frame rate of the sensor system. The acquisition of the object volume with 15 actuator positions takes approx. 5 s. With a pinhole diameter of 20 µm and a pinhole spacing of 65 µm it produces distance information from approx. 135,000 lateral points or approx. 27,000 points per second. For comparison, chromatic confocal point sensors can have a frame rate of several kHz but only record a single lateral channel.

Fig. 6.4 shows the results of a quantitative characterization of the chromatic confocal module. The results are produced in a fiber-based setup according to Fig. 2.17(c) where the chromatic confocal module is used as the lens and a planar mirror is used as the target. A GRIN fiber with a core diameter of 50 µm is shifted across the field and the spectral peak is recorded with a spectrometer. Fig. 6.4(a) shows the spectral peak at different peak positions. The side lobe of the on-axis signal is not present in the simulations and is assumed to be caused by fabrication and alignment errors. Using a different alignment strategy it can be eliminated at the expense of a worse off-axis performance. In Fig. 6.4(b) and Fig. 6.4(c) the measured FWHM of the spectral peak and the position of its maximum are compared to the simulated values. Across the field the measured FWHM values stay below 1.5 times the simulated on-axis performance. This is considered a good system performance. The small differences between the predicted and measured field curvature can be easily compensated through an appropriate calibration procedure.

Fig. 6.5 shows the evaluation lines on the detector of the full sensor system for two different sets of pinhole arrays. It is produced by illuminating the detection pinhole arrays with a white light source. The first set of pinhole array contains pinholes with a diameter of 40 µm and with a spacing of 200 µm. The horizontal axis of the arrays corresponds to the direction of the evaluation lines. The pinholes of the second set have a diameter of 20 µm and are spaced at a distance of 65 µm. To efficiently use the detector area, the pinhole arrays are tilted by 20 degrees with respect to the direction of the evaluation lines. The second set is designed to be used with the micromechanical actuators. Fig. 6.6 illustrates how the target can be imaged at a higher lateral resolution by enabling the actuators. A drawback of the second set of pinhole arrays is a lower confocal discrimination of out-of-focus objects, see e.g. [142]. It leads to a

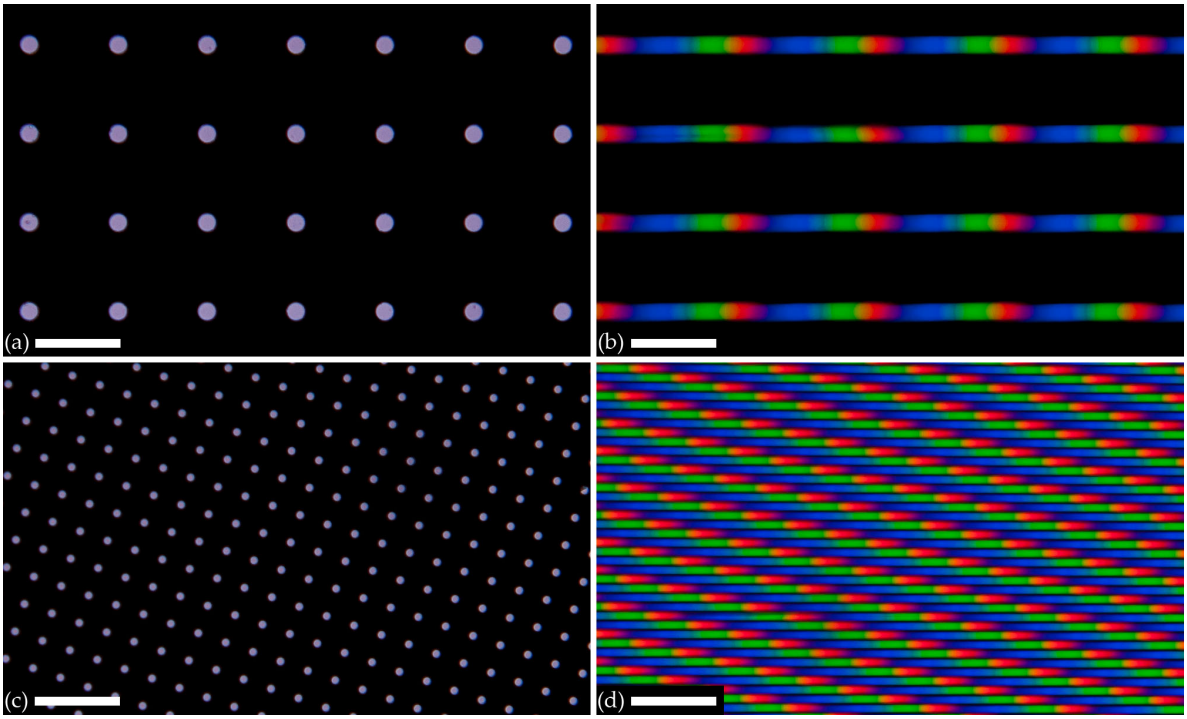

Fig. 6.5: Images of the used pinhole arrays and of the corresponding evaluation lines on the detector. The two detection pinhole arrays shown in Subfigs. (a) and (c) were imaged without the dispersive prism. The evaluation lines shown in Subfigs. (b) and (d) were captured with the dispersion prism in the optical path. Scale bars = 200 µm [235].

lower SNR and can only be used for objects with high reflectivity. The experiments discussed below are thus performed with the first set of pinhole arrays.

The axial resolution of the sensor system can be estimated from the length of the evaluation line on the monochrome detector. It covers 112 pixels with the first and 130 pixels with the second set of pinhole arrays and corresponds to an axial measurement range of 8.4 mm. Under the assumption of a linear relation between the target distance and the pixel position on the detector one detector pixel corresponds to an axial distance increment of 75 µm and 65 µm. These values are by a factor of 16 to 18 larger than those of a point sensor with 2048 spectrometer pixels assigned to the single channel. However, several thousand lateral channels are evaluated in parallel.

Fig. 6.7 shows two exemplary measurements performed with the sensor system. In the first example of Fig. 6.7(a) a three-step staircase profile build from pieces of a polished silicon wafer is imaged with the RGB camera. The three height level result in three different colors of the spectral peak. As the target for the second example a SiO_2 wafer is used. Both the front and the back surface cause a spectral peak. The two peaks are spectrally shifted and visible in Fig. 6.7(b). From the peak distance a waver thickness of 2.070 mm is determined without sub-pixel peak detection. In contrast, the mechanical reference measurement with a micrometer caliper, (Mitutoyo 293-240, 1 µm accuracy, standard deviation of 1.5 µm for 200 measurements) gives a thickness of 2.013 mm. The measurement error of 57 µm is caused by the low image quality of the hyperspectal detection module, the calibration routine, and the evaluation algorithm. It can be reduced with a sub-pixel peak finding algorithm.

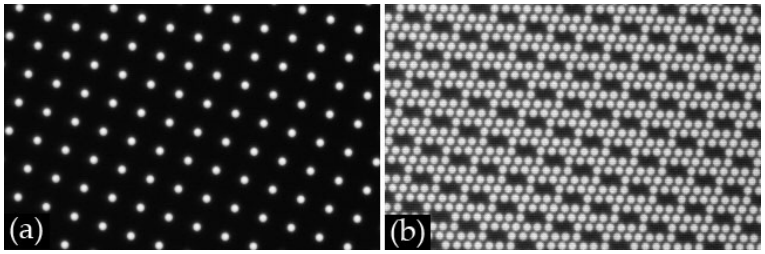

Fig. 6.6: Improved lateral resolution with actuated pinhole arrays. (a) Field points covered by the static pinhole arrays. (b) Overlay of seven discrete field positions covered by the actuated pinhole arrays. In both cases the detection pinhole array was imaged without the dispersive prism onto the detector. Using two additional actuator positions, which are not shown for explanatory reasons, the rectangular black areas in Subfig. (b) can also be sampled [235].

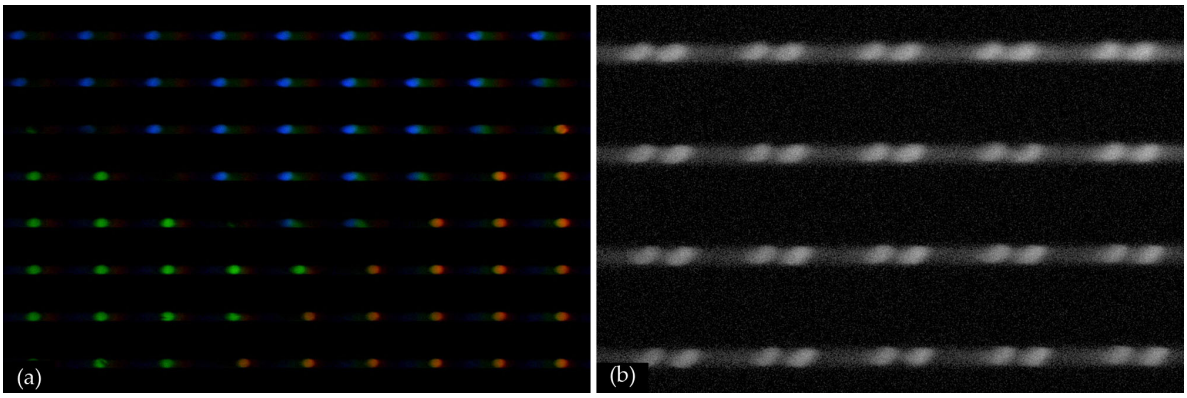

Fig. 6.7: Exemplary measurements of (a) a staircase profile build from three pieces of a silicon wafer and (b) a transparent SiO_2 wafer with a thickness of 2.084 mm. In both cases the static background signal caused by the beam splitter plate were subtracted. To increase the contrast, the pixel values of Subfig. (a) were multiplied by a factor of 1.8 and those of Subfig. (b) by a factor of 5 [235].

In recapitulation, this section describes a new kind of chromatic confocal matrix sensor. It is based on a spectrometric evaluation of the chromatic confocal signal and works independently of the spectral characteristics of the target. At the same time it is capable of evaluating targets with multiple reflecting layers. Previous versions of this sensor type which are proposed in the patent literature require a balancing between lateral and axial resolution. A larger pinhole spacing means that more detector pixels can be assigned for the spectral evaluation of a single channel. The axial resolution is increased at the expense of the lateral resolution which is linked to the pinhole distance. In the newly proposed sensor this restriction is overcome by the use of a micromechanical actuator which enables a movement of the pinhole arrays in discrete steps. This way the lateral resolution can be decoupled from the axial resolution. For a given axial resolution, an increased lateral resolution can be obtained at the expense of the evaluation time. The possibility of enabling and disabling the actuators upon requirement enables new types of multi-purpose sensors. In the experiments the matrix sensor worked as expected and the snap-shot evaluation of wafer thicknesses was demonstrated. Currently, the sensor performance is mainly limited by the hyperspectral detection module and by the evaluation algorithms.

6.3 Hyperspectral imaging systems with actuated lenses

In Chap. 2.6 hyperspectral imaging (HSI) was introduced as the acquisition of spectrally and spatially resolved information. The application of chromatic confocal HSI systems was one of the main research areas within the project "Optical Microsystems for hyperspectral sensing (OpMiSen)" funded by the Bundesministerium für Bildung und Forschung. The main work in this project was done by researchers at Ilmenau University of Technology and University of Freiburg with only minor contributions by the author of this thesis. Some of the findings of the project are included here to show another promising field of application for chromatic confocal imaging systems. This section provides a short summary of two systems published in [233, 234].

The two systems are closely related to the principle described in Chap. 2.6. Instead of the detection pinhole array a pixelated detector with generalized detection pixels is used. In both cases the axial movement of the detector is replaced by tuning the focal length of the hyperchromatic lens. Fig. 6.8 shows the layout of the system published in [233]. The system uses a diffractive Alvarez-Lohmann lens pair for the focal length tuning. To alter the wavelength in focus on the detector, the Alvarez-Lohmann lenses are shifted laterally with respect to each other. The second system realizes the focal length tuning with a tunable fluidic lens and is shown in Fig. 6.9. The simulated spectral filtering characteristics of the two lens systems are presented in Fig. 6.10. For further details the reader is referred to [233, 234]. In both cases the FWHM of the spectral peaks is larger than 7 nm. In principle it can be reduced to less than 1 nm by altering the diameter of the pinholes, the numerical aperture of the hyperchromatic lens, or the LCA of the hyperchromatic lens. This way scanning chromatic confocal HSI systems with high spectral resolution can be implemented. To increase the lateral resolution, the static illumination pinhole array can be replaced with an actuated pinhole array like the one discussed in [235].

6.4 Summary of Chapter 6

In this chapter several chromatic confocal imaging systems were presented. All systems extent the state of the art and are published in recognized journals. They cover the applications of multi-point distance sensing and hyperspectral imaging. With an LCA of several mm all systems operate on a macroscopic scale and are built from custom made components. To obtain a compact setup with a minimum number of optical elements, the systems include diffractive elements for the generation of the LCA. Following the design concepts of Chap. 5 they are not aimed at a minimization of all monochromatic aberrations. Instead, residual aberrations like field curvature or distortion are compensated using appropriate calibration procedures or by varying the position of the generalized detection pixels of the pixelated detector. This way compact systems with minimum weight, size, and cost are realized.

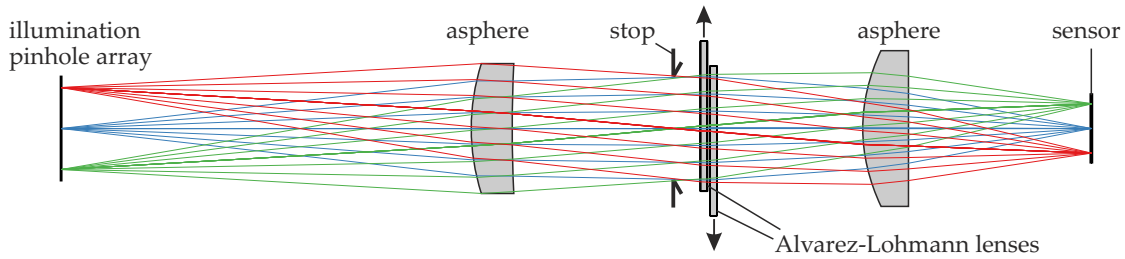

Fig. 6.8: Layout of the chromatic confocal HSI system with focus tuning through a lateral shift of phase plates [233].

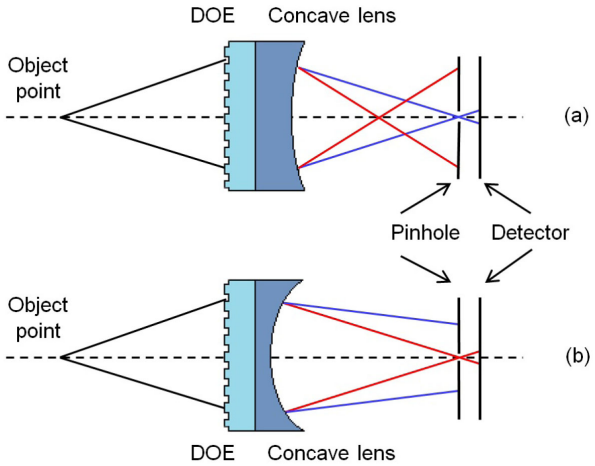

Fig. 6.9: Schematic of the chromatic confocal HSI system with focus tuning through a fluidic lens [234].

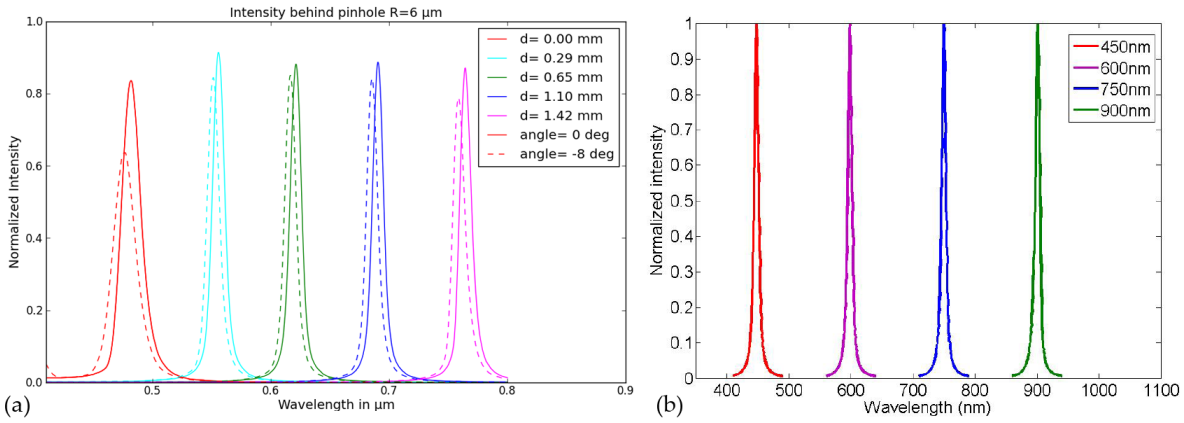

Fig. 6.10: Simulated spectral filtering characteristics of the HSI systems with (a) the Alvarez-Lohmann phase plates [233] and (b) the fluidic lens [234].

7 Summary and outlook

This thesis addresses the question of how to efficiently design application specific chromatic confocal imaging systems. It builds upon prior publications like [172] which are mainly focused on the metrological characteristics of chromatic confocal distance sensors. Aspects like the sub-pixel evaluation of the sensor's spectral peak or the measurement uncertainty are thus excluded from the discussion. Instead, this thesis provides the optical designer with a set of tools which assist him in finding solutions with minimum cost, size, and weight.

As the starting point the two-step lens design process is considered which consists of the generation of a starting system followed by its raytracing-based optimization. The generation of starting systems requires knowledge of both the state of the art and of the methods for manipulating the spectral components of an optical signal. This information is provided in Chap. 2 together with an overview of the system models used in the later chapters.

Of similar importance is a meaningful performance criterion which is available at all stages of the design process. Throughout this thesis the spectral peak of the chromatic confocal system is used as the main performance criterion. On the one hand it is shown how the spectral peak relates to the axial or spectral resolution of the sensor system. On the other hand a new set of signal models is derived which integrates well with the two-step lens design process. It is discussed in Chap. 4 and consist of a collinear, a geometrical, and a wave optical model. All signal models assume incoherently radiating illumination pinholes of finite size and are thus compatible with LED-powered sensor systems. The geometrical and wave optical models include the effects of aberrations and vignetting. The wave optical model also includes diffraction effects and is the most complex of the three models. It requires the numerically challenging calculation of focal fields at heavily defocused planes. In Chap. 3 different numerical calculation approaches are evaluated. Especially the commonly used FFT-based methods are discussed in detail. To overcome the main limitations of these methods a new set of sampling criteria and a new focal field calculation method are derived. In result, the optical designer is provided with fast and flexible tools for calculating the shape of the spectral peak at the different stages of the lens design process. The predictions of these tools agree well with experimental results.

Another essential aspect of the lens design process is a clear understanding of how the collinear system parameters and the monochromatic aberrations influence the shape of the spectral peak and the resolution of the sensor system. This question is addressed in Chap. 5. First, the collinear signal model is used to analyze the impact of parameters like the numerical aperture, the pinhole size, and the lateral magnification. The results are summarized in a concise table which shows the optical designer the main ways of modifying the performance of the starting system. In the second part of Chap. 5 the influence of monochromatic aberrations on the performance of single and double pass systems is evaluated. A specific focus is on the identification of aberrations which are harmless in double pass setups or can be compensated in post processing. By excluding the minimization of these aberrations from the optimization, solutions with low complexity and with a minimum number of elements can be found.

Finally, several chromatic confocal sensor systems are presented in Chap. 6. All of these systems have a longitudinal chromatic aberration of several mm and operate on a macroscopic scale. Following the design concepts of Chap. 5, they use a minimum number of optical components. First, a spectrally multiplexed distance sensor is presented which has the size of a single-point sensor but records the distance information from three lateral points in parallel and transfers it through a single optical fiber. Second, a chromatic confocal matrix sensor with spectrometric signal evaluation is introduced which uses micromechanically actuated pinhole arrays. The sensor can be used in two modes, a static snapshot mode and a dynamic scanning mode with increased lateral resolution. Third, two chromatic confocal hyperspectral imaging systems are presented. They are based on hyperchromatic lenses with tunable focal lengths which image an illumination pinhole array onto a pixelated detector. The focal length tuning is realized with either a fluidic lens or with an Alvarez-Lohmann lens pair.

With exception of some of the results of Chap. 5 which were obtained only recently, all major findings of this thesis are published in renowned journals and are available to a large audience. While these results do not enable a fully automated design of chromatic confocal sensor systems they are expected to simplify the design process of future chromatic confocal sensor systems.

At the same time there is still plenty of room for further research in the field of chromatic confocal imaging systems. The following list provides several exemplary topics:

- Extension of the signal models and design approaches to related imaging systems and measurement principles like chromatic confocal spectral interferometry.
- Extension of the signal models to chromatic confocal line sensors.
- Design of double pass hyperspectral imaging systems to enhance the spectral filtering characteristics and to use the aberration balancing effects of double pass setups.
- Design of chromatic confocal systems for very broadband sources like supercontinuum lasers which start to become available at a competitive price. This topic also includes the development of efficiency achromatized DOEs which offer a high diffraction efficiency over a broad wavelength range, see [39].
- Development of optimized alignment strategies for chromatic confocal sensor systems which derive the alignment state of the system from the field-dependent shape of the spectral peak.
- Development of chromatic confocal multi-channel sensor modules which use 3D pinhole arrays or segmented DOEs to test for specific spectral distributions. Each lateral channel is configured for one specific spectral component of the input signal.

8 Own publications

Journal publications

[1] P. A. Santi, S. B. Johnson, M. Hillenbrand, et al. “Thin-sheet laser imaging microscopy for optical sectioning of thick tissues”. In: *Biotechniques* 46.4 (2009), p. 287.

[2] M. Hillenbrand, B. Mitschunas, C. Wenzel, et al. “Hybrid hyperchromats for chromatic confocal sensor systems”. In: *Adv. Opt. Technol.* 1.3 (2012), pp. 187–194.

[3] R. H. Abd El-Maksoud, M. Hillenbrand, S. Sinzinger, and J. Sasian. “Optical performance of coherent and incoherent imaging systems in the presence of ghost images”. In: *Appl. Opt.* 51.30 (2012), pp. 7134–7143.

[4] R. H. Abd El-Maksoud, M. Hillenbrand, and S. Sinzinger. “Parabasal theory for plane-symmetric systems including freeform surfaces”. In: *Opt. Eng.* 53.3 (2013), p. 031303.

[5] M. Hillenbrand, L. Lorenz, R. Kleindienst, et al. “Spectrally multiplexed chromatic confocal multipoint sensing”. In: *Opt. Lett.* 38.22 (2013), pp. 4694–4697.

[6] P.-H. Cu-Nguyen, A. Grewe, M. Hillenbrand, et al. “Tunable hyperchromatic lens system for confocal hyperspectral sensing”. In: *Opt. Express* 21.23 (2013), pp. 27611–27621.

[7] A. Grewe, M. Hillenbrand, and S. Sinzinger. “Bildgebende hyperspektrale Sensorik unter Einsatz verstimmbarer Optiken”. In: *Photonik* 45.1 (2013), pp. 20–23.

[8] A. Grewe, M. Hillenbrand, and S. Sinzinger. “Hyperspectral imaging sensor systems using tunable lenses”. In: *Phot. Int.* 8 (2013), pp. 20–23.

[9] M. Hillenbrand, A. Hoffmann, D. P. Kelly, and S. Sinzinger. “Fast non-paraxial scalar focal field calculations”. In: *J. Opt. Soc. Am. A* 31.6 (2014), pp. 1206–1214.

[10] M. Hillenbrand, D. P. Kelly, and S. Sinzinger. “Numerical solution of nonparaxial scalar diffraction integrals for focused fields”. In: *J. Opt. Soc. Am. A* 31.8 (2014), pp. 1832–1841.

[11] A. Grewe, M. Hillenbrand, and S. Sinzinger. “Aberration analysis of optimized Alvarez–Lohmann lenses”. In: *Appl. Opt.* 53.31 (2014), pp. 7498–7506.

[12] M. Hillenbrand, B. Mitschunas, F. Brill, et al. “Spectral characteristics of chromatic confocal imaging systems”. In: *Appl. Opt.* 53.32 (2014), pp. 7634–7642.

[13] M. Hillenbrand, R. Weiß, C. Endrödy, et al. “Chromatic confocal matrix sensor with actuated pinhole arrays”. In: *Appl. Opt.* 54.15 (2015), pp. 4927–4936.

[14] Y. Wu, M. Hillenbrand, L. Zhao, et al. “Fresnel transform as a projection onto a Nijboer–Zernike basis set”. In: *Opt. Lett.* 40.15 (2015), pp. 3472–3475.

Conference contributions

[1] M. Hillenbrand, B. Mitschunas, and S. Sinzinger. “Chromatic aberration theory in modern metrology”. In: *Proc. DGaO* (2009), P1.

[2] M. Hillenbrand, S. B. Johnson, P. A. Santi, and S. Sinzinger. “Thin Sheet Laser Imaging Microscopy”. In: *Proc. DGaO* (2009), P50.

[3] M. Hillenbrand, M. Zhao, B. Mitschunas, and S. Sinzinger. “Untersuchungen zur Genauigkeit NURBS-basierter optischer Freiformflächen”. In: *Proc. DGaO* (2010), P36.

[4] M. Hillenbrand, R. H. Abd El-Maksoud, B. Mitschunas, and S. Sinzinger. “Optische Systeme ohne Rotationssymmetrie: Bestimmung von Bildlage und Bildorientierung”. In: *Proc. DGaO* (2011), B12.

[5] M. Hillenbrand, E. Markweg, M. Hoffmann, and S. Sinzinger. “Integrated Hybrid GRIN Lenses”. In: *Proc. DGaO* (2011), P5.

[6] R. H. Abd El-Maksoud, M. Hillenbrand, and S. Sinzinger. “Measuring the refractive index of double-clad fibers using an interferometric technique”. In: *Proc. DGaO* (2011), P32.

[7] R. H. Abd El-Maksoud, M. Hillenbrand, and S. Sinzinger. “Ghost images for optical systems with tilted object plane”. In: *Proc. DGaO* (2011), P38.

[8] J. Werner, M. Zhao, M. Hillenbrand, and S. Sinzinger. “RBF-based optical surfaces”. In: *Proc. DGaO* (2011), P39.

[9] A. Grewe, R. H. Abd El-Maksoud, M. Hillenbrand, and S. Sinzinger. “Optimized tunable Alvarez-Lohmann-Lenses”. In: *Proc. DGaO* (2011), B35.

[10] M. Hillenbrand, B. Mitschunas, S. Homberg, and S. Sinzinger. “Novel vision aids for people suffering from Age-Related Macular Degeneration”. In: *Proc. DGaO* (2012), B28.

[11] A. Grewe, M. Hillenbrand, and S. Sinzinger. “Adaptive confocal approach to hyperspectral imaging”. In: *Proc. EOS Annual Meeting 2012* (2012).

[12] M. Hillenbrand, C. Wenzel, X. Ma, et al. “Hyperchromatic Confocal Sensor Systems”. In: *Proc. 8th EOS Topical Meeting on Diffractive Optics* (2012).

[13] J. Werner, M. Hillenbrand, A. Hoffmann, and S. Sinzinger. “Automatic differentiation in the optimization of imaging optical systems”. In: *Schedae informaticae* 21 (2012), pp. 169–175.

[14] M. Hillenbrand, A. Grewe, M. Bichra, et al. “Chromatic information coding in optical systems for hyperspectral imaging and chromatic confocal sensing”. In: *Proc. SPIE* 8550 (2012), p. 85500D.

[15] E. Markweg, M. Hillenbrand, S. Sinzinger, and M. Hoffmann. “Planar plano-convex microlens in silica using ICP-CVD and DRIE”. In: *Proc. SPIE* 8550 (2012), 85500T.

[16] M. Hillenbrand, A. Grewe, M. Bichra, et al. “Parallelized chromatic confocal sensor systems”. In: *Proc. SPIE* 8788 (2013), p. 87880V.

[17] A. Grewe, M. Hillenbrand, and S. Sinzinger. “Hyperspektales Abbildungssystem unter Verwendung verstimmbarer Alvarez-Lohmann Linsen”. In: *Proc. DGaO* (2013), A7.

[18] J. Werner, M. Hillenbrand, M. Zhao, and S. Sinzinger. “An optimization method for radial NURBS surfaces”. In: *Proc. DGaO* (2013), P54.

[19] X. Ma, A. Grewe, M. Hillenbrand, et al. “Entwicklung eines integrierten multifunktionalen Fluoreszenzdetektors”. In: *Proc. DGaO* (2013), P47.

[20] S. Sinzinger, M. Hillenbrand, and Rania H. Abd-El Maksoud. “Freeform Surfaces in Optical Microsystems: From Parabasal Theory to Applications”. In: *Renewable Energy and the Environment*. Optical Society of America, 2013, FM2B.4.

[21] A. Grewe, M. Hillenbrand, D. Hoffmann, et al. “Fabrication and Replication of Telescope Arrays for Vision Aids”. In: *OSA Technical Digest*. Ed. by Optical Society of America. OSA Technical Digest (online). Kohala Coast, Hawaii: Optical Society of America, 2014, OTu3B.4.

[22] M. Hillenbrand, A. Grewe, B. Mitschunas, et al. “Arrayoptiken - Entwurf, Fertigung und Anwendungen”. In: *Proc. DGaO* (2014), P26.

[23] B. Mitschunas, M. Hillenbrand, and S. Sinzinger. “Miniaturisierte Sehhilfen für AMD Patienten”. In: *Proc. DGaO* (2014), P25.

[24] F. Brill, M. Hillenbrand, A. Grewe, et al. “Vergleich von Signalerzeugungsmodellen für chromatisch-konfokale Sensoren”. In: *Proc. DGaO* (2014), B34.

[25] R. Weiß, R. Kirner, M. Hillenbrand, et al. “Parallelisierte chromatisch-konfokale Profilometrie mit einem Mehrkanalspektrometer”. In: *Proc. DGaO* (2014), A35.

[26] A. Grewe, M. Hillenbrand, and S. Sinzinger. “Hyperspektales Abbildungssystem unter Verwendung verstimmbarer Alvarez-Lohmann Linsen”. In: *Proc. DGaO* (2014), A7.

[27] M. Hillenbrand, B. Mitschunas, D. Hoffmann, et al. “Miniaturized AMD vision aids: principles and realization”. In: *Proc. IWK (Ilmenau Scientific Colloquium)* (2014).

[28] A. Grewe, M. Hillenbrand, and S. Sinzinger. “Imaging systems with Alvarez-Lohmann lenses”. In: *Proc. IWK (Ilmenau Scientific Colloquium)* (2014).

[29] M. Rosenberger, M. Correns, R. Fütterer, et al. “Hyper- and multispectral imaging systems - a survey of different approaches at the Ilmenau University of Technology”. In: *Proc. IWK (Ilmenau Scientific Colloquium)* (2014).

Patents and patent applications

[1] M. Hillenbrand, S. Sinzinger, and B. Mitschunas. “Vision aid for manipulating the retinal image for eyes having macular degeneration”. WO 2014/082998 A1. 2014.

[2] M. Hillenbrand, L. Lorenz, M. Bichra, et al. “Chromatic Confocal Multi-point measurement method and device and use of said device”. DE 102013008582B4. 2015.

Bibliography

[1] I. N. Bronstein and K. A. Semendjajew. *Taschenbuch der Mathematik*. 5th ed. Thun [u.a.]: Deutsch, 2001.

[2] H. Haferkorn. *Bewertung optischer Systeme*. Berlin: Dt. Verl. d. Wiss, 1985.

[3] H. Haferkorn. *Optik. Physikalisch-technische Grundlagen und Anwendungen*. 4th ed. Weinheim: Wiley-VCH, 2003.

[4] J. E. Greivenkamp. *Field guide to geometrical optics*. Vol. 1. SPIE field guides. Bellingham, Wash.: SPIE Press, 2004.

[5] M. Born, E. Wolf, and A. Bhatia. *Principles of optics: Electromagnetic theory of propagation, interference and diffraction of light*. 7th ed. Cambridge: Cambridge University Press, 2005.

[6] R. Kingslake and R. B. Johnson. *Lens design fundamentals*. 2nd ed. London: Academic, 2010.

[7] B. Richards and E. Wolf. "Electromagnetic diffraction in optical systems: II. Structure of the image field in an aplanatic system". In: *Proc. Roy. Soc. Lond. A Mat.* 253 (1959), pp. 358–379.

[8] J. J. Braat, S. van Haver, A. J. E. M. Janssen, and P. Dirksen. "Assessment of optical systems by means of point-spread functions". In: *Progress in Optics* 51 (2008).

[9] J. W. Goodman. *Introduction to Fourier optics*. 3rd ed. Englewood and Colo: Roberts & Co. Publishers, 2005.

[10] J. J. Stamnes. *Waves in focal regions: Propagation, diffraction and focusing of light, sound and water waves*. The Adam Hilger series on optics and optoelectronics. Bristol: Hilger, 1986.

[11] C. J. Bouwkamp. "Diffraction Theory". In: *Rep. Prog. Phys.* 17.1 (1954), p. 35.

[12] O. K. Ersoy. *Diffraction, fourier optics and imaging*. Vol. v.30. Wiley Series in Pure and Applied Optics. Hoboken, NJ: Wiley-Interscience, 2007.

[13] T. M. Kreis, M. Adams, and Jüptner, Werner P. O. "Methods of Digital Holography: A Comparison". In: *Proc. SPIE* 3098 (1997), pp. 224–233.

[14] N. Delen and B. Hooker. "Free-space beam propagation between arbitrarily oriented planes based on full diffraction theory: a fast Fourier transform approach". In: *J. Opt. Soc. Am. A* 15.4 (1998), pp. 857–867.

[15] N. Delen and B. Hooker. "Verification and Comparison of a Fast Fourier Transform-Based Full Diffraction Method for Tilted and Offset Planes". In: *Appl. Opt.* 40.21 (2001), pp. 3525–3531.

[16] F. B. Shen and A. B. Wang. "Fast-Fourier-transform based numerical integration method for the Rayleigh-Sommerfeld diffraction formula". In: *Appl. Opt.* 45.6 (2006), pp. 1102–1110.

[17] G. C. Sherman. "Application of the Convolution Theorem to Rayleigh's Integral Formulas". In: *J. Opt. Soc. Am.* 57.4 (1967), pp. 546–547.

[18] L. Mandel and E. Wolf. *Optical coherence and quantum optics*. Reprint. with corr. Cambridge: Cambridge Univ. Press, 2008.

[19] D. G. Voelz and M. C. Roggemann. "Digital simulation of scalar optical diffraction: revisiting chirp function sampling criteria and consequences". In: *Appl. Opt.* 48.32 (2009), pp. 6132–6142.

[20] M. Hillenbrand, D. P. Kelly, and S. Sinzinger. "Numerical solution of nonparaxial scalar diffraction integrals for focused fields". In: *J. Opt. Soc. Am. A* 31.8 (2014), pp. 1832–1841.

[21] H. H. Hopkins. "Calculation of the Aberrations and Image Assessment for a General Optical System". In: *Opt. Act.* 28.5 (1981), pp. 667–714.

[22] P. Debye. "Das Verhalten von Lichtwellen in der Nähe eines Brennpunktes oder einer Brennlinie". In: *Ann. Phys. Berlin* 335.14 (1909), pp. 755–776.

[23] E. Wolf and Y. Li. "Conditions for the validity of the Debye integral representation of focused fields". In: *Opt. Commun.* 39.4 (1981), pp. 205–210.

[24] Y. Li and E. Wolf. "Three-dimensional intensity distribution near the focus in systems of different Fresnel numbers". In: *J. Opt. Soc. Am. A* 1.8 (1984), pp. 801–808.

[25] G. H. Spencer and Murty, M. V. R. K. "General Ray-Tracing Procedure". In: *J. Opt. Soc. Am.* 52.6 (1962), pp. 672–676.

[26] F. Zernike. "Beugungstheorie des Schneidenverfahrens und seiner verbesserten Form, der Phasenkontrastmethode". In: *Physica* 1.7 (1934), pp. 689–704.

[27] D. Malacara and Z. Malacara. *Handbook of optical design*. 2nd ed. New York: Dekker, 2004.

[28] W. Besenmatter. "The Optical Level System". In: *Opt. Act.* 26.11 (1979), pp. 1377–1388.

[29] B. Mitschunas. "Methodische Unterlagen zum Ansatz pankreatischer Systeme". PhD thesis. Technische Universität Ilmenau, 1986.

[30] Sellmeier. "Zur Erklärung der abnormen Farbenfolge im Spectrum einiger Substanzen". In: *Ann. Phys. Berlin* 219.6 (1871), pp. 272–282.

[31] S. Sinzinger and J. Jahns. *Microoptics*. 2nd ed. Weinheim: Wiley-VCH, 2003.

[32] P. Lalanne, S. Astilean, P. Chavel, et al. "Design and fabrication of blazed binary diffractive elements with sampling periods smaller than the structural cutoff". In: *J. Opt. Soc. Am. A* 16.5 (1999), pp. 1143–1156.

[33] H. Dammann. "Spectral characteristic of stepped-phase gratings". In: *Optik* 53.5 (1979), pp. 409–417.

[34] D. A. Pommet, M. G. Moharam, and E. B. Grann. "Limits of scalar diffraction theory for diffractive phase elements". In: *J. Opt. Soc. Am. A* 11.6 (1994), pp. 1827–1834.

[35] S. M. Ebstein. "Nearly index-matched optics for aspherical, diffractive, and achromatic-phase diffractive elements". In: *Opt. Lett.* 21.18 (1996), pp. 1454–6.

[36] Y. Arieli, S. Ozeri, N. Eisenberg, and S. Noach. "Design of a diffractive optical element for wide spectral bandwidth". In: *Opt. Lett.* 23.11 (1998), pp. 823–824.

[37] K. J. Weible, A. Schilling, H. P. Herzig, and D. R. Lobb. "Achromatization of the diffraction efficiency of diffractive optical elements". In: *Proc. SPIE* 3749 (1999), p. 378.

[38] T. Nakai and H. Ogawa. "Research on multi-layer diffractive optical elements and their application to camera lenses". In: *OSA Trends in Optics and Photonics Series* (2002), DMA2.

[39] B. H. Kleemann, M. Seesselberg, and J. Ruoff. “Design concepts for broadband high–efficiency DOEs”. In: *J. Europ. Opt. Soc. Rap. Public.* 3 (2008), p. 08015.

[40] H. Haidner. “Theorie der Subwellenlängenstrukturen für diffraktive optische Elemente”. PhD thesis. Friedrich-Alexander-Universität Erlangen-Nürnberg, 1994.

[41] A. P. Wood, M.-S. L. Lee, B. Loiseaux, and G. D. Evans. “Broadband efficiency improvements in infrared diffractive optics”. In: *Proc. EMRS DTC Technical Conference* 2004 (2004), B19.

[42] A. P. Wood, M.-S. L. Lee, S. Bansropun, et al. “Broadband efficiency improvements in infrared diffracitve optics: practical aspects”. In: *Proc. EMRS DTC Technical Conference* 2005 (2005), B24.

[43] M.-S. L. Lee, C. Ribot, B. Loiseaux, et al. “Broadband Efficiency Improvements in Infrared Diffracitve Optics”. In: *Proc. EMRS DTC Technical Conference* (2006).

[44] DIN 5031. *Strahlungsphysik im optischen Bereich und Lichttechnik*. 1982.

[45] ISO 80000. *Größen und Einheiten – Teil 7: Licht*. 2008.

[46] D. Gall. *Grundlagen der Lichttechnik: Kompendium*. 2nd ed. Licht und Beleuchtung. München: Pflaum, 2007.

[47] R. Leach. *Optical measurement of surface topography*. Berlin: Springer-Verlag, 2011.

[48] J. B. Pawley, ed. *Handbook of biological confocal microscopy*. 3. ed. New York, NY: Springer, 2006.

[49] M. Minsky. “Microscopy apparatus”. US Patent 3013467. 1961.

[50] C. J. R. Sheppard and A. Choudhury. “Image Formation in the Scanning Microscope”. In: *Opt. Act.* 24.10 (1977), pp. 1051–1073.

[51] C. J. R. Sheppard, J. N. Gannaway, D. Walsh, and T. Wilson. “Scanning optical microscope for the inspection of electronic devices”. In: *Microcircuit Engineering Conference, Cambridge*. 1978.

[52] G. J. Brakenhoff, P. Blom, and P. Barends. “Confocal scanning light microscopy with high aperture immersion lenses”. In: *J. Microsc.* 117.2 (1979), pp. 219–232.

[53] T. Wilson, J. N. Gannaway, and P. Johnson. “A scanning optical microscope for the inspection of semiconductor materials and devices”. In: *J. Microsc.* 118.3 (1980), pp. 309–314.

[54] Van Resandt, R. W. Wijnaendts, Marsman, H. J. B., R. Kaplan, et al. “Optical fluorescence microscopy in three dimensions: microtomoscopy”. In: *J. Microsc.* 138.1 (1985), pp. 29–34.

[55] P. Davidovits and M. D. Egger. “Scanning Laser Microscope for Biological Investigations”. In: *Appl. Opt.* 10.7 (1971), pp. 1615–1619.

[56] S. Kimura and T. Wilson. “Confocal scanning optical microscope using single-mode fiber for signal detection”. In: *Appl. Opt.* 30.16 (1991), pp. 2143–50.

[57] T. Dabbs and M. Glass. “Fiber-optic confocal microscope: FOCON”. In: *Appl. Opt.* 31.16 (1992), pp. 3030–3035.

[58] K. Carlsson and N. Åslund. “Confocal imaging for 3-D digital microscopy”. In: *Appl. Opt.* 26.16 (1987), pp. 3232–3238.

[59] N. Aslund, A. Liljeborg, P.-O. Forsgren, and S. Wahlsten. “Three-dimensional digital microscopy using the PHOIBOSl Scanner”. In: *Scanning* 9.6 (1987), pp. 227–235.

[60] W. B. Amos, J. G. White, and M. Fordham. "Use of confocal imaging in the study of biological structures". In: *Appl. Opt.* 26.16 (1987), pp. 3239–3243.

[61] J. G. White, W. B. Amos, and M. Fordham. "An evaluation of confocal versus conventional imaging of biological structures by fluorescence light microscopy". In: *J. Cell Biol.* 105.1 (1987), pp. 41–48.

[62] T. R. Corle and G. S. Kino. *Confocal scanning optical microscopy and related imaging systems*. San Diego: Academic Press, 1996.

[63] P. Nipkow. "Elektrisches Teleskop". DE Patent 30105. 1885.

[64] M. D. Egger and M. Petran. "New Reflected-Light Microscope for Viewing Unstained Brain and Ganglion Cells". In: *Science* 157.3786 (1967), p. 305.

[65] M. Petran, M. Hadravsky, M. D. Egger, and R. Galambos. "Tandem-Scanning Reflected-Light Microscope". In: *J. Opt. Soc. Am.* 58.5 (1968), pp. 661–664.

[66] G. Q. Xiao and G. S. Kino. "A real-time confocal scanning optical microscope". In: *Proc. SPIE* 809 (1987), pp. 107–113.

[67] A. Ichihara, T. Tanaami, K. ISOZAKI, et al. "High-speed confocal fluorescence microscopy using a Nipkow scanner with microlenses for 3-D imaging of single fluorescent molecule in real time". In: *Bioimages* 4.2 (1996), pp. 57–62.

[68] H. J. Tiziani, M. Wegner, and D. Steudle. "Confocal principle for macro- and microscopic surface and defect analysis". In: *Opt. Eng.* 39.1 (2000), p. 32.

[69] T. Tanaami, S. Otsuki, N. Tomosada, et al. "High-speed 1-frame/ms scanning confocal microscope with a microlens and Nipkow disks". In: *Appl. Opt.* 41.22 (2002), pp. 4704–4708.

[70] S. Inoue and T. Inoue. "Direct-view High-speed Confocal Scanner: The CSU-10". In: *Meth. Cell Biol.* 70 (2002), pp. 87–127.

[71] H.-M. Uhde. "Chromatische Höhenbestimmung mit dem konfokalen Mikroskop". PhD thesis. Universität Stuttgart, 1992.

[72] H. J. Tiziani and H.-M. Uhde. "Three-dimensional analysis by a microlens-array confocal arrangement". In: *Appl. Opt.* 33.4 (1994), pp. 567–572.

[73] H. J. Tiziani, R. Achi, and R. N. Kramer. "Chromatic confocal microscopy with microlenses". In: *J. Mod. Optic.* 43.1 (1996), pp. 155–163.

[74] R. Juskaitis, T. Wilson, M. A. A. Neil, and M. Kozubek. "Efficient real-time confocal microscopy with white light sources". In: *Nature* 383.6603 (1996), pp. 804–806.

[75] M. Liang, R. L. Stehr, and A. W. Krause. "Confocal pattern period in multiple-aperture confocal imaging systems with coherent illumination". In: *Opt. Lett.* 22.11 (1997), pp. 751–753.

[76] P. J. Verveer, Q. S. Hanley, P. W. Verbeek, et al. "Theory of confocal fluorescence imaging in the programmable array microscope (PAM)". In: *J. Microsc.* 189.Part 3 (1998), pp. 192–198.

[77] Q. S. Hanley, P. J. Verveer, M. J. Gemkow, et al. "An optical sectioning programmable array microscope implemented with a digital micromirror device". In: *J. Microsc.* 196.Part 3 (1999), pp. 317–331.

[78] P. J. Smith, C. M. Taylor, A. J. Shaw, and E. M. McCabe. "Programmable array microscopy with a ferroelectric liquid-crystal spatial light modulator". In: *Appl. Opt.* 39.16 (2000), pp. 2664–2669.

[79] F. Bitte, G. Dussler, and T. Pfeifer. "3D micro-inspection goes DMD". In: *Opt. Laser Eng.* 36.2 (2001), pp. 155–167.

[80] R. Artigas, F. Laguarta, and C. Cadevall. "Dual-technology optical sensor head for 3D surface shape measurements on the micro- and nanoscales". In: *Proc. SPIE* 5457 (2004), pp. 166–174.

[81] D. M. Maurice. "A scanning slit optical microscope". In: *Inv. Opthal.* 13 (1973), pp. 1033–1037.

[82] C. J. R. Sheppard and X. Q. Mao. "Confocal Microscopes with Slit Apertures". In: *J. Mod. Optic.* 35.7 (1988), pp. 1169–1185.

[83] G. M. Svishchev. "Microscope for the study of transparent light-scattering objects in incident light". In: *Opt. Spectrosc.* 26 (1969), pp. 171–172.

[84] B. R. Masters and A. A. Thaer. "Real-time scanning slit confocal microscopy of the invivohuman cornea". In: *Appl. Opt.* 33.4 (1994), pp. 695–701.

[85] Y. S. Sabharwal, A. R. Rouse, L. Donaldson, et al. "Slit-scanning confocal microendoscope for high-resolution in vivo imaging". In: *Appl. Opt.* 38.34 (1999), pp. 7133–7144.

[86] R. Artigas, A. Pinto, and F. Laguarta. "Three-dimensional micromeasurements on smooth and rough surfaces with a new confocal optical profiler". In: *Proc. SPIE* 3824 (1999), pp. 93–103.

[87] C. Koester. "Comparison of Various Optical Sectioning Methods". In: *Handbook of Biological Confocal Microscopy*. Ed. by J. Pawley. Springer US, 1995, pp. 525–534.

[88] R. Wolleschensky, B. Zimmermann, and M. Kempe. "High-speed confocal fluorescence imaging with a novel line scanning microscope". In: *J. Biomed. Opt.* 11.6 (2006), p. 064011.

[89] E. J. Botcherby, M. J. Booth, R. Juškaitis, and T. Wilson. "Real-time slit scanning microscopy in the meridional plane". In: *Opt. Lett.* 34.10 (2009), pp. 1504–1506.

[90] M. D. Egger, W. Gezari, P. Davidovits, et al. "Observation of nerve fibers in incident light". In: *Experientia* 25.11 (1969), pp. 1225–1226.

[91] D. Toomre and J. Pawley. "Disk-Scanning Confocal Microscopy". In: *Handbook Of Biological Confocal Microscopy*. Ed. by J. B. Pawley. Springer US, 2006, pp. 221–238.

[92] G. Cox. *Optical imaging techniques in cell biology*. 2. ed. Boca Raton, Fla: CRC Press, 2012.

[93] T. Wilson, R. Juškaitis, N. P. Rea, and D. K. Hamilton. "Fibre optic interference and confocal microscopy". In: *Opt. Commun.* 110.1–2 (1994), pp. 1–6.

[94] M. Gu and D. Bird. "Fibre-optic double-pass confocal microscopy". In: *Opt. Laser Technol.* 30.2 (1998), pp. 91–93.

[95] R. Juskaitis, T. Wilson, and Watson, T. F. "Real-time white light reflection confocal microscopy using a fibre-optic bundle". In: *Scanning* 19.1 (1997), pp. 15–19.

[96] A. R. Rouse and A. F. Gmitro. "Multispectral imaging with a confocal microendoscope". In: *Opt. Lett.* 25.23 (2000), pp. 1708–1710.

[97] C. Liang, K.-B. Sung, R. R. Richards-Kortum, and M. R. Descour. "Design of a high-numerical-aperture miniature microscope objective for an endoscopic fiber confocal reflectance microscope". In: *Appl. Opt.* 41.22 (2002), pp. 4603–4610.

[98] M. Gu. *Principles of three-dimensional imaging in confocal microscopes*. Singapore: World Scientific, 1996.

[99] S. Inoué. "Foundations of Confocal Scanned Imaging in Light Microscopy". In: *Handbook of biological confocal microscopy*. Ed. by J. B. Pawley. New York, NY: Springer, 2006, pp. 1–19.

[100] T. Wilson and C. J. R. Sheppard. *Theory and practice of scanning optical microscopy*. 2nd ed. London: Acad. Press, 1985.

[101] C. J. R. Sheppard and T. Wilson. "Depth of field in the scanning microscope". In: *Opt. Lett.* 3.3 (1978), pp. 115–117.

[102] C. J. R. Sheppard and T. Wilson. "Effects of high angles of convergence on V(z) in the scanning acoustic microscope". In: *Appl. Phys. Lett.* 38.11 (1981), pp. 858–859.

[103] T. R. Corle, C.-H. Chou, and G. S. Kino. "Depth response of confocal optical microscopes". In: *Opt. Lett.* 11.12 (1986), pp. 770–772.

[104] G. S. Kino and G. Q. Xiao. "Real-time scanning optical microscopes". In: *Confocal microscopy*. Ed. by T. Wilson. London and San Diego: Academic Press, 1990.

[105] C. J. R. Sheppard. "Aberrations in high aperture conventional and confocal imaging systems". In: *Appl. Opt.* 27.22 (1988), pp. 4782–4786.

[106] T. Wilson and Carlini, A. R. "The effect of aberrations on the axial response of confocal imaging systems". In: *J. Microsc.* 154 (1989), pp. 243–256.

[107] C. J. R. Sheppard and M. Gu. "Aberration compensation in confocal microscopy". In: *Appl. Opt.* 30.25 (1991), pp. 3563–3568.

[108] M. Gu and C. J. R. Sheppard. "Effects of defocus and primary spherical aberration on three-dimensional coherent transfer functions in confocal microscopes". In: *Appl. Opt.* 31.14 (1992), pp. 2541–2549.

[109] C. J. R. Sheppard, M. Gu, K. Brain, and H. Zhou. "Influence of spherical aberration on axial imaging of confocal reflection microscopy". In: *Appl. Opt.* 33.4 (1994), pp. 616–24.

[110] T. Wilson and Carlini, A. R. "Size of the detector in confocal imaging systems". In: *Opt. Lett.* 12.4 (1987), pp. 227–229.

[111] T. Wilson and Carlini, A. R. "Three-dimensional imaging in confocal imaging systems with finite sized detectors". In: *J. Microsc.* 149.1 (1988), pp. 51–66.

[112] T. Wilson. "The role of detector geometry in confocal imaging". In: *J. Microsc.* 158.2 (1990), pp. 133–144.

[113] V. Drazic. "Three-dimensional Transfer Function Analysis of a Confocal Fluorescence Microscope With a Finite-sized Source and Detector". In: *J. Mod. Optic.* 40.5 (1993), pp. 879–887.

[114] C. J. R. Sheppard and M. Gu. "Imaging performance of confocal fluorescence microscopes with finite-sized source". In: *J. Mod. Optic.* January 2012 (1994), pp. 37–41.

[115] T. Wilson and J. B. Tan. "Finite sized coherent and incoherent detectors in confocal microscopy". In: *J. Microsc.* 182.1 (1996), pp. 61–66.

[116] C. J. R. Sheppard and C. J. Cogswell. "Three-dimensional image formation in confocal microscopy". In: *J. Microsc.* 159.2 (1990), pp. 179–194.

[117] M. Gu, X. Gan, and C. J. R. Sheppard. "Three-dimensional coherent transfer functions in fiber-optical confocal scanning microscopes". In: *J. Opt. Soc. Am. A* 8.7 (1991), pp. 1019–1025.

[118] C. J. R. Sheppard and M. Gu. "The significance of 3-D transfer functions in confocal scanning microscopy". In: *J. Microsc.* 165.3 (1992), pp. 377–390.

[119] M. Gu and C. J. R. Sheppard. "Three-dimensional Coherent Transfer Function in Reflection-mode Confocal Microscopy Using Annular Lenses". In: *J. Mod. Optic.* 39.4 (1992), pp. 783–793.

[120] F. Mauch, W. Lyda, M. Gronle, and W. Osten. "Improved signal model for confocal sensors accounting for object depending artifacts". In: *Opt. Express* 20.18 (2012), pp. 19936–19945.

[121] C. J. R. Sheppard. "Axial resolution of confocal fluorescence microscopy". In: *J. Microsc.* 154 (1989), pp. 237–241.

[122] T. Wilson. "Optical sectioning in confocal fluorescent microscopes". In: *J. Microsc.* 154.2 (1989), pp. 143–156.

[123] S. Kimura and C. Munakata. "Calculation of three-dimensional optical transfer function for a confocal scanning fluorescent microscope". In: *J. Opt. Soc. Am. A* 6.7 (1989), p. 1015.

[124] S. Kimura and C. Munakata. "Depth resolution of the fluorescent confocal scanning optical microscope". In: *Appl. Opt.* 29.4 (1990), pp. 489–494.

[125] M. Gu, C. J. R. Sheppard, and X. Gan. "Image formation in a fiber-optical confocal scanning microscope". In: *J. Opt. Soc. Am. A* 8.11 (1991), pp. 1755–1761.

[126] M. D. Sharma and C. J. R. Sheppard. "Axial resolution in the fibre-optical confocal microscope". In: *Bioimaging* 6.1998 (1998), pp. 98–103.

[127] Sharma, M. D. and C. J. R. Sheppard. "Effects of system geometry on the axial response of the fibreoptical confocal microscope". In: *J. Mod. Optic.* 46.4 (1999), pp. 605–621.

[128] T. Wilson, S. J. Hewlett, and C. J. R. Sheppard. "Use of objective lenses with slit pupil functions in the imaging of line structures". In: *Appl. Opt.* 29.31 (1990), pp. 4705–4714.

[129] T. Wilson and S. J. Hewlett. "Superresolution in confocal scanning microscopy". In: *Opt. Lett.* 16.14 (1991), pp. 1062–1064.

[130] C. J. R. Sheppard and M. Gu. "Improvement of axial resolution in confocal microscopy using an annular pupil". In: *Opt. Commun.* 84.1–2 (1991), pp. 7–13.

[131] M. Kowalczyk, C. J. Zapata-Rodriguez, and M. Martinez-Corral. "Asymmetric apodization in confocal scanning systems". In: *Appl. Opt.* 37.35 (1998), pp. 8206–8214.

[132] G. Barbastathis, M. Balberg, and D. J. Brady. "Confocal microscopy with a volume holographic filter". In: *Opt. Lett.* 24.12 (1999), pp. 811–813.

[133] M. A. A. Neil, R. Juskaitis, T. Wilson, et al. "Optimized pupil-plane filters for confocal microscope point-spread function engineering". In: *Opt. Lett.* 25.4 (2000), pp. 245–247.

[134] G. Boyer. "New class of axially apodizing filters for confocal scanning microscopy". In: *J. Opt. Soc. Am. A* 19.3 (2002), pp. 584–589.

[135] T. Wilson. "Depth response of scanning microscopes". In: *Optik* 81.3 (1989), pp. 113–118.

[136] T. Wilson and S. J. Hewlett. "Imaging in scanning microscopes with slit-shaped detectors". In: *J. Microsc.* 160.2 (1990), pp. 115–139.

[137] S. Kimura and C. Munakata. "Three-dimensional optical transfer function for the fluorescent scanning optical microscope with a slit". In: *Appl. Opt.* 29.7 (1990), pp. 1004–1007.

[138] K. Kobayashi, H. Nakano, H. Matsui, et al. “Confocal scanning laser ophthalmoscope with a slit aperture”. In: *Meas. Sci. Technol.* 2.4 (1991), p. 287.

[139] C. J. R. Sheppard and C. J. Cogswell. “Confocal microscopy with detector arrays”. In: *J. Mod. Optic.* 37.2 (1990), pp. 267–279.

[140] T. Wilson and S. J. Hewlett. “Optical sectioning strength of the direct-view microscope employing finite-sized pin-hole arrays”. In: *J. Microsc.* 163.2 (1991), pp. 131–150.

[141] J. a. Conchello and J. W. Lichtman. “Theoretical analysis of a rotating-disk partially confocal scanning microscope”. In: *Appl. Opt.* 33.4 (1994), pp. 585–96.

[142] E. M. McCabe, D. T. Fewer, A. C. Ottewill, et al. “Direct-view microscopy: Optical sectioning strength for finite-sized, multiple-pinhole arrays”. In: *J. Microsc.* 184.2 (1996), pp. 95–105.

[143] C. M. Taylor and E. M. McCabe. “Effects of source coherence and aperture array geometry on optical sectioning strength in direct-view microscopy”. In: *J. Opt. Soc. Am. A* 19.7 (2002), pp. 1406–1416.

[144] M. Gu and C. J. R. Sheppard. “Effects of defocus and primary spherical aberration on images of a straight edge in confocal microscopy”. In: *Appl. Opt.* 33.4 (1994), pp. 625–30.

[145] M. C. Hutley and R. F. Stevens. “The use of a zone-plate monochromator as a displacement transducer”. In: *J. Phys. E: Sci. Instrum.* 21 (1988), p. 1037.

[146] M. A. Browne, O. Akinyemi, and A. Boyde. “Confocal surface profiling utilizing chromatic aberration”. In: *Scanning* 14.3 (1992), pp. 145–153.

[147] R. Juskaitis and T. Wilson. “A method for characterizing longitudinal chromatic aberration of microscope objectives using a confocal optical system”. In: *J. Microsc.* 195.1 (1999), pp. 17–22.

[148] O. Carrasco-Zevallos, R. L. Shelton, C. A. Olsovsky, et al. “Exploiting chromatic aberration to spectrally encode depth in reflectance confocal microscopy”. In: *Proc. SPIE* 8086 (2011), p. 80861D.

[149] C. A. Olsovsky, R. L. Shelton, M. A. Saldua, et al. “Multidepth imaging by chromatic dispersion confocal microscopy”. In: *Proc. SPIE* 8214 (2012), p. 82140L.

[150] C. Olsovsky, R. Shelton, O. Carrasco-Zevallos, et al. “Chromatic confocal microscopy for multi-depth imaging of epithelial tissue”. In: *Biomed. Opt. Express* 4.5 (2013), pp. 732–740.

[151] J. S. Courtney-Pratt and R. L. Gregory. “Microscope with Enhanced Depth of Field and 3-D Capability”. In: *Appl. Opt.* 12.10 (1973), pp. 2509–2519.

[152] G. Molesini, G. Pedrini, P. Poggi, and F. Quercioli. “Focus-wavelength encoded optical profilometer”. In: *Opt. Commun.* 49.4 (1984), pp. 229–233.

[153] D. M. Gross and C. Daehne. “Process and device to determine the position of an object with respect to a reference.” EP Patent 0142464. 1985.

[154] B. Picard. “Method for optical scanning microscopy in confocal arrangement with large depth of field and apparatus to perform this method”. EP Patent 327425. 1989.

[155] S. Sandoz. “Profilométrie en lumière polychromatique et par microscopie confocale”. PhD thesis. Besancon, France: Université de Franche-Comté, 1993.

[156] H. Perrin, P. Sandoz, and G. Tribillon. “Profilometry by spectral encoding of the optical axis”. In: *Proc. SPIE* 2340 (1994), pp. 366–374.

[157] H. Perrin, P. Sandoz, and G. Tribillon. “Longitudinally dispersive profilometer”. In: *Pure. Appl. Opt.* 4 (1995), p. 219.

[158] S. Sinzinger, V. M. Arrizon, and J. Jahns. “Confocal imaging with diffractive optics and broadband light sources”. In: *Proc. SPIE* 3002 (1997), p. 186.

[159] J. Cohen-Sabban, J. Gaillard-Groleas, and P.-J. Crepin. “Quasi-confocal extended field surface sensing”. In: *Proc. SPIE* 4449 (2001), pp. 178–183.

[160] H.-J. Jordan. “Highly accurate 2D and 3D surface metrology using confocal white-light sensors with chromatic distance coding”. In: *Proc. International Colloquium on Surfaces* 11 (2004), p. 127.

[161] A. K. Ruprecht, T. F. Wiesendanger, and H. J. Tiziani. “Chromatic confocal microscopy with a finite pinhole size”. In: *Opt. Lett.* 29.18 (2004), pp. 2130–2132.

[162] A. K. Ruprecht, C. Pruss, H. J. Tiziani, et al. “Confocal micro-optical distance sensor: principle and design”. In: *Proc. SPIE* 5856 (2005), pp. 128–135.

[163] K. Shi, P. Li, S. Yin, and Z. Liu. “Chromatic confocal microscopy using supercontinuum light”. In: *Opt. Express* 12.10 (2004), pp. 2096–2101.

[164] K. Shi, P. Li, S. Yin, and Z. Liu. “Surface profile measurement using chromatic confocal microscopy”. In: *Proc. SPIE* 5606 (2004), pp. 124–131.

[165] J. Garzon Reyes, J. Meneses, G. Tribillon, et al. “Chromatic confocal microscopy by means of continuum light generated through a standard single-mode fibre”. In: *J. Opt. A - Pure Appl. Op.* 6.6 (2004), pp. 544–548.

[166] C. Pruss, A. K. Ruprecht, K. Körner, et al. “Diffractive Elements for Chromatic Confocal Sensors”. In: *Proc. DGaO* (2005), A1.

[167] P. Lücke. “Confocal micro-optical distance sensor: realization and results”. In: *Proc. SPIE* 5856 (2005), pp. 136–142.

[168] M. Kunkel and J. Schulze. “Noncontact measurement of central lens thickness”. In: *Glass Sci. Technol.* 78.5 (2005), pp. 2–4.

[169] J. Novak and A. Miks. “Hyperchromats with linear dependence of longitudinal chromatic aberration on wavelength”. In: *Optik* 116 (2005), pp. 165–168.

[170] P. Lücke, A. Last, and J. Mohr. “Mikrooptische Sensoren nach dem chromatisch konfokalen Messprinzip”. PhD thesis. Universität Karlsruhe, 2006.

[171] A. Miks, J. Novak, P. Novák, et al. “Theory of chromatic sensor for topography measurements”. In: *Proc. SPIE* 6609 (2007), 66090U.

[172] A. K. Ruprecht. “Konfokale Sensorik zur Hochgeschwindigkeits-Topografiemessung technischer Objekte”. PhD thesis. Stuttgart: Universität Stuttgart, 2008.

[173] H.-J. Jordan. “Optical chromatic confocal probes”. In: *Proc. International Colloquium on Surfaces* 12 (2008), pp. 200–209.

[174] J. Garzon Reyes, T. Gharbi, and J. Meneses. “Real time determination of the optical thickness and topography of tissues by chromatic confocal microscopy”. In: *J. Opt. A - Pure Appl. Op.* 10 (2008), p. 104028.

[175] A. Miks, J. Novak, P. Novák, and P. Kajnar. “Influence of material dispersion on the measurement accuracy of chromatic sensors”. In: *Proc. SPIE* 7389 (2009), 73892K–73892K-6.

[176] M. Hillenbrand, B. Mitschunas, and S. Sinzinger. "Chromatic aberration theory in modern metrology". In: *Proc. DGaO* (2009), P1.

[177] D. Fleischle, W. Lyda, F. Mauch, and W. Osten. "Optical metrology for process control: modeling and simulation of sensors for a comparison of different measurement principles". In: *Proc. SPIE* 2010 (7718), p. 77181D.

[178] A. Miks, J. Novak, and P. Novák. "Analysis of method for measuring thickness of plane-parallel plates and lenses using chromatic confocal sensor". In: *Appl. Opt.* 49.17 (2010), pp. 3259–3264.

[179] C.-H. Niu, W.-Y. Deng, X.-H. Mao, et al. "Theoretical and experimental study on chromatic confocal position sensor". In: *Proc. SPIE* 7853 (2010), 78531B.

[180] W.-Y. Deng, C.-H. Niu, N. Lv, and X. Gao. "Research on chromatic confocal technology for displacement measurement". In: 7997 (2011), 79971Z.

[181] E. Behroodi, A. Mousavian, and H. Latifi. "Design and fabrication of White Light Confocal Microscope with tunable resolution and sensitivity". In: *Proc. SPIE* 8082 (2011), p. 808235.

[182] J. Garzon Reyes, D. Duque, A. Alean, et al. "Diffractive elements performance in chromatic confocal microscopy". In: *J. Phys.: Conf. Ser.* 274 (2011), p. 012069.

[183] M. Hillenbrand, C. Wenzel, X. Ma, et al. "Hyperchromatic Confocal Sensor Systems". In: *Proc. 8th EOS Topical Meeting on Diffractive Optics* (2012).

[184] M. Hillenbrand, B. Mitschunas, C. Wenzel, et al. "Hybrid hyperchromats for chromatic confocal sensor systems". In: *Adv. Opt. Technol.* 1.3 (2012), pp. 187–194.

[185] E. Heidari, K. G. Harding, and R. W. Tait. "Automated cylindrical mapper using chromatic confocal measurement". In: *Proc. SPIE* 8839 (2013), 88390F.

[186] M. Rayer and D. Mansfield. "Chromatic confocal microscopy using staircase diffractive surface". In: *Appl. Opt.* 53.23 (2014), pp. 5123–5130.

[187] E. Behroodi, A. Mousavian, and H. Latifi. "Simulation and fabrication of white light confocal microscope to attain the surface profile using CCD and image processing techniques". In: *Proc. SPIE* 7389 (2009), 73892U.

[188] M. Taphanel, B. Hovestreydt, and J. Beyerer. "Speed-up Chromatic Sensors by Optimized Optical Filters". In: *Proc. SPIE* 8788 (2013), 87880S.

[189] T. Kim, S. H. Kim, D. Do, et al. "Chromatic confocal microscopy with a novel wavelength detection method using transmittance". In: *Opt. Express* 21.5 (2013), pp. 6286–6294.

[190] S. L. Dobson, P.-c. Sun, and Y. Fainman. "Diffractive lenses for chromatic confocal imaging". In: *Appl. Opt.* 36.20 (1997), pp. 4744–4748.

[191] B. S. Chun, K. Kim, and D. Gweon. "Three-dimensional surface profile measurement using a beam scanning chromatic confocal microscope". In: *Rev Sci Instrum* 80.7 (2009), p. 073706.

[192] P. C. Lin, P.-c. Sun, L. Zhu, and Y. Fainman. "Single-Shot Depth-Section Imaging Through Chromatic Slit-Scan Confocal Microscopy". In: *Appl. Opt.* 37.28 (1998), pp. 6764–6770.

[193] A. K. Ruprecht, K. Körner, T. F. Wiesendanger, et al. "Chromatic confocal detection for high speed micro-topography measurements". In: *Proc. SPIE* 5302 (2004), pp. 53–60.

[194] R. Steiner, R. Hibst, K. Stock, et al. “Verfahren und Vorrichtung zur Charakterisierung bewegter Oberflächen”. DE Patent 102006026775. 2007.

[195] K. Koga. “Confocal Microscope”. US Patent 20100097693. 2010.

[196] L.-C. Chen, C.-N. Chen, and Y.-W. Chang. “Slit-scan mutli-wavelength confocal lens module and slit-scan microscopic system and method using the same”. US Patent 20100188742. 2010.

[197] P. Lehmann. “Konfokaler Liniensensor”. DE Patent 10161486. 2003.

[198] L.-C. Chen, Y.-L. Wu, and Y.-W. Chang. “Linear chromatic confocal microscopic system”. US Patent 20120019821. 2012.

[199] M. Hillenbrand, L. Lorenz, R. Kleindienst, et al. “Spectrally multiplexed chromatic confocal multipoint sensing”. In: *Opt. Lett.* 38.22 (2013), pp. 4694–4697.

[200] S. Cha, P. C. Lin, L. Zhu, et al. “Nontranslational three-dimensional profilometry by chromatic confocal microscopy with dynamically configurable micromirror scanning”. In: *Appl. Opt.* 39.16 (2000), pp. 2605–2613.

[201] H. J. Tiziani and H. M. Uhde. “Three-dimensional image sensing by chromatic confocal microscopy”. In: *Appl. Opt.* 33.10 (1994), pp. 1838–1843.

[202] P. M. Lane, R. P. Elliott, and C. E. MacAulay. “Confocal microendoscopy with chromatic sectioning”. In: *Proc. SPIE* 4959 (2003), pp. 23–26.

[203] D. Mendlovic. “Three-dimensional image sensing based on a zone-plate array”. In: *Opt. Commun.* 95 (1993), pp. 26–32.

[204] A. Brückner, W. Buss, T. Egloff, and P. Schreiber. “Optischer Sensor und Verfahren zur optischen Abstands- und/oder Farbmessung”. DE Patent 102005043627. 2007.

[205] Y. Saito and H. Nishida. “Confocal Microscope”. US Patent 6188514. 2001.

[206] L.-C. Chen, Y.-W. Chang, and H.-W. Li. “Full-field chromatic confocal surface profilometry employing digital micromirror device correspondence for minimizing lateral cross talks”. In: *Opt. Eng.* 51.8 (2012), p. 081507.

[207] K. Körner. “Anordnung und Verfahren zur hochdynamischen, konfokalen Technik”. DE Patent 10321885. 2004.

[208] K. Körner. “Verfahren und Anordnung zur schnellen, ortsaufgelösten, flächigen, spektroskopischen Analyse, bzw. zum Spectral Imaging oder zur 3D-Erfassung mittels Spektroskopie”. DE Patent 102006007172. 2007.

[209] R. Graser, R. Hilbst, M. Müller, and K. Stock. “Messanordnung sowie Verfahren zum dreidimensionalen Messen eines Objektes”. DE Patent 102007019267. 2008.

[210] K. Körner, C. Kohler, E. Papastathopoulos, and W. Osten. “Verfahren und Anordnung zur schnellen und robusten konfokalen 3D-Messtechnik”. DE Patent 102006007170B4. 2009.

[211] K. Stock, M. Zint, R. Graser, and R. Hibst. “Messanordnung sowie Verfahren zum dreidimensionalen Messen eines Objektes”. DE Patent 102009025815. 2010.

[212] T. Ertl. “Verfahren zur Ermittlung von Materialcharakteristika eines Objekts”. WO Patent 2011117420. 2011.

[213] T. Scherübl and N. Czarnetzki. “Konfokale mikroskopische Anordnung”. DE Patent 19713362. 1998.

[214] M. Maly and A. Boyde. “Real-time stereoscopic confocal reflection microscopy using objective lenses with linear longitudinal chromatic dispersion”. In: *Scanning* 16 (1994), pp. 187–192.

[215] H.-G. Baumann. “Arrangement for generating a defined longitudinal chromatic aberration in the optical beam path of a confocal microscope”. US Patent 6038066. 2000.

[216] L.-C. Chen, T.-Y. Lin, Y.-W. Chang, and Lin Shyh-Tsong. “Chromatic confocal surface profilometry employing signal recovering methodology for simultaneously resolving lateral and axial cross talk problems”. In: *Proc. SPIE* 8759 (2013), p. 875941.

[217] D. Fleischle, W. Lyda, T. Haist, and W. Osten. “Modeling and simulation of a chromatic-confcal sensor to measure rough surfaces”. In: *Proc. DGaO* 2009 (2009).

[218] D. Fleischle, W. Lyda, F. Mauch, and W. Osten. “Untersuchung zum Zusammenhang von spektraler Abtastung und erreichbarer Messunsicherheit bei der chromatisch-konfokalen Mikroskopie an rauen Objekten”. In: *Proc. DGaO* (2010), A14.

[219] D. Fleischle. “Konzepte und Implementierung für die prozessnahe Integration optischer Sensore”. PhD thesis. Stuttgart, 2012.

[220] International Bureau of Weights and Measures. *JCGM 100:2008: Evaluation of measurement data — Guide to the expression of uncertainty in measurement (GUM)*. 2008.

[221] International Bureau of Weights and Measures. *JCGM 200:2012: International Vocabulary of Metrology – Basic and General Concepts and Associated Terms (VIM)*. 2012.

[222] W. Lyda. “Sensorkommunikation in multiskaligen Messsystemen”. PhD thesis. Stuttgart, 2013.

[223] D. Malacara, ed. *Optical shop testing*. 3. ed. Wiley Series in Pure and Applied Optics. Hoboken, NJ: Wiley, 2007.

[224] C. J. R. Sheppard, T. J. Connolly, J. Lee, and C. J. Cogswell. “Confocal imaging of a stratified medium”. In: *Appl. Opt.* 33.4 (1994), pp. 631–40.

[225] Rayleigh. “XXXI. Investigations in optics, with special reference to the spectroscope”. In: *Philosophical Magazine Series 5* 8.49 (1879), pp. 261–274.

[226] C. M. Sparrow. “On spectroscopic resolving power”. In: *Astrophys. J.* 44 (1916), p. 76.

[227] J. S. Thompson. “Focal isolation monochromator employing accentuation of longitudinal chromatic aberration”. US Patent 3185021. 1965.

[228] G. Retfalvy, P. Sugar, and Z. Zorkoczy. “Selecitve optical detector apparatus utilizing longitudinal chromatic aberration”. US Patent 4742222. 1988.

[229] M. Hinnrichs and G. M. Morris. “Image Multispectral Sensing”. US Patent 5479258. 1995.

[230] D. Lyons and K. Whitcomb. “The DOE in DOIS: a Diffractive Optic Image Spectrometer”. In: *Proc. SPIE* 2689 (1996), pp. 274–283.

[231] J. A. Cox and B. S. Fritz. “Tunable Multispectral Optical Filter and Imaging Apparatus”. US Patent 6101034. 2000.

[232] R. Mercatelli, S. Soria, G. Molesini, et al. “Supercontinuum source tuned by an on-axis monochromator for fluorescence lifetime imaging”. In: *Opt. Express* 18.19 (2010), pp. 20505–20511.

[233] A. Grewe, M. Hillenbrand, and S. Sinzinger. “Hyperspectral imaging sensor systems using tunable lenses”. In: *Phot. Int.* 2013 (2013), pp. 20–23.

[234] P.-H. Cu-Nguyen, A. Grewe, M. Hillenbrand, et al. “Tunable hyperchromatic lens system for confocal hyperspectral sensing”. In: *Opt. Express* 21.23 (2013), pp. 27611–27621.

[235] M. Hillenbrand, R. Weiß, C. Endrödy, et al. “Chromatic confocal matrix sensor with actuated pinhole arrays”. In: *Appl. Opt.* 54.15 (2015), pp. 4927–4936.

[236] K. Körner, C. Kohler, E. Papastathopoulos, et al. “Arrangement for rapid locally resolved flat surface spectroscopic analysis or imaging has flat raster array of pinholes turned about acute angle relative to spectral axis on detector matrix which fills up with elongated su-matrices”. DE Patent 102006007172. 2007.

[237] M. Hillenbrand, A. Grewe, M. Bichra, et al. “Chromatic information coding in optical systems for hyperspectral imaging and chromatic confocal sensing”. In: *Proc. SPIE* 8550 (2012), p. 85500D.

[238] M. Hillenbrand, A. Grewe, M. Bichra, et al. “Parallelized chromatic confocal sensor systems”. In: *Proc. SPIE* 8788 (2013), p. 87880V.

[239] A. Schick. “Confocal spectromerter and method for imaging in a confocal spectrometer”. WO Patent 2013045250. 2013.

[240] J. Haus. *Optical sensors: Basics and applications*. Weinheim: Wiley-VCH, 2010.

[241] G. Berkovic and E. Shafir. “Optical methods for distance and displacement measurements Optical methods for distance and displacement measurements”. In: *Adv. Opt. Photon.* 4 (2012), pp. 441–471.

[242] M. Borengasser, W. S. Hungate, and R. L. Watkins. *Hyperspectral remote sensing: Principles and applications*. Taylor & Francis series in remote sensing applications. Boca Raton, FL: CRC Press, 2008.

[243] D. J. Brady. *Optical imaging and spectroscopy*. Hoboken, N.J.: Wiley, 2008.

[244] N. Hagen and M. W. Kudenov. “Review of snapshot spectral imaging technologies”. In: *Opt. Eng.* 52.9 (2013), p. 090901.

[245] E. Shafir and G. Berkovic. “Expanding the realm of fiber optic confocal sensing for probing position, displacement, and velocity”. In: *Appl. Opt.* 45.30 (2006), pp. 7772–7.

[246] G. Berkovic, E. Shafir, M. a. Golub, et al. “Multi-wavelength fiber-optic confocal position sensor with diffractive optics for enhanced measurement range”. In: 6619 (), 66190U.

[247] G. Berkovic, E. Shafir, M. a. Golub, et al. “Multiple-Fiber and Multiple-Wavelength Confocal Sensing With Diffractive Optical Elements”. In: *IEEE Sensors Journal* 8.7 (2008), pp. 1089–1092.

[248] G. J. Tearney, R. H. Webb, and B. E. Bouma. “Spectrally encoded confocal microscopy”. In: *Opt. Lett.* 23.15 (1998), pp. 1152–1154.

[249] G. J. Tearney, M. Shishkov, and B. E. Bouma. “Spectrally encoded miniature endoscopy”. In: *Opt. Lett.* 27.6 (2002), pp. 412–4.

[250] C. Pitris, B. E. Bouma, M. Shiskov, and G. Tearney. “A GRISM-based probe for spectrally encoded confocal microscopy”. In: *Opt. Express* 11.2 (2003), pp. 120–124.

[251] D. Yelin, I. Rizvi, W. M. White, et al. “Three-dimensional miniature endoscopy”. In: *Nature* 443.7113 (2006), p. 765.

[252] D. Kang, R. W. Carruth, M. Kim, et al. “Endoscopic probe optics for spectrally encoded confocal microscopy”. In: *Biomed. Opt. Express* 4.10 (2013), pp. 1925–1936.

[253] C. Boudoux, S. Yun, W. Oh, et al. “Rapid wavelength-swept spectrally encoded confocal microscopy”. In: *Opt. Express* 13.20 (2005), pp. 8214–8221.

[254] D. Yelin, W. M. White, J. T. Motz, et al. “Spectral-domain spectrally-encoded endoscopy”. In: *Opt. Express* 15.5 (2007), pp. 2432–44.

[255] N. Bedard and T. S. Tkaczyk. “Snapshot spectrally encoded fluorescence imaging through a fiber bundle”. In: *J. Biomed. Opt.* 17.8 (2012), pp. 80508–1.

[256] M. Gronle, W. Lyda, F. Mauch, and W. Osten. “Laterally chromatically dispersed, spectrally encoded interferometer”. In: *Appl. Opt.* 50.23 (2011), pp. 4574–4580.

[257] M. Taphanel and J. Beyerer. “Fast 3D in-line sensor for specular and diffuse surfaces combining the chromatic confocal and triangulation principle”. In: *Proc. IEEE* (2012), pp. 1072–1077.

[258] K. Körner. “Optischer Sensor und Verfahren mittels Triangulation insbesondere zur chromatischen Objekt-Tiefenabtastung”. DE Patent 000010321896. 2004.

[259] K. Körner. “Interferometrischer Sensor zur chromatischen Objekt-Tiefenabtastung”. DE Patent 10321895. 2004.

[260] K. Körner, R. Berger, U. Droste, et al. “Interferometric method and arrangement”. WO Patent 2006042696. 2006.

[261] K. Körner. “Anordnung und Verfahren zur konfokalen, spektralen Zweistrahl - Interferometrie”. DE Patent 102008020902. 2010.

[262] E. Papastathopoulos, K. Körner, and W. Osten. “Chromatically dispersed interferometry with wavelet analysis”. In: *Opt. Lett.* 31.5 (2006), pp. 589–91.

[263] E. Papastathopoulos, K. Körner, and W. Osten. “Chromatic confocal spectral interferometry”. In: *Appl. Opt.* 45.32 (2006), pp. 8244–8252.

[264] J. Schwider and L. Zhou. “Dispersive interferometric profilometer”. In: *Opt. Lett.* 19.13 (1994), pp. 995–997.

[265] U. Schnell, E. Zimmermann, and R. Dandliker. “Absolute distance measurement with synchronously sampled white-light channelled spectrum interferometry”. In: *Pure Appl. Opt.* 4.5 (1995), p. 643.

[266] M. Bail, G. Häusler, J. M. Herrmann, et al. “Optical coherence tomography with the spectral radar: fast optical analysis in volume scatterers by short-coherence interferometry”. In: *Proc. SPIE* 2925 (1996), pp. 298–303.

[267] J. Calatroni, A. L. Guerrero, C. Sainz, and R. Escalona. “Spectrally-resolved white-light interferometry as a profilometry tool”. In: *Opt. Laser Technol.* 28.7 (1996), pp. 485–489.

[268] P. Sandoz, G. Tribillon, and H. Perrin. “High-resolution profilometry by using phase calculation algorithms for spectroscopic analysis of white-light interferograms”. In: *J. Mod. Optic.* 43.4 (1996), pp. 701–708.

[269] M. Wojtkowski, R. Leitgeb, A. Kowalczyk, et al. “In vivo human retinal imaging by Fourier domain optical coherence tomography”. In: *J. Biomed. Opt.* 7.3 (2002), pp. 457–463.

[270] T. Endo, Y. Yasuno, S. Makita, et al. “Profilometry with line-field Fourier-domain interferometry”. In: *Opt. Express* 13.3 (2005), pp. 695–701.

[271] W. Lyda, M. Gronle, D. Fleischle, et al. “Advantages of chromatic-confocal spectral interferometry in comparison to chromatic confocal microscopy”. In: *Meas. Sci. Technol.* 23.5 (2012), p. 054009.

[272] D. N. Fuller, A. L. Kellner, and J. H. Price. "Exploiting chromatic aberration for image-based microscope autofocus". In: *Appl. Opt.* 50.25 (2011), pp. 4967–4976.

[273] J. Garcia, J. Sanchez, X. Orriols, and X. Binefa. "Chromatic aberration and depth extraction". In: *Proc. IEEE* (2000), pp. 762–765.

[274] P. Trouvé, F. Champagnat, G. Le Besnerais, et al. "Passive depth estimation using chromatic aberration and a depth from defocus approach". In: *Appl. Opt.* 52.29 (2013), pp. 7152–7164.

[275] K. A. Nugent, D. Paganin, and T. E. Gureyev. "A Phase Odyssey". In: *Physics Today* 54 (2001), pp. 27–32.

[276] L. Waller, S. S. Kou, C. J. R. Sheppard, and G. Barbastathis. "Phase from chromatic aberrations". In: *Opt. Express* 18.22 (2010), pp. 22817–22825.

[277] W. Harm, C. Roider, A. Jesacher, et al. "Dispersion tuning with a varifocal diffractive-refractive hybrid lens". In: *Opt. Express* 22.5 (2014), pp. 5260–5269.

[278] F. Zernike. "Phase contrast, a new method for the microscopic observation of transparent objects". In: *Physica* 9.7 (1942), pp. 686–698.

[279] J. Millerd, N. Brock, J. Hayes, et al. "Pixelated Phase-Mask Dynamic Interferometer". In: *Proc. SPIE* 5531 (2004), pp. 304–314.

[280] G. Popescu, L. P. Deflores, J. C. Vaughan, et al. "Fourier phase microscopy for investigation of biological structuresand dynamics". In: *Opt. Lett.* 29.21 (2004), pp. 2503–2505.

[281] P. Marquet, B. Rappaz, P. J. Magistretti, et al. "Digital holographic microscopy: a noninvasive contrastimaging technique allowing quantitative visualization ofliving cells with subwavelength axial accuracy". In: *Opt. Lett.* 30.5 (2005), pp. 468–470.

[282] B. C. Platt and R. Shack. "History and principles of Shack-Hartmann wavefront sensing". In: *J. Refrac. Surg.* 17.5 (2001), S573–S577.

[283] Fienup, J. R. "Phase retrieval algorithms: a comparison". In: *Appl. Opt.* 21.15 (1982), pp. 2758–2769.

[284] D. Paganin and Nugent, K. A. "Noninterferometric Phase Imaging with Partially Coherent Light". In: *Phys. Rev. Lett.* 80.12 (1998), pp. 2586–2589.

[285] L. Waller, L. Tian, and G. Barbastathis. "Transport of Intensity phase-amplitude imaging with higher order intensity derivatives". In: *Opt. Express* 18.12 (2010), pp. 12552–12561.

[286] G. Molesini and F. Quercioli. "Pseudocolor effects of longitudinal chromatic aberration". In: *J. Optics* 17.6 (1986), pp. 279–282.

[287] M. D. Robinson and D. G. Stork. "Joint digital-optical design of imaging systems for grayscale objects". In: *Proc. SPIE* 7100 (2008), p. 710011.

[288] B. Milgrom, N. Konforti, M. a. Golub, and E. Marom. "Novel approach for extending the depth of field of Barcode decoders by using RGB channels of information". In: *Opt. Express* 18.16 (2010), pp. 17027–17039.

[289] J. Lim, J. Kang, and H. Ok. "Robust local restoration of space-variant blur image". In: *Proc. SPIE* 6817 (2008), 68170S.

[290] F. Guichard, H. P. Nguyen, R. Tessieres, et al. "Extended depth-of-field using sharpness transport across color channels". In: *Proc. SPIE* 7250 (2009), 72500N.

[291] O. Cossairt and S. Nayar. “Spectral Focal Sweep: Extended Depth of Field from Chromatic Aberrations”. In: *Proc. IEEE* (2010), pp. 1–8.

[292] A. Jesacher, C. Roider, and M. Ritsch-Marte. “Enhancing diffractive multi-plane microscopy using colored illumination”. In: *Opt. Express* 21.9 (2013), pp. 11150–11161.

[293] H. H. Hopkins. “The airy disc formula for systems of high relative aperture”. In: *Proc. Phys. Soc.* 55.2 (1943), p. 116.

[294] C. J. R. Sheppard and M. Gu. “Imaging by a high aperture optical system”. In: *J. Mod. Optic.* 40.8 (1993), pp. 1631–1651.

[295] M. Gu. *Advanced optical imaging theory*. Vol. v. 75. Springer series in optical sciences. Berlin and New York: Springer, 2000.

[296] E. Wolf. “The diffraction theory of aberrations”. In: *Rep. Prog. Phys.* 14.1 (1951), p. 95.

[297] H. Osterberg and L. W. Smith. “Closed Solutions of Rayleigh’s Diffraction Integral for Axial Points”. In: *J. Opt. Soc. Am.* 51.10 (1961), pp. 1050–1054.

[298] J. C. Heurtley. “Scalar Rayleigh-Sommerfeld and Kirchhoff diffraction integrals: A comparison of exact evaluations for axial points”. In: *J. Opt. Soc. Am.* 63.8 (1973), pp. 1003–1008.

[299] R. Aarts, J. Braat, P. Dirksen, et al. “Analytic expressions and approximations for the on-axis, aberration-free Rayleigh and Debye integral in the case of focusing fields on a circular aperture”. In: *J. Europ. Opt. Soc. Rap. Public.* 3 (2008).

[300] G. B. Airy. “On the diffraction of an object-glass with circular aperture”. In: *Trans. Cambridge Phys. Soc.* 5 (1835), p. 283.

[301] M. Born. “Geometrische und undulatorische Abbildungsfehler der optischen Instrumente”. In: *Naturwissenschaften* 20.51 (1932), pp. 921–923.

[302] M. Born. *Optik: ein Lehrbuch der elektronmagnetischen Lichttheorie*. Springer-Verlag, 1933.

[303] B. R. A. Nijboer. “The diffraction theory of aberrations”. PhD thesis. University of Groningen, 1942.

[304] B. R. A. Nijboer. “The diffraction theory of optical aberrations - Part I: General discussion of the geometrical aberrations”. In: *Physica* 10 (1943), pp. 679–692.

[305] B. R. A. Nijboer. “The diffraction theory of optical aberrations - Part II: Diffraction patterns in the presence of small aberrations”. In: *Physica* 13 (1947), pp. 605–620.

[306] K. Nienhuis. “On the influence of diffraction on image formation in the presence of aberrations”. PhD thesis. University of Groningen, 1948.

[307] K. Nienhuis and B. R. A. Nijboer. “The diffraction theory of optical aberrations - Part III: General formulae for small aberrations; experimental verification of the theoretical results”. In: *Physica* 14 (1949), pp. 590–608.

[308] E. Lommel. *Die Beugungserscheinungen einer kreisrunden Oeffnung und eines kreisrunden Schirmchens theoretisch und experimentell bearbeitet von*. Verlag d. K. Akad, 1886.

[309] H. Struve. In: *Mem. Acad. St. Petersbourgh (7)* 34 (1886), p. 1.

[310] G. C. Steward. In: *Phil Trans. R. Soc. A* 225 (1925), p. 131.

[311] A. J. E. M. Janssen. “Extended Nijboer-Zernike approach for the computation of optical point-spread functions”. In: *J. Opt. Soc. Am. A* 19.5 (2002), pp. 849–857.

[312] J. J. M. Braat, P. Dirksen, and A. J. E. M. Janssen. "Assessment of an extended Nijboer-Zernike approach for the computation of optical point-spread functions". In: *J. Opt. Soc. Am. A* 19.5 (2002), pp. 858–870.

[313] S. van Haver and A. J. E. M. Janssen. "Advanced analytic treatment and efficient computation of the diffraction integrals in the extended Nijboer-Zernike theory". In: *J. Europ. Opt. Soc. Rap. Public.* 8 (2013), p. 13044.

[314] S. Bagheri, D. P. d. Farias, G. Barbastathis, and M. A. Neifeld. "Reduced-complexity representation of the coherent point-spread function in the presence of aberrations and arbitrarily large defocus". In: *J. Opt. Soc. Am. A* 23.10 (2006), pp. 2476–2493.

[315] D. Ramos-Lopez, A. Martinez-Finkelshtein, and D. R. Iskander. "Computational aspects of the through-focus characteristics of the human eye". In: *J. Opt. Soc. Am. A* 31.7 (2014), pp. 1408–1415.

[316] A. E. Conrady. In: *Mon. Not. R. Astron. Soc.* 79 (1919), p. 575.

[317] A. Buxton. In: *Mon. Not. R. Astron. Soc.* 81 (1921), p. 547.

[318] L. C. Martin. In: *Mon. Not. R. Astron. Soc.* 82 (1922), p. 310.

[319] A. Buxton. In: *Mon. Not. R. Astron. Soc.* 83 (1923), p. 475.

[320] R. Kingslake. "The Diffraction Structure of the Elementary Coma Image". In: *Proc. Phys. Soc.* 61.2 (1948), p. 147.

[321] H. H. Hopkins. "The Numerical Evaluation of the Frequency Response of Optical Systems". In: *Proc. Phys. Soc.* 70.10 (1957), p. 1002.

[322] A. C. Ludwig. "Computation of radiation patterns involving numerical double integration". In: *IEEE Trans. Antennas Propag* AP-16 (1968), pp. 767–769.

[323] H. H. Hopkins and M. J. Yzuel. "The Computation of Diffraction Patterns in the Presence of Aberrations". In: *Opt. Act.* 17.3 (1970), pp. 157–182.

[324] L. N. Hazra. "Numerical evaluation of a class of integrals for image assessment". In: *Appl. Opt.* 27.16 (1988), pp. 3464–3467.

[325] T. Gravelsaeter and J. J. Stamnes. "Diffraction by circular apertures. 1: Method of linear phase and amplitude approximation". In: *Appl. Opt.* 21.20 (1982), pp. 3644–3651.

[326] A. Miks, J. Novak, and P. Novak. "Method for numerical integration of rapidly oscillating functions in diffraction theory". In: *Int. J. Numer. Meth. Eng.* 82.4 (2010), pp. 525–536.

[327] J. J. Stamnes, B. Spjelkavik, and H. Pedersen. "Evaluation of Diffraction Integrals Using Local Phase and Amplitude Approximations". In: *Opt. Act.* 30.2 (1983), pp. 207–222.

[328] L. A. D'Arcio, J. J. Braat, and H. J. Frankena. "Numerical evaluation of diffraction integrals for apertures of complicated shape". In: *J. Opt. Soc. Am. A* 11.10 (1994), pp. 2664–2674.

[329] J. A. C. Veerman, J. J. Rusch, and Urbach, H. Paul. "Calculation of the Rayleigh-Sommerfeld diffraction integral by exact integration of the fast oscillating factor". In: *J. Opt. Soc. Am. A* 22.4 (2005), pp. 636–646.

[330] G. A. Evans and J. R. Webster. "A comparison of some methods for the evaluation of highly oscillatory integrals". In: *J. Comput. Appl. Math.* 112.1–2 (1999), pp. 55–69.

[331] A. Iserles and S. P. Norsett. "On Quadrature Methods for Highly Oscillatory Integrals and Their Implementation". In: *Bit. Numer. Math.* 44.4 (2004), pp. 755–772.

[332] S. Olver. "Numerical Approximation of Highly Oscillatory Integrals". PhD thesis. University of Cambridge, 2008.

[333] P. J. Harris and K. Chen. "An efficient method for evaluating the integral of a class of highly oscillatory functions". In: *J. Comput. Appl. Math.* 230.2 (2009), pp. 433–442.

[334] L. F. Shampine. "Integrating oscillatory functions in Matlab". In: *Int. J. Comput. Math.* 88.11 (2011), pp. 2348–2358.

[335] L. F. Shampine. "Matlab program for quadrature in 2D". In: *Appl. Math. Comp.* 202.1 (2008), pp. 266–274.

[336] W. Evans and A. Torre. "On numerical integration with high-order quadratures: with application to the Rayleigh-Sommerfeld integral". In: *Appl. Phys. B* 109 (2012), pp. 295–309.

[337] T. Young. In: *Phil Trans. Roy. Soc.* 92 (1802), p. 26.

[338] G. A. Maggi. "Sulla Propagazione libera e perturbata delle onde luminose in un mezzo isotropo". In: *Ann. Mattem.* 16 (1888), pp. 21–48.

[339] A. Rubinowicz. "Die Beugungswelle in der Kirchhoffschen Theorie der Beugungserscheinungen". In: *Ann. Phys. Lpz.* 53 (1917), pp. 257–278.

[340] A. Rubinowicz. "Zur Kirchhoffschen Beugunstheorie". In: *Ann. Phys. Lpz.* 73 (1924), pp. 339–364.

[341] K. Miyamoto and E. Wolf. "Generalization of the Maggi-Rubinowicz theory of the boundary diffraction wave - Part I". In: *J. Opt. Soc. Am.* 52 (1962), pp. 615–625.

[342] K. Miyamoto and E. Wolf. "Generalization of the Maggi-Rubinowicz theory of the boundary diffraction wave - Part II". In: *J. Opt. Soc. Am.* 52 (1962), pp. 626–637.

[343] J. B. Keller. "Geometrical Theory of Diffraction". In: *J. Opt. Soc. Am.* 52.2 (1962), pp. 116–130.

[344] R. C. Hansen. *Geometric theory of diffraction*. IEEE Press selected reprint series. New York: Institute of Electrical and Electronics Engineers, 1981.

[345] G. L. James. *Geometrical theory of diffraction for electromagnetic waves*. 3. ed. rev. Vol. 1. IEE electromagnetic waves series. Stevenage, Herts.: Peregrinus, 1986.

[346] V. A. Borovikov and B. E. Kinber. *Geometrical theory of diffraction*. Vol. 37. IEE electromagnetic waves series. London: Institution of Electrical Engineers, 1994.

[347] C. J. Ryan and L. Peters. "Evaluation of edge-diffracted fields including equivalent currents for the caustic regions". In: *IEEE T. Antenn. Propag.* 17.3 (1969), pp. 292–299.

[348] W. D. Burnside and L. Peters. "Axial RCS of Finite Cones by the Equivalent Current Concept with Higher Order Diffraction". In: *Radio Sci.* 7.10 (1972), pp. 943–948.

[349] E. F. Knott and T. B. A. Senior. "Comparison of three high-frequency diffraction techniques". In: *Proc. IEEE* 62.11 (1974), pp. 1468–1474.

[350] K. Schwarzschild. "Die Beugungsfigure im Fernrohr weit ausserhalb des Focus". In: *Sitzb. München. Akad. Wiss., Math.-Phys. Kl* 28 (1898), pp. 271–294.

[351] N. G. van Kampen. "An asymptotic treatment of diffraction problems". In: *Physica* 14 (1949), pp. 575–589.

[352] A. Erdelyi. *Asymptotic expansions*. repr. New York, NY: Dover, 1956.

[353] R. B. Dingle. *Asymptotic expansions: Their derivation and interpretation*. London: Acad. Press, 1973.

[354] P. S. Kildal. "Asymptotic approximations of radiation integrals: Endpoint and double endpoint diffraction". In: *Radio Sci.* 19 (1984), pp. 805–811.

[355] A. W. Greynolds. "Propagation of generally astigmatic Gaussian beams along skew ray paths". In: *Proc. SPIE* 560 (1985), pp. 33–50.

[356] J. E. Harvey, R. G. Irvin, and R. N. Pfisterer. "Modeling physical optics phenomena by complex ray tracing". In: *Opt. Eng.* 54.3 (2015), p. 035105.

[357] A. W. Greynolds. "Vector formulation of the ray-equivalent method for general Gaussian beam propagation". In: *Proc. SPIE* 679 (1986), pp. 129–133.

[358] S. van Haver and Janssen, A. J. E. M. "Truncation of the series expressions in the advanced ENZ-theory of diffraction integrals". In: *J. Europ. Opt. Soc. Rap. Public.* (2014).

[359] J. J. Braat. "Correction factor Debye integral for the small numerical aperture case". Delft, August 31, 2009.

[360] E. O. Brigham. *The fast Fourier transform and its applications*. Prentice-Hall signal processing series. Englewood Cliffs, N.J: Prentice Hall, 1988.

[361] F. Zhang, G. Pedrini, and W. Osten. "Reconstruction algorithm for high-numerical-aperture holograms with diffraction-limited resolution". In: *Opt. Lett.* 31.11 (2006), pp. 1633–1635.

[362] K. Matsushima. "Shifted angular spectrum method for off-axis numerical propagation". In: *Opt. Express* 18.17 (2010), pp. 18453–18463.

[363] L. R. Rabiner, R. W. Schafer, and C. M. Rader. "The Chirp z-Transform Algorithm and Its Application". In: *Bell System Technical Journal* 48.5 (1969), pp. 1249–1292.

[364] L. Bluestein. "A linear filtering approach to the computation of discrete Fourier transform". In: *IEEE Transactions on Audio and Electroacoustics* 18.4 (1970), pp. 451–455.

[365] V. Nascov and P. C. Logofatu. "Fast computation algorithm for the Rayleigh-Sommerfeld diffraction formula using a type of scaled convolution". In: *Appl. Opt.* 48.22 (2009), pp. 4310–4319.

[366] J.-c. Li, P. Tankam, Z.-j. Peng, and P. Picart. "Digital holographic reconstruction of large objects using a convolution approach and adjustable magnification". In: *Opt. Lett.* 34.5 (2009), pp. 572–574.

[367] S. Odate, C. Koike, H. Toba, et al. "Angular spectrum calculations for arbitrary focal length with a scaled convolution". In: *Opt. Express* 19.15 (2011), pp. 14268–14276.

[368] X. Yu, T. Xiahui, Q. Yingxiong, et al. "Band-limited angular spectrum numerical propagation method with selective scaling of observation window size and sample number". In: *J. Opt. Soc. Am. A* 29.11 (2012), pp. 2415–2420.

[369] T. Shimobaba, K. Matsushima, T. Kakue, et al. "Scaled angular spectrum method". In: *Opt. Lett.* 37.19 (2012), pp. 4128–4130.

[370] B. M. Hennelly, D. P. Kelly, D. S. Monaghan, and N. Pandey. "Zoom Algorithms for Digital Holography". In: *Information Optics and Photonics*. Ed. by B. Javidi and T. Fournel. Springer New York, 2010, pp. 187–204.

[371] M. Hillenbrand, A. Hoffmann, D. P. Kelly, and S. Sinzinger. "Fast non-paraxial scalar focal field calculations". In: *J. Opt. Soc. Am. A* 31.6 (2014), pp. 1206–1214.

[372] L. Onural. "Sampling of the Diffraction Field". In: *Appl. Opt.* 39.32 (2000), pp. 5929–5935.

[373] L. Onural. "Exact analysis of the effects of sampling of the scalar diffraction field". In: *J. Opt. Soc. Am. A* 24.2 (2007), pp. 359–367.

[374] P. Picart and P. Tankam. "Analysis and adaptation of convolution algorithms to reconstruct extended objects in digital holography". In: *Appl. Opt.* 52.1 (2013), A240–A253.

[375] D. Mas, J. Garcia, C. Ferreira, et al. "Fast algorithms for free-space diffraction patterns calculation". In: *Opt. Commun.* 164.4–6 (1999), pp. 233–245.

[376] K. Matsushima and T. Shimobaba. "Band-limited angular spectrum method for numerical simulation of free-space propagation in far and near fields". In: *Opt. Express* 17.22 (2009), pp. 19662–19673.

[377] A. Stern and B. Javidi. "Sampling in the light of Wigner distribution". In: *J. Opt. Soc. Am. A* 21.3 (2004), pp. 360–366.

[378] T. Kozacki. "Numerical errors of diffraction computing using plane wave spectrum decomposition". In: *Opt. Commun.* 281.17 (2008), pp. 4219–4223.

[379] T. Kozacki, K. Falaggis, and M. Kujawinska. "Computation of diffracted fields for the case of high numerical aperture using the angular spectrum method". In: *Appl. Opt.* 51.29 (2012), pp. 7080–7088.

[380] D. P. Kelly, W. T. Rhodes, J. T. Sheridan, and B. M. Hennelly. "Analytical and numerical analysis of linear optical systems". In: *Opt. Eng.* 45.8 (2006), p. 088201.

[381] D. P. Kelly. "Numerical calculation of the Fresnel transform". In: *J. Opt. Soc. Am. A* 31.4 (2014), pp. 755–764.

[382] A. W. Lohmann, R. G. Dorsch, D. Mendlovic, et al. "Space-bandwidth product of optical signals and systems". In: *J. Opt. Soc. Am. A* 13.3 (1996), pp. 470–473.

[383] D. Mas, J. Pérez, C. Hernández, et al. "Fast numerical calculation of Fresnel patterns in convergent systems". In: *Opt. Commun.* 227.4–6 (2003), pp. 245–258.

[384] D. Mendlovic and A. W. Lohmann. "Space–bandwidth product adaptation and its application to superresolution: fundamentals". In: *J. Opt. Soc. Am. A* 14.3 (1997), pp. 558–562.

[385] D. Mendlovic, A. W. Lohmann, and Z. Zalevsky. "Space–bandwidth product adaptation and its application to superresolution: examples". In: *J. Opt. Soc. Am. A* 14.3 (1997), pp. 563–567.

[386] A. V. Oppenheim and R. W. Schafer. *Discrete-time signal processing*. 3. ed., internat. ed. Upper Saddle River, NJ [u.a.]: Pearson, 2010.

[387] Saleh, Bahaa E. A. and M. C. Teich. *Fundamentals of photonics*. 2nd ed. Wiley Series in Pure and Applied Optics. Hoboken, N.J: Wiley Interscience, 2007.

[388] D. P. Kelly, J. T. Sheridan, and W. T. Rhodes. "Finite-aperture effects for Fourier transform systems with convergent illumination. Part I: 2-D system analysis". In: *Opt. Commun.* 263.2 (2006), pp. 171–179.

[389] D. P. Kelly, B. M. Hennelly, J. T. Sheridan, and W. T. Rhodes. "Finite-aperture effects for Fourier transform systems with convergent illumination. Part II: 3-D system analysis". In: *Opt. Commun.* 263.2 (2006), pp. 180–188.

[390] P. Lobaz. “Reference calculation of light propagation between parallel planes of different sizes and sampling rates”. In: *Opt. Express* 19.1 (2011), pp. 32–39.

[391] D. Asoubar, Z. Site, F. Wyrowski, and M. Kuhn. “Parabasal field decomposition and its application to non-paraxial propagation”. In: *Opt. Express* 20.21 (2012), pp. 23502–23517.

[392] M. Kanka, R. Riesenberg, and H. J. Kreuzer. “Reconstruction of high-resolution holographic microscopic images”. In: *Opt. Lett.* 34.8 (2009), pp. 1162–1164.

[393] M. Kanka, A. Wuttig, C. Graulig, and R. Riesenberg. “Fast exact scalar propagation for an in-line holographic microscopy on the diffraction limit”. In: *Opt. Lett.* 35.2 (2010), pp. 217–219.

[394] M. Kanka. “Bildrekonstruktion in der digitalen inline-holographischen Mikrsokopie”. PhD thesis. Technische Universität Ilmenau, 2011.

[395] P. Lobaz. “Memory-efficient reference calculation of light propagation using the convolution method”. In: *Opt. Express* 21.3 (2013), pp. 2795–2806.

[396] A. Wuttig, M. Kanka, H. J. Kreuzer, and R. Riesenberg. “Packed domain Rayleigh-Sommerfeld wavefield propagation for large targets”. In: *Opt. Express* 18.26 (2010), pp. 27036–27047.

[397] F. Gori. “Fresnel transform and sampling theorem”. In: *Opt. Commun.* 39.5 (1981), pp. 293–297.

[398] M. Hillenbrand, B. Mitschunas, F. Brill, et al. “Spectral characteristics of chromatic confocal imaging systems”. In: *Appl. Opt.* 53.32 (2014), pp. 7634–7642.

[399] V. N. Mahajan. *Optical Imaging and Aberrations, Part II: Wave Diffraction Optics*. 2nd ed. PM209. Bellingham: Society of Photo-Optical Instrumentation Engineers (SPIE), 2011.

[400] P. E. R. A. Stokseth, S. Diego, La Jolla, and P. Agency. “Properties of a Defocused Optical System”. In: *J. Opt. Soc. Am.* 59.10 (1969), pp. 1314–1321.

[401] H.-C. Lee. “Review of image-blur models in a photographic system using the principles of optics”. In: *Opt. Eng.* 29.5 (1990), pp. 405–421.

[402] A. E. Savakis and H. J. Trussell. “On the accuracy of PSF representation in image restoration”. In: *IEEE T. Image Process.* 2.2 (1993), pp. 252–259.

[403] M. Subbarao and G. Surya. “Depth from defocus: A spatial domain approach”. In: *Int. J. Comput. Vision* 13.3 (1994), pp. 271–294.

[404] M. Sakano, N. Suetake, and E. Uchin. “A robust point spread function estimation for out-of-focus blurred and noisy images based on a distribution of gradient vectors on the polar plane”. In: *Opt. Rev.* 14.5 (2007), pp. 297–303.

[405] A. P. Pentland. “A new sense for depth of field”. In: *IEEE T. Pattern Anal.* 4 (1987), pp. 523–531.

[406] J. Jahns and S. J. Walker. “Two-dimensional array of diffractive microlenses fabricated by thin film deposition”. In: *Appl. Opt.* 29 (1990), pp. 931–936.

[407] H. Gross, H. Zügge, M. Peschka, and F. Blechinger. *Handbook of optical systems*. Vol. / ed. by Herbert Gross ; Vol. 3. Handbook of optical systems. Weinheim: Wiley-VCH-Verl, 2007.

[408] J. F. Aguilar and E. R. Mendez. “On the Limitations of the Confocal Scanning Optical Microscope as a Profilometer”. In: *J. Mod. Optic.* 42.9 (1995), pp. 1785–1794.

[409] C. Wenzel. “Entwurf eines hybriden Sensors nach dem chromatisch konfokalen Messprinzip”. PhD thesis. Ilmenau: Technische Universität Ilmenau, 2011.

[410] M. Rahlves, B. Roth, and E. Reithmeier. “Systematic errors on curved microstructures caused by aberrations in confocal surface metrology”. In: *Opt. Express* 23.8 (2015), pp. 9640–9648.

[411] M. Bass, V. N. Mahajan, Van Stryland, Eric W, et al. *Handbook of optics*. 3rd ed. New York: McGraw-Hill, 2010.

[412] P. Török, S. J. Hewlett, and P. Varga. “The role of specimen-induced spherical aberration in confocal microscopy”. In: *J. Microsc.* 188.2 (1997), pp. 158–172.

[413] T. Wilson, ed. *Confocal microscopy*. London and San Diego: Academic Press, 1990.

[414] G. Courtes. “An Integral Field Spectrograph (IFS) for Large Telescopes”. In: *Instrumentation for Astronomy with Large Optical Telescopes*. Ed. by C. M. Humphries. Vol. 92. Astrophysics and Space Science Library. Dordrecht: Springer Netherlands, 1982, pp. 123–128.

[415] C. Endrödy, H. Mehner, A. Grewe, and M. Hoffmann. “Linear micromechanical stepping drive for pinhole array positioning”. In: *J. Micromech. Microeng.* 25.5 (2015), p. 055009.